UNIVERSITÉ LOUIS PASTEUR STRASBOURG

N° d'ordre : 5486

Thèse présentée pour obtenir le grade de
Docteur de l'Université Louis Pasteur
Strasbourg I

Discipline: Télédétection

par Geng-Ming JIANG

Retrievals of land surface emissivity and land surface temperature from MSG1-SEVIRI data

Soutenue publiquement le 29 Octobre 2007

Membres du jury

Directeur de Thèse : M. Zhao-Liang LI
Rapporteur Interne : M. Ernest HIRSCH
Rapporteur Externe : M. José A. SOBRINO
Rapporteur Externe : M. Zhongbo SU

There is no royal road to science, and only those who do not dread the fatiguing climb of its steep paths have a chance of gaining its luminous summits.

Karl Marx, German revolutionist

Acknowledgments

I would like to give foremost thanks to my supervisor, Dr. Li Zhao-Liang, for his instructions in my PhD research. As Chinese, I learned lots of things from him in the past three years, which would help me succeed in my new career.

I appreciate Dr. Cheng Wang for his help in my application of the PhD candidate position. I am thankful to the head of TRIO (Télédétection Radiométrie Imagerie Optique), Dr. Françoise Nerry, for her helpful attitude in solving many of the administrative affaires and to all my colleagues in TRIO, and they are Prof. Marc-Philippe Stoll, Raphaël Luhahé, Dr. Jélila Labed, Prof. Marcel Raffy, Dr. Yoshitate Takakura, Dr. Jérôme Colin, Jawad ElSayed Ahmad, Samia Aïnouz, Weimin Wang, Qingfeng Shen, Roman Roux, and etc. Thanks are given to my friends known in Strasbourg. I spent lots of happy time with them, and I will never forget them.

Special thanks are given to the reviewers, Prof. Ernest HIRSCH, Prof. José A. SOBRINO and Prof. Zhongbo (Bob) SU, for their hard work and valuable advice to perfect my thesis.

My sincere thanks are given to my wife for her unselfish support and sacrefice. It is my wife who always supports and encourages me to continue and it comes today. Sincere thanks are also given to my parents and my siblings. They concern everything I did and everything happened to me, and they are always proud of me. Their supports go with my growth, and I do not let them be disappointed.

It is difficult for me to quote everyone here. I simply make a point of saying that I appreciate everyone who helped me or gave me spirit supports.

This research was fully funded by the project EAGLE (Exploitation of AnGular effects in Land surfacE observations from satellites) through contract No.: SST3 CT2003 502057 in the Sixth Framework Program (FP6) of EU.

Résumé

L'étude de la biosphère terrestre et de son évolution prend actuellement une place très importante à l'échelle internationale. La découverte de phénomènes comme le réchauffement de l'atmosphère terrestre par effet de serre en est d'un exemple marquant. Les conclusions du dernier IPCC (Intergovermental Panel on Climate Change) confirment la nécessité d'une telle étude. Pour réaliser le suivi et l'analyse de l'évolution de notre planète, un certain nombre de grands programmes nationaux et internationaux ainsi que le Programme Mondial de Recherche sur le Climat (World Climate Research Project: WCRP) ont été élaborés. Parmi les "variables diagnostiques" caractérisant l'évolution de la planète et l'état de notre environnement, la température de surface tient une place particulière. La température de surface (LST) est en effet un paramètre commun à plusieurs thématiques et sa connaissance donne des informations sur les variations spatio-temporelles de l'état d'équilibre de surface. De ce fait, elle est reconnue comme un des paramètres prioritaires et fait l'objet d'attentions particulières dans l'étude de notre environnement. Un autre paramètre important est l'émissivité de surface (ε). Sa connaissance permet en effet, de contribuer à la discrimination des différents types de surface et à la détermination par radiométrie passive de la température de surface.

Pour obtenir une analyse régionale et globale, la télédétection infrarouge thermique (IRT) est donc un outil extrêmement intéressant. La télédétection IRT a essentiellement pour objectif la mesure de la température et de l'émissivité de surface. En effet, dans l'IRT, le rayonnement émis par la surface terrestre dépend non seulement de sa température, mais aussi de son émissivité. Cet avantage a son revers car, indépendamment des problèmes atmosphéri ques présents dans tous les domaines spectraux, l'interprétation quantitative des données radiométriques dans le domaine IRT est particulièrement difficile. Il n'est en effet pas possible en radiométrie passive de séparer, sur des bases physiques, dans la luminance observée, les contributions dues à l'émissivité des contributions dues à la température de surface. Pour cette raison, la détermination de la température de surface à partir de l'espace nécessite non seulement des corrections atmosphériques, mais également la connaissance de l'émissivité.

Ce travail porte sur l'élaboration et la mise au point de méthodes permettant de déterminer à la fois la température et l'émissivité de surface à partir des données d'instrument SEVIRI (Spinning Enhanced Visible and Infra-Red Imager) embarqué sur la deuxième génération des satellites Météosat (MSG). Il s'inscrit dans le projet EAGLE (Exploitation of AnGular effects in Land surfacE observations from satellites) retenu et financé par la Commission Européenne dans le cadre du programme FP6 pour une période de 3 ans et demi à partir du 1er février 2004. Cette étude a comme objectifs scientifiques d'évaluer et de minimiser ou de corriger des effets angulaires et temporels induits inévitablement sur des données satellitaires comme les instruments MODIS, AATSR, SEVIRI.

Cette thèse comprend 7 chapitres.

Le première chapitre est une introduction.

Dans le deuxième chapitre, nous rappelons les définitions de base de radiométrie IRT en mettant l'accent sur la problématique méthodologique et instrumentale de la mesure des paramètres de surface. Nous décrivons ensuite brièvement le code de transfert radiatif MODTRAN, développé par l'AFRL pour calculer la transmission atmosphérique et la luminance émise par l'atmosphère à la résolution spectrale de 2 cm-1 (20 cm-1 dans les UV), et les principaux caractéristiques de l'instrument SEVIRI à bord du satellite MSG (la deuxième génération du satellite géostationnaire) développé par l'Agence spatiale européenne (ESA) et EUMETSAT. A la fin de ce chapitre, nous donnerons la description des données SEVIRI (niveau 1.5) fournies par l'EUMETSAT.

Le troisième chapitre de ce travail est consacré à l'inter-étalonnage des canaux infrarouge thermiques (IRT) et infrarouge moyens (IRM) de SEVIRI avec les canaux MODIS considérés ici comme bien étalonnés. Cette étape est essentielle pour assurer la qualité radiométrique des données SEVIRI permettant de restituer la température et l'émissivité de surface avec une précision acceptable.

Deux méthodes, l'une basée sur le principe de correspondance de raies (ray-matching), et l'autre sur le transfert radiatif, sont présentées et appliquées à l'inter-étalonnage des canaux 4, 9 et 10 de SEVIRI/MSG. La méthode "ray-matching", qui ne prend pas en compte les différences spectrales des différents capteurs, est simple et directe. Elle utilise les pixels coïncidents spatialement et temporellement sous les mêmes angles d'observations pour transférer l'étalonnage d'un capteur considéré comme bien calibré à un autre. La méthode de transfert radiatif est une façon plus complexe de transférer l'étalonnage, Elle est basée sur la théorie du transfert radiative et sur des mesures coïncidentes.

Les données du niveau 1.5 de MSG1-SEVIRI, le masque de nuage de MSG, les données du niveau L1B de MODIS (MOD021KM) et les données géographiques de MODIS (MOD03) sur la zone tropicale (Longitude: 45W-45E; latitude: 10S-10N) en juillet 2005 et 2006 ont été utilisées. Les résultats obtenus par les deux méthodes d'inter-étalonnage ont montré que les étalonnages à bord des canaux 4, 9 et 10 de SEVIRI sont cohérents entre les années 2005 et 2006, les canaux 9 et 10 de SEVIRI sont bien étalonnés, par contre, pour le canal 4 de SEVIRI, la différence de température de brillance entre SEVIRI et MODIS varie de 0.8 K à -1.9 K quand la BT varie de 280 K à 320 K.

Ce travail a fait l'objet d'un article qui a été soumis à la revue 'International Journal of Remote Sensing' en Février 2007.

Nous abordons dans le quatrième chapitre la restitution de l'émissivité de surface à partir d'une combinaison des données IRT et IRM de SEVIRI/MSG. L'estimation directe de l'émissivité de surface à partir des données satellites est impossible, et les difficultés principales viennent de la correction des effets atmosphériques et de la séparation entre la température et l'émissivité de surface dans la luminance mesurée. Pour corriger les effets atmosphériques, une nouvelle méthode a été développée tant pour les canaux IRM que pour les canaux IRT. Pour les canaux IRM, compte tenu qu'ils sont moins sensibles à la variation de vapeur d'eau dans l'atmosphère, les données atmosphériques (fournies par l'ECMWF : European Centre for Median-range Weather Forecast) les plus proches en temps de l'acquisition des données satellitaires ont été utilisées pour les images où aucune autre donnée atmosphérique n'est disponible. Pour les canaux IRT, un modèle décrivant le cycle diurne de la température de surface journalière a été développé. La séparation de la température et l'émissivité de surface est basée sur le concept des Indices Spectraux Indépendants de Température (TISI) construit avec un canal dans IRM et un canal dans IRT. Le modèle de type RossThick-LiSparse BRDF a été adopté et utilisé pour décrire la réflectivité bidirectionnelle dans le canal IRM. Les résultats de deux combinaisons différentes (combinaison de canaux 4 et 9 et de canaux 4 et 10 de

SEVIRI) et de deux jours successifs sur six sites spécifiques à l'Afrique du Nord (Longitude : 7.0E-15.7E; latitude : 30.2N-37.7N) montrent que les restitutions des émissivités sont cohérentes. La variation de l'émissivité dans le canal 4 de MSG1-SEVIRI est de 0.5 pour des sols nus à 0.96 pour des végétations denses, tandis que les émissivités dans les canaux MSG1-SEVIRI 9 et 10 sont entre 0.9 à 0.95 pour des sols nus et entre 0.95 à 1.0 pour les végétations denses. Pour les végétations denses, l'émissivité dans le canal de MSG-SEVIRI 9 est plus grande que celle dans le canal 10, tandis que l'inverse est observé sur des sols nus. L'écart type entre deux combinaisons de canaux sur toute la région étudiée est 0.017 pour l'émissivité dans le canal 4, 0.008 pour l'émissivité dans le canal 9 et 0.007 pour l'émissivité dans le canal 10.

Les restitutions des émissivités ont été ensuite effectuée à une zone (région) plus étendue (Longitude : 20W-60E; latitude : 0-60N) et dans saisons différentes. Les cartes d'émissivité en 2004, 2005 et 2006 ont été produites pour cette zone étendue.

Ce travail a donné lieu à une publication dans la revue 'Remote Sensing of Environment'.

Le cinquième chapitre se rapporte à la détermination de la température de surface à partir des données dans les canaux 9 (10.8 μm) et 10 (12.0 μm) de MSG1-SEVIRI. Deux méthodes de la restitution ont été utilisées : la méthode mono canal et la méthode multispectrale (méthode de type Split-Window). La méthode à mono canal consiste à utiliser un modèle de transfert radiatif de l'atmosphère de façon à évaluer les termes de l'équation de transfert radiatif en fournissant le profil atmosphérique qui peut être obtenu, soit par radiosondages, soit par des sondeurs satellitaires verticaux, soit encore à partir de données climatiques. La précision obtenue pour la température de surface restituée en utilisant cette méthode est directement liée à la précision avec laquelle sont connus le profil de l'atmosphère ainsi que l'émissivité de surface, et évidemment à la qualité du modèle de transfert radiatif atmosphérique. Les données dans le canal 9 de MSG-SEVIRI ont été utilisées du fait de sa moins sensibilité à la variation de vapeur d'eau atmosphérique. La méthode de type split-window est le plus souvent utilisée dans la bande 10.5-12.5μm. Elle repose sur l'absorption différentielle atmosphérique dans deux canaux adjacents. Le différentiel d'atténuation atmosphérique n'est pratiquement déterminé que par la seule absorption due à la vapeur d'eau. Cette méthode consiste à exprimer la température de surface cherchée sous la forme d'une combinaison linéaire des températures de brillance mesurées dans les deux canaux adjacents. Compte tenu de la grande simplicité de cette méthode, nous l'avons adoptée dans notre étude pour la détermination de la température de surface à partir des données SEVIRI. En utilisant les quatre atmosphères standards prescrites dans le code MODTRAN et en considérant les géométries d'observation de SEVIRI, nous avons pu développer un algorithme de type split-window pour SEVIRI. Les résultats de simulation montrent que la température de surface peut être obtenue par cet algorithme avec une précision meilleure que 1K pour des angles d'observation inférieurs à 50 degrés.

En appliquant la méthode Split Window et la méthode à mono canal sur les zones de la péninsule de l'Ibérie et d'Afrique du Nord, nous avons constaté que les deux températures sont en bon accord, la différence moyenne étant inférieure à 1 K.

Le sixième chapitre est consacré à une validation (intercomparaison) de la température de surface obtenue à partir des données SEVIRI avec celles obtenue à partir des données MODIS et AATSR. La validation de la température de surface obtenue par satellite avec des mesures de terrain est une tâche difficile, car la mesure satellite représente une zone de km×km souvent hétérogène, tandis que la mesure de terrain représente au mieux quelques m2. Du fait de la basse résolution spatiale de mesures IRT (3km × 3km) SEVIRI, il est difficile de trouver un site homogène étendu pour valider la

température de surface obtenue à partir des données SEVIRI. Nous avons donc proposé dans cette étude de la comparer avec le produit de la température de surface considéré bien validé obtenu avec les données MODIS. Nous avons aussi comparé cette température obtenue par SEVIRI avec celle obtenue par AATSR.

Un ré-échantillonnage spatial pondéré de la surface a été effectué pour mettre toutes les températures de surface obtenues à partir des données AATSR, des données MODIS et des données MSG-SEVIRI dans le système de coordonnée WGS 84 (le Système Géodésique Mondial 1984) avec une résolution 0.1×0.1 en longitude et latitude. Les résultats de cette intercomparaison montrent que toutes les températures de surface obtenues sont en bon accord avec une différence comprise entre 1-2 K.

Il faut noter que, bien qu'une image de disque terrestre est acquise par le MSG1-SEVIRI au même temps UTC, les heures locales des pixels diffèrent de l'un à l'autre. Ceci empêchera des applications de la température de surface à l'échelle régionale et globale. Dans notre étude, le modèle du cycle diurne de la température journalière développé dans le chapitre précédent a été utilisé pour chaque pixel pour produire une carte de la température de surface à la même heure locale pour tous les pixels. Plusieurs cartes de la température de surface couvrant l'Europe et l'Afrique du Nord ont ainsi été produites.

En conclusion, ce travail a permis de montrer l'avantage des satellites géostationnaires pour la détermination des émissivités de surface par rapport aux satellites polaires et de proposer des méthodes permettant d'inter-étalonner les instruments et de calculer la température de surface à partir des luminances mesurées par les satellites géostationnaires. Ce travail a aussi montré qu'il était possible de corriger les effets atmosphériques canal par canal en utilisant des données atmosphériques fournies par l' ECMWF et le modèle du cycle diurne de la température de surface journalière.

Ce travail ouvre des perspectives intéressantes. Dans la restitution de l'émissivité de surface, l'exactitude de cette restitution dépend principalement de l'exactitude de correction atmosphérique et de la performance du modèle BRDF. Les performances du modèle RossThick-LiSparse BRDF et du nouvel schéma de correction atmosphérique développés dans cette étude devront donc être évaluée de façon précise

Bien que la restitution de la température de surface à partir des données IRT soit une approche maintenant mûre, elle est vulnérable à l'impact de nuages. La télédétection micro-onde passive permet observer la terre dans presque toutes les conditions atmosphériques. Cependant, la méthodologie de détermination de cette température à partir des données micro-ondes passives n'est pas encore bien établie et doit être développée. La combinaison des données IRT et micro-onde est un axe prometteur pour la détermination de la température de surface pour toutes les conditions atmosphériques et avec une résolution spatiale adéquate.

Table of contents

List of Figures

List of Tables

Remote Sensing is not a panacea for resource development and management problems. However it can provide the data which are the basic tools for sound resource inventorying, monitoring and management.

Bale *et al*. 1974

1 Introduction

Currently, the study of the terrestrial biosphere and its evolution is a hot topic on an international scale. Scientists are accumulating evidence that human industrial and agricultural activities may be accelerating naturally occurring changes in our climate, and that we are contributing to such hazards as global warming, rising sea level, ozone depletion, acid rain, and loss of biodiversity. The conclusions of the recent IPCC (Intergovemental Panel on Climate Changes) confirm the need for such study. A number of national and international programs, such as the World Research Program on the Climate (World Climate Research Project: WCRP), are focusing on this study. Among the "diagnostic variables" characterizing the evolution of the Earth and the state of our environment, Land Surface Temperature (LST) holds an important place.

LST is one of the key parameters in the physics of land surface processes, combining surface-atmosphere interactions and the energy fluxes between the atmosphere and the ground (Sellers et al., 1988). LST is required for a wide variety of scientific studies – from climatology to hydrology to ecology and biogeology, such as the energy budget modeling and evaportranspiration modeling (Serafini, 1987; Bussieres et al., 1990), estimating soil moisture (Price, 1990), frost detection and forecasting, monitoring the state of the crops (Casellas and Sobrino, 1989), studying land and sea breezes and nocturnal cooling. LST is also a good indicator of the greenhouse effect, and radiative transfer simulations based on observed surface temperature data show a positive correlation between the normalized greenhouse effect and the surface temperature (Sinha, 1995). Accurate LSTs would not only help estimating surface energy and water balances, thermal inertia and soil moisture (Seguin et al., 1994; Tarpley, 1994; Sobrino et al., 1998;), it would also enable an analysis of the global surface temperature and its variability within a long period of time.

One key parameter to derive LST is Land Surface Emissivity (LSE). LSE is the ratio of the radiance emitted by an actual land surface at some temperature to the theoretical radiance emitted by a blackbody with the same temperature. It is a measure of a material's ability to absorb and radiate energy. LSE is an intrinsic property of the surface and is almost independent of temperature under

natural conditions (Becker and Li, 1990a), e.g., the channel-averaged emissivity in AVHRR channel 3 for coarse sand changes only 0.004 over the temperature range of 240-320 K (Wan and Dozier, 1996). Different materials possess different spectral behavior (Salisbury and D'Aria, 1992), and LSE may vary with view angles (Dozier and Warren, 1982; Labed and Stoll, 1991; Rees and James, 1992). LSE can also support more accurate retrievals of atmospheric properties, such as temperature and moisture profiles from multi-spectral satellite radiance measurement.

Satellite remote sensing is the only viable means to extract long-term and large-scale LSTs (Goïta and Royer, 1997). During the past decades, a series of sensors have been developed and launched into space, such as the Advanced Very High Resolution Radiometer (AVHRR), the MODerate resolution Imaging Spectroradiometer (MODIS) and the Advanced Along Track Scanning Radiometer (AATSR), which are respectively onboard the polar-orbit satellites NOAA, Terra/Aqua and ENVISAT. Because of the heterogeneity of land surface, the satellite measurements usually come from mixed pixels. At satellite pixel scale, LSE refers to the area-weighted and channel-averaged emissivity, and LST refers to the radiometric surface temperature corresponding to the Field Of View (FOV) of a radiometer (Becker and Li, 1995; Norman and Becker, 1995; Prata et al., 1995; Wan and Dozier, 1996).

However, direct estimation of LSE and LST from passive satellite measurements is not possible. Besides the atmospheric perturbations, the separation between LST and LSE is also a challenge in passive Thermal InfraRed (TIR) remote sensing. The reason lies in the "missing equation": Independent of the atmospheric effects in all optical spectral regions, for a sensor with N infrared spectral channels, there are N measurements but N+1 unknown (N channel emissivities plus one surface temperature). For resolving this ill-posed problem, additional assumptions are necessary to constrain the extra degree-of-freedom, which has led to different temperature-emissivity separation methods. The temperature-emissivity separation methods include the classification-based emissivity retrieval method (Snyder et al., 1998), the reference channel method (Vincent et al., 1975; Kahle et al., 1980; Kahle, 1987; Kahle and Alley, 1992), the emissivity normalization method (Gillespie, 1985 & 1998; Realmuto, 1990), the spectral ratio method (Watson, 1992a), the two-temperature method (Watson, 1992b), the alpha emissivity method (Kealy and Gabell, 1990) and the physics-based emissivity-temperature decoupling method based on Temperature Independent Spectral Indices (TISI) concept (Becker and Li, 1990a). The TISI method has been successfully applied to the LSE retrievals from the data in AVHRR channels 3, 4 and 5 (Goïta and Royer, 1997; Nerry et al., 1998; Sobrino, 2001; petitcolin et al., 2002a, 2002b; Dash et al., 2005) and from the data in MODIS channels (Petitcolin and Vermote, 2002). However, because both the AVHRR and MODIS instruments are onboard the polar-orbit satellites, the actual pixels sizes may be different for a given area from one overpass to another due to different view angles and this will introduce large errors if the land surface is heterogeneous. Furthermore, to obtain sufficient number of angle configurations for the bi-directional reflectivities used in the retrieval of the emissivity in MIR (Mid-Infra-Red) channel, usually 2- to 3-month observations are required and land surface properties may change during that long period.

LST retrieval algorithms are based on the radiative transfer theory, and the single channel method (Ottlé and Vidal-Madjar, 1992) and the split-window method (McMillin, 1975) are two commonly used algorithms. The split-window method was originally proposed to estimate sea surface temperature from satellite measurements based on the differential absorption in two adjacent infrared channels, and then was extended to land surface. The simple extension to land surface of the split-window methods developed for sea surface temperature estimation would lead to unacceptable errors,

and the main reasons lie in the spectral and spatial variations of LSE, temperature variation, heterogeneous land surfaces, and atmospheric variation (Price, 1984; Becker, 1987; Wan and Dozier, 1989). The split-window method has been improved and successfully applied to the LST retrievals from the infrared data of AVHRR and MODIS (Price, 1984; Becker, 1987; Becker and Li, 1990b; Kerr et al., 1992; Prata, 1993 & 1994; Wan and Dozier, 1989 & 1996; Sobrino et al., 1991, 1994 & 1996). Furthermore, the validation of LSTs estimated from satellite remote sensing data with in situ measurements is very difficult because of the high spatial variations in LSTs.

Meteosat Second Generation (MSG) is a new generation of the geostationary satellite developed by European Space Agency (ESA) and EUropean organization for the exploitation of METeorological SATellite (EUMETSAT). MSG's main payload is the optical imaging radiometer, the so called Spinning Enhanced Visible and Infrared Imager (SEVIRI). SEVIRI has 12 spectral channels covering from visible to infrared (Schmetz et al., 2002a), and provides measurements of the Earth-disc every 15 minutes at fixed view angles, but the solar angles change every 15 minutes during daytime, making it particularly suitable for LSE and LST determinations by the day/night TISI concept.

The research work of this thesis, which was fully financed by the EAGLE project (Exploitation of AnGular effects in Land surface observations from satellites; Contract No.: SST3 CT2003 502057), focuses on the retrievals of LSE and LST from the infrared data of MSG1-SEVIRI (Meteosat Second Generation-1 – Spinning Enhanced Visible and Infra-Red Imager) and the LST cross-validations with the MODIS/Terra LST products and the AATSR LSTs.

The thesis is organized into seven chapters. Chapter 2 describes the fundamental radiometric theory, MODTRAN, sensors and data. Chapter 3 aims at the cross-calibrations of MSG1-SEVIRI infrared channels 4, 9 and 10 with the channels of Terra-MODIS. Two methods, the ray-matching method and the radiative transfer modeling method, were developed. Chapter 4 presents the land surface emissivity retrievals from the infrared data of MSG1-SEVIRI based on the TISI concept, in which a new atmospheric correction scheme was developed and two BRDF models were evaluated. Chapter 5 depicts the land surface temperature retrievals from MSG1-SEVIRI data and AATSR data, including the single channel method and the generalized split-window method. The time normalization of the SEVIRI LSTs by the Diurnal Temperature Cycle (DTC) model was also presented in this chapter. Chapter 6 is devoted to the SEVIRI LST cross-validations with the MODIS/Terra LST products and the AATSR LST. The last chapter is the summary and conclusions.

2 Fundamental radiometric theory, MODTRAN, sensors and data

2.1 Fundamental radiometric theory for remote sensing over infrared spectrum

According to the Planck's law, the spectral radiance of electromagnetic radiation from a black body is related to the temperature T:

$$L(T,\lambda) = \frac{C_1}{\lambda^5\left[\exp(C_2/\lambda T)-1\right]} \tag{2.1}$$

with C_1=1.19104×10^8 Wm^2 μm^4 sr^{-1} and C_2=1.43877×10^4 μm K.

where L(T, λ) is the energy that is quantifiable in terms of spectral radiance (W m^{-2} sr^{-1} μm^{-1}), defined as the energy per unit time per unit wavelength per unit solid angle crossing an unit area perpendicular to the viewing direction of the sensor, and λ is the wavelength in μm.

An important parameter connected to the spectral radiance is the spectral emissivity, $\varepsilon(\theta_v, \lambda)$, which is the ratio of the spectral radiance actually emitted by an object with some temperature at a view zenith angle θ_v to the spectral radiance emitted by a black body at the same temperature given by Equation (2.1). According to the difinition, only the black body has an emissivity of 1, and the natural bodies are usually non-black bodies (i.e., $0<\varepsilon(\theta_v,\lambda)<1$). Hence, spectral radiance emitted at wavelength λ (μm) from a natural surface (non-black body) at temperature T_s (K) is given by the spectral emissivity times the Planck's function:

$$L(T_s,\theta_v,\lambda) = \varepsilon(\theta_v,\lambda)L(T_s,\lambda) = \varepsilon(\theta_v,\lambda)\frac{C_1}{\lambda^5\left[\exp(C_2/\lambda T_s)-1\right]} \tag{2.2}$$

For the spectral radiance measured by a sensor at Top Of Atmosphere (TOA), the atmospheric effects can not be ignored. Atmospheric effects include absorption, emission and scattering (Franca and Cracknell, 1994). Figure 2.1 demonstrates the radiative transfer at an infrared wavelength λ. Surface emission ([1] in Figure 2.1) is expressed by Equation (2.2), which depends not only on surface temperature T_s and wavelength λ, but also on the view zenith angle θ_v. Part of the spectral radiance emitted and scattered by the atmosphere reaches the surface, the so-called atmospheric downwelling radiance, and then reflected by it towards the sensor ([2] in Figure 2.1), and another part upwards reaches the sensor ([5] in Figure 2.1) which is called the atmospheric upwelling radiance. For the MIR

spectrum in daytime, direct solar irradiance penetrates the atmosphere and part of it reaches the surface, and then is reflected by the surface towards the sensor ([3] in Figure 2.1). The surface emission, the reflected atmospheric downwelling radiance and the reflected direct solar irradiance ([4] in in Figure 2.1) upwards penetrate the atmosphere and part of them reach the sensor after the absorption and scattering of the atmosphere. Therefore the total radiance at wavelength λ reaching the sensor is given by:

$$L(T,\theta_v,\lambda) = L_G(T_g,\theta_v,\lambda)\tau(\theta_v,\lambda) + L_{atm\uparrow}(\theta_v,\lambda) \tag{2.3}$$

where T refers to the brightness temperature at satellite level, θ_v is the view zenith angle, $L_G(T_g, \theta_v, \lambda)$ is the total spectral radiance at gound level, T_g is the brightness temperature at ground level, $\tau(\theta_v,\lambda)$ is the total atmospheric spectral transmittance, $L_{atm\uparrow}(\theta_v,\lambda)$ is the upwelling atmospheric spectral radiance, and $L_G(T_g, \theta_v, \lambda)$ is the spectral radiance measured at ground level given by

$$L_G(T_g,\theta_v,\lambda) = \varepsilon(\theta_v,\lambda)L(T_s,\lambda) + \left[1-\varepsilon(\theta_v,\lambda)\right]L_{atm\downarrow}(\lambda) + \rho_b(\theta_v,\theta_s,\varphi,\lambda)E_{sun}(\theta_s,\lambda) \tag{2.4}$$

where $L_{atm\downarrow}(\lambda)$ is the downwelling atmospheric spectral radiance divided by π, $\rho_b(\theta_v, \theta_s, \varphi, \lambda)$ is the bi-directional spectral reflectivity, φ is the relative azimuth angle between the view azimuth angle and the solar azimuth angle, $E_{sun}(\theta_s, \lambda)$ is the direct solar spectral irradiance at ground level, and θ_s is the solar zenith angle.

For the spectral radiance in TIR channels and the night-time measurements in MIR channels, $E_{sun}(\theta_s, \lambda)$ equals to 0. For the daytime measurements in a MIR channel, besides the radiance emitted by the atmosphere itself, $L_{atm\uparrow}(\theta_v,\lambda)$ and $L_{atm\downarrow}(\lambda)$ also include the solar irradiance diffused by the atmosphere.

Real sensors measure radiance neither at a particular wavelength nor over the whole electromagnetic spectrum, but over a finite range. As we know, the atmosphere is relatively transparent in the so-called atmospheric windows at 3-5 μm and 8-13 μm, where atmospheric absorption is minimum or signals are least attenuated. The channel response functions define the channel ranges and characterize the response of a sensor to available radiance in a particular wavelength range. Usually, the response functions are normalized to 1, and for real calculations the spectral radiance is convolved with the response function.

At satellite level, for a cloud-free atmosphere under local thermodynamic equilibrium, the radiance measured in an infrared channel *i*, the so-called channel-averaged radiance, is given by (Li et al. 1999):

$$L_i(T_i,\theta_v) = \frac{\int_0^\infty f_i(\lambda)\tau(\theta_v,\lambda)L_G(T_g,\theta_v,\lambda)d\lambda}{\int_0^\infty f_i(\lambda)d\lambda} + \frac{\int_0^\infty f_i(\lambda)L_{atm\uparrow}(\theta_v,\lambda)d\lambda}{\int_0^\infty f_i(\lambda)d\lambda} \tag{2.5}$$

where $f_i(\lambda)$ is the spectral response function of the channel *i*.

At ground level, the integrated radiance $L_{G,i}(T_{g,i}, \theta_v)$ over the spectral range of the channel *i* from Equation (2.4) is given by:

$$L_{G,i}(T_{g,i},\theta_v)=\frac{\int_0^\infty f_i(\lambda)\left\{\varepsilon(\theta_v,\lambda)L(T_s,\lambda)+\left[1-\varepsilon(\theta_v,\lambda)\right]L_{atm\downarrow}(\lambda)+\rho_b(\theta_v,\theta_s,\varphi,\lambda)E_{sun}(\lambda)\right\}d\lambda}{\int_0^\infty f_i(\lambda)d\lambda} \tag{2.6}$$

where $T_{g,i}$ is the brightness temperature at ground level in the channel *i*.

For the channels with narrow spectral range (~1.0 μm), Equations (2.5) and (2.6) can be simplified (Li et al., 1999) as following without introducing significant errors.

$$L_i(T_i,\theta_v)=\tau(\theta_v)L_{G,i}(T_{g,i},\theta_v)+L_{atm\uparrow i}(\theta_v) \tag{2.7}$$

$$L_{G,i}(T_{g,i},\theta_v)=\varepsilon_i(\theta_v)L_i(T_s)+(1-\varepsilon_i(\theta_v))L_{atm\downarrow i}+\rho_{b,i}(\theta_v,\theta_s,\varphi)E_{sun}(\theta_s) \tag{2.8}$$

with $\psi_i=\int_0^\infty f_i(\lambda)\psi(\lambda)d\lambda/\int_0^\infty f_i(\lambda)d\lambda$, where ψ stands for τ, L_G, L, $L_{atm\uparrow}$, ε, $L_{atm\downarrow}$, E_{sun} or ρ_b.

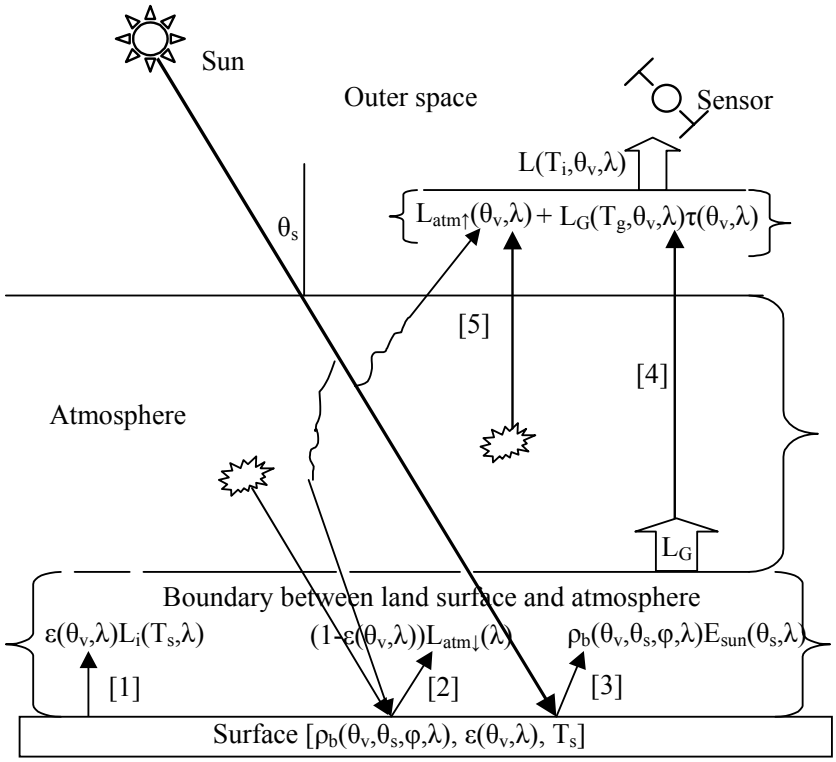

Figure 2.1. Radiative transfer at an infrared wavelength λ (μm)

Similar to the definition of spectral emissivity, the channel-averaged emissivity definition should include the temperature dependency via the Planck function. However, in terrestrial temperature range, the channel-averged emissivity is almost independent of surface temperature T_s (Becker and Li, 1990a; Wan and Dozier, 1996).

For land surface, the pixels of satellite sensors consist usually of mixed rather than pure substances, and the temperatures of the substances may different from each other. It is necessary to re-define LSE and LST for the whole pixel area for the heterogeneous and non-isothermal surfaces. Based on the results of recent research, LSE refers to the area-weighted and channel-averaged emissivity and LST refers to the radiometric surface temperature which depends not only on the distributions of surface temperature and emissivity within a pixel but also on the channel used to measure it (Becker and Li, 1995; Norman and Becker, 1995; Prata et al., 1995; Wan and Dozier, 1996).

The radiative transfer Equations (2.5) and (2.6) or Equations (2.7) and (2.8) are the fundamental theory of this research, and the radiative transfer process can be simulated by the radiative transfer code MODTRAN.

2.2 MODTRAN and atmospheric data

MODTRAN (MODerate spectral resolution atmospheric TRANsmittance and radiance code) was developed by AFRL/VSBT (Air Force Research Lab, Space Vehicles Directorate) in collaboration with Spectral Sciences, Inc. MODTRAN code calculates atmospheric transmittance and radiance for frequencies from 0 to 50,000 cm^{-1} at moderate spectral resolution, primarily 2 cm^{-1} (20 cm^{-1} in the UV). The original development of MODTRAN was driven by a need for higher spectral resolution and greater accuracy than that provided by the LOWTRAN series of band model algorithms. Except for its molecular band model parameterization, MODTRAN adopts all the LOWTRAN 7 (now fully obsolete) capabilities, including spherical refractive geometry, solar and lunar source functions, and scattering (Rayleigh, Mie, single and multiple), and default profiles (gases, aerosols, clouds, fogs, and rain).

The latest version, MODTRAN 4.0, which was used in this research work, follows the earlier MODTRAN 3 series, and remains the state-of-the-art atmospheric band model radiation transport model. MODTRAN 4.0 adds some new features, such as two Correlated-k (CK) options, azimuth dependent DISTORT option, upgraded ground surface modeling, high-speed option and so on, making the calculation more accurate than the former version (Berk et al., 1998; MODTRAN 4.0 User's Manual). MODTRAN 4.0 has been available to the public since January, 2000.

Table 2.1. Air temperatures at the first boundary and the total water vapor contents of the six standard model atmospheres prescribed in MODTRAN

Model atmosphere	T_0 (Kelvin)	W (g/cm^2)
Tropical	299.7	4.11
MLS	294.2	2.92
MLW	272.2	0.85
SAS	287.2	2.08
SAW	257.2	0.42
1976 U S Standard	288.2	1.42

T_0 is the air temperature at the first boundary and W represents the column water vapor content.

MODTRAN prescribes six standard model atmospheres: Tropical, Mid-Latitude Summer (MLS), Mid-Latitude Winter (MLW), Sub-Arctic Summer (SAS), Sub-Arctic Winter (SAW) and 1976 U S Standard. The model atmospheres define a 36-layer atmosphere and contain the following data for each layer: altitude, pressure, temperature, water vapor density, and layer concentration of ozone,

methane, nitrous oxide, carbon monoxide, carbon dioxide, oxygen, nitric oxide, sulphur dioxide, nitrogen dioxide, and ammonia. Table 2.1 gives the air temperatures of the first boundary and the column water vapor contents of the six standard atmospheres. Figure 2.2 shows the pressure profiles, temperature profiles and relative humidity profiles of the six standard atmospheres.

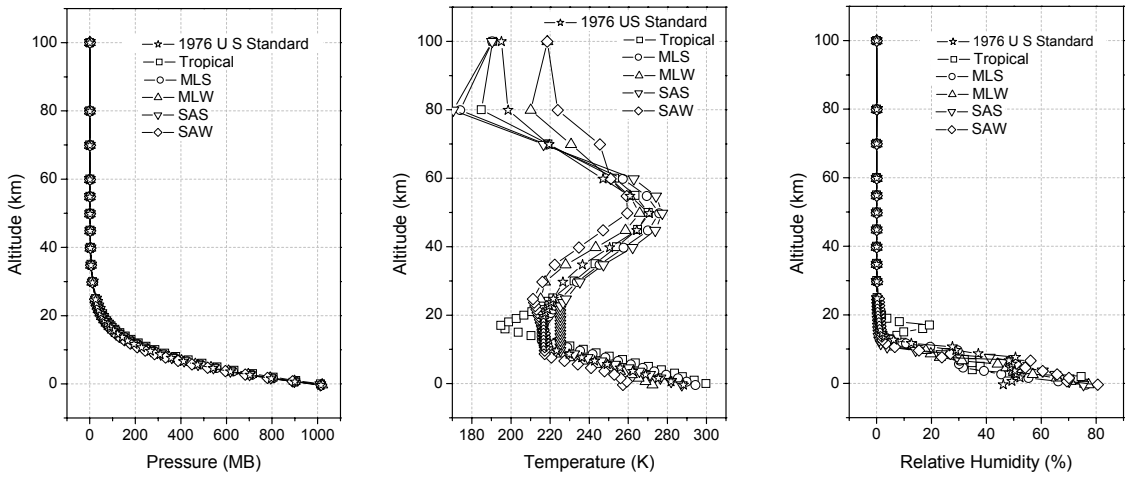

Figure 2.2. Pressure profiles, temperature profiles and relative humidity profiles of the six standard model atmospheres prescribed in MODTRAN

In addition to the six standard model atmospheres, MODTRAN also provides New Model Atmosphere option to enable users to define their own atmospheric profiles, such as radiosounding data and ECMWF (European Center for Medium-Range Weather Forecasts) data. Here, we highlighted the ECMWF data.

The ECMWF reanalysis (ERA) operational deterministic model data provide 21-level profiles of pressure (P), temperature (T), relative humidity (RH), and geo-potential (GP) with spatial resolutions of 0.5° in both latitude and longitude at four main UTC times: 0:00, 6:00, 12:00 and 18:00 (Table 2.2) (ECMWF report, 1995).

Table 2.2. Description of the ECMWF data

Data: Geo-Potential (GP), air temperature (^{o}C) and relative humidity (%)		
Sampling	Step	Limits
Temporal	6 hours	
Geographical: Latitude	0.5°	90S – 90N
Geographical: Longitude	0.5°	180W – 180E
Vertical	21 levels*	To altitude about 48 KM

*Levels of pressure are 1000, 925, 850, 700, 500, 400, 300, 250, 200, 150, 100, 70, 50, 30, 20, 10, 7, 5, 3, 2 and 1 hPa

MODTRAN is controlled by a single input file, which consists of a sequence of six or more CARDS. Note that, the MODTRAN input requires the altitude of each level instead of GP. To convert GP into the altitude H in km, the following equation is applied

$$H = \frac{GP \times R_E}{1000 g_{\eta,0} R_E - GP} \tag{2.9}$$

with $g_{\eta,0}=9.80616\times(1.0-2.6373\times10^{-3})\cos(2\eta)+5.9\times10^{-6}\cos^2(2\eta)$ and R_E= 6371.23 km.

where $g_{\eta,0}$ is the acceleration of gravity at latitude η and at altitude 0, and R_E is the average radius of the Earth.

Table 2.3. Spectral channel characteristics of MSG1-SEVIRI instrument

Channel No.	Channel name	Characteristics of spectral channel (μm)			Short-term radiometric error performances	Main gaseous absorber or window
		$\lambda_{central}$*	λ_{min}	λ_{max}		
1	VIS0.6	0.640	0.56	0.71	0.27 at 5.3 W/(m^2 sr μm)	Window
2	VIS0.8	0.809	0.74	0.88	0.21 at 3.6 W/(m^2 sr μm)	Window
3	NIR1.6	1.635	1.50	1.78	0.07 at 0.75 W/(m^2 sr μm)	Window
4	IR3.9	3.920	3.48	4.36	0.17 K at 300 K	Window
5	WV6.2	6.306	5.35	7.15	0.21 K at 250 K	Water vapor
6	WV7.3	7.357	6.85	7.85	0.12 K at 250 K	Water vapor
7	IR8.7	8.711	8.30	9.10	0.10 K at 300 K	Window
8	IR9.7	9.671	9.38	9.94	0.29 K at 255 K	Ozone
9	IR10.8	10.788	9.80	11.80	0.11 K at 300 K	Window
10	IR12.0	11.943	11.00	13.00	0.15 K at 300 K	Window
11	IR13.4	13.352	12.40	14.40	0.15 K at 300 K	Carbon dioxide
12	HRV	Broad channel (about 0.4 – 1.1μm)			0.63 at 1.3 W/(m^2 sr μm)	Window/Water vapor

*Central wavelength was calculated by $\lambda_{central} = \int_0^\infty \lambda f_i(\lambda)d\lambda / \int_0^\infty f_i(\lambda)d\lambda$.

2.3 MSG1-SEVIRI and MSG products

Meteosat Second Generation (MSG) is a new generation of the geostationary satellite developed by European Space Agency (ESA) and EUMETSAT. The total program, including launchers, ground segment and operation of the satellites, cost more than 12 years and 1.3 billion Euros financed by EUMETSAT. Development and building the first satellite (MSG1) cost 475 million Euros financed for 2/3 by ESA and for 1/3 by EUMETSAT. The MSG1 was launched on August 29, 2002 by the Ariane 5 rocket.

MSG1's main payload is the optical imaging radiometer, the so called Spinning Enhanced Visible and Infrared Imager (SEVIRI), which was manufactured by European industry under the leadership of Astrium SAS in Toulouse, France. With its 12 spectral channels covering from visible to infrared (Table 2.3 and Figure 2.3) (Schmetz et al., 2002a), SEVIRI will provide 20 times more information than the previous generation of sensors onboard the Meteosat satellites, offering new and, in some cases, unique capabilities for cloud imaging and tracking, fog detection, measurement of the Earth

surface and cloud top temperatures, tracking of ozone patterns, as well as many other improved measurements. The research work of this thesis focuses on the retrievals of LSE and LST from MSG1-SEVIRI data, in which at least one MIR channel and one TIR channel are required. Hence, we used the data in the infrared channels 4, 7, 9 and 10 of MSG1-SEVIRI (Blue colored in Table 2.3 and Figure 2.3).

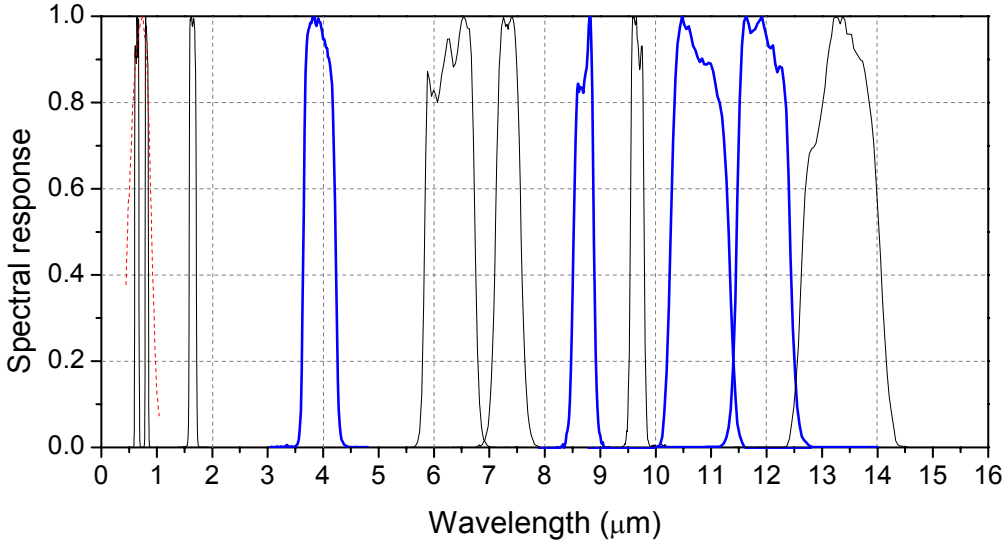

Figure 2.3. Spectral responses of MSG1-SEVIRI channels
(HRV channel is in red dash)

The spatial resolutions at the sub-satellite point of MSG1-SEVIRI channels are 1.0 km for the High Resolution Visible (HRV) channel and 3.0 km for the infrared and the other visible channels. Its short-term radiometric errors are less equal than 0.17 K for the four infrared window channels (Table 2.3). MSG1-SEVIRI provides measurements of the Earth-disc (centered at 0 longitude and 0 latitude) every 15 minutes in 12 spectral channels at fixed view angles, but the solar angles change every 15 minutes during daytime, making it particularly suitable for LST and LSE determinations using day/night TISI concept.

Figure 2.4 shows the MSG1-SEVIRI's mechanical scanning principle. MSG1 locates at an altitude of 36,000 km and at 0 latitude and 0 longitude, and the SEVIRI instrument scans the Earth from east to west and then from south to north. The Earth's radiation enters the instrument at every revolution through a 50 cm × 80 cm aperture. The nominal repeat cycle of 15 min was the driver in selecting the number of detectors per channel and the spin rate (100 rpm). Twelve minutes are allocated to the imaging phase, leaving three minutes for calibration, retrace and stabilization. The 1 km resolution of the HRV channel is achieved by using 9 broad-band detection elements. The other channels are sampled at 3 km resolution by using 3 narrow-band detection elements per channel. A combination of a Sun-synchronization triggering pulse with the master clock signal starts the sampling of detectors signals which lasts 30 ms. The data are then buffered in a stretching memory and multiplexed with other necessary data in a 600 ms time frame. The raw data transmission to Earth at L-band (3.2 Mb/s) is continuous. Figure 2.5 displays MSG1-SEVIRI's view geometries, in which the view angles refer to the angles at ground level, and a colour image of the Earth acquired by it. The view zenith angles are

distributed as a series of concentric circles centered at 0° longitude and 0° latitude and increase from 0° (the centre) to near 90° (outside). The view azimuth angles, varying between 0° and 360°, increase clock-wise from the south direction. The sizes of the whole Earth disc are 3712×3712 except for the data in the HRV channel.

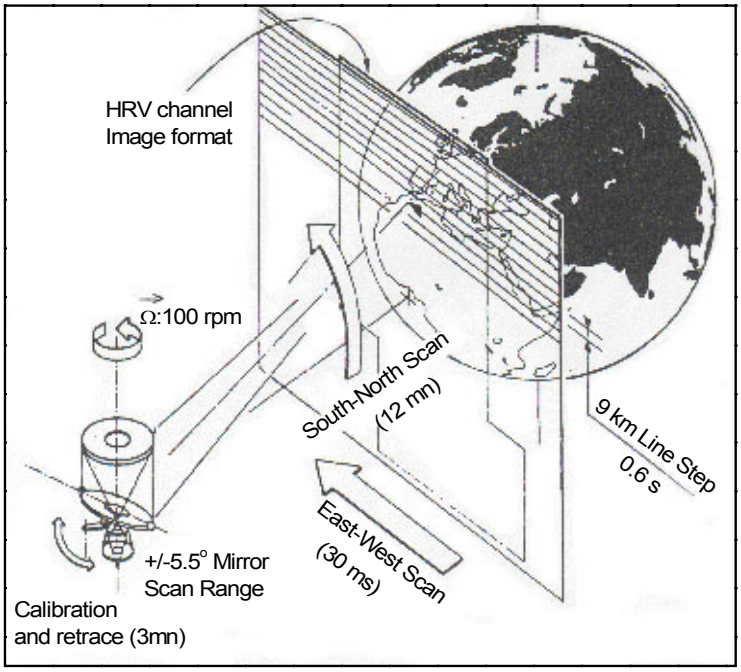

Figure 2.4. MSG1-SEVIRI's mechanical scanning principle
(Cited from http://www.esa.int/, but modified)

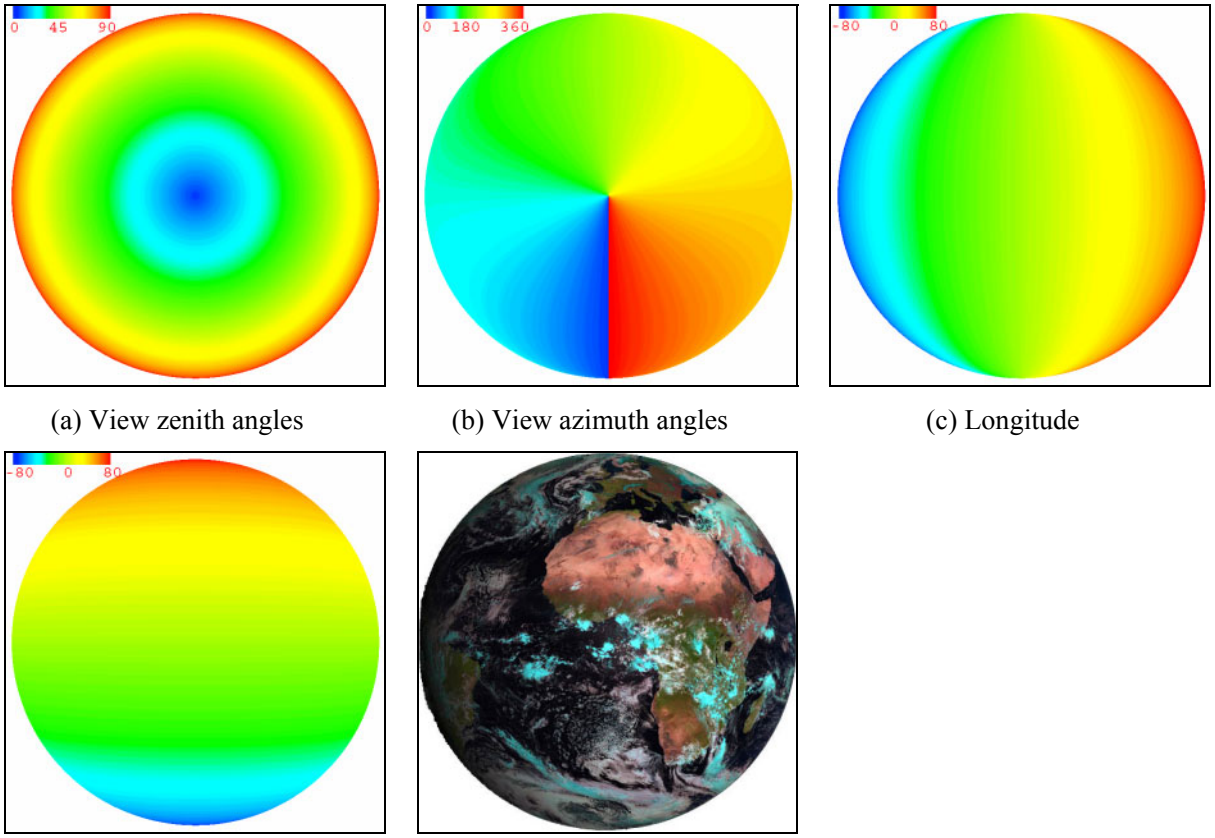

(a) View zenith angles (b) View azimuth angles (c) Longitude

(d) Latitude (e) Color image

Figure 2.5. MSG1-SEVIRI's view geometries and a color image of the Earth acquired by it (The image sizes in SEVIRI infrared channels: 3712×3712)

The primary product of the MSG system is the MSG Level 1.5 product, which is derived from geometrically and radiometrically corrected level 1.0 image data. The MSG Level 1.5 images are processed in such a way that all image pixels are remapped onto a reference image corresponding to an image taken by the MSG satellite. In addition, all image lines are aligned and the coordinates of the image pixels of the different channels are adjusted so that they correspond to the information from the same point on the Earth's surface.

Another useful product is the MSG cloud mask. The MSG cloud mask product is an image-based product derived from the results of scenes analysis and provides, for every cycle, information on the possible occurrence of clouds within each pixel. A central objective is to delineate all absolutely cloud-free pixels in a satellite scene with a high degree of confidence. The MSG cloud mask product provides the following information: i) no cloud, clear surface. ii) no cloud, surface types snow/ice. iii) no cloud, sun-glint over sea. iv) cloudy, 50%, 75% and 100% probabilities. v) no-processed, or missing data. The MSG cloud mask data are stored in the Native files, and in each file, there are total four images each with sizes of 928×928.

The MSG products can be ordered and downloaded from the website http://archive.eumetsat.org.

The image data are stored as digital counts in binary files, such as Native, BSQ and so on. The relation between the binary pixel count and the physical radiance is fully defined for each spectral channel by the following relation (Schmetz et al., 2002b):

$$L = CAL\_offset + CAL\_slope * Count \tag{2.10}$$

where L is the physical radiance in mW/m^2 sr cm^{-1} measured by MSG1-SEVIRI at TOA; *CAL_offset* is the offset constant between the pixel count and the physical radiance; *CAL_slope* is the linear calibration coefficient; *Count* is the binary pixel count between 0 and 1023.

The calibration info (the slope and the offset) can be extracted from the file header. Table 2.4 gives the calibration coefficients of the 12 SEVIRI channels.

Table 2.4. Calibration coefficients of MSG1-SEVIRI channels

Channel No.	*CAL_slope*	*CAL_offset*
1	0.0229502	-1.17046
2	0.0292159	-1.49001
3	0.0232793	-1.18724
4	0.00365867	-0.186592
5	0.00831811	-0.424224
6	0.0386220	-1.96972
7	0.126744	-6.46392
8	0.103961	-5.30202
9	0.205034	-10.4568
10	0.222311	-11.3379
11	0.157607	-8.03795
12	0.0313764	-1.60020

In the MSG-MPEF (Meteorological Products Extraction Facility), the following analytic relation between the equivalent brightness temperature (T_i) and the SEVIRI radiance is adopted (Schmetz et al., 2002b).

$$T_i = \left[C_2' \nu_c / \log\left(\frac{C_1' \nu_c^3}{L} + 1\right) - B \right] / A \tag{2.11}$$

with C_1'=1.19104×10^{-5} mW m^{-2} sr^{-1} (cm^{-1})$^{-4}$, C_2'=1.43877 K (cm^{-1})$^{-1}$

where ν_c is the central wavenumber of a SEVIRI channel, and A and B are coefficients given in Table 2.5.

Table 2.5. Values of the central wavenumber and the coefficients A and B for MSG1-SEVIRI infrared channels

Channel No.	ν_c (in cm^{-1}),	A	B (K)
04	2569.094	0.9959	3.471
05	1598.566	0.9963	2.219
06	1362.142	0.9991	0.485
07	1149.083	0.9996	0.181
08	1034.345	0.9999	0.060
09	930.659	0.9983	0.627
10	839.661	0.9988	0.397
11	752.381	0.9981	0.576

Vice versa, the analytic relation between the radiance and the equivalent brightness temperature for MSG1-SEVIRI infrared channels is given by the following formula

$$L_i(T_i) = C_1' v_c^3 / \left\{ \exp\left[C_2' v_c / (AT_i + B) \right] - 1 \right\} \tag{2.12}$$

in which, the variables are the same as the ones in Equation (2.11).

Note that, the radiance in Equations (2.11) and (2.12) is in unit mW/m^2 sr/cm. To convert the radiance in mW/m^2 sr/cm into the one in W/(m^2 sr μm), one can multiply by $10/\lambda_{central}^2$ (SPT software), however, it should be cautious that this simple conversion may introduce significant errors if inaccurate central wavelength was used. To obtain more accurate radiance in W/(m^2 sr μm), one should be suggested using Equation (2.1) instead of the simply conversion. In this work, based on the Planck's law, look-up tables were created to implement the conversion of radiances in different units. The absolute difference between the temperatures calculated by Equation (2.1) and by the analytical relation is not great than 0.02 K.

As already mentioned in the section 2.1, the simplified Equations (2.7) and (2.8) are only qualified for those channels with narrow spectral range. For MSG1-SEVIRI channels 4, 7, 9 and 10, a simple simulation analysis will help to check whether Equations (2.7) and (2.8) are valid or not. Assuming that the brightness temperature at ground level is 300 K (i.e., $T_{g,i}$=300 K), the model atmosphere is MLS, the view zenith angle at ground level is 45°, the meteorological visibility is 23 km and the surface altitude is 0.687 km, the differences between the radiances L_i and the corresponding brightness temperature T_i at TOA by Equation (2.5) and Equation (2.7) are given in Table 2.6. From the results, we notice that, for SEVIRI channels 7, 9 and 10, the differences are very small (<0.15% or <0.1 K), but for SEVIRI channel 4, the relative error is up to 8% (~1.9 K). Therefore, for SEVIRI channels 7, 9 and 10, Equations (2.7) and (2.8) are accurate enough to describe the radiative transfer procedure, whereas for SEVIRI channel 4, one should be suggested to use Equations (2.5) and (2.4) instead of Equations (2.7) and (2.8), because SEVIRI channel 4 possesses a wide spectral range and the spectral variation in MIR channel is very strong (Nerry et al., 2004).

Table 2.6. Simulated radiances L_i and the corresponding T_i at TOA by Equations (2.5) and (2.7) in SEVIRI channels 4, 7, 9 and 10

	Channel 4 (IR3.9)		Channel 7 (IR8.7)		Channel 9 (IR10.8)		Channel 10 (IR12)	
	Radiance W/(m^{2}srμm)	T_i (K)	Radiance W/(m^{2}srμm)	T_i (K)	Radiance W/(m^{2}srμm)	T_i (K)	Radiance W/(m^{2}srμm)	T_i (K)
Eq. (2.5)	0.5021	293.79	8.403	292.40	8.890	294.88	8.083	293.15
Eq. (2.7)	0.5434	295.68	8.394	292.34	8.895	294.92	8.092	293.24
Δ	-0.0413	-1.89	0.009	0.06	-0.005	-0.04	-0.009	-0.09

Atmosphere: MLS; θ_v=45°; Meteorological visibility=23 km; Surface altitude=0.687 km

The SEVIRI Pre-processing Toolbox (SPT) software, which has been primarily developed to support the processing of the SEVIRI data by the scientific community, is a simple set of IDL (Interactive Data Language) routines to read the MSG Level 1.5 data in the non-graphics file formats distributed by the EUMETSAT Archive Data Retrieval Service. One should take care of the bugs in the SPT software, for example, the use of inaccurate central wavelengths to convert the radiances in

different units will cause an error up to 0.8 K. Besides the SPT software, we developed a set of C programs to facilitate the processing of the MSG1-SEVIRI data in the following research work.

Besides the SEVIRI data, the MODIS and AATSR data were also involved in the research work of this thesis.

2.4 MODIS and AATSR instruments

The MODerate-resolution Imaging Spectroradiometer (MODIS) is a key instrument onboard the Terra (EOS AM) and Aqua (EOS PM). MODIS/Terra and MODIS/Aqua are viewing the entire Earth's surface every 1 to 2 days, acquiring data in 36 co-registered spectral channels (0.4 – 14.4μm) and at moderate resolution (0.25—1.0 km). For detail information about MODIS characteristics, please see Appendix B. In the 36 spectral channels, roughly speaking, MODIS channels 20 (3.788 μm), 22 (3.971 μm) and 23 (4.051 μm) are corresponding to MSG1-SEVIRI channel 4 (3.9 μm), and MODIS channels 31 and 32 are, respectively, corresponding to MSG1-SEVIRI channels 9 (10.8 μm) and 10 (12.0 μm) (Red curves in Figure 2.6). In this work, the MODIS/Terra L1B data (MOD021KM), the MODIS/Terra land surface temperature Products (MOD11_L2 and MOD11B1) and the MODIS/Terra Geolocation product (MOD03) were utilized. All the MODIS data are stored in files with HDF data format.

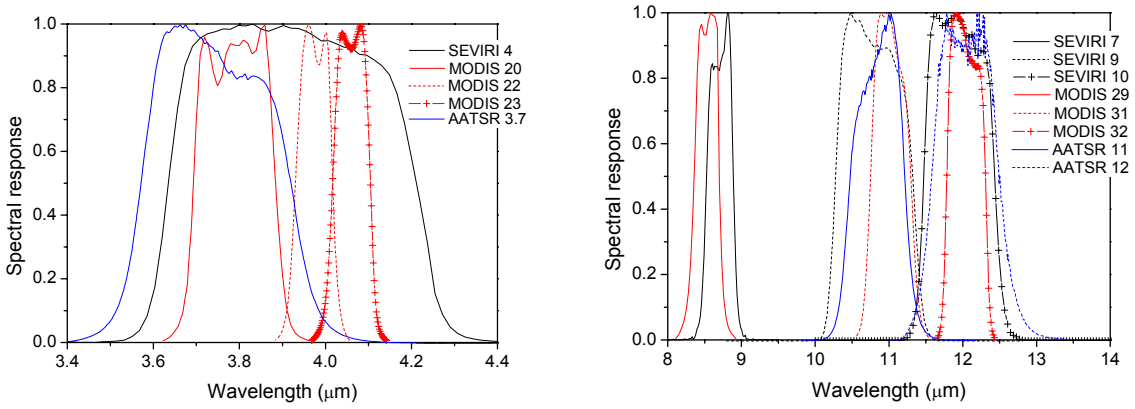

Figure 2.6. Spectral responses of the middle infrared (left) and thermal infrared (right) channels of SEVIRI, MODIS and AATSR

The Advanced Along Track Scanning Radiometer (AATSR) is one of the Announcement of Opportunity (AO) instruments on board ENVISAT. The AATSR instrument is unique in its use of along track scanning to provide two views of the surface and thus improve atmospheric correction. The surface is first viewed along the direction of the orbit track, at an angle of 55°, as the spacecraft flies towards the scene. Then, 150 seconds later, or when the satellite has moved approximately 1000 km forward along the ground track, a second observation is made of the same scene at the sub-satellite point, as shown in Figure 2.7. Table 2.7 gives the parameters of the AATSR instrument. AATSR has seven spectral channels covering from visible to infrared. It is the most recent in a series of instruments designed to measure Sea Surface Temperature (SST) to high levels of accuracy and precision required for the monitoring and detection of climate change. The AATSR instrument is

unique in its use of along track scanning to provide both nadir and forward views of the surface and thus improve atmospheric correction. The AATSR channel IR3.7 (3.7 μm) corresponds to MSG1-SEVIRI channel 4, and AATSR channels IR11 (11.0 μm) and IR12 (12.0 μm) correspond to MSG1-SEVIRI channels 9 and 10, respectively (Blue curves in Figure 2.6). AATSR level 1B data were used in this work.

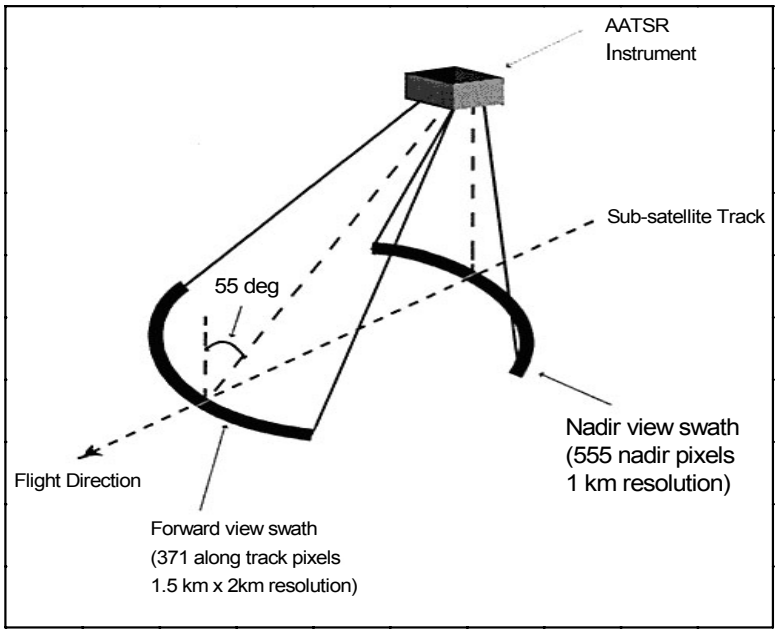

Figure 2.7. AATSR viewing geometry
(Cited from http://envisat.esa.int/, but modified)

Table 2.7 Parameters of the AATSR instrument

Parameter Name	Content
Infrared channels	1.6 μm, 3.7 μm, 10.85 μm and 12.0 μm
Visible channels	0.555 μm, 0.67 μm and 0.865 μm
Spatial Resolution	1 km × 1km
Radiometric Resomution	0.1 K
SST Accuracy	better than 0.5 K
Swath Width	500 km
Operation	continuously over full orbit
Data Rate	625 kb/s
Mass	101 kg
Power	100 W

3 Cross-calibrations of MSG1-SEVIRI infrared channels with the channels of Terra-MODIS

3.1 Introduction

The cross-calibration is an operation that relates the outputs of a given sensor, in a certain spectral channel, to the output of one or more sensors measured in other channels (Asem et al., 1986).

Much research on the cross-calibration has been done in recent years. Teillet et al. (2001) used the nearly coincident matching tandem scenes to cross-calibrate the solar reflective spectral channels of Landsat-7 ETM+ (Enhanced Thematic Mapper Plus) and Landsat-5 TM (Thematic Mapper), incorporating adjustments for spectral channel differences between the two Landsat sensors. Heidinger et al. (2002) proposed a cross-calibration approach for the reflectance channels using coincident and near nadir acquisitions of MODIS over Alaska and Siberia. Doelling et al. (2004a & 2004b) used the coincident, co-angled and co-located measurements to transfer the calibrations of MODIS and GOES-12 (Geostationary Operational Environmental Satellite) to SEVIRI, and found that the brightness temperatures in SEVIRI channel 4 are ~6.7 K colder than the ones in the corresponding MODIS and GOES-12 channels, and the brightness temperatures in SEVIRI channels 9 are ~1.5 K higher. However, the use of the coarse spatial resolutions and the large angle differences in the ray-matching limit the accuracy of the results of Doelling et al, and it is uncertain what the greater SEVIRI bandwith impacts on (Doelling et al., 2004a & 2004b). The above approaches can be categorized into the ray-matching method. This method does not take into account the spectral differences between two sensors, and will lead to unacceptable errors when spectral differences are large.

Considering the disadvantage of the ray-matching method, a radiative transfer modeling method was widely used. Asem et al. (1986) used one or both AVHRR infrared channels to simulate the radiance in Meteosat infrared channel 1 (IR 1, 11.45 μm) based on the radiative transfer modeling. Merchant et al. (2003) used the well-characterized Along-Track Scanning Radiometer 2 (ATSR-2) as a reference to determine calibration correction for GMS-5 VISSR (Geostationary Meteorological Satellite 5, Visible and Infrared Spin Scan Radiometer) via the radiative transfer modeling, and validated it well against in-situ measurements of sea surface temperatures. Liu and Li (2004) implemented the calibration of the Multi-channel Visible and Infra-Red Scanning radiometer (MVIRS) onboard China's polar-orbit meteorological satellite (FY-1D) against MODIS channels by the 6S radiative transfer model and a BRDF (Bidirectional Reflectance Distribution Function) model, and obtained a calibration accuracy of 5%. Vermote and Saleous (2006) proposed a new approach to AVHRR cross-calibration in the visible to shortwave-infrared spectral domain using a priori well calibrated MODIS sensor and a BRDF model to characterize the directional behavior of a stable desert

site. Although the radiative transfer modeling method can obtain more accurate results, it is more complicated, especially for visible channels.

As we know, the SEVIRI is the main payload onboard MSG1. Although the SEVIRI instrument provides a Calibration Unit (CALU) for the in-orbit calibration of the infrared channels, the measurements are still affected by the accumulated frozen contaminants (Coste et al., 2004). In our recent research, we found that the LSTs derived from the two split-window channels of MSG1-SEVIRI are systematically higher than the LSTs extracted from the MODIS/Terra LST product MOD11B1, which means that calibration discrepancies may exist between the two sensors. The MODIS is one of the key instruments for the NASA's Earth Observing System (EOS), and it has been proved to be well calibrated and has long term stability (Guenther et al., 2002; Minnis et al., 2002; Xiong et al., 2002 & 2003; Barnes et al., 2003). Hereafter, the SEVIRI refers to the sensor onboard MSG1, and the MODIS refers to the one onboard the Terra (AM-1).

The data in SEVIRI channels 4, 9 and 10 can be used to derive land surface emissivities using the TISI (Temperature Independent Spectral Indices) concept (Becker and Li, 1990a; Jiang et al., 2006), and then to estimate land surface temperature by the split-window method (Jiang et al., 2005). In this work, we focused on the cross-calibrations of SEVIRI channels 4, 9 and 10 with corresponding MODIS channels 20 (3.8μm), 22(4.0μm), 23(4.1μm), 31(11.0μm) and 32 (12.0μm) uing the ray-matching method and the radiative transfer modeling method, and highlighted the strong effects caused by the spectral differences between the SEVIRI and MODIS channels as well as the calibration discrepancies between these two instruments. Different from the former research, more strict matching conditions will be used in the ray-matching method and the radiative transfer modeling method, which will be detailed in the data processing section. In the section 3.2, the cross-calibration methods will be recalled, including the ray-matching method, the radiative transfer modeling method and the method development with MODTRAN 4.0 fed with the adjusted Tropical profiles. The section 3.3 will describe the study area, the related data and the data processing. The section 3.4 will be devoted to the results and analysis, and the summary and conclusions will be given in the last section.

3.2 Methods and algorithm development

Two methods, the ray-matching method and the radiative transfer modeling method, were recalled and applied to the cross-calibrations of SEVIRI channels 4, 9 and 10 with corresponding MODIS channels 20, 22, 23, 31 and 32.

3.2.1 Ray-matching method

The ray-matching method is a simple and direct way to use the coincident, co-angled and co-located pixels to transfer the calibration of one well-calibrated sensor to another one (Doelling et al., 2004a). As mentioned in the introduction of this chapter, this method does not account for the spectral differences between different sensors. However, the RM method has the advantage not to consider whether the pixels are cloud contaminated or not, because it is not based on the radiative transfer theory which is strongly affected by clouds and accurate cloud detection in satellite data over land and oceans is a difficult task (Simpson and Gobat, 1995a & 1995b).

3.2.2 Radiative transfer modeling method

3.2.2.1 Theory

The radiative transfer theory is presented in the section 2.1.

Figure 2.6 shows the normalized spectral responses of the MIR and TIR channels of SEVIRI and MODIS. Figure 2.6 reveals that SEVIRI channel 4 covers MODIS channels 20, 22 and 23, and MODIS channels 31 and 32 almost fully fall within SEVIRI channels 9 and 10, respectively. When the SEVIRI and MODIS simultaneously observe the same surface area with temperature T_s at the same view zenith angle θ_v and view azimuth angle φ_v, the brightness temperatures at TOA observed by the two sensors may be related to each other by a function *g*.

$$T_{4,s}(\theta_v) = g_4(T_{20,m}, T_{22,m}, T_{23,m}, \theta_v) \tag{3.1a}$$

$$T_{j,s}(\theta_v) = g_j(T_{i,m}, \theta_v) \tag{3.1b}$$

where $T_{4,s}$, $T_{20,m}$, $T_{22,m}$ and $T_{23,m}$ are the brightness temperatures at TOA in SEVIRI channel 4, MODIS channels 20, 22 and 23, respectively. Subscripts *s* and *m* represent the SEVIRI and the MODIS, respectively. $T_{j,s}$ is the brightness temperature at TOA in SEVIRI channel j (j=9 or 10), and $T_{i,m}$ is the brightness temperature at TOA in MODIS channel *i* (*i*=31 or 32).

It should be noted that, because SEVIRI channel 4 possesses a wide spectral range and the spectral variation in MIR channel is very strong (Nerry et al., 2004), the use of Equations (2.7) and (2.8) instead of Equations (2.5) and (2.4) for SEVIRI channel 4 will lead to an error of ~2 K (Jiang et al., 2006).

Because the radiative transfer modeling method is based on the radiative transfer theory, it can take into account the effects caused by the differences of sensor's spectral responses. Furthermore, it may be used in different view zenith and azimuth angles (Asem et al., 1987). Its disadvantages lie on the complicated procedure and the cloud-free requirement.

3.2.2.2 Numerical experiment

Because of the homogeneity, the relatively flat surface and the well-known emissivity, sea is an ideal calibration site and selected in much research (Asem et al, 1987; Merchant et al., 2003; Doelling et al., 2004a). However, the narrow dynamic range of sea surface temperature in a short period of time, which is usually less than 20°C, limits the calibration accuracy for very low/high temperatures. Considering the special view geometries of SEVIRI and MODIS, in our work, we selected the vegetated Central Africa as well as the sea region as study area, which will be detailed in the section 3.3.

In this work, we selected the spectral emissivities of water, vegetation and soil extracted from the MODIS UCSB Emissivity Library (http://www.icess.ucsb.edu/modis/EMIS/html/em.html) to account for the spectral differences in both MIR and TIR channels between SEVIRI and MODIS based on the land cover types of the study area (see the section 3.3). For the TIR channels, the channel averaged emissivities in SEVIRI and MODIS channels were firstly calculated, and then the emissivity

relationship between SEVIRI and MODIS channels was built using a linear fit (Figure 3.1). One can obtain:

$$\varepsilon_{31} = 0.87583 \times \varepsilon_{9} + 0.122 \tag{3.2}$$

$$\varepsilon_{32} = 1.01086 \times \varepsilon_{10} - 0.010 \tag{3.3}$$

where ε_9 and ε_{10} are, respectively, the emissivities in SEVIRI channels 9 and 10, and ε_{31} and ε_{32} are, respectively, the emissivities in MODIS channels 31 and 32.

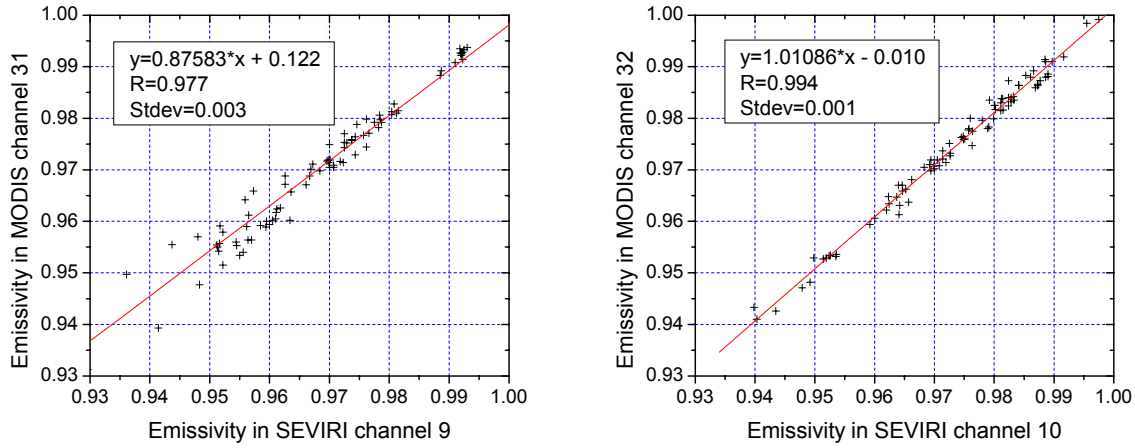

Figure 3.1. Relationships between the emissivities in the two split-window channels of SEVIRI and MODIS according to the spectral emissivities of water, vegetation and soil extracted from the MODIS UCSB Emissivity Library

The fitting correlation coefficients are greater than 0.977 and the standard deviations are less than 0.003. Therefore, if we know the emissivity in a TIR channel of one sensor, the emissivity in the corresponding channel of another sensor can be inferred. In the radiative transfer modeling, the emissivities in the two split-window channels of SEVIRI go from 0.94 to 1.0 with a step of 0.02, and the emissivities in the corresponding MODIS channels were calculated in terms of Equations (3.2) and (3.3).

As mentioned above, the use of the simplified radiative transfer equations will lead to large error in the calculation of the brightness temperature at TOA in SEVIRI channel 4 (Jiang et al., 2006), therefore, the brightness temperature at TOA in SEVIRI channel 4 should be calculated based on the spectral emissivity as well as the atmospheric spectral parameters. Because more than 80 spectral samples in the MODIS UCSB Emissivity Library are available, if water, vegetation and soil are taken into account, it is not a good solution to use all of them in the radiative transfer modeling. Based on the above mentioned facts and the emissivity distribution in the MIR channels, seven samples were selected from the MODIS UCSB Emissivity Library to represent water, vegetation and soil (Figure 3.2). Another problem connected to the MIR channels is that the surface reflected solar irradiance and the surface emission are approximately equal (Li and Becker, 1993), and the BRDF of the study area is not well known. Although the reflected solar irradiance on sea surface is small, the glint is difficult

to preclude. To avoid the drawbacks caused by the solar irradiance, only night-time measurements were considered in the radiative transfer modeling.

MODTRAN is a good radiative transfer code developed by AFRL/VSBT in collaboration with Spectral Sciences, Inc. MODTRAN code calculates atmospheric transmittance and radiance for frequencies from 0 to 50,000 cm^{-1} at moderate spectral resolution, primarily 2 cm^{-1} (20 cm^{-1} in UV), and has been widely used in much research (MODTRAN 4.0 User's Manual; Berk et al., 1998; Sobrino et al., 2004). The most recent version of MODTRAN was used to implement the numerical experiment in this work. Considering the study area, only the Tropical model atmosphere, which is prescribed in MODTRAN, was used in the numerical experiment. In order to make the model atmosphere more representative for the natural cases, the profiles of the air temperatures and water vapor contents of the Tropical model atmosphere were adjusted. The adjusted temperature amount is ±10 K for the first boundary level with step of 5 K, and will be decreased with the increase of height until to the tropopause. For the levels higher than tropopause, no adjustment was carried out. So the first boundary layer temperature T_0 goes from 289.7 to 309.7 K after the adjustment. The atmospheric water vapor profiles were scaled from 0.2 to 1.5 with a step of 0.1, and the profiles with water vapor content higher than 6.0 g/cm^2, which seldom happen in clear sky condition, were discarded.

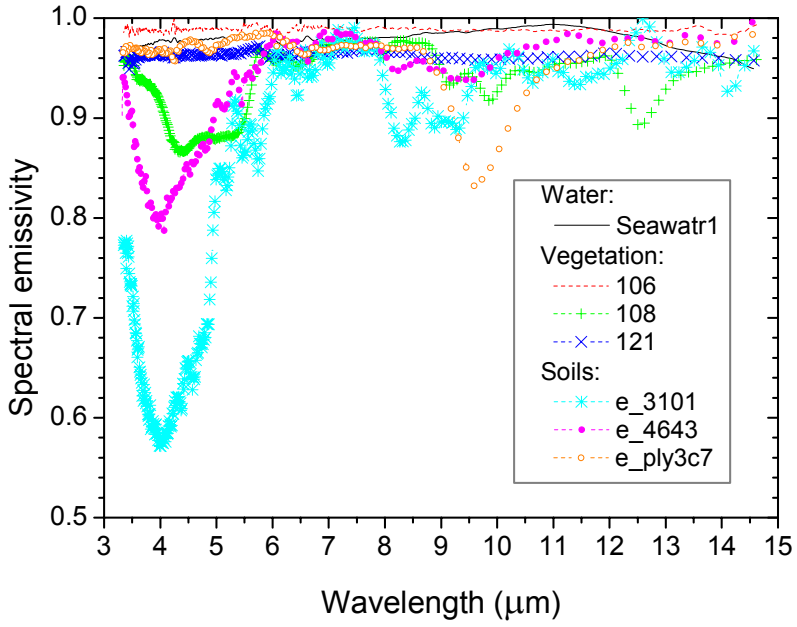

Figure 3.2. Seven samples selected from the MODIS UCSB Emissivity Library representing water, vegetation and soil
(Seawatr1: Sea water; 106: Leaf of Cypress; 108: Leaf of Eucalyptus tree; 121: Leaf of Evergreen Pear; e_3101: Soil 90p3101S from Nebraska Soil Lab; e_4643: Soil 88p4643S from Nebraska Soil Lab; e_ply3c7: Surface from Railroad Valley)

Although Byrne (1979) observed a difference as much as 20.0 K between the air temperature and the warmer surface temperature of dry ground, here, a difference of 10 K was adopted considering the Tropical region and the observation time. The LST ranges from T_0-5 to T_0+10 with a step of 5 K, and the sea surface temperature varies from T_0-3.0 to T_0+3.0 (Trokhimovski et al., 1998) with a step of 3.0

K. For night-time measurements, the surface temperatures were constrained between 285 K and 300 K, whereas they were limited between 285 K and 315 K for both daytime and night-time measurements.

Six view zenith angles at ground level, 0°, 10°, 20°, 30°, 40° and 50°, were used in the numerical experiment.

For all the adjusted Tropical profiles at different view zenith angles, MODTRAN 4.0 will work out the corresponding atmospheric parameters in the radiative transfer equations. The brightness temperatures at TOA in both MIR and TIR channels of SEVIRI and MODIS were calculated in terms of the spectral responses, the atmospheric parameters, the surface temperatures and the surface emissivities. The brightness temperatures at TOA, which are observed by SEVIRI and MODIS under the same surface conditions, the same atmospheric conditions and the same view geometries, are called measurement pairs. If we set the MODIS simulated brightness temperatures as X-axis and the SEVIRI simulated brightness temperatures as Y-axis, and took the simulations at the view zenith angle of 30° as an example, the relationship of the simulated brightness temperatures between MODIS and SEVIRI is shown in Figure 3.3a. Figure 3.3a shows that the simulated brightness temperatures in SEVIRI channels are linearly proportional to the simulated brightness temperatures in the corresponding MODIS channels. We tried a quadratic fit and no apparent improvement had been obtained. When the simulated brightness temperatures in MODIS channels vary from 280 K to 320 K, the temperature adjustments (differences of simulated brightness temperatures between MODIS and SEVIRI) at the view zenith angle 30° are shown in Figure 3.3b. Figure 3.3b reveals that the simulated brightness temperatures in MODIS channel 20 and 32 are, respectively, higher than the ones in SEVIRI channel 4 and 10, whereas the simulated brightness temperatures in MODIS channel 31 are slightly lower than the ones in SEVIRI channel 9, and the temperature adjustrment is temperature dependent. It should be noted that this temperature adjustment is caused by the differences of the spectral responses between MODIS and SEVIRI channels.

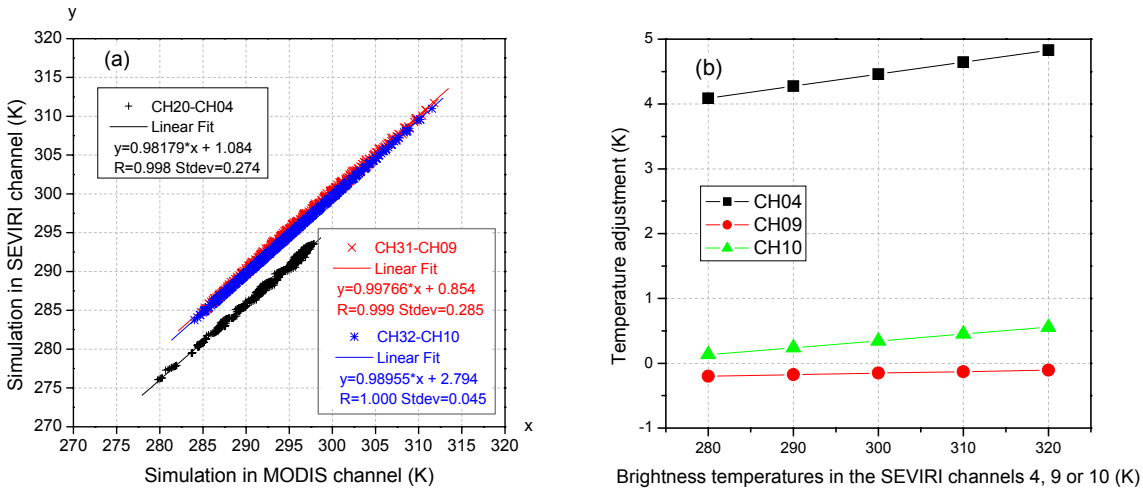

Figure 3.3. Relationship of the simulated brightness temperatures between MODIS and SEVIRI (a), and the temperature adjustments for SEVIRI channels 4, 9 and 10 (b) at a VZA of 30°
(CH20, CH31 and CH32 stand for MODIS channels 20, 31 and 32, respectively; CH04, CH09 and CH10 stand for SEVIRI channels 4, 9 and 10, respectively; R is the correlation coefficient and Stdev represents Standard deviation)

As mentioned previously, MODIS channels 20, 22 and 23 are almost covered by SEVIRI channel 4. If the simulated brightness temperatures in SEVIRI channel 4 are expressed as a linear function of the simulated brightness temperatures in MODIS channels 20, 22 and 23, the fitting standard deviation (Stdev) will dramatically decrease.

Based on the facts mentioned above, Equations (3.1a) and (3.1b) can be therefore rewritten as

$$T_{4,s}(\theta_v) = a_4(\theta_v) + b_4(\theta_v)T_{20,m}(\theta_v) + c_4(\theta_v)T_{22,m}(\theta_v) + d_4(\theta_v)T_{23,m}(\theta_v) \qquad (3.4a)$$

$$T_{j,s}(\theta_v) = a_j(\theta_v) + b_j(\theta_v)T_{i,m}(\theta_v) \qquad \text{(i=31, j=9 or i=32, j=10)} \qquad (3.4b)$$

where a_4, b_4, c_4, d_4, a_j and b_j are unknown coefficients, which are functions of the view zenith angles.

The coefficients in Equations (3.4a) and (3.4b) were obtained by a linear fit at the six view zenith angles, and are shown in Figure 3.4a. Figure 3.4b shows that the fitting standard deviations are 0.03 K for the MIR channels, and ~0.28 K for the channels centered around 11.0 μm, and ~0.05 K for the channels centered around 12.0 μm at the six view zenith angles. All the fitting correlation coefficients are greater than 0.99. For an arbitrary view zenith angle between 0° and 50°, the coefficients were linearly interpolated from those coefficients of the two adjacent view zenith angles.

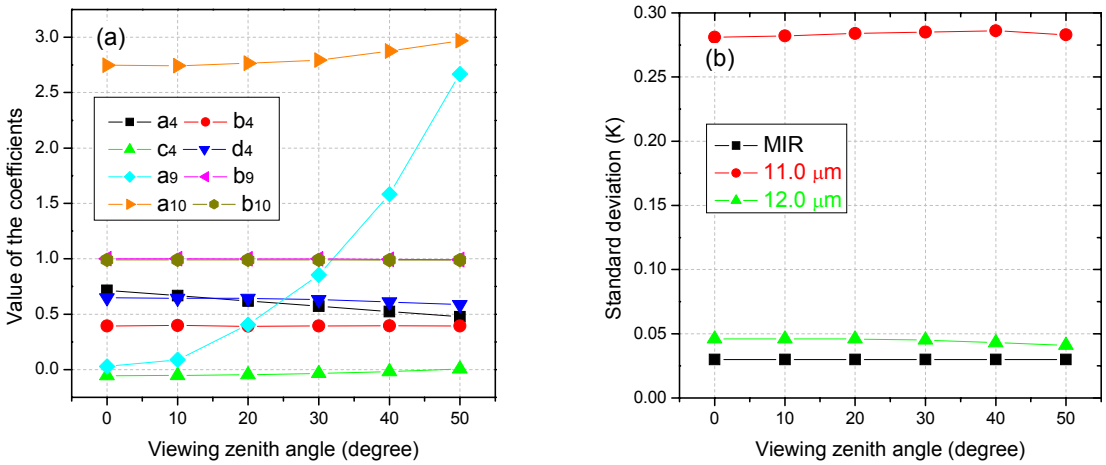

Figure 3.4. Fitting value of the coefficients in Equations (3.4a) and (3.4b) (a) and the fitting standard deviations versus the view zenith angles (b)
(MIR is the acronym of Middle-Infra-Red)

3.3 Study area, related data and data processing

In this work, two methods, the ray-matching method and the radiative transfer modeling method, were applied to the cross-calibrations of SEVIRI infrared channels 4, 9 and 10 with the corresponding MODIS channels. In both methods, we required that the two sensors quasi-simultaneously observe a same area with identical or nearly identical view zenith angles and view azimuth angles.

As we know, Terra is a sun-synchronous and near polar satellite, and the MODIS instrument onboard it is a cross-track scanner. It descends across the equator from north-east to south-west at local time 10:30am, and ascends over the equator from south-east to north-west at night (Figure 3.5). Whereas, the SEVIRI instrument is onboard the geostationary satellite MSG1 locating at a height of 36,000 km at 0° longitude and 0° latitude, and the view geometries were detailed in Figure 2.5. Because of the special view geometries of the SEVIRI and the MODIS, all qualified pixels are symmetric with respect to the location (0°, 0°) (the white crosses in Figure 3.6), therefore we selected a study area with the longitude going from 45W to 45E and the latitude going from 10S to 10N (Figure 3.6). In this area, the left-hand part is mainly the Atlantic Ocean and the right-hand part is mainly the vegetated land surface of Central Africa.

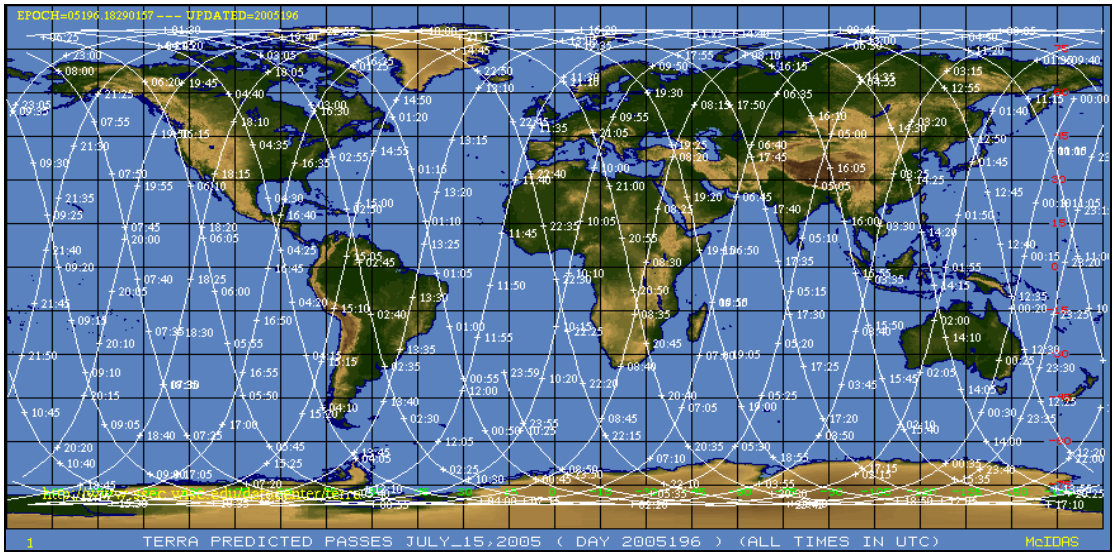

Figure 3.5. Terra orbit track on July, 15, 2005 (UTC time)

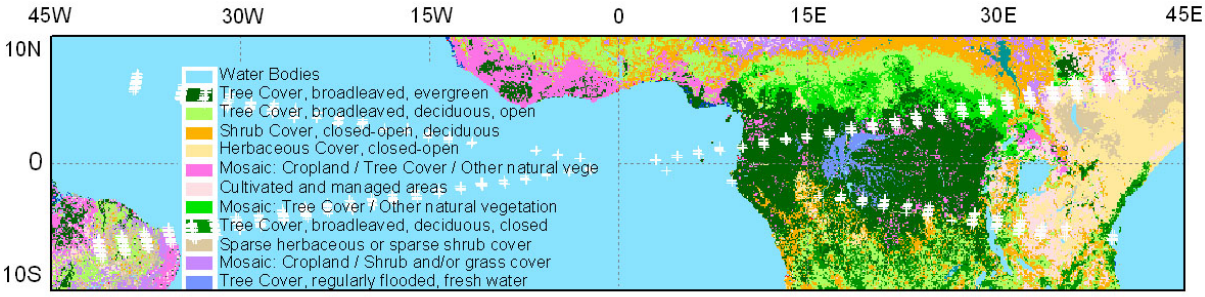

Figure 3.6. Map of the study area and the qualified pixels (white crosses)
(White crosses: $\Delta VZA<0.5°$, $\Delta VAA<1.0°$ and $\Delta Time<10$ minutes; Generated from the Global Land Cover 2000 produced by IES)

The MSG Level 1.5 product, the MSG cloud mask, the 1 KM MODIS/Terra L1B data (MOD021KM) and the corresponding MODIS/Terra Geolocation data (MOD03) covering the study area in July of 2005 and July of 2006 were provided by EUMETSAT and NASA, respectively. The radiances in SEVIRI channels 4, 9 and 10, and in MODIS channels 20, 22, 23, 31 and 32, and the view geometry data, including the longitude, the latitude, the view zenith angles and the view azimuth

angles, were extracted or calculated using SPT (SEVIRI Pre-processing Toolbox) software and self-developed C++ programs. The MSG cloud masks were utilized to eliminate the cloudy pixels in the radiative transfer modeling, because the radiative transfer theory works only under clear sky conditions, however, both cloudy and clear sky pixels were qualified without discrimination in the ray-matching method.

In order to carry out the cross-calibrations, the measurements of the SEVIRI and MODIS instruments should be accurately matched. In our work, without accounting for the effects of point spread function (Huang et al., 2002), all satellite data and cloud masks were aggregated into the WGS 84 (World Geodetic System 1984) coordinate system with longitude and latitude resolutions of 0.1° by the following equation.

$$R_i = \sum_{j=1}^{N} \omega_j R_j \Big/ \sum_{j=1}^{N} \omega_j \qquad \text{with } \omega_j = S_{j,p}/S_j. \tag{3.5}$$

In wich R_i is the aggregated value of the target pixel *i*, N is the total input pixel count, ω_j is the weight of pixel j, $S_{j,p}$ is the partial area of pixel j fallen into the target pixel *i*, S_j is the total area of pixel j, and R_j is the value of the pixel j.

Figure 3.7 demonstrates the pixel aggregation. As we know, the pixel's coordinates actually represent the central location of that pixel. Therefore, the corner coordinates of a pixel are easily calculated by averaging four neighboring pixels' coodinates, and four corner coordinates can also define that pixel. Figure 3.7 shows a large pixel in red and a series of small pixels in blue defined by corner coordinates. Based on the spatial relationship, the weight ω_j of the small pixels are calculated, and then the aggregated value of the large pixel is obtained. Note that, the areas of all input pixels are almost equal, because of the close spatial distribution.

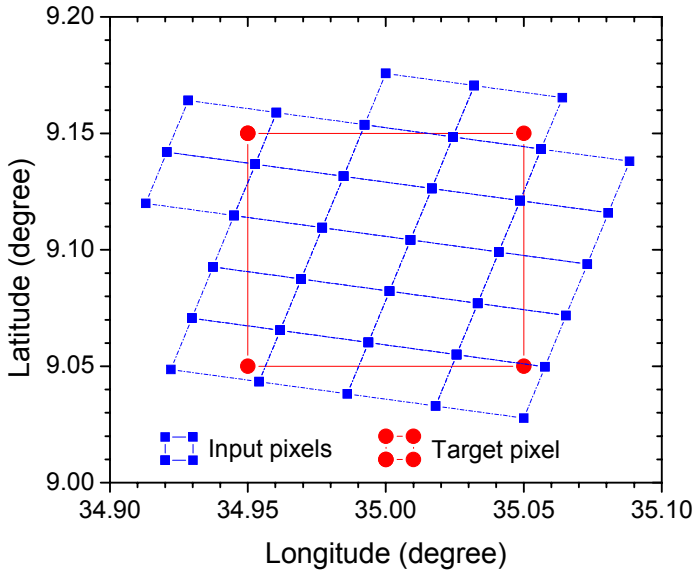

Figure 3.7. Pixel aggregation

Liu et al. (2006) revealed that the pixel aggregation using temperature instead of radiance will lead to an error up to 0.2 K due to the surface heterogeneity. This error is significant in the calibration. Here, the aggregated radiance of target pixel was first calculated in terms of Equation (3.5), and then converted into brightness temperature using a radiance-temperature look-up table created for SEVIRI and MODIS channels. In the pixel aggregation for the MODIS data, the bowtie effect was also considered and removed (Jiang et al., 2004). For the MSG cloud mask, only those aggregated pixels with all input pixels cloud free were still indicated as cloud free. The view zenith and azimuth angles were also aggregated into the study area. After the pixel aggregation, we found that the images extracted from the MSG Level 1.5 product were not well matched with images extracted from the MODIS/Terra L1B product. From a theoretical point of view, if two images were accurately matched, the Root Mean Square Error (RMSE) difference between them should be the minimum. Based on the minimum RMSE principle, the images extracted from the MSG Level 1.5 product were accurately matched with the images extracted from MODIS/Terra L1B product.

In practice, the coincident, co-angle and co-location qualifications are difficult to satisfy, and the approximate matching is usually applied. After the pixel aggregation and the coordinate matching, all the SEVIRI and MODIS data were put into one geodetic system and the ray-matchinig was easily implemented one pixel by one pixel in the entire study area. In this work, those pixels with the view zenith angle differences between the two sensors less than 0.5° ($\Delta VZA<0.5°$), the view azimuth angle differences less than 1° ($\Delta VAA<1°$) and the time differences less than 10 minutes ($\Delta Time<10$ minutes; the solar zenith angle difference $\leq 2°$) were picked out. In the radiative transfer modeling, besides the view angle and time constraints, the cloud free condition is also required, and then the simulated brightness temperatures in SEVIRI channels from the MODIS measurements were calculated by Equations (3.4a) and (3.4b). It should be noted that the SEVIRI sensor scans the Earth disc from the south towards the north with a time cycle of ~15 min, and the UTC time recorded in the file name of the MSG Level 1.5 product is the starting time of scanning. Therefore, to match the images, the times of the SEVIRI images should be ~7.5 min less than the times of the corresponding MODIS images over the study area.

3.4 Results and analysis

For the ray-matching method, the measured brightness temperature pairs in July, 2005 and July, 2006 in SEVIRI and MODIS channels with the view zenith angle differences less than 0.5°, the view azimuth angles difference less than 1.0° and the time differences less than 10 minutes were picked out and directly graphed in Figure 3.8. About 900 pixels are qualified in July of each year, and the view zenith angles cover a range from 2° to 52°. Figure 3.8d shows the temperature adjustments (temperature difference between MODIS measurement and SEVIRI measurement) in a function of the brightness temperatures measured in SEVIRI channels 4, 9 and 10. Figure 3.8 depicts that the calibrations of SEVIRI infrared channels are consistent in both July, 2005 and July, 2006. The brightness temperatures measured in SEVIRI channel 4 are obviously lower than the ones measured in MODIS channel 20, while the brightness temperatures measured in SEVIRI channels 9 and 10 are, respectively, higher than the ones measured in MODIS channels 31 and 32. Figure 3.8d shows that, if the brightness temperature in SEVIRI channels varies from 280 K to 320 K, the temperature adjustment ΔBT [$\Delta BT=BT(MODIS)-BT(SEVIRI)$] increases linearly from 4.4 K to 5.9 K for SEVIRI channel 4, from -0.44 K to -0.75 K for SEVIRI channel 9 and from -0.03 K to -0.21 K for SEVIRI channel 10. Although the brightness temperatures at TOA in SEVIRI channels 4, 9 and 10 are

lower/higher than the ones in the corresponding MODIS channels, here it is hard to decide whether the brightness temperatures in SEVIRI channels are actually underestimated or overestimated, because the spectral responses of one channel directly and strongly affect the brightness temperatures in that channel as shown in Figure 3.4b. However, we can qualitatively analyze the results by comparing Figure 3.8d with Figure 3.4b, and found that the temperature adjustments for the brightness temperatures in SEVIRI channels 4, 9 and 10 are similar, implying that the temperature difference revealed by the ray-matching method is mainly contributed by the differences of spectral function of the two sensors.

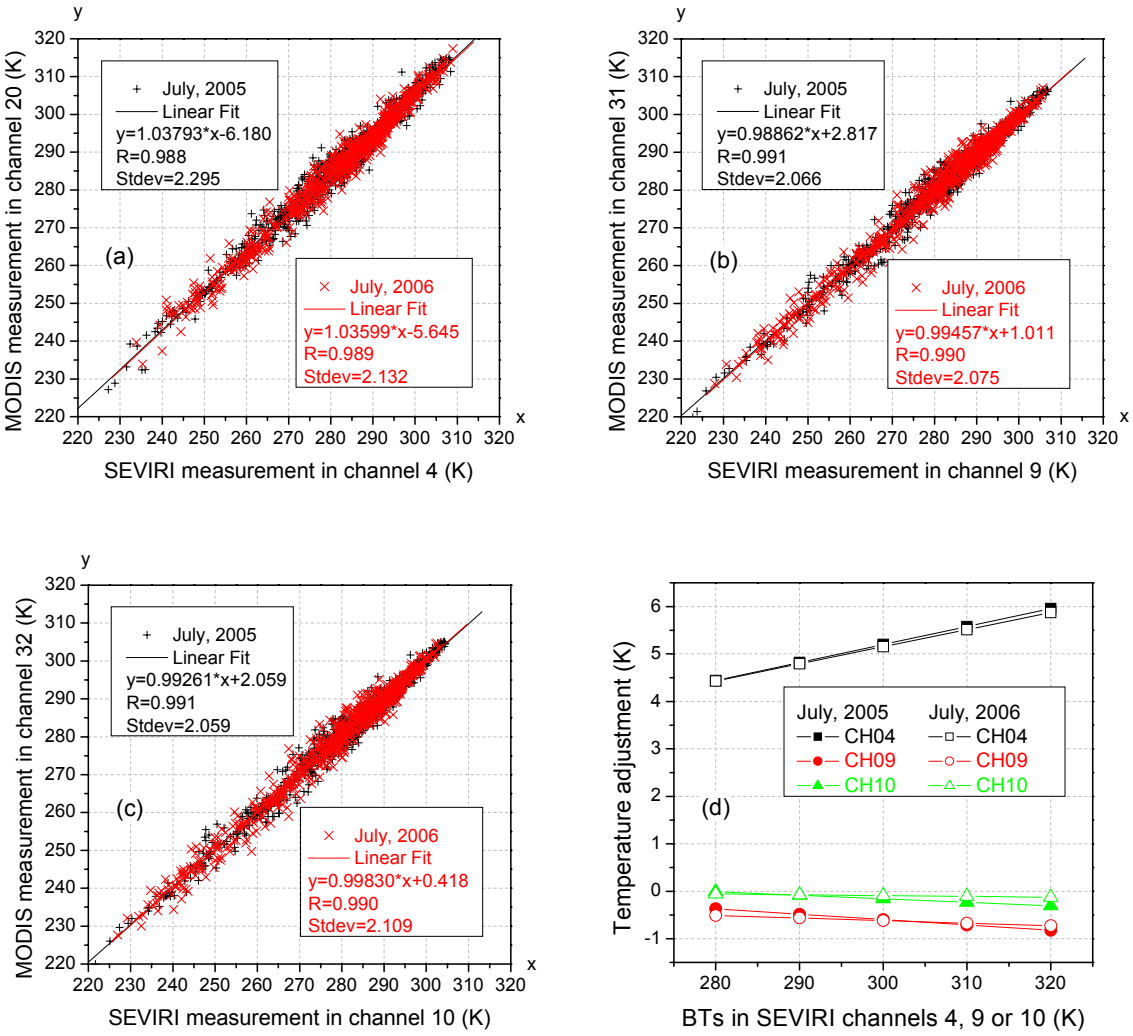

Figure 3.8. Results obtained by the ray-matching method for the MIR and TIR channels of SEVIRI and MODIS in July, 2005 (Black) and 2006 (Red) and the temperature adjustments
(Temperature adjustment: Temperature difference between measurements of MODIS and SEVIRI; R is the Correlation coefficient; Stdev represents Standard deviation; CH04, CH09 and CH10 stand for SEVIRI channels 4, 9 and 10, respectively; BT is the acronym of Brightness Temperature)

Compared to the former research, the results obtained by the ray-matching method in this work for SEVIRI channels 4 and 9 are basically consistent with the results of Doelling et al. (2004a & 2004b), but the temperature adjustments found in this work are much smaller than these reported by Doelling

et al. Because more strict matching conditions were applied in this work, the results obtained by the ray-matching method in this work may be more accurate and reliable than the results of Doelling et al. (2004a & 2004b).

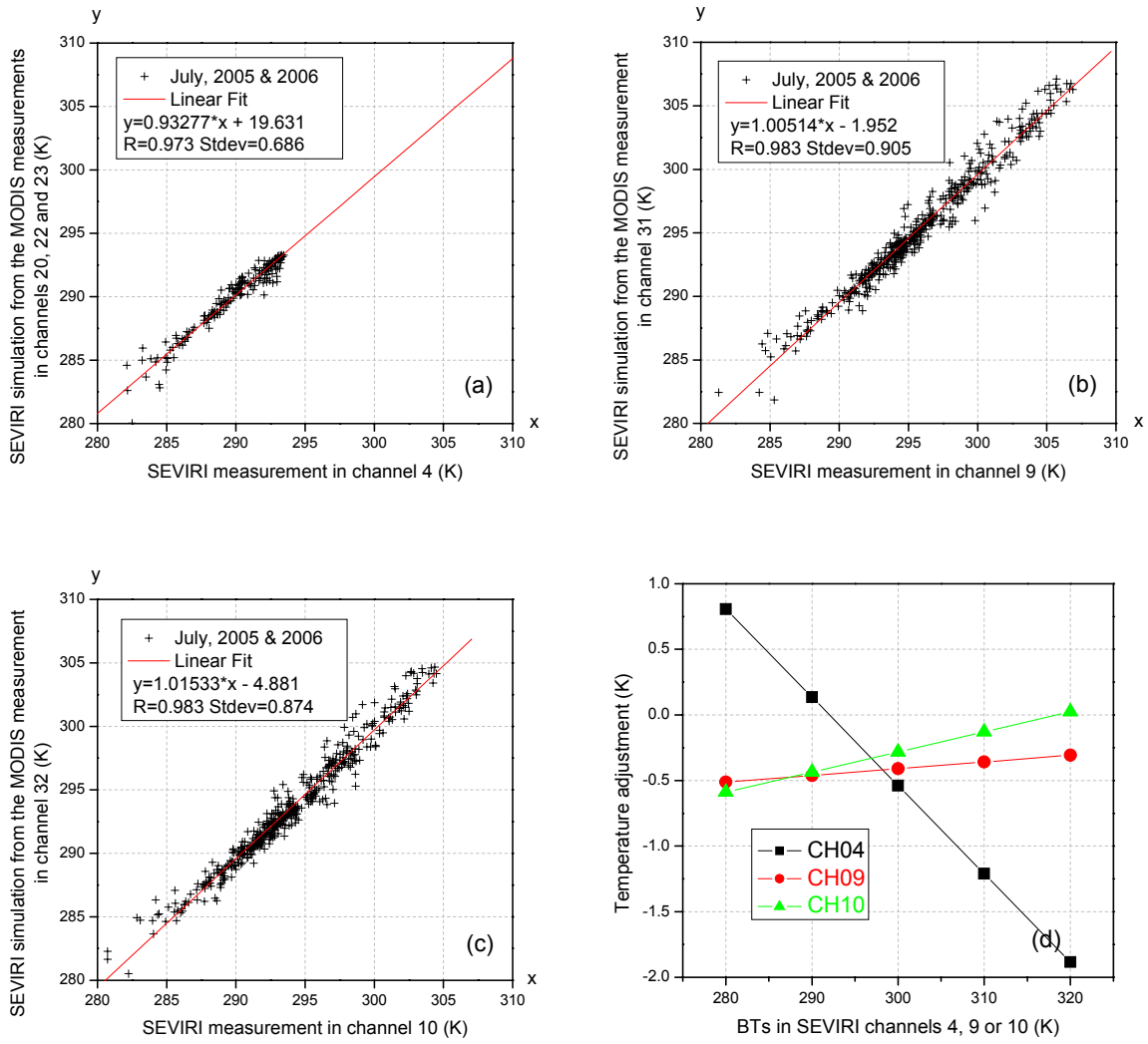

Figure 3.9. Results obtained by the radiative transfer modeling method in July 2005 and 2006 and the temperature adjustments
(Temperature adjustment: Temperature difference between SEVIRI brightness temperatures calculated from the measurements in the corresponding MODIS channel(s) by Equations (3.4a) and (3.4b) and the actual SEVIRI measured brightness temperatures; R, Stdev, CH04, CH09 and CH10 are the same as ones in Figure 3.8)

As for the radiative transfer modeling, in addition to the angular and time constraints used in the ray-matching method, the pixels indicated as cloud-contaminated by the MSG cloud masks and the pixels with view zenith angles greater than 50° were excluded, only ~80 qualified pixels in the MIR channel and ~200 qualified pixels in the TIR channels for each year. Since the cross-calibrations are consistent in July, 2005 and July, 2006 as shown in Figure 3.8, the qualified pixels in 2005 and 2006 were put together in the linear fit to obtain stable results. Figure 3.9 shows the relationships between

the simulated brightness temperatures in SEVIRI channels 4, 9 and 10 calculated from the measurements in the corresponding MODIS channels by Equations (3.4a) and (3.4b) and the actual brightness temperatures measured in the same channels by SEVIRI. As shown in Figure 3.9d, for the range of the brightness temperatures in SEVIRI channels from 280 K to 320 K, the temperature adjustments (temperature difference between SEVIRI brightness temperatures calculated from the measurements in the corresponding MODIS channel(s) by Equations (3.4a) and (3.4b) and SEVIRI measured brightness temperatures) vary linearly from 0.81 K to -1.88 K for SEVIRI channel 4, from -0.51 K to -0.31 K for SEVIRI channel 9 and from -0.59 to 0.02 K for SEVIRI channel 10.

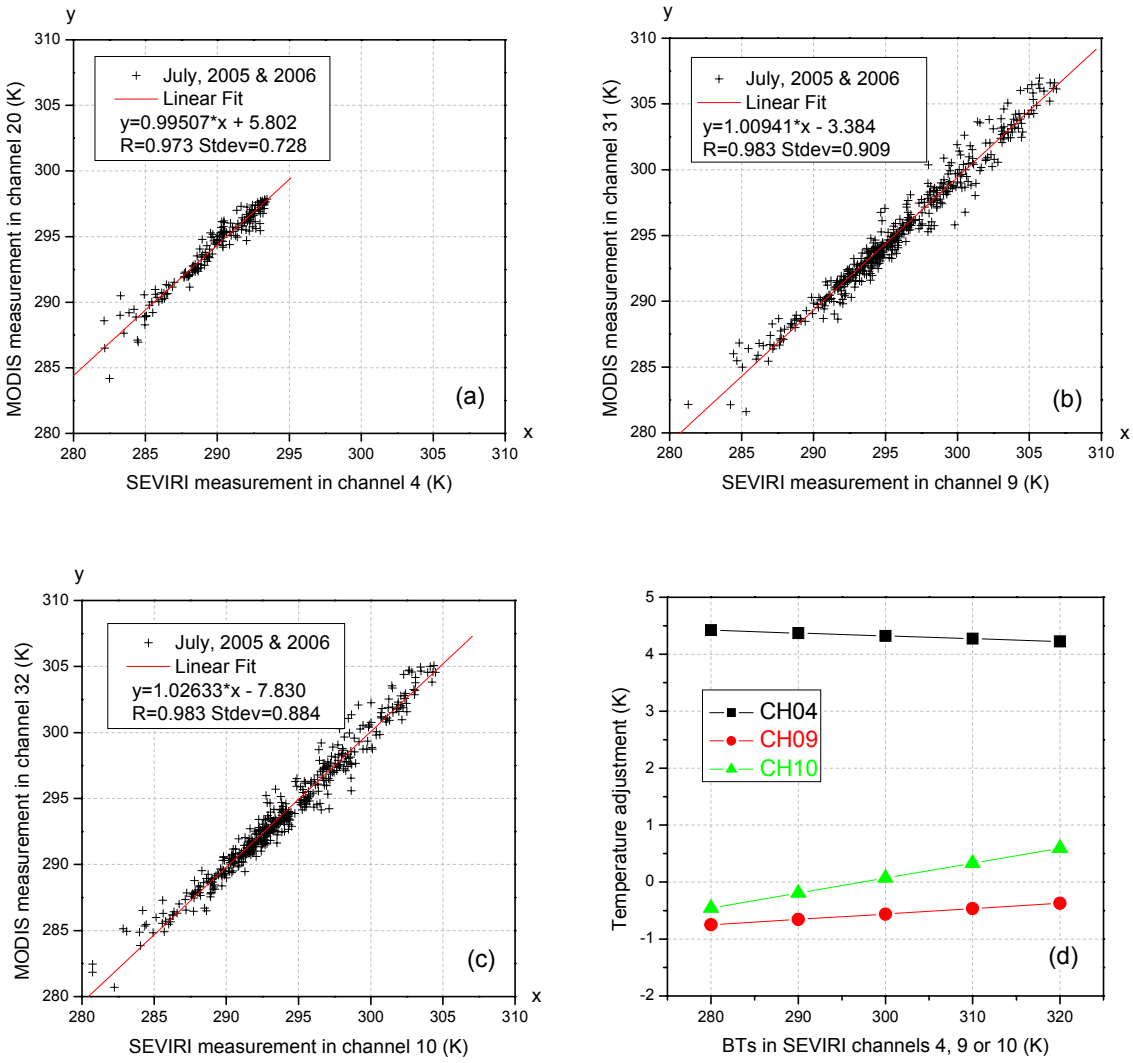

Figure 3.10. Same as the ones in Figure 3.8, but with the same pixels used in Figure 3.9

In order to compare the results obtained by the ray-matching method with these obtained by the radiative transfer modeling method, we redrawn Figure 3.8 using the same pixels as used in the radiative transfer modeling. Figure 3.10 shows the relationship of the brightness temperatures for the qualified pixels between the measurements in MODIS channels 20, 31, 32 and the corresponding measurements in SEVIRI channels 4, 9, 10. As shown in Figure 3.10d, for the brightness temperatures

ranging from 280 K to 320 K, the temperature adjustments ΔBTs are about 4.3 K for SEVIRI channel 4, and they vary from -0.75 K to 0.37 K for SEVIRI channel 9 and from 0.46 K to 0.60 K for SEVIRI channel 10.

The differences between the results obtained by the ray-matching method in Figure 3.10 and the results obtained by the radiative transfer modeling method in Figure 3.9 again validate that the spectral effects can not be neglected, especially for the MIR channels of SEVIRI and MODIS. Compared Figure 3.9d with Figure 3.4b and Figure 3.10d, if the temperature adjustments in Figure 3.10d were reduced by the corresponding average temperature differences shown in Figure 3.4b, the obtained differences are almost the same as the results obtained by the radiative transfer modeling method (Figure 3.9d).

As mentioned previously, because the radiative transfer modeling method can eliminate the temperature differences caused by the spectral differences and there are large differences of the spectral responses between SEVIRI and MODIS channels, the results obtained by the radiative transfer modeling method in this study are more accurate and reliable than the results obtained by the ray-matching method, and the use of the cross-calibration results obtained by the radiative transfer modeling method is recommended in practical applications. Here, the results acquired by the radiative transfer modeling method are listed below for convenience.

$$T_{4,s,R} = 0.93277 \times T_{4,s} + 19.631 \tag{3.6a}$$

$$T_{9,s,R} = 1.00514 \times T_{9,s} - 1.952 \tag{3.6b}$$

$$T_{10,s,R} = 1.01533 \times T_{10,s} - 4.881 \tag{3.6c}$$

where $T_{4,s,R}$, $T_{9,s,R}$ and $T_{10,s,R}$ are the re-calibrated brightness temperatures at TOA in SEVIRI channels 4, 9 and 10, respectively.

The temperature adjustments in SEVIRI channels 4, 9 and 10 will ultimately affect the LST retrieval. After the re-calibration, the brightness temperatures in SEVIRI channel 9 is abount 0.4 K lower than the original one, and the temperature adjustment for SEVIRI channel 10 changes from -0.46 K to 0.60 K when brightness temperature varies from 280 K to 320 K. This will make the brightness temperatures in SEVIRI channels 9 and 10 and the temperature difference between them to decrease, leading to the decrease of LST estimated by the split-window algorithm (Becker and Li, 1990b; Wan and Dozier, 1996; Sobrino and Romaguera, 2004).

3.5 Summary and conclusions

This work addressed the cross-calibrations of MSG1-SEVIRI infrared channels 4, 9 and 10 with the corresponding Terra-MODIS channels. The ray-matching method (Doelling et al, 2004a) and the radiative transfer modeling method (Asem et al., 1987) were recalled and applied to the cross-calibrations.

The ray-matching method is a simple and direct way to use the coincident, co-angled and co-located pixels to transfer the calibration of one well-calibrated sensor to another. The radiative transfer modeling method was developed using the radiative transfer code MODTRAN 4.0 fed with the adjusted Tropical profiles. The spectral effects on emissivities were taken into account in terms of the

MODIS UCSB Emissivity Library. For the MIR channels, seven spectral emisivity samples representing vegetation, soil and water were used. For the two split-window channels, linear regression equations based on the spectral emissivities of water, vegetation and soil extracted from the MODIS UCSB Emissivity Library were built to interpret the emissivity relationship between SEVIRI and MODIS channels. The results of the numerical experiment show that, the brightness temperatures in SEVIRI channels 4 and 10 are, respectively, lower than the ones in MODIS channels 20 and 32, but the brightness temperatures in SEVIRI channel 9 are slightly higher than the ones in MODIS channel 31. The brightness temperature differences between MODIS and SEVIRI are mainly caused by the differences of the spectral responses, and are found to be temperature dependent.

Considering the special view geometries of SEVIRI and MODIS, a tropical region, with the longitude going from 45W to 45E and the latitude going from 10S to 10N, was selected as the study area. The MSG Level 1.5 product, the MSG cloud mask, the 1KM MODIS/Terra L1B product (MOD021KM) and the MODIS/Terra Geolocation product (MOD03) covering the whole study area in July, 2005 and July, 2006 were used in the cross-calibration. All the data were aggregated into the WGS 84 coordinate system with the longitude and latitude resolutions of 0.1° by an area-weighted aggregation algorithm (Equation (3.5) & Figure 3.7). Based on the minimum RMSE principle, the SEVIRI images were accurately matched with the MODIS images. In the cross-calibration, only those measurement pairs with the view zenith angle differences less than 0.5°, the view azimuth angle differences less than 1.0° and the time differences less than 10 minutes were considered.

The results obtained by the ray-matching method show that the calibrations of SEVIRI channels 4, 9 and 10 against MODIS channels are consistent in 2005 and 2006. The brightness temperatures measured in SEVIRI channel 4 are obviously lower than the ones measured in MODIS channel 20, while the brightness temperatures measured in SEVIRI channels 9 and 10 are, respectively, higher than the ones measured in MODIS channels 31 and 32. The results obtained by the ray-matching method show that, for brightness temperatures ranging from 280 K to 320 K, the temperature adjustments ΔBTs increases from 4.4 K to 5.9 K for SEVIRI channel 4, and they vary from -0.44 K to -0.75 K for SEVIRI channel 9 and from -0.03 K to -0.21 K for SEVIRI channel 10. The temperature adjustments found in this work are much smaller than these reported by Doelling et al. (2004a & 2004b), but they are basically consistent. Because more strict matching conditions were applied, the results obtained by the ray-matching method in this work may be more accurate and reliable than the results of Doelling et al. (2004a & 2004b). Because the ray-matching method can not account for the effects of the different spectral responses between SEVIRI and MODIS, it is hard to decide whether the brightness temperatures in SEVIRI channels are overestimated or underestimated.

As for the radiative transfer modeling method, the results show that, for the range of the brightness temperatures in SEVIRI channels from 280 K to 320 K, the temperature adjustments (temperature difference between the SEVIRI brightness temperatures calculated from the measurements in the corresponding MODIS channel(s) by Equations (3.4a) and (3.4b) and the SEVIRI measured brightness temperatures) vary linearly from 0.81 K to -1.88 K for SEVIRI channel 4, from -0.51 K to 0.31 K for SEVIRI channel 9 and from -0.59 to 0.02 K for SEVIRI channel 10. Qualitative analysis shows that the results obtained by the radiative transfer modeling method are consistent with the results obtained by the ray-matching method if the brightness temperature differences caused by the spectral responses were taken into account in the ray-matching.

Because of the large differences of the spectral responses between SEVIRI and MODIS channels, the use of the results obtained by the radiative transfer modeling method to re-calibrate the SEVIRI

data is recommended. The re-calibrations will make the differences between the brightness temperatures in SEVIRI channels 9 and 10 and the temperature differences between them to decrease, and consequently remove the overestimate of the LSTs retrieved from the SEVIRI data with the split-window method.

In the following chapters, the satellite data in SEVIRI channels 4, 7 and 9 will be re-calibrated using Equations (3.6a), (3.6b) and (3.6c), respectively.

4 Land surface emissivity retrievals from MSG1-SEVIRI data

4.1 Introduction

LSE is a key parameter in the retrieval of Land Surface Temperature (LST) (Becker and Li, 1990b; Wan and Dozier, 1989 & 1996; Sobrino and Romaguera, 2004). However, direct estimation of LSE from passive satellite measurements is not possible. One of the main difficulties in the use of satellite data is the need to correct for atmospheric perturbations. Apart from the atmospheric effects in all wavelengths, the separation between LSE and LST is a challenge in the passive TIR remote sensing. During the past two decades, significant progress has been made in the retrievals of LSE and LST from passive thermal infrared data.

Snyder et al. (1998) proposed a classification-based emissivity retrieval method. In this approach, a pixel is classified as one of the fourteen 'emissivity classes' based on the conventional land cover classification and dynamic and seasonal factors, such as snow cover and vegetation index. The emissivity models that they developed provide a range of values for each emissivity class by combining various spectral component measurements with structural factors. The classification-based emissivities in MODIS channels 31 and 32 serve as input parameters in the operational generation of the MODIS/Terra LST product MOD11_L2. A large uncertainty may exist in the classification-based emissivities, especially in semi-arid and arid regions, and this will lead to a poor accuracy of retrieved LST, which will be detailed in the LST cross-validation chapter.

Van-De-Griend and Owe (1993) showed that the thermal emissivity ε (in the 8-14 μm spectral range) is highly correlated with NDVI (Normalized Difference Vegetation Index) for different surface types: ε=a+bln(NDVI) (a and b are unknown coefficients). Valor and Caselles (1996) developed a theoretical model that relates the emissivity to the NDVI and an operational methodology to obtain the effective emissivity from satellite images, and they obtained a good result. Sobrino and Raissouni (2000) proposed a NDVI threshold method to determine the emissivities in AVHRR channels 4 and 5 using the NDVIs calculated from the atmospherically corrected data in AVHRR channels 1 and 2. The NDVI threshold method shows a promising result and can be applied to obtain LSE and LST from NOAA data without loosing accuracy (Sobrino et al., 2001).

Vincent et al. (1975) proposed a reference channel method, and then this method was further developed and used by Kahle et al. (1980, 1987 and 1992). This method assumes that the emissivity in a reference channel *r* has a constant value $\varepsilon_r^{\#}$ for all pixels, i.e., $\varepsilon_r=\varepsilon_r^{\#}$. Considering the constant emissivity in channel r and knowing atmospheric parameters (τ_r, $L_{atm\uparrow,r}$ and $L_{atm\downarrow,r}$), an approximate

surface temperature $T_s^{\#}$ is derived for each pixel by the inversion of the radiative transfer equations. This temperature is then used to derive the emissivities in the remaining channels.

Gillespie (1985) presented an emissivity normalization method, and this method was used by Realmuto (1990) and Gillespie et al. (1998). This method assumes a constant emissivity in all N infrared channels for a given pixel, which leads to N temperatures to be calculated for each pixel. The maximum temperature is considered to be the LST and then used to derive emissivities in the other channels as it is done with the reference method.

Kealy and Gabell (1990) proposed an alpha emissivity method. Based on the Wien's approximation of the Planck equation, the emissivity is directly related to the radiances at ground level. As Li et al. (1999) pointed out, this method is difficult to use when dealing with the measured radiance because the reflected downwelling atmospheric radiance is neglected in constructing the alpha.

Watson (1992a) developed a spectral ratio method based on the concept that, although the spectral radiances are very sensitive to small changes in temperature, the ratios are not. The ratio method is limited by both the noise and spectral bandwidth. Watson (1992b) also proposed a two-temperature method, and this method was applied to the retrievals of LST and LSE from MSG1-SEVIRI data (Peres and DaCamara, 2004). This method retrieves emissivity from two radiance measurements at two times. Although the two-temperature method possesses the advantage that the emissivity is determined without any priori assumption, it is strongly sensitive to noise.

Gillespie et al. (1998) developed a Temperature/Emissivity Seperation (TES) method for ASTER instrument. ASTER's TES algorithm hybridizes three established algorithms, first estimating the normalized emissivity and then calculating emissivity band ratios. An empirical relationship predicts the minimum emissivity from the spectral contrast of the ratioed values, permitting recovery of the emissivity spectrum. TES uses an iterative approach to remove reflected sky irradiance.

Becker and Li. (1990a) proposed a physics-based emissivity-temperature decoupling method in terms of the Temperature Independent Spectral Indices (TISI) concept, which requires constant Temperature Independent Spectral Indices of Emissivities (TISIEs) between day and night. According to the evaluation results of Li et al. (1999), TISI method is recommended to use in proper application. This method has been successfully applied to the LSE retrievals from the data in AVHRR channels 3, 4 and 5 (Goïta and Royer, 1997; Nerry et al., 1998; Sobrino, 2001; Petitcolin et al., 2002a, 2002b; Dash et al., 2005) and the LSE retrievals from the data in MODIS channels (Petitcolin and Vermote, 2002). However, because both the AVHRR and the MODIS are onboard of polar-orbit satellites, the actual pixel sizes may be different for a given area from one overpass to another due to the different view angles and this could introduce large error if the surface is heterogeneous. Moreover, to obtain a sufficient number of angle configurations for the bi-directional reflectivities used in the retrieval of the emissivity in MIR channel, usually 2- to 3-month observations are required and land surface properties may change during that long period.

As described in the section 2.2, MSG1-SEVIRI provides measurements of the Earth-disc (centered at 0° longitude and 0° latitude) every 15 minutes in 12 spectral channels at fixed view angles, but the solar angles change every 15 minutes during daytime, making it particularly suitable for LSE and LST determinations by day/night TISI concept. Because of the heterogeneity of land surface and low spatial resolution of MSG1-SEVIRI, LSE in this thesis refers to the directional r-emissivity defined by Norman and Becker (1995).

In this work, we focus on the LSE retrievals from the combined MIR and TIR data of MSG1-SEVIRI using the TISI concept. The atmospheric correction was implemented by the use of MODTRAN 4.0 fed with the ECMWF data, combined a modified Diurnal Temperature Cycle (DTC) model of Göttsche and Olesen (2001) and Schädlich et al. (2001) to account for the temporal interpolation. This method will be applied to the MSG Level 1.5 product to retrieve directional emissivities in SEVIRI channels 4, 9 and 10. In the section 4.2, the theoretical method to retrieve LSEs is briefly presented, including the atmospheric correction scheme and the decoupling of LST and LSE from radiance. In the section 4.3, the study areas and data are described. In the sections 4.4 and 4.5, the LSE retrieval method was applied to a small area and a large area, including the data processing, the results and the results analysis. Finally, the summary and conclusions are given in the section 4.6.

4.2 Method

The radiative transfer theory is presented in the section 2.1.

4.2.1 Retrievals of directional emissivities in SEVIRI channels 4, 7, 9 and 10

During daytime, the surface reflected solar irradiance and the surface emitted radiance in the MIR channel (~3.9μm) have comparable magnitude if the surface albedo in this channel is around 0.1 (Li and Becker, 1993). The direct solar irradiance serves as an active source, which can be used to retrieve firstly the bi-directional reflectivity and then the directional emissivity in the MIR channel (Becker and Li, 1990a; Li and Becker, 1993). The directional emissivities in the TIR channels are then inferred from the emissivity in the MIR channel by the use of the TISI concept again (Becker and Li, 1990a; Li and Becker, 1993; Li et al., 2000; Petitcolin et al., 2002b). Hereafter, we recall the various steps.

Introducing the quantity of $B_i(\theta_v)$

$$B_i(\theta_v) = \int_0^\infty f_i(\lambda)\left\{\varepsilon(\theta_v,\lambda)L(T_s,\lambda) + \left[1-\varepsilon(\theta_v,\lambda)\right]L_{atm\downarrow}(\lambda)\right\}d\lambda \Big/ \int_0^\infty f_i(\lambda)d\lambda \qquad (4.1)$$

and for the MIR channel of SEVERI (channel 4) assuming that

$$\int_0^\infty f_4(\lambda)\rho_{b,4}(\theta_v,\theta_s,\varphi,\lambda)E_{sun}(\lambda)d\lambda \Big/ \int_0^\infty f_4(\lambda)d\lambda = \rho_{b,4}(\theta_v,\theta_s,\varphi)E_{sun,4} \qquad (4.2)$$

From Equations (2.6), (4.1) and (4.2), the bi-directional reflectivity in SEVIRI channel 4 is given by

$$\rho_{b,4}(\theta_v,\theta_s,\varphi) = \frac{L_{G,4}(T_{g,4},\theta_v) - B_4(\theta_v)}{E_{sun,4}} \qquad (4.3)$$

In Equation (4.3), $L_{G,4}(T_{g,4}, \theta_v)$ can be computed by inverting Equation (2.5), which will be detailed in the atmospheric correction section, and $E_{sun,4}$ will be estimated from the ECMWF reanalysis data with MODTRAN 4.0. The quantity $B_4(\theta_v)$ can be estimated following the method used by Nerry et al. (1998) based on the assumption that TISIs do not change between day and night:

$$B_4(\theta_v) = \frac{C^{day}}{C^{night}} \left[\frac{B_j^{day}(\theta_v)}{B_j^{night}(\theta_v)} \right]^{n_4/n_j} B_4^{night}(\theta_v) \tag{4.4}$$

with $C = \prod_{i=1}^{2} C_i^{a_i}$ (a_4=1 and a_j=-n_4/n_j, j is the number of TIR channel) and $C_i = \frac{1 - \frac{L_{atm\downarrow i}}{L_i(T_s)}}{1 - \frac{L_{atm\downarrow i}}{B_i}}$.

Where superscripts *day* and *night* indicate day and night measurements, respectively, n_i is the exponent of the power law approximation: $R_i=m_i T_{g,i}^{ni}$ (R_i is the radiance in channel *i*).

The coefficients m_i and n_i depend on the spectral characteristics of the sensor (Becker and Li, 1990a) and have been determined by the Levenberg-Marquardt least squares fit method in order to solve the equation. Table 4.1 gives the values of the m_i and n_i coefficients for SEVIRI channels 4, 7, 9 and 10, and the errors (RMSE and maximum error) for the temperature ranging from 280 K to 320 K with a step of 0.1 K. In order to eliminate the combined errors due to the use of power law approximation, n_i/n_j was calculated as a whole to solve the equation $R_i=\alpha_{ij}(R_j)^{nij}$ with $n_{ij}=n_i/n_j$ (i=4, 7, 9 or 10; j=7, 9 or 10 and i≠j; α_{ij} is an unknown coefficient). Table 4.2 gives the value of the coefficients α_{ij} and n_{ij} for the temperature varying from 280 K to 320 K with a step of 0.1 K.

Table 4.1. Values of the coefficients *m* and *n* and fitting errors for SEVIRI channels 4, 7, 9 and 10

Channel	4 (IR3.9)	7 (IR8.7)	9 (IR10.8)	10 (IR12.0)
m	9.7260E-031	1.3885E-012	7.4113E-010	8.8283E-009
n	12.1117	5.5393	4.5127	4.1017
RMSE (K)	0.20	0.20	0.19	0.19
Max error (K)	0.47	0.47	0.46	0.45
Error at 300 K (K)	0.22	0.22	0.21	0.21

Temperature range: 280 – 320 K, step: 0.1 K

Table 4.2. Values of the coefficients $\alpha_{i,j}$ and n_i/n_j for SEVIRI channels 4, 7, 9 and 10

channel	7 (IR8.7)		9 (IR10.8)		10 (IR12.0)	
	α_{ij}	n_{ij}	α_{ij}	n_{ij}	α_{ij}	n_{ij}
4 (IR3.9)	8.20752E-5	2.1865	3.10793E-6	2.6840	5.89719E-7	2.9530
7 (IR8.7)			0.22375	1.2275	0.10462	1.3506
9 (IR10.8)	3.38619	0.8146			0.53835	1.1002
10 (IR12.0)	5.31986	0.7404	1.75566	0.9089		

$n_{ij} = n_i/n_j$ and $n_{ji} = 1/n_{ij}$. Temperature range: 280 – 320 K, step: 0.1 K

The corrective factor C_i will be evaluated in this way: $L_{atm\downarrow i}$ is calculated by MODTRAN fed with the ECMWF data. Except for the daytime radiance in SEVIRI channel 4, the B_i is the measured radiance atmospherically corrected. Taking C^{day}/C^{night}=1.0 in Equation (4.4), a rather good approximation of B_4^{day} can be calculated. The surface temperature T_s is approximately calculated using

an emissivity of 0.96. Nerry et al. (1998) revealed that the uncertainties in the estimation of the corrective factors have a minor impact on final results. Hence, the bi-directional reflectivity can be directly retrieved from the radiances at ground level.

$$\rho_{b,4}(\theta_v,\theta_s,\varphi)=\frac{L_{G,4}(\theta_v)-\dfrac{C^{day}}{C^{night}}\left[\dfrac{B_j^{day}(\theta_v)}{B_j^{night}(\theta_v)}\right]^{n4/nj}B_4^{night}(\theta_v)}{E_{sun,4}} \tag{4.5}$$

For an opaque medium in thermal equilibrium, directional emissivity is related to directional hemispherical reflectivity by the Kirchhoff's law:

$$\varepsilon(\theta_v)=1-\rho_h(\theta_v) \tag{4.6}$$

where $\rho_h(\theta_v)$ is defined by Nicodemus (1965)

$$\rho_h(\theta_v)=\int_0^{2\pi}\int_0^{\pi/2}\rho_b(\theta_v,\theta_s,\varphi)\sin(\theta_s)\cos(\theta_s)d\theta_s d\varphi \tag{4.7}$$

In order to derive the emissivities in SEVIRI channels 7, 9 and 10, the two-channel $TISI_{i,j}$ indices are introduced (Becker and Li,1990a) and assumed again that they do not change between day and night. One can obtain:

$$\varepsilon_i(\theta_v)=\frac{\left[\varepsilon_4(\theta_v)\right]^{n_i/n_4}}{(TISI_{4,i}^{night})^{n_i}} \qquad i=7,\ 9 \text{ or } 10 \tag{4.8}$$

and

$$\varepsilon_j(\theta_v)=\frac{\left[\varepsilon_i(\theta_v)\right]^{n_j/n_i}}{(TISI_{i,j})^{n_j}} \qquad i=7,\ 9 \text{ or } 10,\ j=7,\ 9 \text{ or } 10\ (i\neq j) \tag{4.9}$$

with $TISI_{i,j}=\left[\dfrac{B_i(\theta_v)}{m_iC_i}\right]^{1/n_i}\left[\dfrac{B_j(\theta_v)}{m_jC_j}\right]^{-1/n_j}$, i=7, 9 or 10; j=7, 9 or 10 ($i\neq j$)

In the following, two combinations (combinations of SEVIRI channels 4 and 9 and of SEVIRI channels 4 and 10) will be used to estimate the bi-directional reflectivities in SEVIRI channel 4, two groups of emissivities can therefore be obtained for each channel. Hereafter, we referred to $\varepsilon_4^{(1)}$, $\varepsilon_7^{(1)}$, $\varepsilon_9^{(1)}$ and $\varepsilon_{10}^{(1)}$ as the estimated emissivities in SEVIRI channels 4, 7, 9 and 10 using the combination of SEVIRI channels 4 and 9, and referred to $\varepsilon_4^{(2)}$, $\varepsilon_7^{(2)}$, $\varepsilon_9^{(2)}$ and $\varepsilon_{10}^{(2)}$ as the derived emissivities in SEVIRI channels 4, 7, 9 and 10 using the combination of SEVIRI channels 4 and 10.

Here, let us evaluate the errors introduced in $\rho_{b,4}(\theta_v, \theta_s,\varphi)$ and $\varepsilon_4(\theta_v)$ by the assumption made in Equation (4.2) in terms of the spectral data extracted from the MODIS UCSB Emissivity Library.

$$\Delta\rho_{b,4}=\int_0^{\infty}f_4(\lambda)\rho_{b,4}(\theta_v,\theta_s,\varphi,\lambda)E_{sun}(\lambda)d\lambda\Big/\left[E_{sun,4}\int_0^{\infty}f_4(\lambda)d\lambda\right]-\rho_{b,4}(\theta_v,\theta_s,\varphi) \tag{4.10}$$

Three types of materials, vegetation, soil and sand & sandy soil, were used in the evaluation, and they were assumed to be Lambertian reflectors because of the shortage of multiple-angle observations. Table 4.3 gives the mean, maximum and minimum errors in $\rho_{b,4}(\theta_v, \theta_s, \varphi)$, and the mean errors in $\varepsilon_4(\theta_v)$ under the atmospheric conditions of MLS, MLW, Tropical and 1976 US Standard with a view zenith angle of 45°. For the vegetation and soil materials, the reflectivity $\rho_{b,4}(\theta_v, \theta_s, \varphi)$ is averagely slightly overestimated, while the opposite is observed for the sand & sandy soil materials. The absolute mean errors in $\rho_{b,4}(\theta_v, \theta_s, \varphi)$ are less equal than 0.0014 and the absolute mean errors in $\varepsilon_4(\theta_v)$ are less equal than 0.004. From the results, it can be concluded that the errors in both $\rho_{b,4}(\theta_v, \theta_s, \varphi)$ and $\varepsilon_4(\theta_v)$ introduced by the assumption made in Equation (4.2) can be ignored.

Table 4.3. Errors introduced in $\rho_{b,4}(\theta_v, \theta_s, \varphi)$ and $\varepsilon_4(\theta_v)$ by the assumption made in Equation (4.2) in terms of the MODIS UCSB Emissivity Library and the model atmospheres in MODTRAN

Type	$\Delta\rho_{b,4,Mean}$	$\Delta\rho_{b,4,Maximum}$	$\Delta\rho_{b,4,Minimum}$	$\Delta\varepsilon_4(\theta_v)$
Vegetation	-0.0003	0.0002	-0.0022	0.001
Soil	-0.0004	0.0009	-0.0026	0.001
Sand & Sandy soil	0.0014	0.0031	-0.0012	-0.004

Model atmospheres: MLS, MLW, Tropical and 1976 U S Standard; view zenith angle: 45°

4.2.2 BRDF models: Modified Minnaert's model and RossThick-LiSparse-R model

As we know, land surface does not scatter the solar irradiance in equal quantities in all directions. In fact, it shows a behavior far from being a Lambertian reflector. Bi-directional Reflectance Distribution Function (BRDF) gives the reflectance as a function of illumination geometry and view geometry. Figure 4.1 depicts the angles that BRDF is dependent on. The BRDF is also spectral dependent and is determined by the structural and optical properties of land surface. Many BRDF models have been developed to describe the bi-directional reflectance, and they can be categorized into two types: the purely empirical model and the semi-empirical model. For the purely empirical BRDF models, there is no physical basis for such kernels beyond their description of BRDF-like shape, such as the Minnaert's BRDF model (1941) and the Walthall's model (Walthal et al., 1985; Nilson and Kuusk, 1989). Whereas, the semi-empirical BRDF models were derived from more complex physical theory through simplifying assumptions and approximations, such as the Roujean's model (1992), the Wanner's model (Wanner et al., 1995) and the LiSparse-Dense BRDF model (Li and Strahler, 1992). Here, we highlighted the modified Minnaert's model and the kernel-driven RossThick-LiSparse-R model.

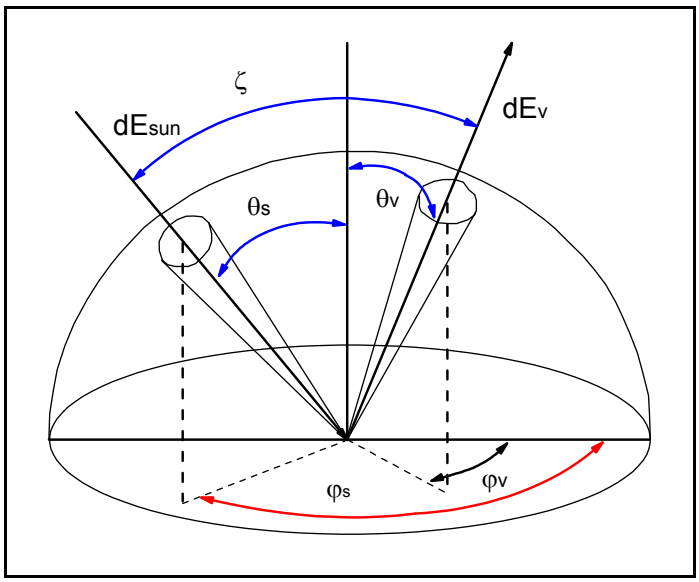

Figure 4.1. Concepts and parameters of the BRDF
(Sandmeier and Itten, 1999, modified; ζ is the phase angle; dE_{sun} is the differencetial increment of the direct solar irradiance at sun zenith angle, and dE_v is the corresponding differential increment of the reflected solar radiance)

Minnaert (1941) proposed an empirical BRDF model to describe the non-Lambertian behavior of land surface. The Minnaert's BRDF model has been widely used in planetary astronomy. Because it does not consider the azimuthal dependence, the Minnaert's model is not sufficient to describe the directional reflectance of structured surfaces, such as forest. Li et al. (2000) modified it, adding a third parameter to take care of the relative azimuth angle $\varphi=|\varphi_s-\varphi_v|$, and successfully applied it to the modeling of the bi-directional reflectivities in AVHRR channel 3 (Petitcolin et al., 2002a). In this work, the anisotropy factor $b(1-k^2)$ from Equation (11) in the paper published by Petitcolin et al. (2002a) is replaced by an unique parameter γ to obtain a stable minimization.

$$\rho_{b,4}(\theta_v,\theta_s,\varphi)=\rho_0\left[\cos(\theta_v)\cos(\theta_s)\right]^{k-1}\left[1+\gamma\sin(\theta_v)\sin(\theta_s)\cos(\varphi)\right] \tag{4.11}$$

where ρ_0 is the reflectivity under the condition that both the view zenith angle and the solar zenith angle equal to zero (i.e., $\theta_v=\theta_s=0$). k is a parameter between 0 and 1. For a Lambertian reflector, k equals to 1. γ is the anisotropy factor.

Combining Equations (4.6), (4.7) and (4.11), one can obtain the directional emissivity in SEVIRI channel 4

$$\varepsilon_4(\theta_v)=1-\frac{2\pi}{k+1}\rho_0\cos^{k-1}(\theta_v) \tag{4.12}$$

The RossThick-LiSparse-R model is a kernel-driven BRDF model. The linearity of kernel-driven model is advantageous to global BRDF and albedo processing needs in several respects, most notably analytical invertibility, making possible look-up table approaches in albedo calculation, accommodation of mixed pixel situations, and spatial scaling (Wanner et al., 1995). The kernel-driven BRDF model is given below as a linear sum of terms characterizing different scattering modes.

$$\rho(\theta_v, \theta_s, \varphi) = \sum_i k_i \bullet f_i(\theta_v, \theta_s, \varphi) \tag{4.13}$$

where ρ is the bi-directional reflectance. k_i is the *ith* model parameter, and f_i is the ith model kernel.

The theoretical basis of these semi-empirical kernel-driven models is that the land surface reflectance typically consists of three components: the isotropic scattering, the volumetric scattering and the geometric-optical surface scattering (Roujean et al., 1992).

$$\rho(\theta_v, \theta_s, \varphi) = k_{iso} + k_{vol} \bullet f_{vol}(\theta_v, \theta_s, \varphi) + k_{geo} \bullet f_{geo}(\theta_v, \theta_s, \varphi) \tag{4.14}$$

where k_{iso} is the isotropic scattering term, k_{vol} is the coefficient of the volumetric kernel f_{vol}, and k_{geo} is the coefficient of the geometric kernel f_{geo}.

The Roujean's model (Roujean et al., 1992) was developed specially for the correction of satellite data over a wide variety of surface types, and the volume kernel is a suitable expression for Equation (4.14). Roujean's volume kernel is a single scattering solution to the classic canopy radiative transfer equation by Ross (1981) for plane-parallel dense vegetation canopy with uniform leaf angle distribution, and equal leaf reflectance and transmittance. It does not account for the hotspot phenomenon either.

$$f_{vol}(\theta_v, \theta_s, \varphi) = \frac{4}{3\pi} \frac{1}{\cos\theta_v + \cos\theta_s} \bullet \left[(\frac{\pi}{2} - \xi)\cos\xi + \sin\xi \right] - \frac{1}{3} \tag{4.15}$$

where ζ is the phase angle, related to conventional angles by

$$\cos\xi = \cos\theta_v \cos\theta_s + \sin\theta_v \sin\theta_s \cos\varphi \tag{4.16}$$

A geometric kernel, the LiSparse kernel derived by Wanner et al. (1995), has been justified to work well with measured data. This kernel is derived from the geometric-optical mutual shadowing BRDF model developed by Li and Strahler (1992), unlike the geometrical kernel in the Roujean's BRDF model, in which the mutual shadowing between protrusions is ignored. The original form of this kernel is not reciprocal in θ_v and θ_s, and then was modified into a reciprocal form under the assumption that the sunlit component simply varies as $1/\cos(\theta_s)$ (Lucht, 1998; Lucht and Louis, 2000). Hereafter, the reciprocal LiSparse kernel is called LiSparse-R:

$$f_{geo} = f_{LSR} = O(\theta_v, \theta_s, \varphi) - \sec\theta_v' - \sec\theta_s' + \frac{1}{2}(1 + \cos\xi')\sec\theta_v' \sec\theta_s' \tag{4.17}$$

where

$$O = \frac{1}{\pi}(t - \sin t \cos t)(\sec\theta_v' + \sec\theta_s') \tag{4.18}$$

$$\cos t = \frac{h}{b} \frac{\sqrt{D^2 + (\tan\theta_v' \tan\theta_s' \sin\varphi)^2}}{\sec\theta_v' + \sec\theta_s'} \tag{4.19}$$

$$D = \sqrt{\tan^2\theta_v^{'} + \tan^2\theta_s^{'} - 2\tan\theta_v^{'}\tan\theta_s^{'}\cos\varphi} \tag{4.20}$$

$$\cos\xi^{'} = \cos\theta_v^{'}\cos\theta_s^{'} + \sin\theta_v^{'}\sin\theta_s^{'}\cos\varphi \tag{4.21}$$

$$\theta_v^{'} = \tan^{-1}(\frac{b}{r}\tan\theta_v) \qquad \theta_s^{'} = \tan^{-1}(\frac{b}{r}\tan\theta_s) \tag{4.22}$$

where O is the overlap area between the view and solar shadows. The term cos(t) should be constrained to the range [-1, 1], as value outside this range imply no overlap and should be discarded. h/b and b/r are the dimensionless crown relative height and shape parameters, respectively. In MODIS BRDF/Albedo products, h/b=2 and b/r=1, i.e., the spherical crows are separated from the ground by half their diameter. These settings will be used in the modeling of the bi-directional reflectivities in SEVIRI channel 4. Generally, the shape of the crown affects the BRDF more than their relative height (Wanner et al., 1995).

The combination of the Roujean's volumetric model and the LiSparse-R model is the so-called RossThick-LiSparse-R BRDF model, which has been used in the MODIS at-launch BRDF/Albedo algorithm (MODIS BRDF/Albedo Product: ATBD version 5). This model has been widely validated with its modeling ability, its performance with sparse angular sampling and its less sensitivity to noise, and the retrievals are generally reliable (Hu et al., 1997; Privette et al., 1997).

In this work, the RossThick-LiSparse-R was an option to model the atmospherically corrected bidirectional reflectance at ground level in SEVIRI channel 4 (3.9μm). As we know, the SEVIRI sensor is onboard a geostationary satellite MSG1, and it observes a large area of solar angular measurements every 15 minutes at fixed view zenith angles but various sets of relative azimuth angles. Pokrovsky et al. (2003) pointed out that the BRDF sampling will be a warping of the perpendicular plane towards the backscattering area, away from the tropical belt, with the exception of the summer season. The lack of measurements in the principal plane, where the angular effects are amplified, will lead to biased estimations of the BRDF.

According to Equations (4.6), (4.7), and (4.14), the directional emissivity in SEVIRI channel 4 is given by

$$\varepsilon_4(\theta_v) = 1 - \pi k_{iso} - k_{vol} \bullet If_{vol}(\theta_v) - k_{geo} \bullet If_{geo}(\theta_v) \tag{4.23}$$

with $If_x(\theta_v) = \int_0^{2\pi}\int_0^{\pi/2} f_x(\theta_v, \theta_s, \varphi)\sin(\theta_s)\cos(\theta_s)d\theta_s d\varphi$, in which the subscription *x* represents *vol* or *geo*.

As shown in Equation (4.23), the integrals of $If_{vol}(\theta_v)$ and $If_{geo}(\theta_v)$ over the solar zenith angle and the solar azimuth angle are complicated mathematical expressions, because the volumetric kernel f_{vol} and the geometrical kernel f_{geo} are not as the functions as the ones in the modified Minnaert's BRDF model which can be directly worked out over the angles. For a certain view zenith angle ranging between 0° and 80°, we calculated the integrals $If_{vol}(\theta_v)$ and $If_{geo}(\theta_v)$ with a step of 0.05° (~8.73×10^{-4} radian) for both solar zenith angle and solar azimuth angle. Figure 4.2 is the integrated results and shows that the integral $If_{vol}(\theta_s)$ is proportional to the view zenith angle, whereas the integral $If_{geo}(\theta_s)$ is inversely proportional to the view zenith angle. Several non-linear expressions involving view zenith angle θ_v were investigated with respect to their ability to provide a simple functional representation of

the integrals $If_{vol}(\theta_v)$ and $If_{geo}(\theta_v)$. It was found that the Exponential Growth function (Equation (4.24)) and the Gauss function (Equation (4.25)) provided very good fits to $If_{vol}(\theta_v)$ and $If_{geo}(\theta_v)$, respectively.

$$If_{vol}(\theta_v) = A_0 + A_1 \exp(\theta_v / t_1) \tag{4.24}$$

$$If_{geo}(\theta_v) = B_0 + \frac{B_1}{\omega\sqrt{\pi/2}} \exp\left[-2\left(\frac{\theta_v - \theta_c}{\omega}\right)^2\right] \tag{4.25}$$

where A_0, A_1, t_1, B_0, B_1, θ_c and ω are unknown parameters.

Table 4.4 Fitting parameters of Equations (4.24) and (4.25)

Function	A_0 (B_0)	A_1 (B_1)	t_1 (ω) (degree)	θ_c (degree)
$If_{vol}(\theta_v)$	-0.02990	0.01278	21.43823	
$If_{geo}(\theta_v)$	-2.01124	-29.40855	68.81710	90.95449

The Levenberg-Marquardt minimization scheme was applied in the fitting procedure. The integrals and the fitting results are shown in Table 4.4 and Figure 4.2, and they are nearly indistinguishable. Therefore, two relatively simple mathematical expressions (4.24) and (4.25) will be used in the calculation of the directional emissivities in SEVIRI channel 4. Such representations are more convenient in land surface modeling than look-up tables of the kernel integrals.

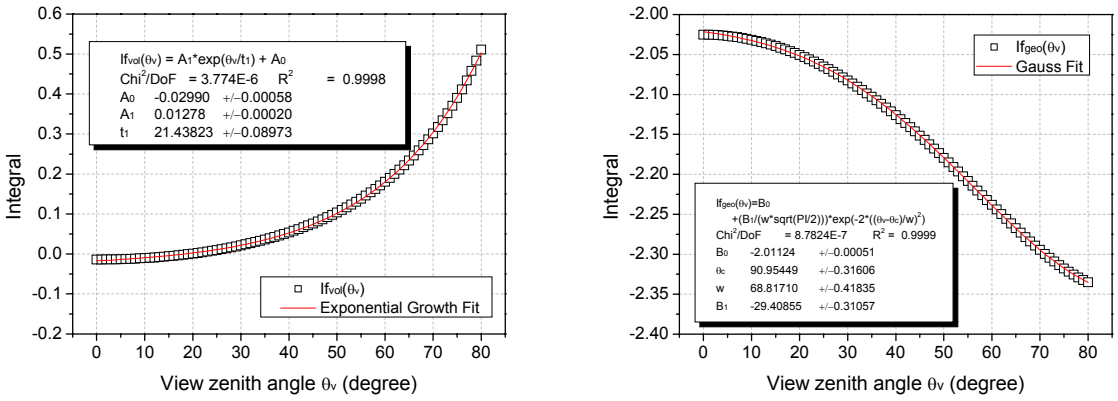

Figure 4.2. Integrals and the fitting results of the volumetric kernel and the geometric kernel in the RossThick-LiSparse-R model

4.2.3 Atmospheric correction and DTC model

The retrieval of land surface emissivity requires time series of radiances $L_{G,i}(\theta_v, T_g)$ at ground level, but satellites measure radiances $L_i(\theta_v, T_i)$ at TOA, therefore atmospheric correction has to be performed firstly. In this work, we used the ECMWF data with the radiative transfer code (MODTRAN 4.0) to correct for atmospheric perturbations. Although the ECMWF data have much

higher temporal and spatial resolutions than the traditional meteorological radiosondings, they are still very coarse when compared to the temporal and spatial resolutions of the MSG1-SEVIRI data. To tackle the problems of atmospheric corrections, a new atmospheric correction scheme is presented below.

For the images acquired at UTC times 0:00, 6:00, 12:00 and 18:00, when ECMWF data are available, the atmospheric correction is carried out in the following way: (1) Calculation of atmospheric parameters τ_i, $L_{atm\uparrow i,}$ $L_{atm\downarrow i}$ and $E_{sun,4}$ for each atmospheric profile; (2) Spatial interpolation of the atmospheric parameters into the image coordinates. In this work, a simple bi-linear interpolation method was applied; (3) Correction of atmospheric effects by use of Equation (2.5) or (2.7) to obtain the radiance L_G or brightness temperature $T_{g,i}$ at ground level.

However, as mentioned previously, SEVIRI channel 4 can not be regarded as a channel with narrow spectral range. The inversion of Equation (2.5) to obtain the radiance in SEVIRI channel 4 at ground level is very difficult. Here, we introduce the temperature-dependent and channel-averaged transmittance of SEVIRI channel 4 defined by

$$\tau_4(\theta_v, T_{g,4}) = \frac{\int_0^\infty f_4(\lambda) L_G(T_{g,4}, \theta_v, \lambda) \tau(\theta_v, \lambda) d\lambda}{\int_0^\infty f_4(\lambda) L_G(T_{g,4}, \theta_v, \lambda) d\lambda} \tag{4.26}$$

In this way, Equation (2.5) can be rewritten as

$$L_4(\theta_v, T_4) = \tau_4(T_{g,4}, \theta_v) L_{G,4}(T_{g,4}, \theta_v) + L_{atm\uparrow 4}(\theta_v) \tag{4.27}$$

Under MLS conditions, when $T_{g,4}$ increases with amount of 10 K, the changes of channel 4 average transmittance are less than 0.6% as shown in Table 4.5. This means that, the quantity $\tau_4(T_{g,4}, \theta_v)$ can be obtained accurately enough with an approximate temperature. Thus the radiance at ground level in SEVIRI channel 4 can be obtained in this way: (1) Computation of the approximate brightness temperature $T_{g,4a}$ at ground level in SEVIRI channel 4 by Equation (2.7). (2) Calculation of SEVIRI channel 4 average transmittance $\tau_4(T_{g,4a}, \theta_v)$ by Equation (4.26). (3) Inversion of Equation (4.27) to obtain SEVIRI channel 4 radiance at ground level using $\tau_4(T_{g,4a}, \theta_v)$ instead of $\tau_4(\theta_v)$ in Equation (4.11). Comparing Equation (4.27) with Equation (2.7), we notice that SEVIRI channel 4 acts like a channel with narrow spectral range after the introducing of the temperature-dependent and channel averaged transmittance.

Table 4.5. The relationship between the temperature-dependent and channel averaged transmittance and the brightness temperature at ground level in SEVIRI channel 4

$T_{g,4}$ (K)	280	290	300	310	320
$\tau_4(T_{g,4}, \theta_v)$	0.6284	0.6320	0.6353	0.6384	0.6412

Model atmosphere: MLS; θ_v=45 ^{o}; Transmittance in SEVIRI channel 4 in Equation (2.7): $\tau_4(\theta_v)$=0.6993

Another problem connected to atmospheric correction is that, for the images acquired NOT at the UTC times 0:00, 6:00, 12:00 and 18:00, there are no corresponding atmospheric data available. In the former research, time-nearest atmospheric data were used to correct the atmospheric effects in both

MIR and TIR images (Nerry et al., 1998). This method may lead to large errors for the TIR channels because they are very sensitive to the change of water vapor content in the atmosphere.

Figure 4.3 shows that, under MLS conditions, when water vapor content changes from 0.29 to 4.5 g/cm^2 and view zenith angle varies from 0° to 50°, the total transmittances and the atmospheric upwelling radiances in SEVIRI channel 4 have small changes, while the total transmittances and the atmospheric upwelling radiances in SEVIRI channels 9 and 10 change dramatically with the variation of the water vapor content. This means that, for the data not acquired at the UTC times 0:00, 6:00, 12:00 and 18:00, the spatially interpolated and time-nearest atmospheric parameters can be used to correct the atmospheric attenuation in SEVIRI channel 4 without introducing significant errors, but can not be applied to the data in SEVIRI channels 9 and 10. Figure 4.3 also reveals that SEVIRI channel 10 is more sensitive to the water vapor content in the atmosphere than SEVIRI channel 9.

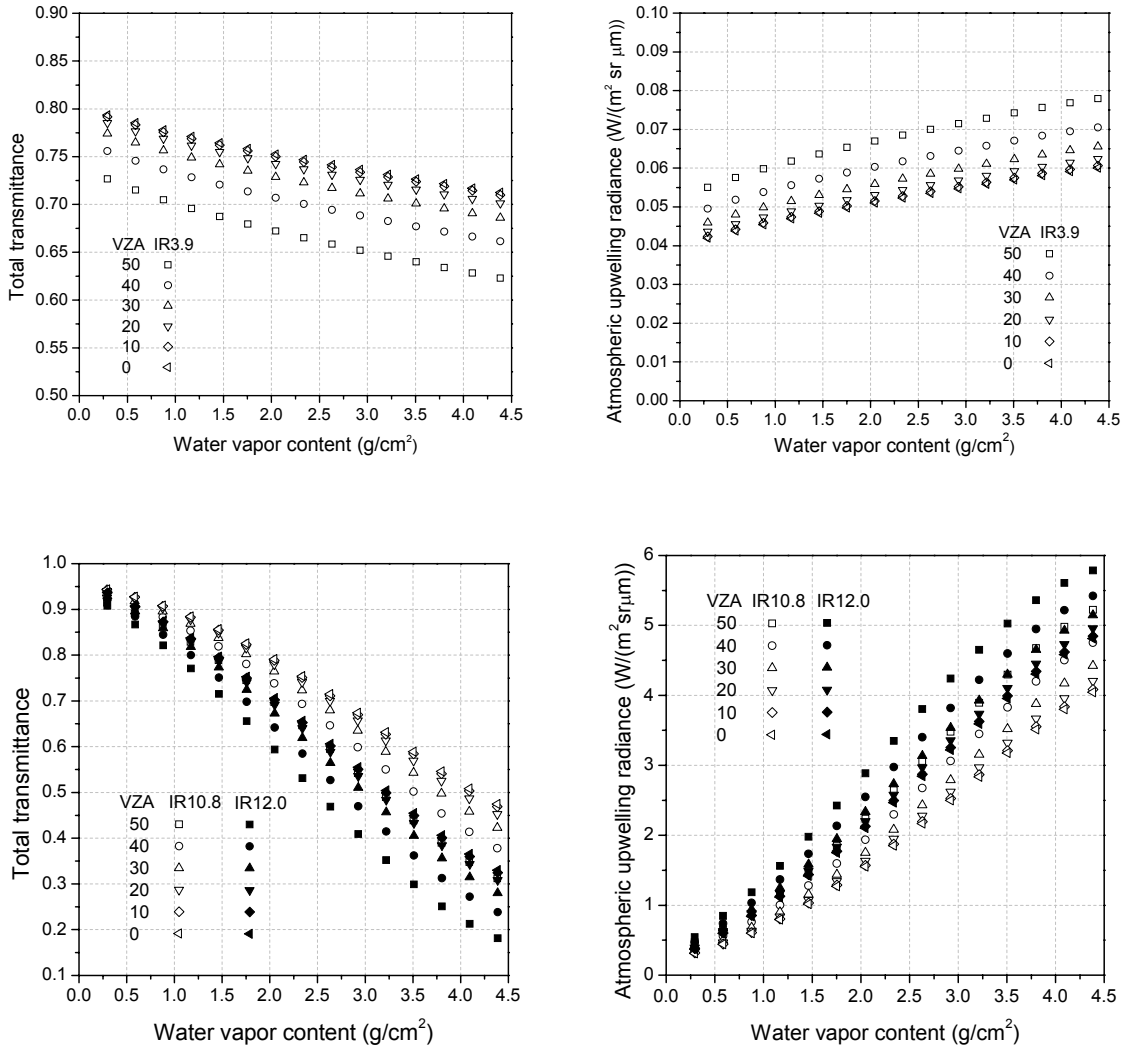

Figure 4.3. Total transmittance and atmospheric upwelling radiance versus atmospheric water vapor content at six view zenith angles: 0°, 10°, 20°, 30°, 40° and 50° in SEVIRI channels 4 (IR3.9), 9 (IR10.8) and 10 (IR12.0)
(Model atmosphere: MLS; VZA is the acronym of the View Zenith Angle)

For the images in SEVIRI channels 9 and 10 acquired NOT at UTC times 0:00, 6:00, 12:00 and 18:00, the two-part semi-empirical DTC model used by Göttsche and Olesen (2001) and Schädlich et al. (2001) was modified and applied to the temporal interpolation. Here, the development of the DTC model is recalled.

Assuming the one dimension periodic heating of a uniform half-space of constant thermal properties, the temperature obeys the diffusion equation

$$\kappa \frac{\partial^2 T}{\partial z^2} = \frac{\partial T}{\partial t} \tag{4.28}$$

where T=T(z, t) is the temperature at distance z below the surface and local solar time *t*, and *k* is the thermal diffusivity of the half-space.

$$\kappa = \frac{K}{\rho c} \tag{4.29}$$

where ρ is the density of soil and *c* is the thermal capacity, *K* is the thermal conductivity.

A solution of cosine function to Equation (4.28) is:

$$T(z,t) = a + b\cos\left(\beta(t - td) - z/\delta\right)\exp(-z/\delta) \tag{4.30}$$

with $\delta = \sqrt{\frac{2\kappa}{\beta}}$, the damping depth of the temperature diurnal cycle, or $\delta = \sqrt{\frac{2}{\beta}}\frac{P}{\rho c}$, P is the thermal inertial, β is the angular frequency, td is the time at which the temperature reaches its maximum, and a and b are unknown coefficients.

A solution of exponential function to Equation (4.28) is:

$$T(z,t) = b_1 + b_2 \exp(\alpha(t - t_c) - z/\delta) \tag{4.31}$$

with $\delta = \sqrt{\frac{\kappa}{\alpha}}$ or $\delta = \frac{P}{\rho c\sqrt{\alpha}}$.

Where b_1 and b_2 are unknown coefficients, α is the decay coefficient, and t_c is the sunset time.

Correspondingly temperature at land surface (z=0), Equations (4.30) and (4.31) can be rewritten as the following Equations (4.32a) and (4.32b), respectively.

$$T(t) = a + b\cos(\beta(t - td)) \tag{4.32a}$$

$$T(t) = a + b\exp(\alpha(t - tc)) \tag{4.32b}$$

During the daytime without cloud contamination, the land surface temperature changes with the variation of the local solar irradiation. After sunset, the land surface temperature decreases naturally and, as described by Newton's law of cooling, exponential decrease function is a typical function for natural decay processes (Schädlich et al., 2001; Göttsche and Olesen, 2001). Equations (4.32a) and (4.32b) can therefore be used to describe the DTC during the daytime and night-time, respectively.

Moreover, because land surface is not generally flat for most cases, the sunset time may be not the start time of attenuation. Here, a parameter t_s is substituted for t_c to represent the start time of attenuation. Therefore, the final two-part DTC model is rewritten as following.

$$T_s(t) = a + b\cos(\beta(t - td)) \qquad t \le t_s \tag{4.33a}$$

$$T_s(t) = b_1 + b_2 \exp(\alpha(t - t_s)) \qquad t > t_s \tag{4.33b}$$

The DTC is continuous at the time t_s and we assume that the first derivatives of the two parts at the time t_s are also equal. This leads to Equations (4.34a) and (4.34b).

$$a + b\cos(\beta(ts - td)) = b_1 + b_2 \tag{4.34a}$$

$$-b\beta\sin(\beta(ts - td)) = \alpha b_2 \tag{4.34b}$$

Combining Equations (4.34a) and (4.34b), one can obtain:

$$b_2 = -\frac{b\beta\sin(\beta(ts - td))}{\alpha} \tag{4.35a}$$

$$b_1 = a + b\cos(\beta(ts - td)) - b_2 \tag{4.35b}$$

Finally, there are totally six parameters in the two-part DTC model defined by Equations (4.33a) and (4.33b): the unknown coefficients a and b, the angular frequency β, the time td at which temperature reaches its maximum, the decaying coefficient α and the starting time of attenuation t_s. In contrast to the models used by Schädlich et al. (2001) and Göttsche and Olesen (2001), the modified model needs less prior knowledge.

However, only four atmospheric parameters are available for each location every day after the spatial interpolation. To use the DTC model in the atmospheric correction for the TIR images, two assumptions were made: the DTCs at TOA and at ground level have the same angular frequency β and the same starting time of attenuation t_s. The parameters β and t_s are firstly determined in the fitting procedure to the brightness temperatures at TOA and are then used as known parameters in the fitting procedure at ground level. The thermal behavior of brightness temperatures at ground level can be represented by the determined model parameters and thus the radiance measured at ground level at any given time can be predicted.

Because of the effect of the reflected direct solar irradiance in SEVIRI channel 4, the DTC model may not work any more, and therefore it is not applied to the atmospheric correction for the images in SEVIRI channel 4. As mentioned previously, the spatially interpolated and time-nearest atmospheric parameters will be used to correct the atmospheric attenuation in SEVIRI channel 4.

It should be noted that, Equations (4.35a) and (4.35b) are non-linear model and the estimation of the non-linear model parameters requires the user to provide starting values for the unknown parameters. The starting values must be reasonably close to the "true" values. Bad starting values may cause the regression to converge to a local minimum rather than the global minimum that defines the least squares estimates.

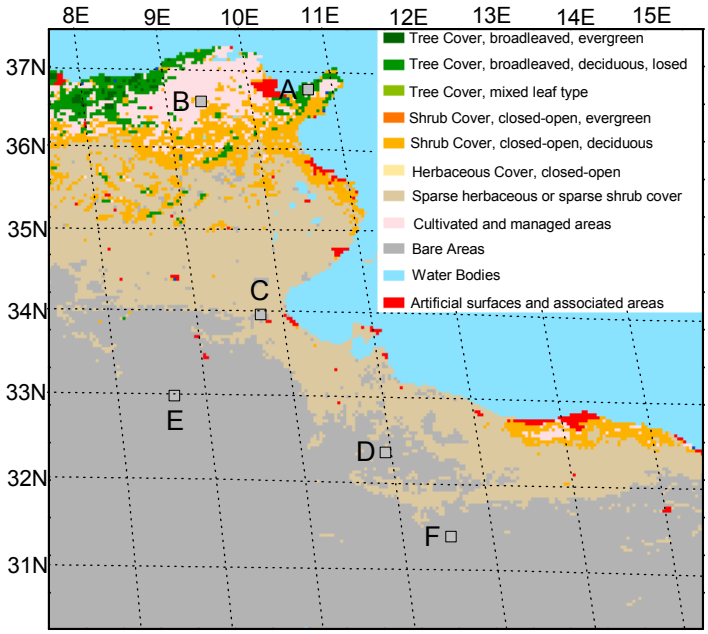

Figure 4.4. Map of the small study area
(Land cover types were generated from the Global Land Cover 2000 map produced by IES)

4.3 Study areas and data descriptions

Two study areas, a small area and a large area, were used in the LSE retrievals.

The small study area goes from latitude 30.2N to 37.7N and from longitude 7.0E to 15.7E (Figure 4.4). In this region, the main land cover types are bare areas, cultivated and managed areas, and sparse herbaceous or sparse shrub cover (Global Land Cover 2000). Six specific locations over the small study area (Table 4.6), including vegetated and bare areas, were selected as the examples to demonstrate the LSE retrievals. Note that, the locations D and E are, respectively, closest to the areas 1 and 2 in the work of Nerry et al. (1998) and the areas T_1 and T_2 in the work of Petiticolin et al. (2002a & 2002b). The distance between location D and the area 1 (T_1) is about 2 km, and the distance between E and 2 (T_2) is about 1.7 km. The time span of the SEVIRI data over the small area is from 4:00am July 15, 2004 to 7:00am July 17, 2004.

Table 4.6. Description of the six specific locations over the small study area

No.	Longitude	Latitude	Land cover type*
A	10.667E	36.779N	Tree Cover, broadleaved, deciduous, closed
B	9.361E	36.597N	Cultivated and managed areas
C	9.700E	33.964N	Bare area
D	10.904E	32.343N	Bare area
E	8.598E	32.973N	Bare area
F	11.504E	31.376N	Bare area

*According to the Global Land Cover 2000 map produced by IES

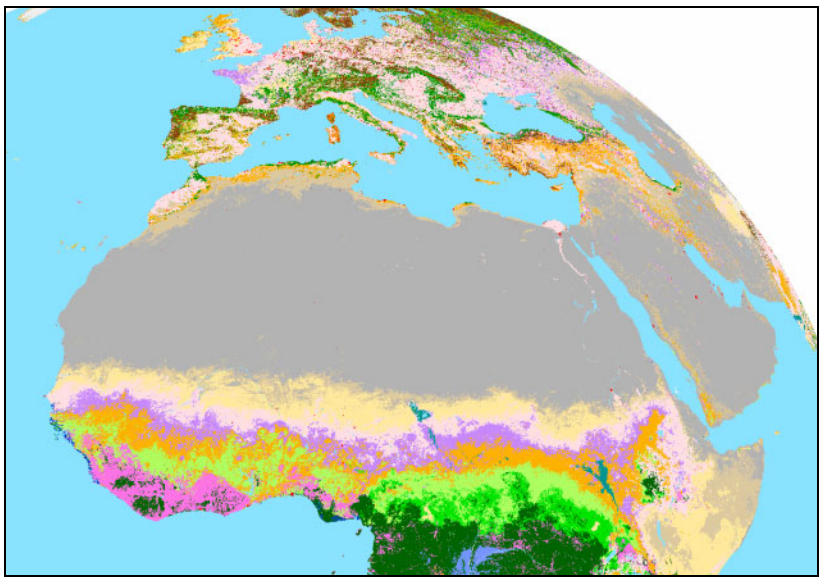

Figure 4.5. Map of the large study area
(Legends are the same as the ones in Figure 4.4)

The large study area covers the land surfaces with the latitude going from 0 to 60N and the longitude varying from 20W to 60E (Figure 4.5). In contrast to the small study area, the large study area has more complicated terrain, land cover types and climate conditions. Tow continuous time spans were used for the large study area. One goes from July 14, 2004 to July 20, 2004, and the other varies from July 10, 2005 to July 15, 2005. Besides the two continuous time spans, the LSEs in SEVIRI channels 4, 7, 9 and 10 on the dates listed in Table 4.7 were also estimated over the large study area.

In order to demonstrate the variations of the emissivities in SEVIRI channels 4, 7, 9 and 10 in the two continuous time spans, another four locations over the large study area were selected (Table 4.8). The location H is the same area as the location C in Table 4.6.

Table 4.7. Other dates in 2004, 2005 and 2006 for the LSE retrievals over the large study area

	Jan.	Feb.	March	April	May	June	July	Aug.	Sept.	Oct.	Nov.	Dec.
2004		10	11	13	16	3	1	13	17	13	15	
2005	4	10	17	12	6	1	2	4	2	5	8	
2006		20-22 25-26	5-7 12-13									

Table 4.8. Descriptions of the four selected locations over the large study area

No.	Longitude	Latitude	Land cover type	Comment
G	2.07W	39.03N	Cultivated and managed area	Barrax site, Spain
H	9.70E	33.96N	Bare area	Location C in Table 4.6
I	30.96E	30.90N	Cultivated and managed area	Nile River Delta, Egypt
J	28.29E	27.98N	Bare area	Desert in Egypt

The primary data used in this work include the MSG Level 1.5 product, MSG cloud mask product and ECMWF data, which have been detailed in Chapter 2. Other ancillary data include the daily averaged horizontal visibility data, the global GTOPO30 DEM (Digital Elevation Model) data, and the SEVIRI view geometry data etc.

The daily averaged horizontal visibility data observed at ground meteorological stations (ftp://ftp.ncdc.noaa.gov/pub/data/globalsod/) were used in this work to indicate the amount of aerosols.

The global GTOPO30 DEM data downloaded from USGS website were utilized to determine the length of the atmospheric path between surface and satellite in the calculation of the atmospheric parameters. The horizontal resolution of the GTOPO30 DEM data is 30 arc seconds (approximately 1 kilometer).

By the way, in order to evaluate the performance of the DTC model, the in situ LSTs measured directly by a radiometer on a cement driveway (119.83W, 34.45N) every five minutes on two sunny days, February 21 and 22 of 2003, and the data measured in the Hapex-Mobilhy field campaign in 1986 were also used. The day, June 16, 1986, was a golden day, and the measurements on that day at the stations Castel Jaloux, Castelnau and Tieste (Table 4.9) were selected to evaluate the performance of the DTC model.

Table 4.9. Description of the four selected locations in field measurements

Station/Location	Longitude	Latitude	Land cover type*
Cement	-119.830	34.450	Cement
Castelnau	0.045	43.585	Indian corn
Castel Jaloux	0.125	44.323	Indian corn
Tieste	0.025	43.547	Indian corn

4.4 Application to the small study area

Over the small study area, only the emissivities in SEVIRI channels 4, 9 and 10 were derived, and the modified Minnaert's model was used to describe the non-Lambertian behavior of land surface.

4.4.1 Data processing

The cloud masks used in this work were extracted from the MSG cloud mask product. Although the central objective of MSG cloud mask product is to delineate all absolutely cloud-free pixels with high degree of confidence, there are still some surfaces indicated as clear-sky which are actually cloud-contaminated. For a pixel, if the measured brightness temperature is more than 1.0 K lower than the DTC model predicted, we labeled this measurement cloud-contaminated and eliminated it in the next fitting procedure. The fitting procedure was repeated until all the differences between the modeled brightness temperatures and the measured brightness temperatures were less than 1.0 K.

The images in SEVIRI channels 4, 9 and 10 were extracted from the MSG Level 1.5 product by the SEVIRI Pre-processing Toolbox (SPT) from July 15 to July 17, 2004 over the small study area.

The ECMWF data were detailed in the section 2.2. The ECMWF data within the small study areas from July 15, 2004 to July 17, 2004 were transformed into the spatial domain and the T, RH and GP profiles for 21 pressure levels were extracted.

The daily averaged horizontal visibility data observed at ground meteorological stations are the only possible rough indications on the amount of aerosols. They were used in association with standard aerosols types described in the MODTRAN 4.0. Because the ground meteorological stations are discretely distributed on land surfaces, a spatial interpolation was carried out to calculate the horizontal visibilities at the grids of the ECMWF profiles,

Schumaker (1976) gives an overview of two-dimensional interpolation methods. It turned out that weighted averages is the method that meets our demand. The so-called Shepard method (Shepard, 1968) provides an optimized weighting function ω_i for a number of M data points situated within a circle around the evaluated pixel.

$$\omega(r) = \begin{cases} \dfrac{1}{r} & 0 < r < R/3 \\ \dfrac{27}{4R}\left(\dfrac{r}{R} - 1\right)^2 & R/3 < r < R \\ 0 & r > R \end{cases} \tag{4.36}$$

where R is the circle radius and r is the actual distance between the evaluated pixel and the pixel within the circle.

In particular, the smooth transition of ω_i to zero avoids instabilities during a change in the composition of the data points used. During the processing of a whole image, the cycle radius changes dynamically in terms of actual data point distribution. The visibility V is calculated by

$$V = \frac{\sum_{i=1}^{M} \omega_i^n(r) V_i}{\sum_{i=1}^{M} \omega_i^n(r)} \tag{4.37}$$

where V_i is the visibility at station i, and n is the exponent of ω_i.

The Shepard method uses an exponent n and a radius R as parameters. An empirically determined constant exponent n=2.0 and a dynamic radius produce good results. The radius R is the distance between the evaluated point and the sixth nearest neighbor of the evaluated point with respect to all data points. The use of six points (M=6) is based on the consideration of computational time (Schroedter et al., 2003).

In addition, the SEVIRI's view angles (Figure 2.5) were also interpolated into the grids of the ECMWF data by the nearest neighboring method. As already mentioned previously, the SEVIRI's view zenith angles refer to the angles at ground level, but MODTRAN input requires view zenith angles at observation level. We set the observation height to 100 km and converted the view zenith angles at ground level to the ones at observation level by the following equation

$$VZA_O = 180 - a\sin(R_E \sin(VZA_G)/(R_E + 100))) \tag{4.38}$$

where VZA_O is the view zenith angle at observation level of 100 km, and VZA_G is the view zenith angle at ground level.

The solar angles at each ECMWF grid in the daytime were calculated by a self-developed program.

MODTRAN is controlled by a single input file, which consists of a sequence of six or more CARDS. Compared to the input file for the TIR channels, in addition to the difference of spectral range, the input file for the MIR channel contains solar illumination geometries and date information.

The processing of millions of the ECMWF profiles is a heavy task. We developed a simple program to automatically control the running of MODTRAN with input (tp5) and output (tp7) files. The program first puts a tp5 file into the input directory of MODTRAN, and then runs the MODTRAN, and finally picks out the tp7 file. This action repeated until all the ECMWF profiles were processed. The output tp7 files were filtered with the SEVIRI spectral responses to obtain the atmospheric parameters. We also developed a set of programs in the processing of the SEVIRI images, in addition to the use of SPT software.

Over the small study area, the atmospheric correction of the SEVIRI images in the channels 4, 9 and 10 at UTC times 5:57, 11:57, 17:57 and 23:57 were performed by the use of MODTRAN 4.0 fed with the ECMWF atmospheric profiles at UTC times 6:00, 12:00, 18:00 and 0:00 (Next day), respectively. For SEVIRI channel 4, the images acquired from time 6:57UTC to 8:57UTC were corrected with the atmospheric profiles at 6:00UTC, the images acquired from time 9:12UTC to 14:57UTC were corrected with the atmospheric profiles at 12:00UTC and the images acquired from time 15:12UTC to 16:57UTC with the atmospheric profiles at 18:00UTC. The direct solar irradiances at ground level were calculated by the use of MODTRAN 4.0 with the approximate atmospheric profiles. For the images in SEVIRI channels 9 and 10, the DTC model was used to correct the atmospheric effects as described above. The starting values of the unknown parameters in the DTC model were firstly set to the same values for all pixels, and then the fitting results were used as the starting values of the unknown model parameters in the next minimization. In the fitting procedure, the observation with relative error between the modeled and the measured brightness temperatures greater than 1.0 K and the pixels with the observation number less than 80 (total 96 observations per day) were discarded. The bi-directional reflectivities in SEVIRI channel 4 of the combinations 4-9 and 4-10 were calculated from time 6:57 to 16:57 for each clear-sky pixel with an interval of 15 min. Those observations with solar zenith angle greater than 60^o were discarded and the image acquired at UTC time 23:57 was used as the nighttime data to construct the TISIs. Here, the modified Minnaert's BRDF model was used to describe the bi-directional reflectivities over the small study area. A Levenberg-Marquardt minimization scheme was utilized to determine the parameters ρ_0, b and γ in Equation (4.11) of each pixel. If the absolute difference between the measured and modeled bi-directional reflectivities is greater than two times the RMSE, this measurement will be discarded. In order to invert the BRDF model correctly, the minimum number of measurements has been set to seven. Ultimately, the directional emissivities in SEVIRI channel 4 were modeled by Equation (4.12) and the directional emissivities in SEVIRI channels 9 and 10 were calculated by Equation (4.8) or (4.9).

Figure 4.6 demonstrates the data processing scheme. It is mainly composed of three parts: (1) Correction of the atmospheric effects for the images acquired at the UTC times 5:57, 11:57, 17:57 and

23:57; (2) Correction of the atmospheric effects for the images acquired at other UTC times by the new atmospheric correction scheme. For the images in SEVIRI channel 4, the time-nearest and spatially interpolated atmospheric profiles are used, while for the images in SEVIRI TIR channels, the DTC model will be applied; (3) Retrievals of the emissivities in SEVIRI channels 4, 7, 9 and 10 by the TISI concept and the BRDF models (the modified Minnaert's model or the RossThick-LiSparse-R model).

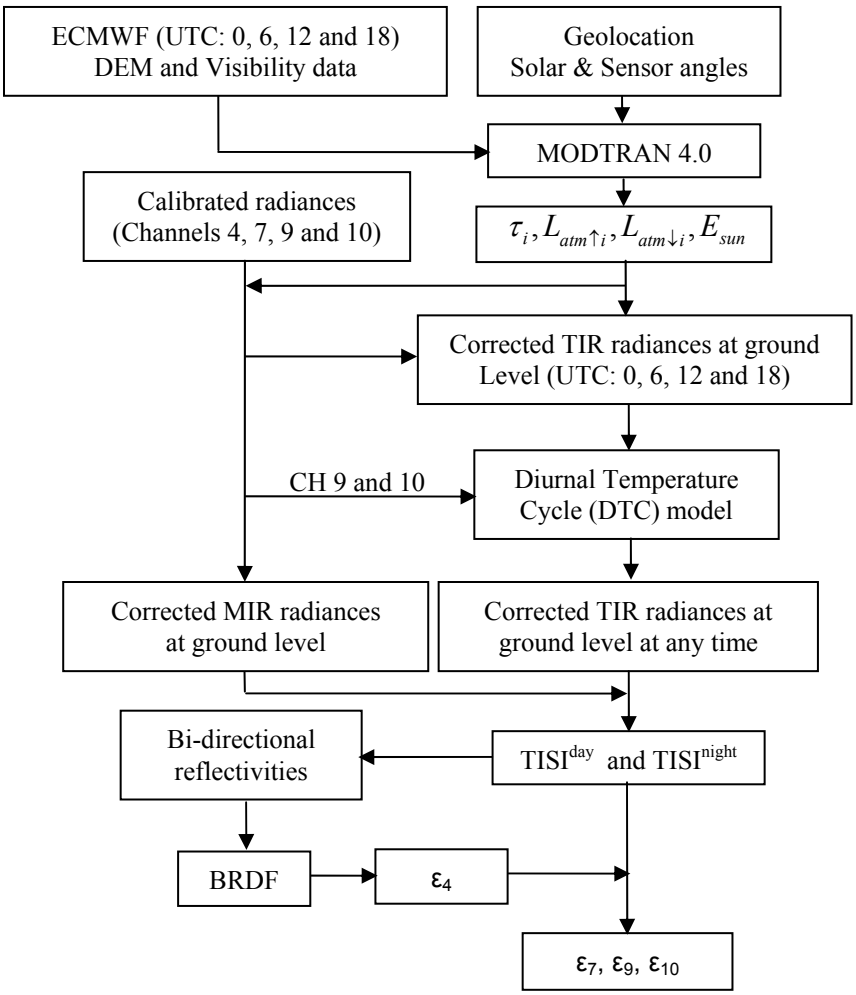

Figure 4.6. Data processing scheme

4.4.2 Results and analysis

4.4.2.1 Performance of the DTC model with in situ data

Figure 4.7 shows the DTCs measured on the cement, at the three stations in the Hapex-Mobilhy campaign (rectangle symbol) and the modeled results by the DTC model (solid curves). Table 4.10 gives the fitted value of the six parameters in the DTC model and the RMSEs. According to the results shown in Figure 4.7 and Table 4.10, almost all the fitting errors are less than 1 ^{o}C and all the RMSEs are less than 0.5 ^{o}C, which demonstrates that the DTC model works well with the in situ LSTs.

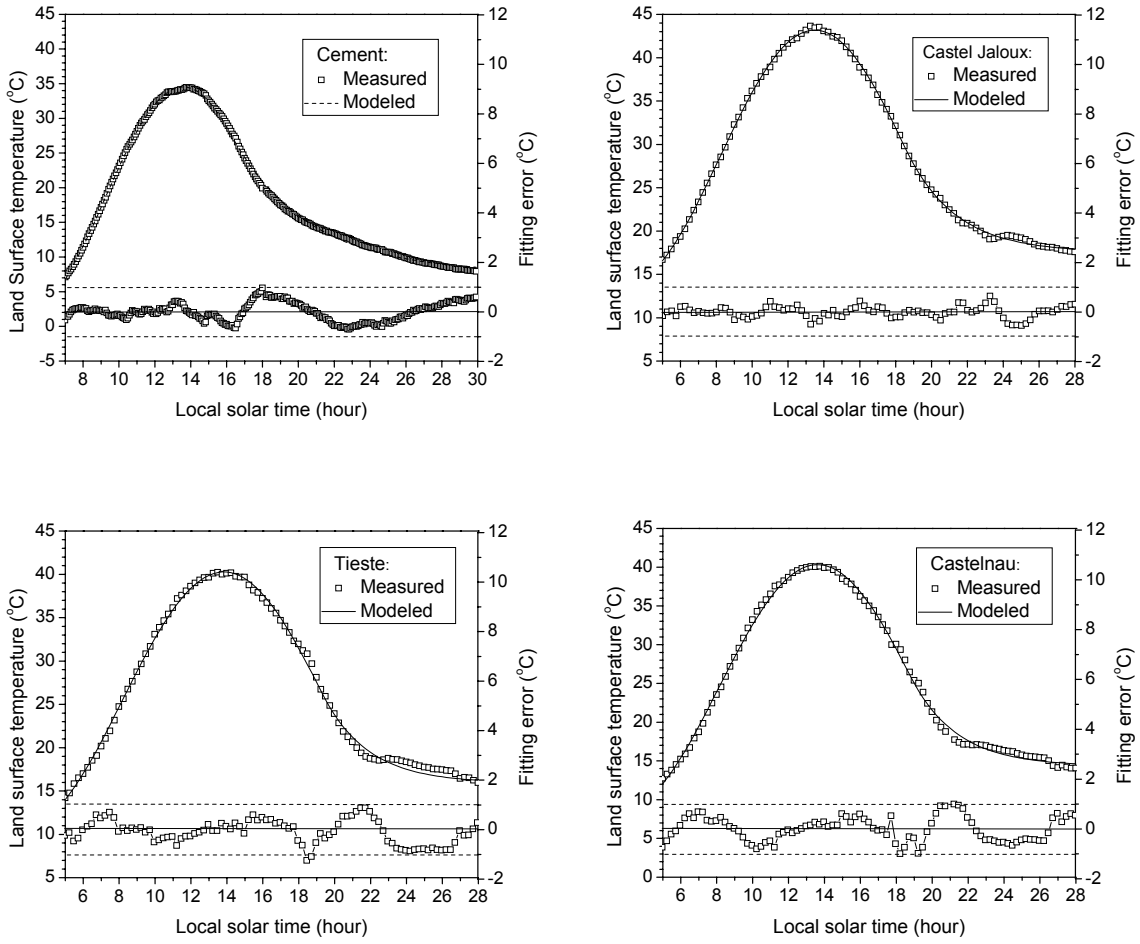

Figure 4.7. Measured DTCs and the modeled results by the DTC model

Table 4.10. Parameters of the DTC model and the fitting RMSEs for the in-situ measurements

Station / Location	a	b	β	td (hour)	α	t_s (hour)	RMSE (°C)
Cement	18.24	16.28	0.36	13.57	-0.24	16.20	0.37
Castel Jaloux	28.49	14.70	0.30	13.49	-0.36	18.56	0.23
Courrensan	24.45	12.91	0.27	13.82	-0.30	18.80	0.40
Castelnau	24.40	15.93	0.28	13.61	-0.39	18.81	0.49
Tieste	25.45	14.83	0.28	13.84	-0.40	19.31	0.49

4.4.2.2 Results at the six specific locations

Figure 4.8 illustrates the atmospheric corrections by the DTC model for the images in SEVIRI channels 9 and 10 at the six selected locations. As shown by the results, the DTC model also works well with the brightness temperatures at TOA on both vegetated and bare areas. The results also show that, without the priori knowledge about angular frequency β, the modified DTC model can describe the DTCs very well. The brightness temperature at TOA in SEVIRI channel 9 is a little bit higher than the brightness temperature at TOA in SEVIRI channel 10, but the corrected brightness temperatures at ground level are very close.

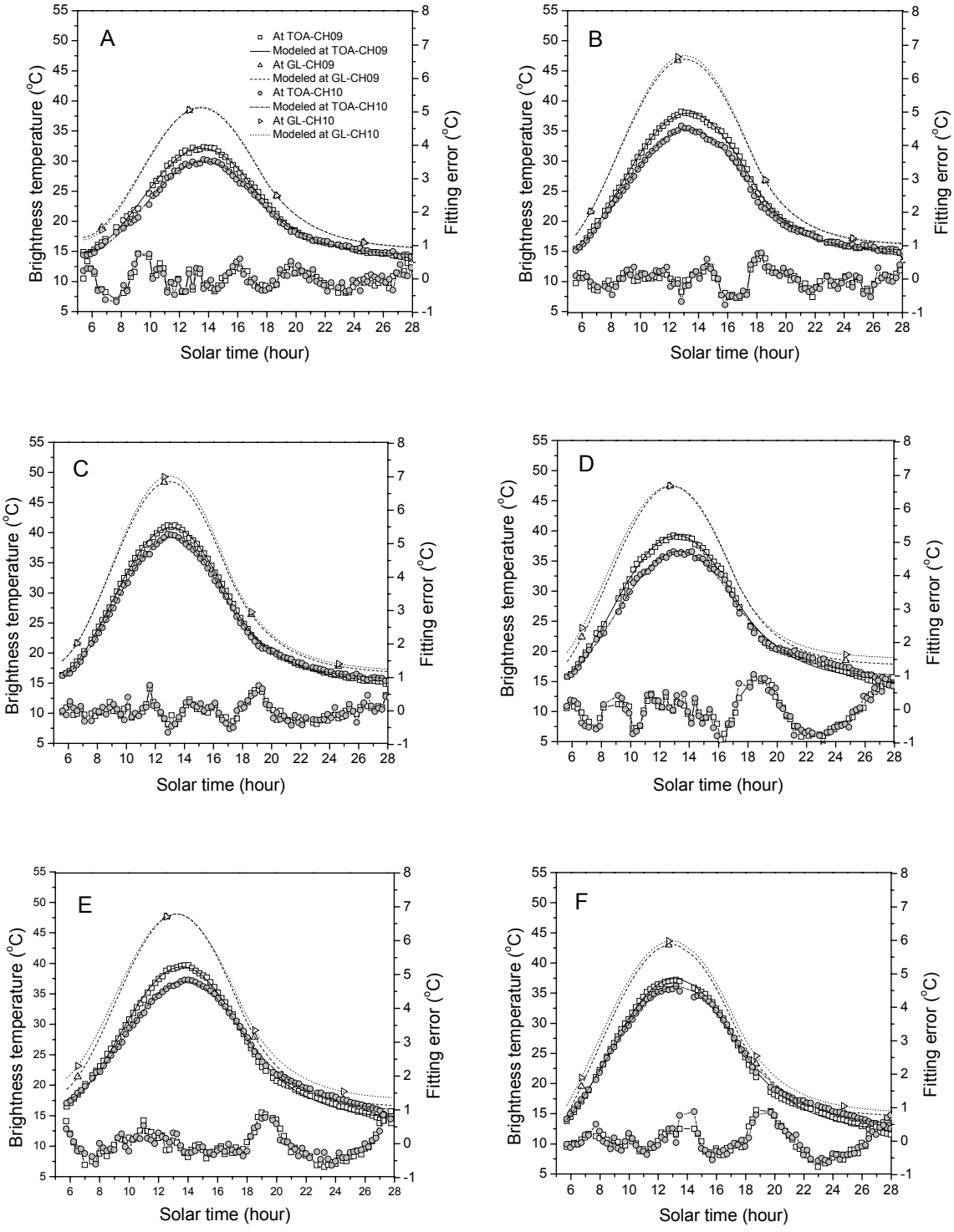

Figure 4.8. Atmospheric corrections for the data in SEVIRI channels 9 and 10 by the DTC model and the fitting errors at the six specific locations on July 15, 2004
(DTC stand for Diurnal Temperature Cycle; GL is the abbreviation of Ground Level; solar time>24: time of the next day)

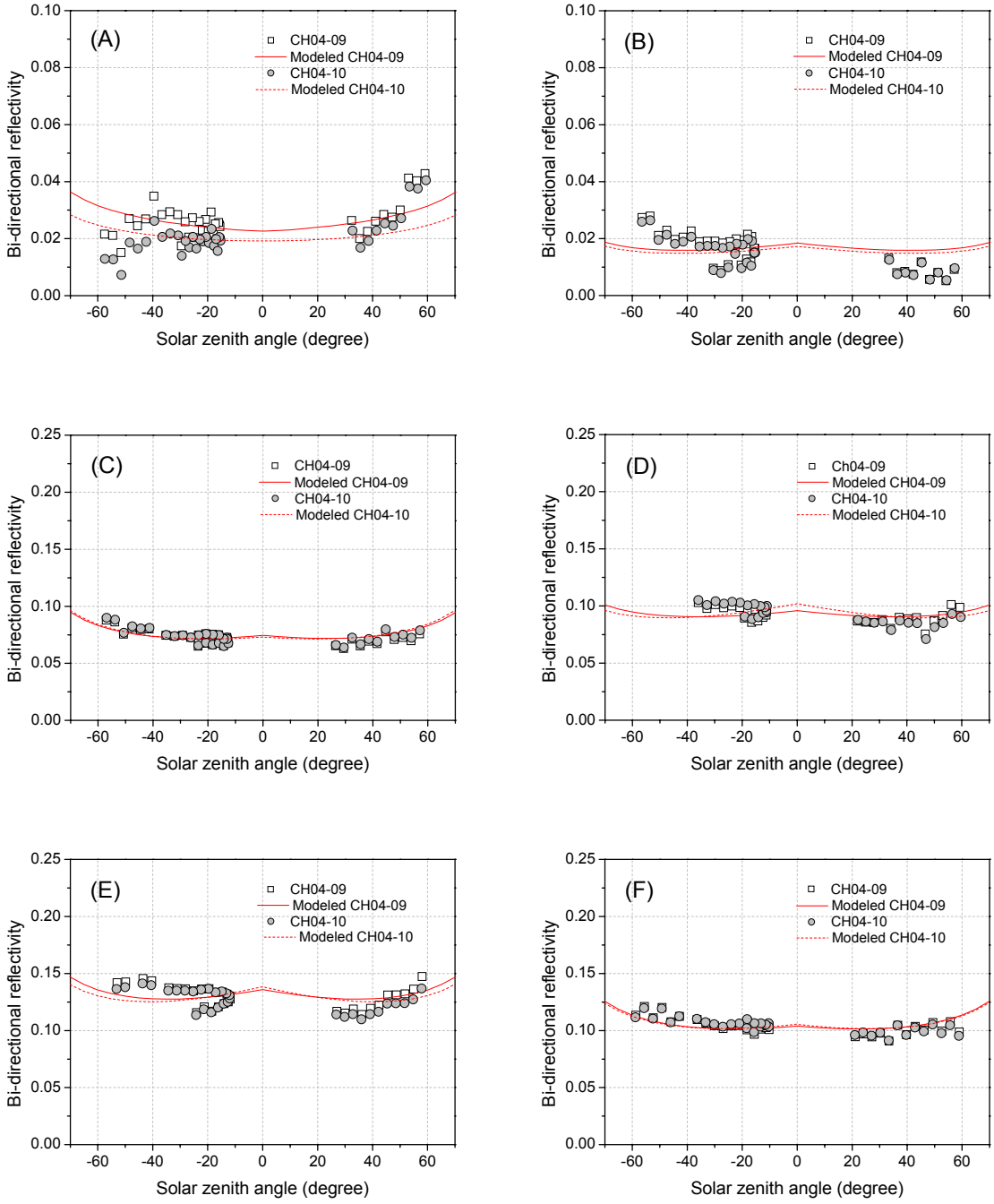

Figure 4.9. Normalized bi-directional reflectivities in SEVIRI channel 4 at the MSG1-SEVIRI's view angles versus the solar zenith angle θ_s by Equation (4.39) at the six specific locations on July 15, 2004
(θ_s<0 for the $|\varphi_s-\varphi_v|=0^o$ half plane and θ_s>0 for the $|\varphi_s-\varphi_v|=180^o$ half plane; CH04-09 stands for the combination of SEVIRI channels 4 and 9; CH04-10 stands for the combination of SEVIRI channels 4 and 10)

The bi-directional reflectivity is a function of view zenith angle (θ_v), solar zenith angle (θ_s) and the relative azimuth angle (φ). In order to draw the bi-directional reflectivities in two-dimension figures, the bi-directional reflectivities were normalized to a common relative azimuth angle $\varphi_0=0^o$ for the

backscattering and φ_0=180° for the forward scattering by the following equation, if the modified Minnaert's BRDF modeled was used:

$$\rho_{b,4}(\theta_v,\theta_s,\varphi_0)=\frac{\rho_{b,4}(\theta_v,\theta_s,\varphi)\left[1+\gamma\sin(\theta_v)\sin(\theta_s)\cos(\varphi_0)\right]}{1+\gamma\sin(\theta_v)\sin(\theta_s)\cos(\varphi)} \tag{4.39}$$

Figure 4.9 depicts the normalized bi-directional reflectivities at the six locations in SEVIRI channel 4 for the two combinations observed at different solar illuminating geometry (θ_s<0 for backscattering and θ_s>0 for forward-scattering). The bi-directional reflectivity changes with the solar zenith angles, which confirms that the land surface does not behave as a Lambertian reflector. From the angle-dependent reflectivities, we can infer without doubt that the estimated emissivities are also angle-dependent according to the modified Minnaert's model and the Kirchhoff's law. The bi-directional reflectivities at the bare area locations are usually higher than the ones at the vegetated locations, and also possess much stronger directional property. Figure 4.10 shows the relationship between the measured and the modeled bi-directional reflectivities in SEVIRI channel 4 at the six locations. For the bi-directional reflectivities lower than 0.05, which correspond to the vegetated locations A and B, the modeled results are not very good, and large divergences are found between the modeled reflectivities and the measured reflectivities, which may due to the non-linear property and the poor performance of the modified Minnaert's model at the vegetated locations. Anyway, most of the modeled errors are less than 0.01, and the mean and standard deviation of the reflectivity differences are equal to -0.0003 and 0.0075, respectively. Figure 4.10 demonstrates that the angular variations of the bi-directional reflectivity are well described by the modified Minnaert's model.

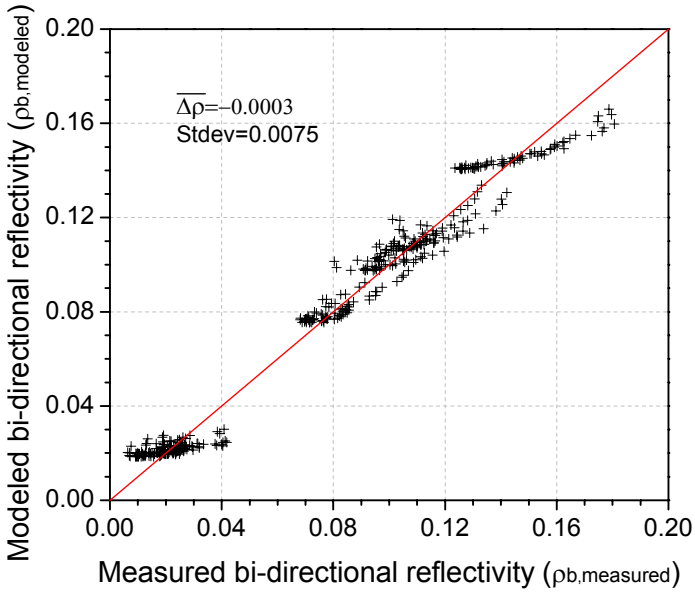

Figure 4.10. Modeled bi-directional reflectivities versus the measured bi-directional reflectivities by the modified Minnaert's model at the six specific locations on July 15, 2004
($\Delta\rho=\rho_{b,measured}-\rho_{b,modeled}$, and Stdev stands for the standard deviation of $\Delta\rho$. Same symbol for all locations and the two combinations CH04-09 and CH04-10)

Figure 4.11, Figure 4.12 and Table 4.11 present the parameters retrieved with the combination of SEVIRI channels 4 and 9 and the combination of SEVIRI channels 4 and 10 at the six locations and in the two consecutive days July 15 and July 16, 2004. From a theoretical point of view, the parameters retrieved with the two different combinations should be identical, if there is no error introduced in the measurements and data processing. The maximum absolute difference between the two combinations, at the six specific locations, is 0.0054 for ρ_0, 0.020 for ε_4, 0.008 for ε_7, and 0.010 for both ε_9 and ε_{10}, and the modeled RMSEs of the bi-directional reflectivities are less than 0.0110. In the two successive days, July 15 and July 16 of 2004, for each combination, the maximum absolute difference is 0.017 for ε_4, 0.006 for ε_7, and 0.008 for both ε_9 and ε_{10}. The consistent retrievals of the two different combinations and two successive days indicate that the method works well and the data were accurately processed. The emissivity differences between the two split-window channels 9 and 10 are also presented in the last graph in Figure 4.12, which reveal that the differences are slightly greater than zero at the densely vegetated location A and close to zero at the location B, while the emissivity differences between SEVIRI channels 9 and 10 are about -0.012 at the location C, about -0.023 at the location D, about -0.026 at the location E, and about -0.020 at the location F.

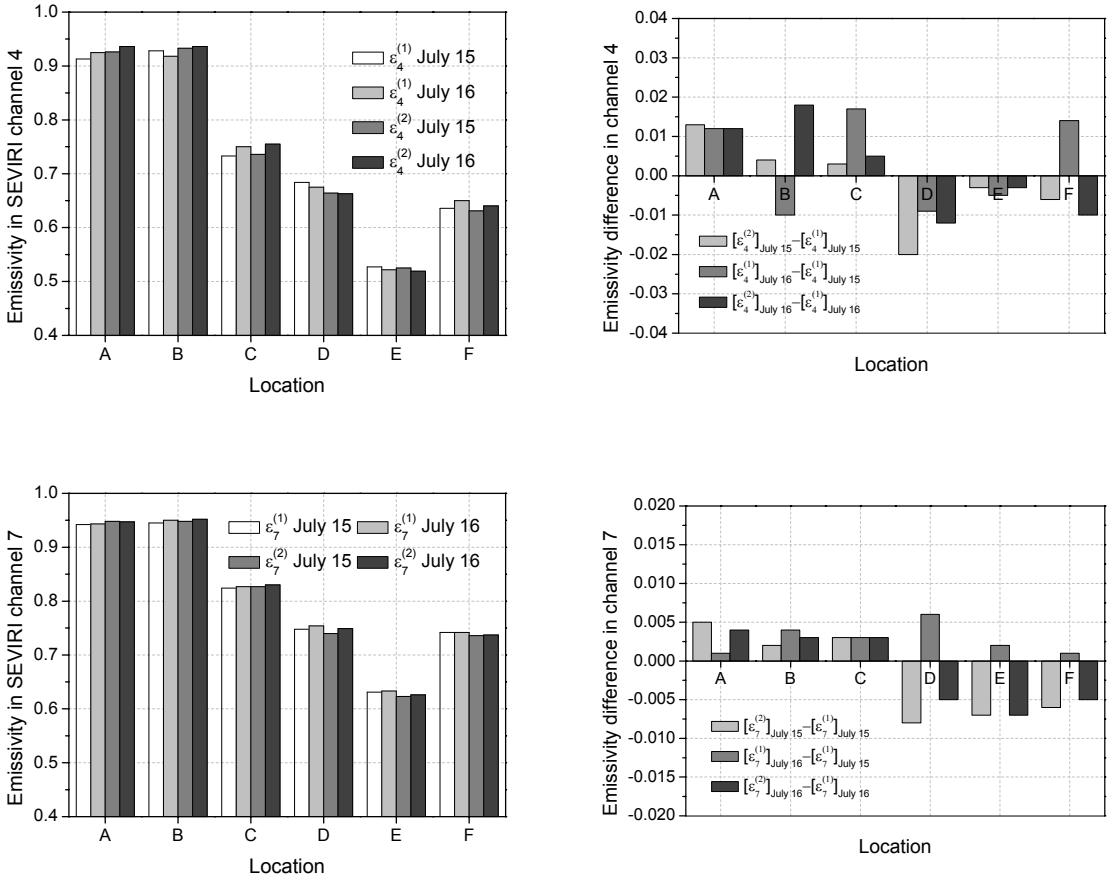

Figure 4.11. Retrieved directional emissivities modeled by the modified Minnaert's model in SEVIRI channels 4 and 7 (left) and the emissivity differences at the six specific locations (right) on July 15 and July 16 of 2004
($\varepsilon_4^{(1)}$ and $\varepsilon_7^{(1)}$ stand for, respectively, the derived emissivities in SEVIRI channels 4 and 7 using the combination of SEVIRI channels 4 and 9; $\varepsilon_4^{(2)}$ and $\varepsilon_7^{(2)}$ represent, respectively, the estimated emissivities in SEVIRI channels 4 and 7 using the combination of channels 4 and 10)

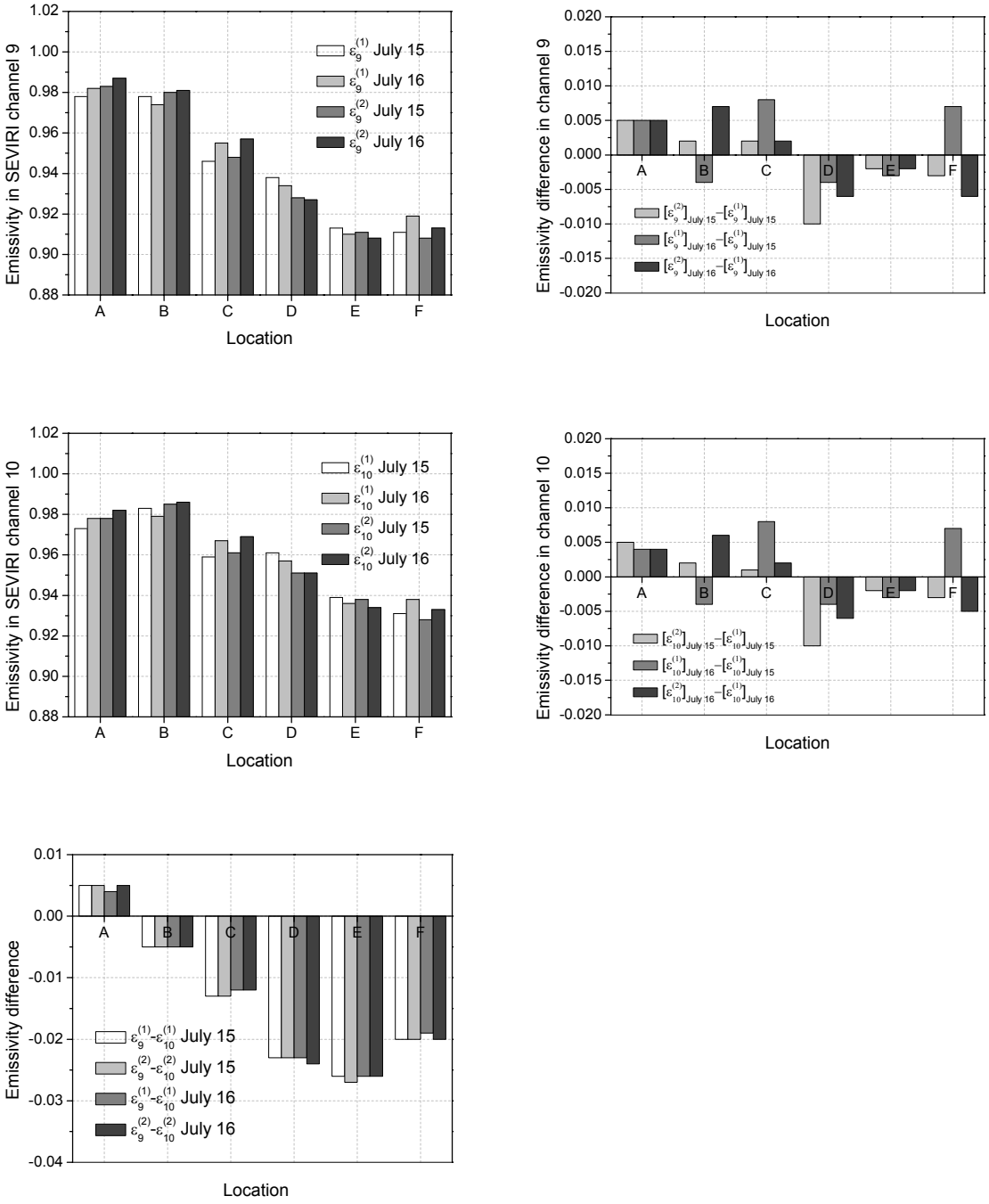

Figure 4.12. Same as the ones in Figure 4.11, but for the emissivities in SEVIRI channels 9 and 10 and the emissivity differences between them
($\varepsilon_9^{(1)}$ and $\varepsilon_{10}^{(1)}$ stand for, respectively, the derived emissivities in SEVIRI channels 9 and 10 using the combination of SEVIRI channels 4 and 9; $\varepsilon_9^{(2)}$ and $\varepsilon_{10}^{(2)}$ represent, respectively, the estimated emissivities in SEVIRI channels 9 and 10 using the combination of channels 4 and 10)

Table 4.11, Figure 4.11 and Figure 4.12 also reveal that the reflectivities at nadir for vegetated areas are low, and for bare areas are much higher. The directional emissivities in SEVIRI channels 4 and 7 are higher than 0.90 for vegetated areas, while for bare areas, the directional emissivities in SEVIRI channels 4 and 7 are usually less than 0.90. The directional emissivities in SEVIRI channels 9

and 10 are higher than 0.95 for the vegetated areas and less than 0.95 for the bare areas. Note that, according to the ASTER Spectral Library (http://speclib.jpl.nasa.gov/) and the MODIS UCSB Emissivity Library, the emissivities estimated with the current method at the four bare areas are too low, especially at the location E (ε_9 and ε_{10} are ~0.91 and ~0.94, respectively), and the emissivity differences among them are up to 0.3 in SEVIRI channels 4 and 7, 0.06 in SEVIRI channel 9 and 0.035 in SEVIRI channel 10. The lowest values occur in sandy regions where the emissivity may be as low as 0.92 at 11 μm (Sutherland, 1979). Over highly vegetated surface, the emissivity is known to be spectrally uniform and higher than 0.98 at 11 μm (Salisbury and D'Aria, 1992). Moreover, the results of Petitcolin and Vermote (2002) reveal that, the decrease amount of the emissivities in the two split-window channels over bare area is up to 0.02, when view zenith angles change from 0° to 60°. Therefore, the emissivities in SEVIRI channels 4, 7, 9 and 10 at the six specific locations are acceptable.

Table 4.11. Value of ρ_0, k and γ parameters of modified Minnaert's model, and the RMSEs between the measured and the modeled bi-directional reflectivities at the six locations

No.	Combination*	ρ_0		k		γ		$(\Delta\rho_{b4})_{rms}$	
		July 15	July 16	July 15	July 16	July 15	July 16	July 15	July 16
A	CH04-09	0.0202	0.0173	0.6518	0.6445	-0.1487	0.4457	0.0050	0.0087
	CH04-10	0.0172	0.0147			-0.0155	0.4824	0.0062	0.0087
	Δ	0.0030	0.0026			-0.1332	-0.0367		
B	CH04-09	0.0164	0.0185	0.6310	0.6158	0.4754	0.4589	0.0079	0.0093
	CH04-10	0.0154	0.0145			0.4903	0.4802	0.0074	0.0125
	Δ	0.001	0.004						
C	CH04-09	0.0611	0.0580	0.6145	0.6296	0.2521	0.2883	0.0055	0.0060
	CH04-10	0.0604	0.0568			0.2026	0.2735	0.0051	0.0060
	Δ	0.0007	0.0012			-0.0149	-0.0213		
D	CH04-09	0.0856	0.0803	0.8009	0.6937	0.2438	0.3200	0.0070	0.0074
	CH04-10	0.0910	0.0833			0.3872	0.3491	0.0090	0.0067
	Δ	-0.0054	-0.003			-0.1434	-0.0291		
E	CH04-09	0.1225	0.1133	0.7470	0.6452	0.2868	0.1471	0.0103	0.0067
	CH04-10	0.1230	0.1140			0.3696	0.1849	0.0110	0.0077
	Δ	-0.0005	-0.0007			-0.0828	-0.0378		
F	CH04-09	0.0913	0.0930	0.7069	0.7756	0.1935	0.1279	0.0063	0.0069
	CH04-10	0.0925	0.0957			0.2302	0.1432	0.0068	0.0073
	Δ	-0.0012	-0.0027			-0.0367	-0.0153		

*CH04-09 stands for the combination of SEVIRI channels 4 and 9; CH04-10 stands for the combination of SEVIRI channels 4 and 10

Table 4.12 shows the modeled directional emissivities at the locations D and E at view zenith angles 0° and 60° in our work (July 15, 2004) and in the work of Nerry et al. (1998) and Petitcolin et al. (2002a & 2002b). The modeled directional emissivities in the TIR channels were calculated from the corresponding emissivities in the MIR channel by Equation (4.8) in terms of the angle-independent property of TISI (Petitcolin et al., 2002b). At the location D, the maximum absolute emissivity difference in the MIR channel between our results and their results is 0.025 at the nadir view angle and is up to 0.054 at 60°, and the absolute differences in the TIR channels are less than 0.02. At the

location E, the maximum absolute emissivity difference in the MIR channel between our results and their results is 0.043 at the nadir view angle and is 0.042 at 60°, and the absolute differences in the TIR channels are less than 0.026. Comparing to the location E, the results at the location D are much closer to their results. In summary, the modeled directional emissivities at the locations D and E are basically consistent with the ones of Nerry et al. (1998) and Petitcolin et al. (2002a & 2002b). These differences may due to different spatial resolutions, different sensors and different observing times.

Table 4.12. Modeled directional emissivities at the locations D and E

	Location	ε_3^{AVHRR} or $\varepsilon_4^{(1)}$		ε_4^{AVHRR} or $\varepsilon_9^{(1)}$		ε_5^{AVHRR} or $\varepsilon_{10}^{(1)}$	
		0°	60°	0°	60°	0°	60°
Nerry et al. (1998)	1	0.687	0.603				
	2	0.550	0.461				
Petitcolin et al. (2002a & 2002b)	T_1	0.726	0.672	0.959	0.941	0.970	0.953
	T_2	0.602	0.517	0.941	0.906	0.958	0.926
In our work	D	0.701	0.657	0.947	0.924	0.969	0.948
	E	0.559	0.475	0.935	0.880	0.958	0.906

ε_3^{AVHRR}, ε_4^{AVHRR} and ε_5^{AVHRR} stand for the directional emissivities in AVHRR channels 3, 4 and 5, respectively; The locations 1, T_1 and D represent the same area, and do the locations 2, T_2 and E. $\varepsilon_4^{(1)}$, $\varepsilon_9^{(1)}$ and $\varepsilon_{10}^{(1)}$ were estimated on July 15 of 2004.

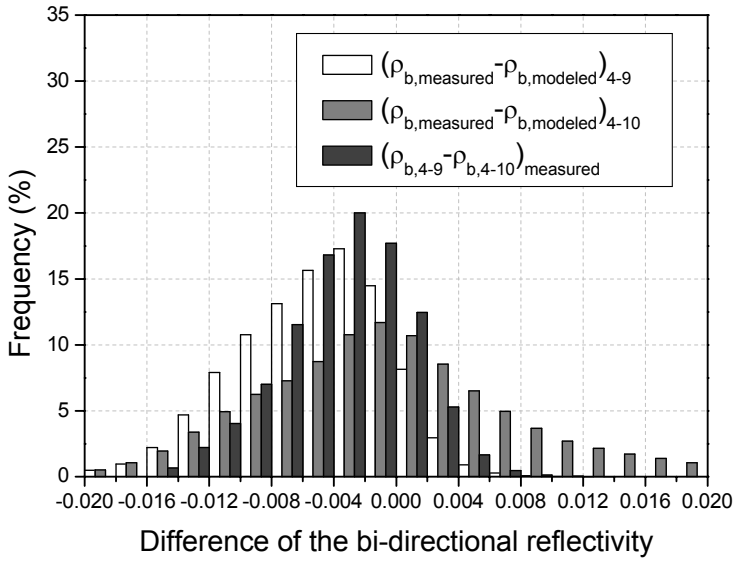

Figure 4.13. Histogram of the differences between the measured and the modeled bi-directional reflectivities by the modified Minnaert's model over the small study areas from time 6:57UTC to 16:57UTC on July 15, 2004
(The red and the green represent the differences between the measured reflectivities ($\rho_{b,measured}$) and the modeled reflectivities ($\rho_{b,measured}$) derived using the combination CH04-09 and the combination CH04-10, respectively. The blue stands for the differences of the measured bi-directional reflectivities estimated using the combination CH04-09 and the combination CH04-10)

4.4.2.3 Retrieved Parameters over the entire small study area

Figure 4.13 shows the histograms of the reflectivity differences using the modified Minnaert's model over the small study area. About 80% of the differences between the measured and the modeled bi-directional reflectivities of the two combinations are distributed within ±0.01, while about 93% of the differences between the measured reflectivity of the combination CH04-09 and the measured reflectivity of the combination CH04-10 are distributed within ±0.01.

In the retrievals of the emissivities in SEVIRI channels 4, 7, 9 and 10, it was assumed that the TISIs do not change between day and night. Figure 4.14 displays the TISIs at the six specific locations from the UTC time 19:12 to 23:57 on July 15 of 2004, and Table 4.13 gives the corresponding averages and standard deviations. The TISIs fluctuate with the time, and the standard deviations are not greater than 0.002, which means that the TISIs are quiet stable from the time shortly after sunset to midnight. The results are consistent with the ones of Petitcolin and Vermote. (2002), and the assumption will not introduce large errors. Figure 4.14 and Table 4.13 also reveal that the TISIs over vegetated areas are always larger than the ones over bare areas.

Note that, to construct the TISIs in Figure 4.14, the radiances in SEVIRI channel 4 at ground level were calculated using the spatially interpolated and time nearest ECMWF data and the radiance in SEVIRI channels 9 and 10 at ground level were predicted using the DTC model. Because of the TISIs' stablility and the ECMWF data, the TISIs at UTC time 23:57 were used to estimate the emissivities in SEVIRI channels 4, 7, 9 and 10.

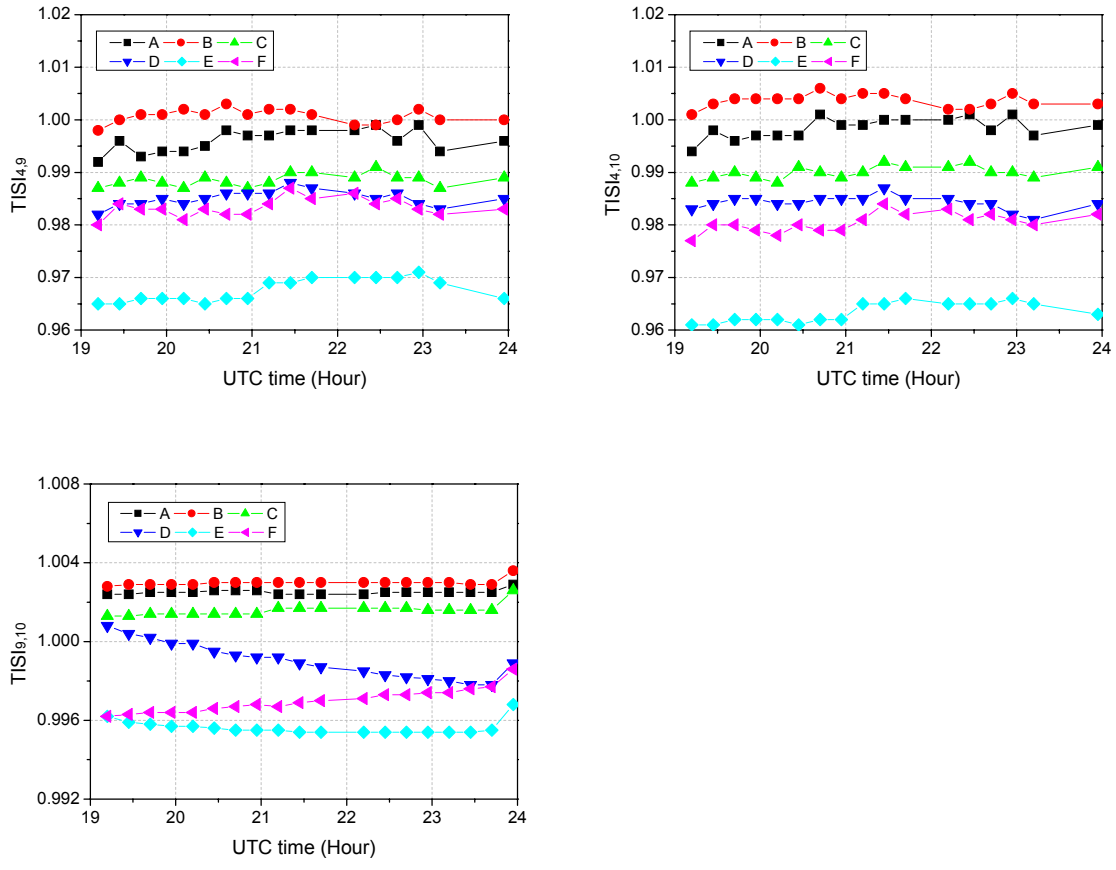

Figure 4.14. TISIs at the six specific locations from the UTC time 19:12 to 23:57 on July 15, 2004

Table 4.13. Mean and standard deviation of TISIs from the UTC 19:12 to 23:57 on July 15, 2004 at the six specific locations

	$TISI_{4,9}$		$TISI_{4,10}$		$TISI_{9,10}$	
	Mean	Stdev	Mean	Stdev	Mean	Stdev
A	0.996	0.002	0.998	0.002	1.0025	0.0001
B	1.001	0.001	1.004	0.001	1.0030	0.0002
C	0.989	0.001	0.99	0.001	1.0016	0.0003
D	0.985	0.001	0.984	0.001	0.9990	0.0009
E	0.968	0.002	0.963	0.002	0.9956	0.0004
F	0.983	0.002	0.980	0.002	0.9970	0.0006

Stdev is the abbreviation of the standard deviation.

Over the entire small study area, Figure 4.15 shows that $TISI_{4,9}$ and $TISI_{4,10}$ range from 0.96 (Bare areas) to 1.0 (Vegetated areas), while $TISI_{4,7}$ varies between 0.99 and 1.05, and $TISI_{9,10}$ ($TISI_{10,9}$=1/ $TISI_{9,10}$) ranges from 0.99 to 1.01. $TISI_{4,10}$ and $TISI_{9,10}$ are, respectively, slightly higher than $TISI_{4,9}$ and $TISI_{10,9}$ over the vegetated areas, and the opposite is observed over the bare areas.

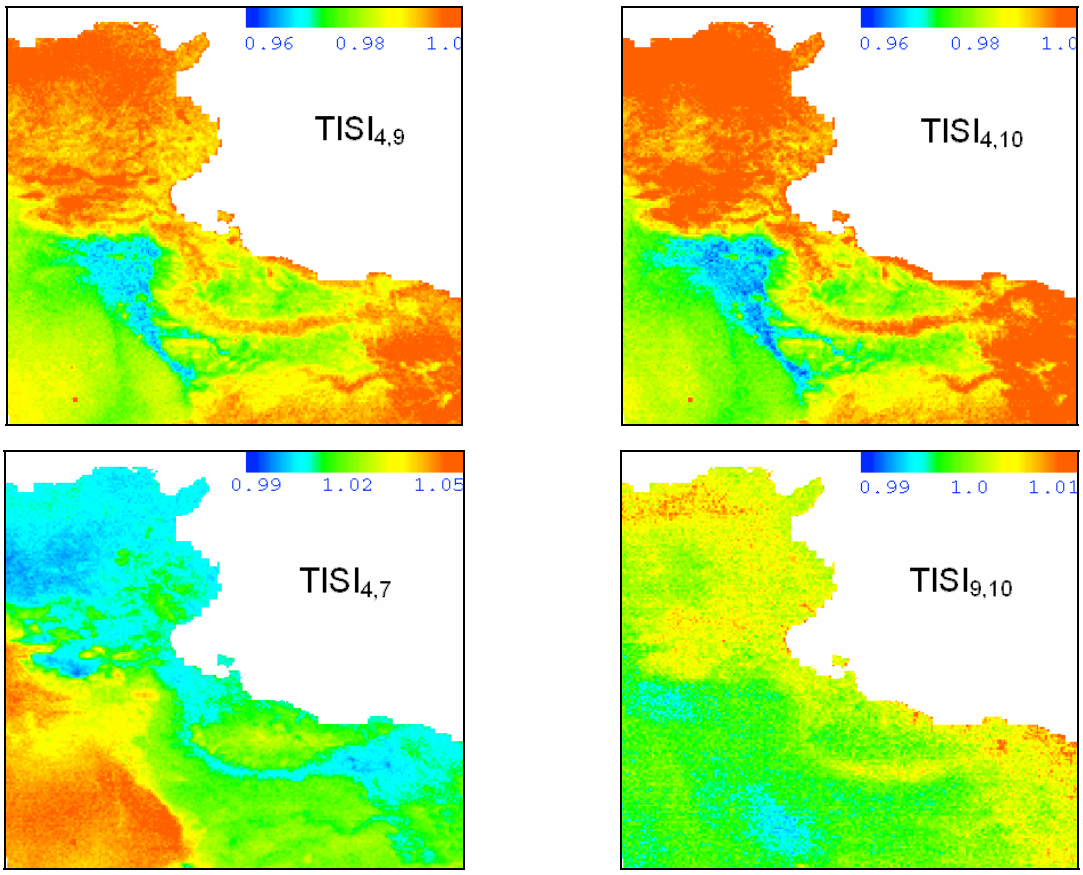

Figure 4.15. Maps of TISIs at UTC time 23:57 on July 15, 2004 ($TISI_{10,9}$=1/$TISI_{9,10}$)

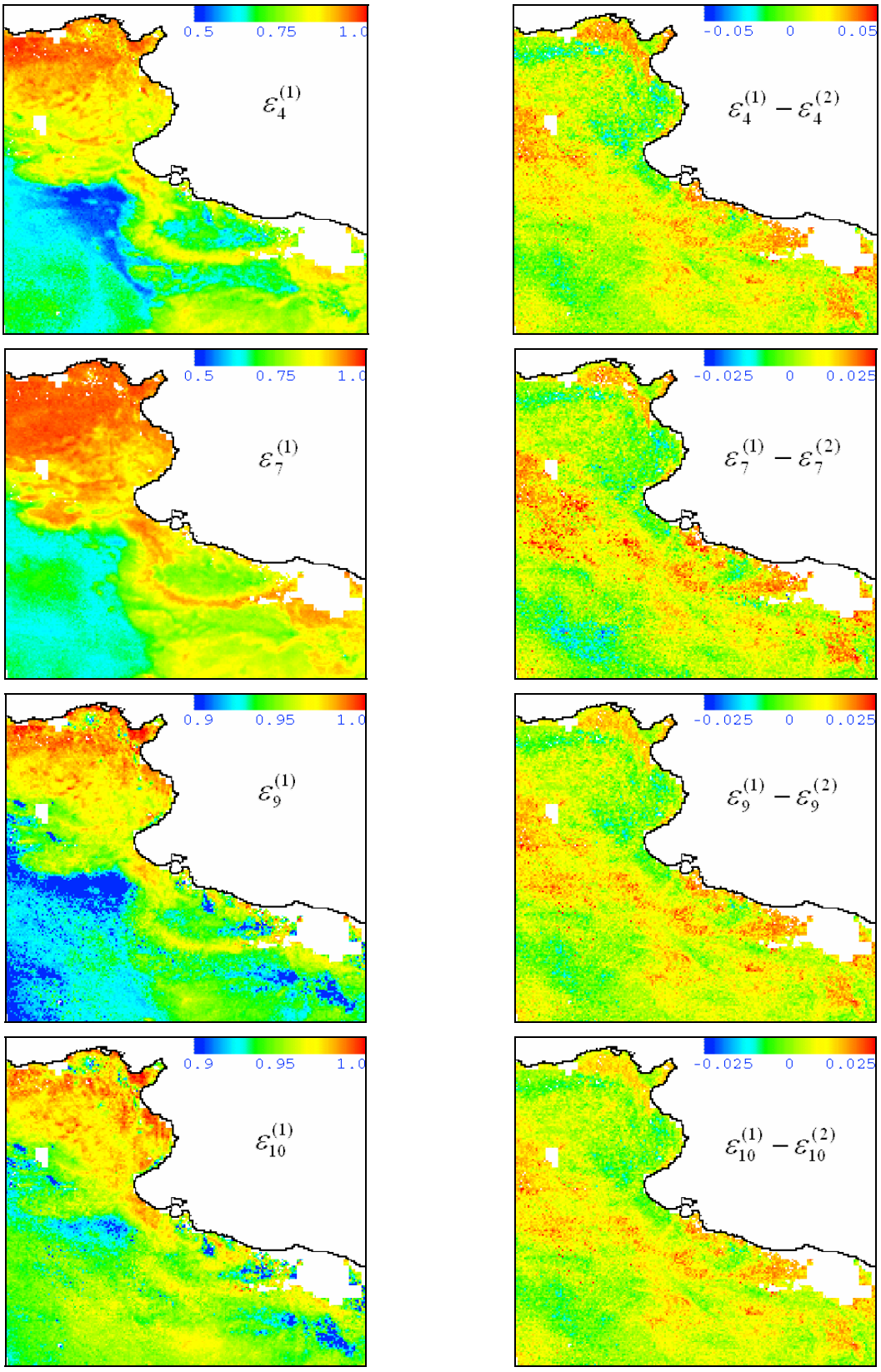

Figure 4.16. Maps of the directional emissivities in SEVIRI channels 4, 7, 9 and 10 modeled by the modified Minnaert's model for the two combinations on July 15, 2004
(The white in land represents NULL value and the symbols are the same as the ones in Figure 4.11)

The directional emissivities in SEVIRI channel 4 were modeled by the modified Minaert's model and the Kirchhoff's law. The directional emissivities in SEVIRI channels 7, 9 and 10 are calculated by Equations (4.8) and (4.9). Figure 4.16 displays the emissivity maps over the small study area on July 15, 2004. The results reveal that the directional emissivities in SEVIRI channels 4 and 7, which range between 0.5 and 0.96, are rather homogeneous with values over the vegetated areas, but are quiet lower over the bare areas. The directional emissivities in SEVIRI channels 9 and 10 are usually less than 0.95 for the bare areas, as observed in the south-western areas, and are usually higher than 0.95 for the vegetated areas. Moreover, the directional emissivity in SEVIRI channel 9 is slightly higher than the directional emissivity in SEVIRI channel 10 over densely vegetated areas, while over the bare areas, the opposite is observed.

Figure 4.17 shows the histograms of the differences of the emissivities retrieved using the two combinations on July 15, 2004, which appear to be normally distributed. ~76% of $|\varepsilon_4^{(1)} - \varepsilon_4^{(2)}|$ are distributed within ±0.02; ~73% of $|\varepsilon_7^{(1)} - \varepsilon_7^{(2)}|$, ~70% of $|\varepsilon_9^{(1)} - \varepsilon_9^{(2)}|$ and ~85% of $|\varepsilon_{10}^{(1)} - \varepsilon_{10}^{(2)}|$ are distributed within ±0.01. The RMSE of the emissivity differences over the entire small study area between the two combinations is 0.017 for the emissivities in SEVIRI channel 4, 0.013 for the emissivities in SEVIRI channel 7, 0.008 for the emissivities in SEVIRI channel 9 and 0.007 for the emissivities in SEVIRI channel 10.

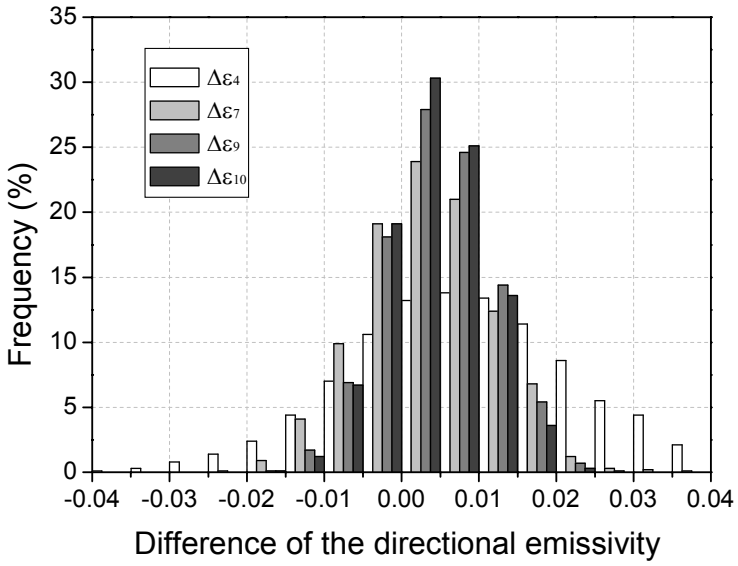

Figure 4.17. Histogram of the differences of the directional emissivities between two combinations (Modeled by the modified Minnaert's model between the combinations CH04-09 and CH04-10 over the small study area on July 15, 2004; $\Delta\varepsilon_i = \Delta\varepsilon_i^{(1)} - \Delta\varepsilon_i^{(2)}$ and i=4, 7, 9 or 10; Symbols are the same as the ones in Figure 4.11)

The results in this work are qualitatively consistent with former results estimated from the AVHRR data over the same areas (Petitcolin et al., 2002a, 2002b).

4.4.3 Evaluation of the RossThic-LiSparse-R model

Because of the imperfect performance of the modified Minnaert's model in the BRDF modeling, as shown in Figure 4.9 and Figure 4.10, the RossThick-LiSparse-R model is used here to evaluate its performance in the modeling of the bi-directional reflectivities. The bi-directional reflectivies at the six specific locations (Figure 4.5) were again normalized to a common relative azimuth angle φ_0=0° for the backscattering and φ_0=180° for the forward scattering by the following equation, if the RossThick-LiSparse-R model was used:

$$\rho_{b,4}(\theta_v,\theta_s,\varphi_0)=\frac{\rho_{b,4}(\theta_v,\theta_s,\varphi)\left[K_{iso}+K_{vol}f_{vol}(\theta_v,\theta_s,\varphi_0)+K_{geo}f_{geo}(\theta_v,\theta_s,\varphi_0)\right]}{K_{iso}+K_{vol}f_{vol}(\theta_v,\theta_s,\varphi)+K_{geo}f_{geo}(\theta_v,\theta_s,\varphi)} \tag{4.40}$$

Similar to Figure 4.9, Figure 4.18 shows that the normalized bi-directional reflectivity in SEVIRI channel 4 changes with the solar zenith angle. Different from the results at the locations B, C, D and E, the bi-directional reflectivities at the densely vegetated location A are nearly unchangable when the solar zenith angles vary from -60° to 60°. This reveals that the angular effects on the directional emissivity are very weak at densely vegetated locations, but at the partly vegetated or bare area locations, the angular effects are very strong. Figure 4.18 reveals that the bi-directional reflectivities are very well described by the RossThick-LiSparse-R model. Compared to the results in Figure 4.9, the modeled results in Figure 4.18 are much better, and much stronger angular effects are observed by the RossThick-LiSparse-R model. Figure 4.19 shows the reflectivities modeled by the RossThick-LiSparse-R model versus the measured reflectivities, and most of the differences between them are less than 0.005, which is also better than the results in Figure 4.10. The excellent performances of the RossThick-LiSparse-R model are determined by the model itself, physics-based and NOT non-linear, which is strongly different from the modified Minnaert's model in nature. It should be noted that, further examinations show that some valid bi-directional reflectivities were excluded from the regression by the non-linear modified Minnaert's model, but were kept by the RossThick-LiSparse-R model.

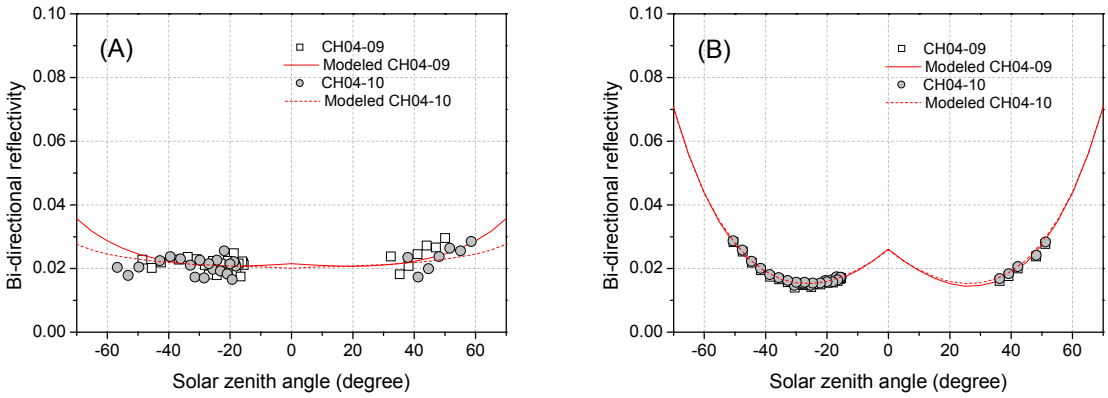

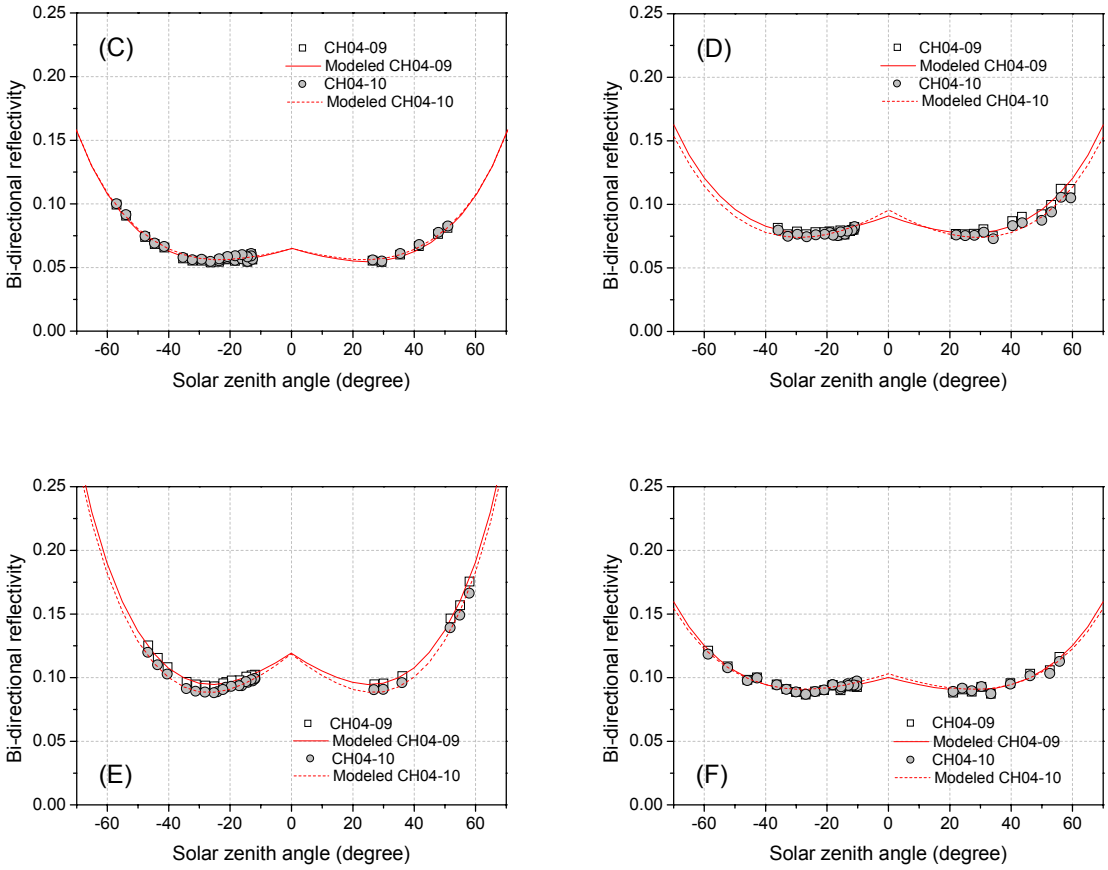

Figure 4.18. Same as the ones in Figure 4.9, but by the RossThick-LiSparse-R model

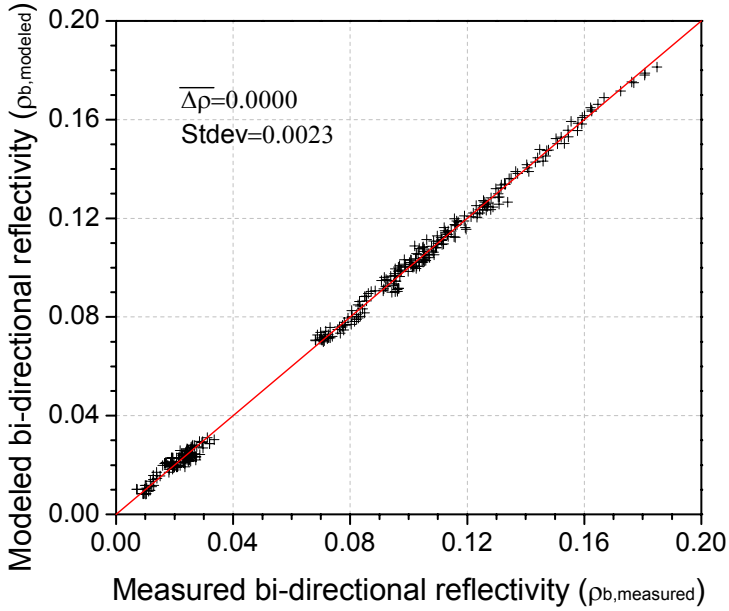

Figure 4.19. Same as the ones in Figure 4.10, but using the RossThick-LiSparse-R model ($\Delta\rho=\rho_{b,measured} - \rho_{b,modeled}$; Stdev represents the standard deviation of $\Delta\rho$)

Similar to Figure 4.11 and Figure 4.12, Figure 4.20 displays the directional emissivities in SEVIRI channels 4, 7, 9 and 10 modeled by the RossThick-LiSparse-R model at the six specific locations. The emissivity differences in SEVIRI channels 4 and 7 over the bare areas are slightly bigger than the ones over the vegetated areas. The absolute emissivity differences in SEVIRI channel 4 are less than 0.017, and the absolute emissivity differences in SEVIRI channels 7, 9 and 10 are less than 0.01 at the six specific locations.

Table 4.14 gives the comparisons between the directional emissivities modeled by the RossThick-LiSparse-R model and the modified Minnaert's model at the six specific locations on July 15, 2004. Almost all the directional emissivities modeled by the RossThick-LiSparse-R model are higher than the ones modeled by the modified Minnaert's model, especially over the bare areas, which is up to 0.046 for ε_4, 0.023 for ε_7, 0.023 for ε_9 and ε_{10}. From the fiiting results of the bi-directional reflectivities, the fitting differences between the two models can not lead to such large emissivity differences. Actually, the large emissivity differences come from the BRDF models: different expression form and different model parameters. Although, the two BRDF models can describe the non-Lambertian behavior of land surface, the emissivity differences between them can not be ignored, especially over the bare area.

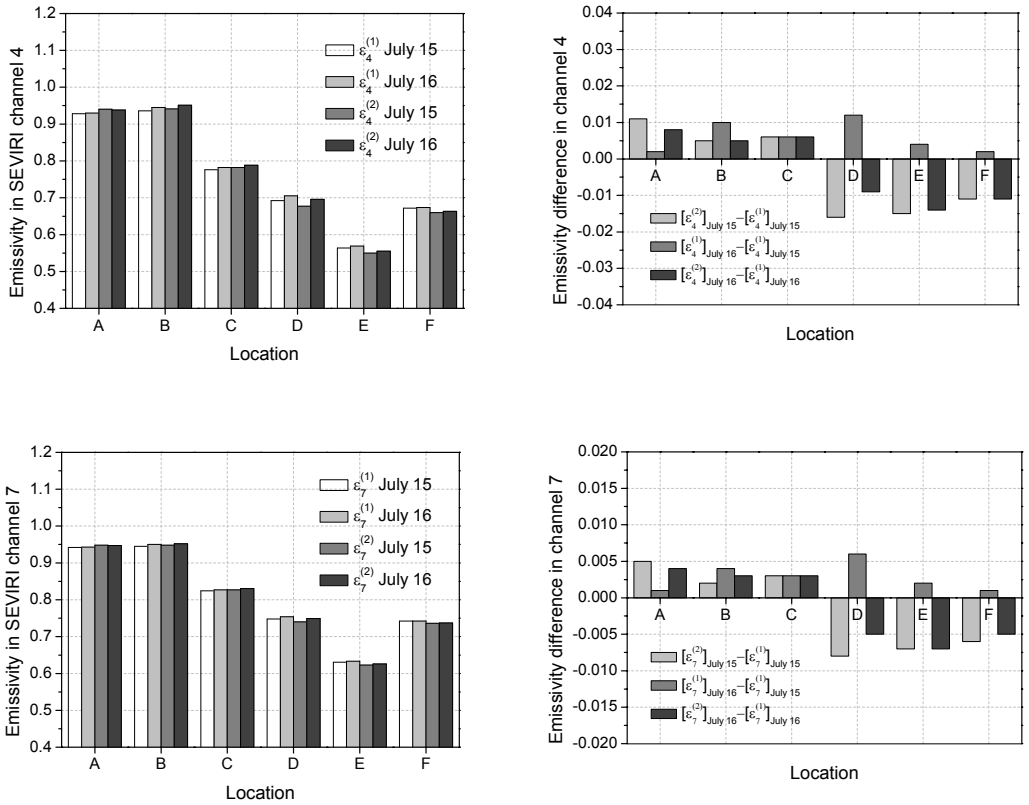

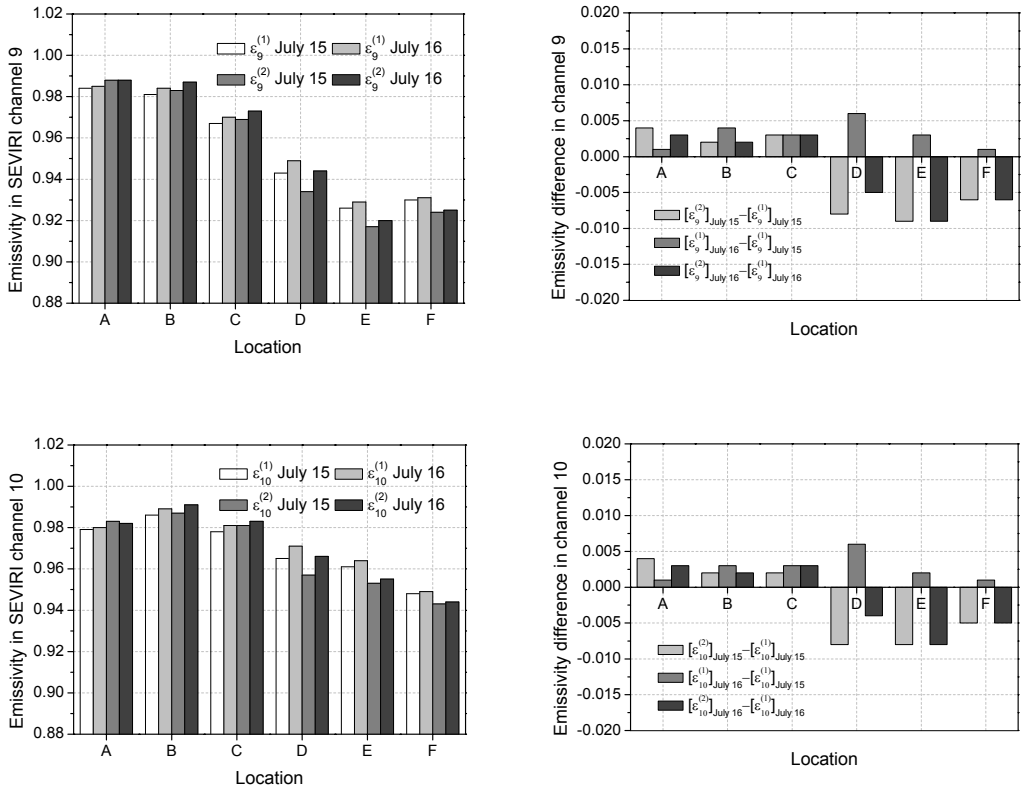

Figure 4.20. Same as the ones in Figure 4.11, but modeled by the RossThick-LiSparse-R model

Table 4.14. Comparisons between the directional emissivities modeled by the RossThick-LiSparse-R model and the modified Minnaert's model on July 15 of 2004

Location	Model*	$\varepsilon_4^{(1)}$	$\varepsilon_4^{(2)}$	$\varepsilon_7^{(1)}$	$\varepsilon_7^{(2)}$	$\varepsilon_9^{(1)}$	$\varepsilon_9^{(2)}$	$\varepsilon_{10}^{(1)}$	$\varepsilon_{10}^{(2)}$
A	RL	0.928	0.940	0.942	0.948	0.984	0.988	0.979	0.983
	MM	0.913	0.926	0.935	0.941	0.978	0.983	0.973	0.978
	Δε	0.015	0.014	0.007	0.007	0.006	0.005	0.006	0.005
B	RL	0.936	0.941	0.945	0.948	0.981	0.983	0.986	0.987
	MM	0.928	0.933	0.942	0.944	0.978	0.980	0.983	0.985
	Δε	0.008	0.008	0.003	0.004	0.003	0.003	0.003	0.002
C	RL	0.776	0.782	0.824	0.827	0.967	0.969	0.978	0.981
	MM	0.733	0.736	0.803	0.804	0.946	0.948	0.959	0.961
	Δε	0.043	0.046	0.021	0.023	0.021	0.021	0.019	0.02
D	RL	0.692	0.677	0.748	0.740	0.943	0.934	0.965	0.957
	MM	0.684	0.664	0.743	0.733	0.938	0.928	0.961	0.951
	Δε	0.008	0.013	0.005	0.007	0.005	0.006	0.004	0.006
E	RL	0.564	0.550	0.631	0.623	0.926	0.917	0.961	0.953
	MM	0.527	0.525	0.611	0.610	0.903	0.901	0.939	0.938
	Δε	0.037	0.025	0.02	0.013	0.023	0.016	0.022	0.015
F	RL	0.672	0.660	0.742	0.736	0.930	0.924	0.948	0.943
	MM	0.636	0.631	0.724	0.720	0.911	0.908	0.931	0.928
	Δε	0.036	0.029	0.018	0.016	0.019	0.016	0.017	0.015

*RL and MM are, respectively, the acronyms of the RossThick-LiSparse-R model and the modified Minnaert's model.

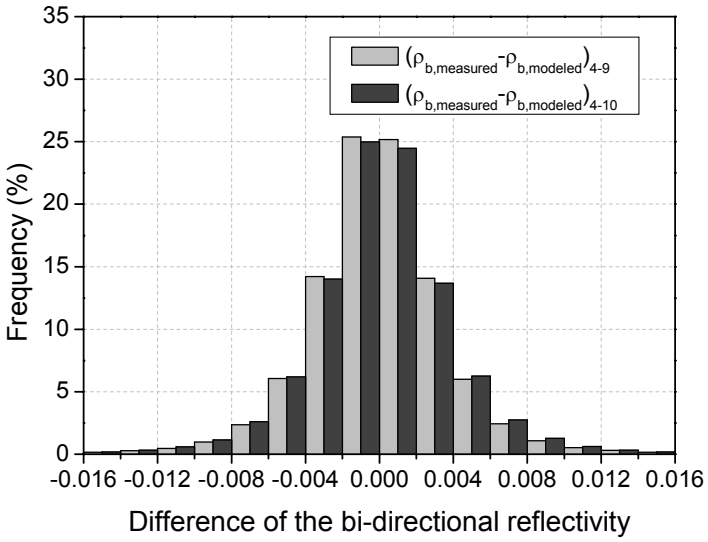

Figure 4.21. Same as the ones in Figure 4.13, but using the RossThick-LiSparse-R model

Similar to Figure 4.17, Figure 4.21 shows the hitograms of the differences between the measured and the modeled bi-directional reflectivities using the RossThick-LiSparse-R model over the entire small study area on July 15 of 2004, and 97.6% of $(\rho_{b,measured}- \rho_{b,modeled})_{4-9}$ and 94.9% of $(\rho_{b,measured}- \rho_{b,modeled})_{4-10}$ are distributed within ±0.01. The results in Figure 4.21 are much better than the ones in Figure 4.17. Figure 4.22 displays the histograms of the differences of the emissivities estimated by the two combinations on July 15 of 2004.74.7% of $|\varepsilon_4^{(1)}- \varepsilon_4^{(2)}|$ are less than 0.02, and 74.3% of $|\varepsilon_7^{(1)}- \varepsilon_7^{(2)}|$, 74.8% of $|\varepsilon_9^{(1)}- \varepsilon_9^{(2)}|$ and 78.2% of $|\varepsilon_{10}^{(1)}- \varepsilon_{10}^{(2)}|$ are distributed within ±0.01. Little difference exists between Figure 4.17 and Figure 4.22.

Totally, the RossThick-LiSparse-R model is much better than the modified Minnaert's model in the modeling of the bi-directional reflectivities, and the emissivity differences caused by the two models can not be ignored, especially over bare areas. Therefore, the use of the RossThick-LiSparse-R model in the estimation of the directional emissivity in SEVIRI channel 4 is recommended.

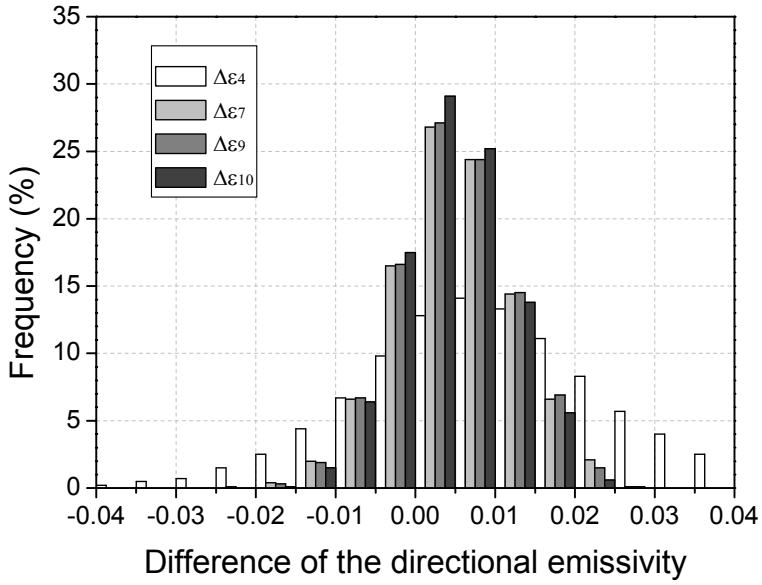

Figure 4.22. Same as the ones in Figure 4.17, but using the RossThick-LiSparse-R model

4.4.4 Sensitivity analysis at the six specific locations

The main errors associated with the retrievals of the bi-directional reflectivities come from the instrumental NEΔT (Noise Equivalent Temperature difference), the atmospheric quantities, the approximation to calculate C_i, the use of power law of approximation, and TISI (Nerry et al., 1998; Petitcolin et al. 2002a, 2002b). The results of Nerry et al. (1998) reveal that the instrumental error is weak compared to the others, and the error on the bi-directional reflectivity due to the approximation made in the method is ~3%, and the main source of error is the atmospheric error, which is highly dependent on the accuracy of the atmospheric water vapor content. An error of 1.0 g/cm^2 on atmospheric water vapor content would lead to a relative error of ~18% on the bi-directional reflectivity.

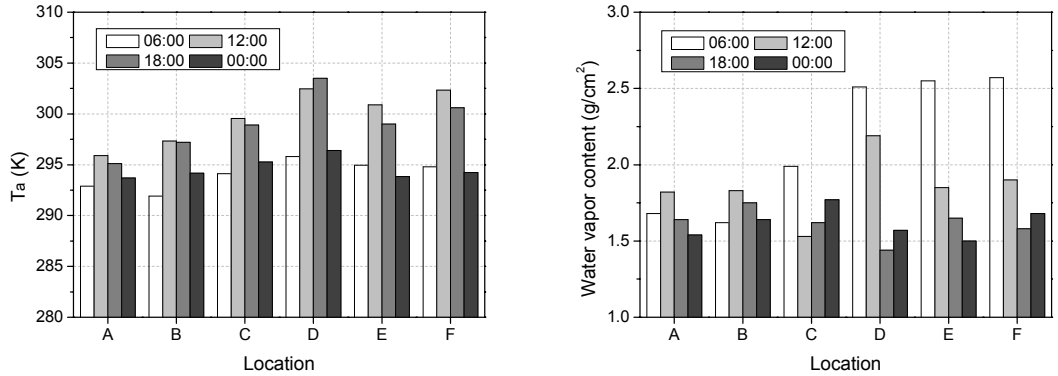

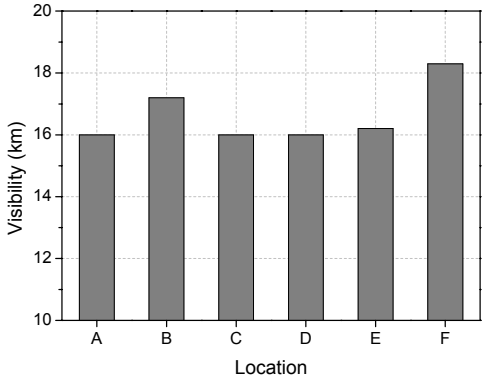

Figure 4.23. First boundary air temperature (T_a), water vapor content and visibility at the six specific locations on July 15, 2004

In this work, the atmospheric profiles were extracted from the ECMWF data, which are composed of pressure profiles, air temperature profiles, relative humidity profiles and so on. The daily averaged horizontal visibility data were also used to rough indicate the amount of aerosols. The errors in the atmospheric data were finally transfered to the estimated emissivities. Here, we used the data at the six specific locations (Table 4.6) to demonstrate how much the emissivities will change, if the air temperatures, the water vapor content or the visibility vary with certain quantity.

At the six specific locations, on July 15, 2004, the atmospheric water vapor contents range between 1.3 and 2.6 g/cm^2, and the air temperatures at the first boundary vary between 290 and 305 K, and the visibilities change between 15 and 19 km (Figure 4.23). The adjustment quantity to the first boundary air temperature is set to ±5.0 K, and decreases with the height until to the tropopause, above which no adjustment is carried out. The adjustment quantity to the water vapor content is ±50%, and the adjustment quantity to the visibility is set to ±5.0 km. The emissivities in SEVIRI channels 4, 7, 9 and 10 were re-derived with the adjusted atmospheric data by the method described previously (the RossThick-LiSparse-R model was used). Figure 4.24 shows the emissivity differences between the emissivities estimated by the adjusted atmospheric data and by the normal atmospheric data at the six specific locations using the RossThick-LiSparse-R model. Same adjustments of atmospheric data lead to different emissivity variations at different locations. Generally, the directional emissivities in SEVIRI channels 4, 7, 9 and 10 are most sensitive to the changes of the water vapor contents (W- & W+) and the increase of the air temperatures (T_a+), and the maximum absolute emissivity differences are 0.170 for ε_4, 0.076 for ε_7, 0.067 for ε_9, and 0.114 for ε_{10}. while the impacts of the changes of the visibilities and the decreases of the air temperatures on the directional emissivities are relatively weak, and the emissivity differences are less than 0.05 for ε_4, and less than 0.04 for ε_7, ε_9 and ε_{10}.

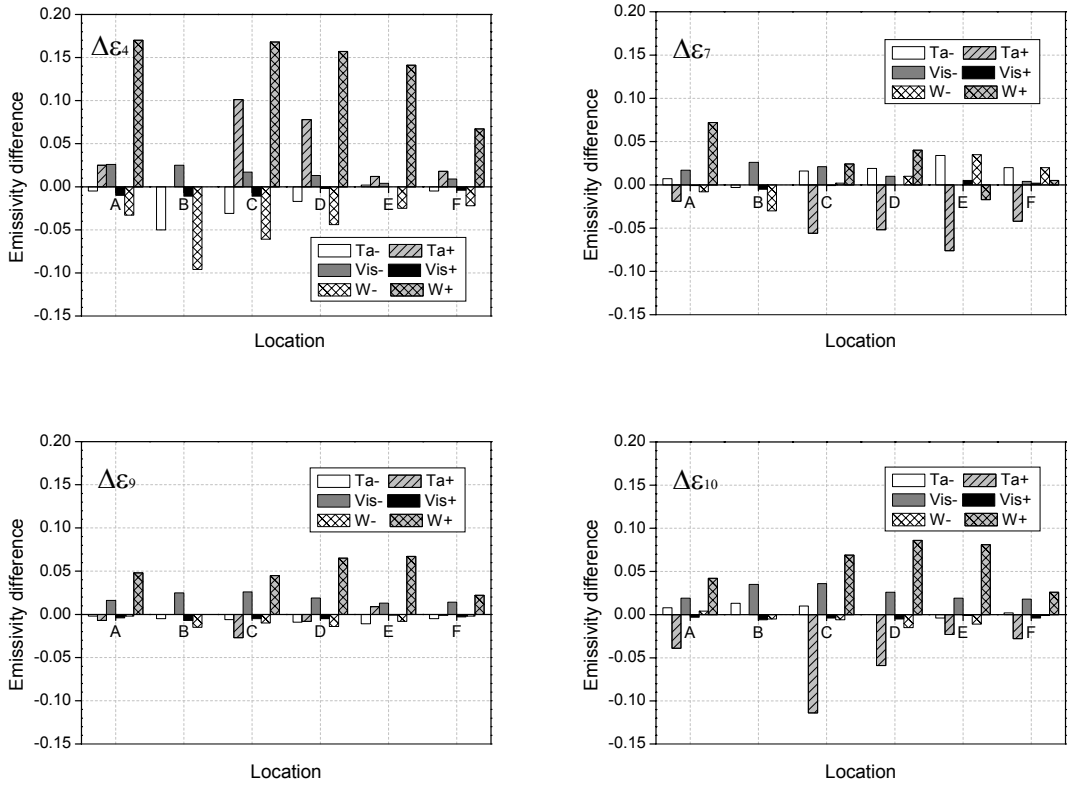

Figure 4.24. Emissivity differences in SEVIRI channels 4, 7, 9 and 10 with the changes of atmospheric parameters at the six specific locations on July 15, 2004
(BRDF model: RossThick-LiSparse-R; Ta+ and Ta- stand for the increment and the decrease of the air temperature with an amount of 5.0 K, respectively; Vis+ and Vis- represent the increment and the decrease of the visibility with a quantity of 5.0 km, respectively; W+ and W- represent the increment and the decrease of the water vapor content with 50%, respectively)

4.5 Application to the large study area and emissivity composite

Over the large study area, the RossThick-LiSparse-R model was used instead of the modified Minnaert's model to describe the bi-directional reflectivities in SEVIRI channel 4, because of its excellent performance in the BRDF modeling. Because SEVIRI channel 9 is less sensitive to the variation of atmospheric water vapor content than SEVIRI channel 10, the combination of SEVIRI channels 4 and 9 was used in the retrievals of the directional emissivities in SEVIRI channels 4, 7, 9 and 10.

4.5.1 Data processing

After the successful application to the small study area located on the northern region of Africa, the LSE retrievals were then applied to the large study area ranging from 20W to 60E and from 0 to 60N, and to two continuous time spans going from July 14 to July 20, 2004 and from July 10 to July 15, 2005 and 31 dates listed in Table 4.7.

The data processing over the large study area and the long terms was very time consuming, especially the calculation of the atmospheric parameters using MODTRAN fed with the ECMWF data. In order to make the retrievals possible, we relax some of the constraints used for the small study area.

The LST variation in daytime is strongly affected by the cloud contamination, but the case is different at night when differential surface heating is absent. From a theoretical point of view, one clear sky measurement in nighttime is adequate to resolve Equations (4.33a) and (4.33b). In order to make the minimization stable and reliable, we set eight as the minimum number of the clear sky measurements required at night. In daytime, the brief slots less than 1.5 hours with cloud contamination were also tolerated, but the total number of the brief slots should not be greater than four. In the fitting regression, the measurement with difference between the DTC modeled brigtness temperature and the measured brightness temperature greater than two times the RMSE was excluded in the next minimization, and the regression process repeated until all measurements were qualified. If the RMSE was less than 0.5 K, the criterion was set to 0.5 K.

In order to accelerate the speed of the ECMWF data processing, only those ECMWF profiles fallen into the area with valid output of the DTC model were processed, and the frequency increment in the MODTRAN input was set to 5. As mentioned in the atmospheric correction over the small study area, the daytime atmospheric parameters in SEVIRI channel 4, mainly the direct solar irradiance at ground level, were calculated every 15 min. Because of the time cost, it is not convenient to do that over the large area. To simplify the data processing, we assume that the solar irradiance at ground level simply varies as a cosine function.

$$E_{sun}(t) = A_s + B_s \cos \beta_s (t - 12) \tag{4.41}$$

where A_s, B_s and β_s are unknown coefficients, and t is the local solar time.

The daytime atmospheric parameters in SEVIRI channel 4 were calculated at seven UTC times 6:00, 8:00, 10:00, 12:00, 14:00, 16:00 and 18:00. The selection of the seven UTC times is to guarantee the correct inversion of Equation (4.41). In terms of the ECMWF output at the seven UTC times and Equation (4.41), the direct solar irradiance at ground level at other times were predicted. The daytime radiances at TOA in SEVIRI channel 4 were corrected to ground level by the use of the time nearest atmospheric parameters at the seven UTC times.

The bi-directional reflectivities with solar zenith angle greater than 70^o were discarded over the large area. The emissivities in SEVIRI channels 4, 7, 9 and 10 were estimated by the use of the combination of SEVIRI channels 4 and 9.

As Petitcolin et al. (2002b) demonstrated, the TISIs are quiet stable during a short period of time. In order to eliminate the effects of clouds as many as possible, median composite maps of TISIs were calculated from the measurements at the five UTC times 23:57 (last night), 5:57, 11:57, 17:57 and 23:57. It should be noted that the $TISI_{4,9}$ can not be obtained in daytime because of the solar irradiance in SEVIRI channel 4. In terms of the sunrise and sunset times, the pixels contaminated by solar irradiance were easily distinguished. Corresponding to the TISI composite, composite maps of B_4^{night} and B_9^{night} in Equation (4.5) were also generated, which means that TISI, B_4^{night} and B_9^{night} come from the measurements at the same time.

4.5.2 Results and analysis

The emissivities in SEVIRI channels 4, 7, 9 and 10 over the large study area on the dates listed in Table 4.7 and from July 14, 2004 to July 19, 2004 and from July 10, 2005 to July 14, 2005 were successfully estimated.

Here, we took the emissivities in SEVIRI channels 4, 7, 9 and 10 on February 10 of 2004 as examples to demonstrate the retrieved results. Figure 4.25 displays the emissivity maps on February 10, 2004 over the large study area. Figure 4.25 shows that the estimated emissivities have clear textures, and most of the emissivities in SEVIRI channels 4 and 7 vary between 0.6 and 1.0, while most of the emissivities in SEVIRI channels 9 and 10 change between 0.9 and 1.0. Figure 4.25 also reveals that the emissivities over the vegetated areas (e.g., Central Africa) are usually higher than the ones over the bare areas (e.g., North Africa). Because of the cloud contamination and the algorithm limitations, such as the requirements of the minimum observation number in the DTC modeling and the BRDF modeling, lots of emissivities were not successfully derived over some areas.

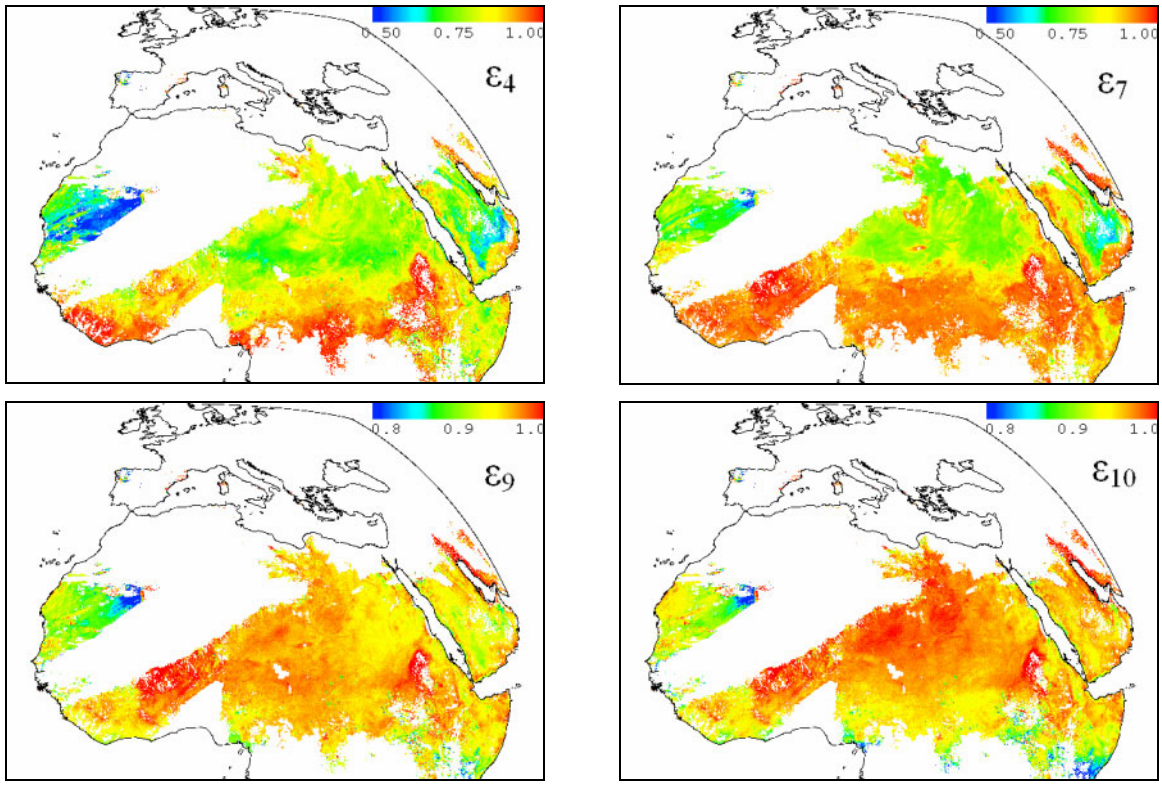

Figure 4.25. Maps of the directional emissivities in SEVIRI channels 4, 7, 9 and 10 on February 10, 2004 over the large study area

As we know, LSE changes with vegetation coverage and moisture content, but it does not significantly change in several days unless dew, rain and/or snow occurs during that short period of time particularly for bare soils in arid and semi-arid areas, for which the land surface is dry for most of time (kerr et al., 1992; MODIS LST ATBD version 3.3). Figure 4.26 shows the emissivities in SEVIRI channels 4, 7, 9 and 10 at Locations G, H, I and J modeled by the RossThick-LiSparse-R model. The emissivities fluctuate with dates.

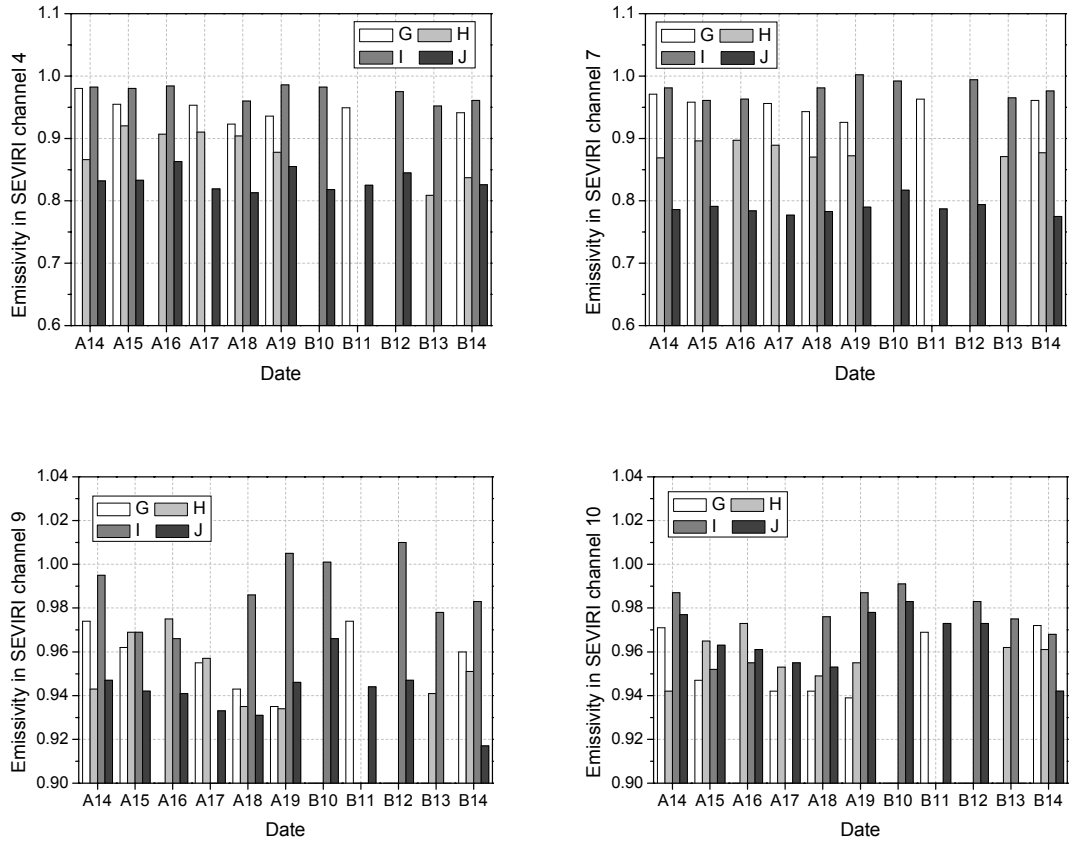

Figure 4.26. Emissivities in SEVIRI channels 4, 7, 9 and 10 at Locations G, H, I and J modeled by the RossThick-LiSparse-R model
(A14-A19 represent the dates from 14 to 19 July of 2004 and B10-B14 represent the dates from 14 to 19 July of 2005)

Table 4.15. Median and standard deviation of the emissivities in SEVIRI channels 4, 7, 9 and 10 from July 14 to July 19 of 2004 at Locations G, H, I and J

2004	ε_4		ε_7		ε_9		ε_{10}	
	Median	Stdev	Median	Stdev	Median	Stdev	Median	Stdev
G	0.953	0.022	0.956	0.017	0.955	0.015	0.942	0.013
H	0.907	0.021	0.889	0.013	0.957	0.017	0.955	0.011
I	0.982	0.011	0.981	0.016	0.986	0.017	0.976	0.017
J	0.833	0.020	0.786	0.005	0.942	0.007	0.963	0.011

Stdev is the abbreviation of standard deviation.

Table 4.16. Same as the ones in Table 4.15, but from July 10 to July 14 of 2005

2005	ε_4		ε_7		ε_9		ε_{10}	
	Median	Stdev	Median	Stdev	Median	Stdev	Median	Stdev
G	0.949	0.006	0.963	0.001	0.974	0.010	0.972	0.002
H	0.837	0.020	0.877	0.004	0.951	0.007	0.962	0.001
I	0.975	0.014	0.992	0.014	0.983	0.015	0.983	0.010
J	0.826	0.012	0.794	0.018	0.947	0.020	0.973	0.018

Table 4.15 and Table 4.16 give, respectively, the median and standard deviations of the emissivities in SEVIRI channels 4, 7, 9 and 10 at Locations G, H, I and J from July 14 to 19 of 2004 and from July 10 to 14 of 2005. The results show that all the standard deviations are ~0.016 for the emissivities in SEVIRI channel 4, and are ~0.012 for the emissivities in SEVIRI channels 7, 9 and 10. The fluctuating errors of the emissivities shown in Table 4.15 and Table 4.16 are within the theoretical error scope (Nerry et al., 1998). Based on the facts above, assuming that the directional emissivities during a short period of time do not change, a median composite was carried out on the directional emissivities from July 15 to July 19, 2004, and from July 10 to July 14, 2005. The median was used because it is a more robust estimator than the others (Becker and Li, 1995). Figure 4.27 and Figure 4.28 show, respectively, the composite maps of the directional emissivities in SEVIRI channels 4, 7, 9 and 10 from July 14, 2004 to July 19, 2004, and from July 10, 2005 to July 14, 2005. The emissivity composite maps display clear textures, especially over the Iberian Peninsula and the north-east Africa, where clear sky happens often. The directional emissivities in SEVIRI channels 4 and 7 change between 0.5 and 1.0, and they are usually higher than 0.85 over the vegetated areas, such as the Europe, while they are very low over the bare areas, such as the Sahara desert. The directional emissivities in SEVIRI channels 9 and 10 are usually higher than 0.85, and the emissivities over the vegetated areas are higher than the ones over the bare areas. Over the densely vegetated area, such as the Iberian Peninsula, the emissivities in SEVIRI channel 9 are slightly higher than the ones in SEVIRI channel 10.

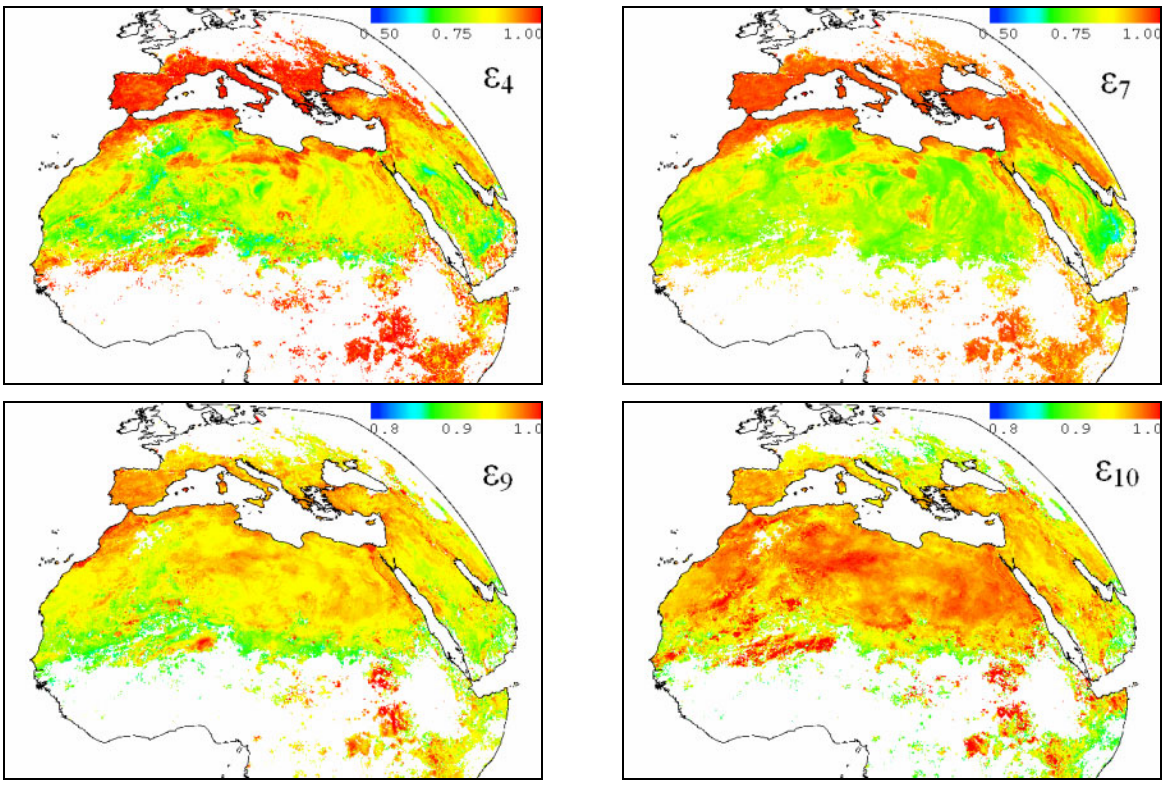

Figure 4.27. Median composite maps of the directional emissivities in SEVIRI channels 4, 7, 9 and 10 from July 14 to July 19, 2004 over the large study area

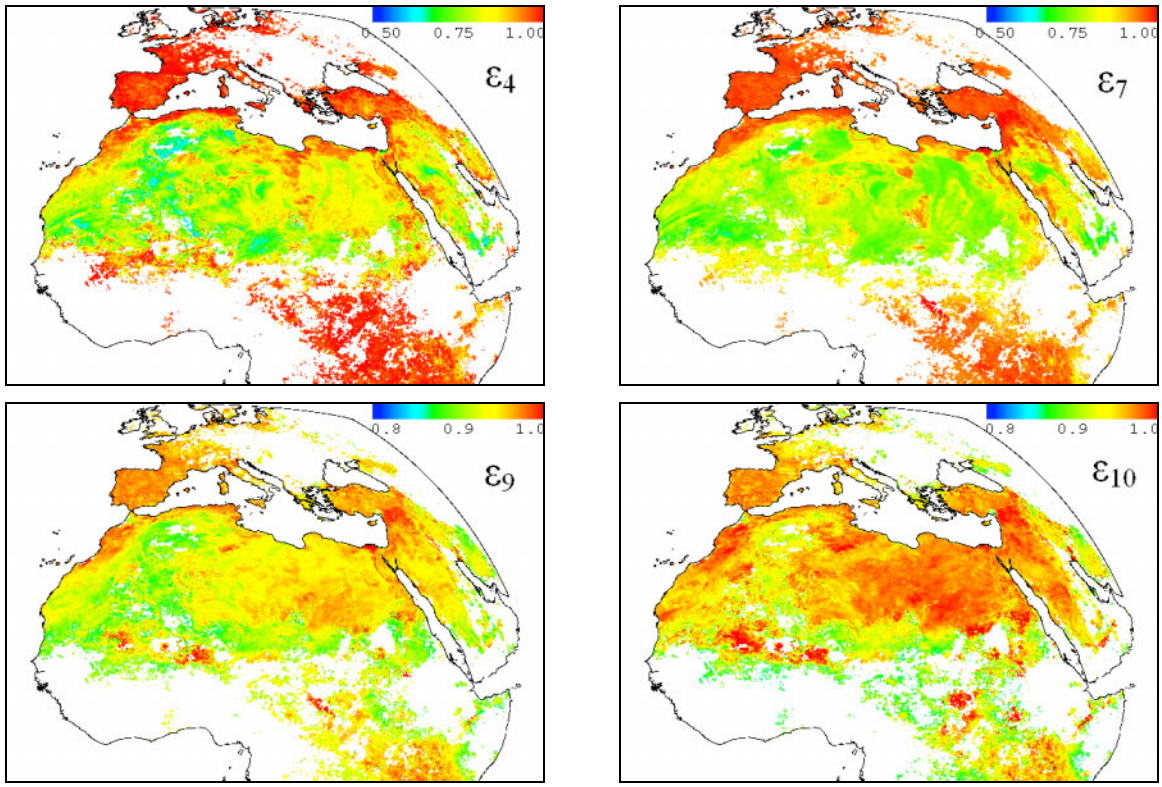

Figure 4.28. Median composite maps of the directional emissivities in SEVIRI channels 4, 7, 9 and 10 from July 10, 2005 to July 14, 2005 over the large study area

4.6 Summary and conclusions

In this chapter, we addressed a method to retrieve the LSEs from the combined mid-infrared and thermal infrared data of the MSG1-SEVIRI. As known from the radiative transfer equations, the main difficulties in the retrievals of LST from satellite data are the need to correct for the atmospheric perturbations and the variable surface emissivities. To tackle the problems of the low temporal and spatial resolutions of the ECMWF data, a modified atmospheric correction scheme was developed. For the images acquired at UTC times 0:00, 6:00, 12:00 and 18:00 when the ECMWF atmospheric data are available, the atmospheric corrections were carried out in the following steps: (1) Calculation of the atmospheric parameters for each atmospheric profiles with MODTRAN 4.0. (2) Spatial interpolation of all calculated atmospheric parameters into the image coordinates. (3) Atmospheric correction based on the radiative transfer equations. However, as mentioned previously, because SEVIRI channel 4 can not be regarded as a channel with narrow spectral range, the atmospheric corrections for the image in SEVIRI channel 4 is difficult. This problem was resolved by introducing the temperature dependent channel-averaged transmittance. For the images acquired at times without atmospheric data, the time-nearest atmospheric profiles were used for the images in SEVIRI channel 4, while the DTC model was used for the atmospheric correction in SEVIRI channels 9 and 10. (4) The directional emissivities in SEVIRI channels 4, 7, 9 and 10 were estimated by the TISI concept, the BRDF models (the modified Minnaert's model and the RossThick-LiSparse-R model) and the Kirchhoff's law.

A small area (30.2N—37.7N, 7.0E—15.7E) and a large area (0—60N, 20W—60E) were selected as study areas (Figure 4.5). The MSG Level 1.5 product, MSG cloud mask and ECMWF data were primary data used in the LSE retrievals. The time span of the SEVIRI data over the small study area is

from July 15 to July 17, 2004. While, for the large study area, two continuous time spans (July 14 – July 19, 2004 & July 10 – July 14, 2005) and 31 dates listed in Table 4.7 were used.

The results at the six specific locations modeled by the modified Minnaert's model, including vegetated areas and bare areas, show that: (1) The modified DTC model works well on both vegetated and bare areas, and the modified Minnaert's model can well describe the bi-directional reflectivities over bare areas; (2) The differences between the values of each parameter ρ_0, ε_4, ε_9 and ε_{10} in two successive days by the use of the two combinations are small; (3) The bi-directional reflectivities depend on the solar zenith angles, which verifies that the land surface is a non-Lambertian reflector and of course the derived emissivities are view zenith angle dependent. (4) The modeled bi-directional reflectivities and directional emissivities at the locations D and E are basically consistent with the results of Nerry et al. (1998) and Petitcolin et al. (2002a & 2002b).

The TISIs and directional emissivities in SEVIRI channels 4, 9 and 10 were mapped over the small area on July 15, 2004. TISIs are found to be close to unity for vegetated areas and low in bare areas. The range of the directional emissivities in SEVIRI channel 4 is very large, going from 0.5 for the bare areas to 0.96 for the densely vegetated areas. The directional emissivities in SEVIRI channels 9 and 10 are usually from 0.9 to 1.0. Over the bare areas, they are usually less than 0.95, and the emissivities in SEVIRI channel 10 are greater than the ones in SEVIRI channel 9. Over vegetated areas, they are usually greater than 0.95, and the directional emissivities in SEVIRI channel 9 are slightly higher than the ones in SEVIRI channel 10. ~76% of $|\varepsilon_4^{(1)} - \varepsilon_4^{(2)}|$ are distributed within ±0.02, ~73% of $|\varepsilon_7^{(1)} - \varepsilon_7^{(2)}|$, ~70% of $|\varepsilon_9^{(1)} - \varepsilon_9^{(2)}|$ and ~85% of $|\varepsilon_{10}^{(1)} - \varepsilon_{10}^{(2)}|$ are distributed within ±0.01. The RMSE of the emissivity differences over the entire small study area between the two combinations is 0.017 for the emissivity in SEVIRI channel 4, 0.008 for the emissivity in SEVIRI channel 9 and 0.007 for the emissivity in SEVIRI channel 10.

The modeling results at the six specific locations reveal that the RossThick-LiSparse-R model is much better than the modified Minnaert's model in the modeling of the bi-directional reflectivities, and the emissivity differences caused by the two models can not be ignored. The use of the RossThick-LiSparse-R model in the estimation of the emissivity in SEVIRI channel 4 is recommended.

Over the large area and in the long terms, the bi-directional reflectivities were derived only by the combination of SEVIRI channels 4 and 9, and the RossThick-LiSparse-R model was used instead of the modified Minnaert's model to describe the non-Lambertian property of land surface. In order to apply the LSE retrievals to the large area and long terms, some modifications were made in the data processing, such as the DTC modeling, the atmospheric corrections of the images in SEVIRI channel 4 and the TISI composite. The directional emissivities in SEVIRI channels 4, 7, 9 and 10 over the large area from July 14, 2004 to July 19, 2004 and from July 10, 2005 to July 14, 2005 and on the dates listed in Table 4.7 were estimated. The results of the emissivities in SEVIRI channels 4, 7, 9 and 10 at Locations G, H, I and J reveal that they do not significantly change in several days. Therefore, median composite maps of the emissivities in SEVIRI channels 4, 7, 9 and 10 were, respectively, generated for the two time spans. The emissivity composite maps have clear textures. Over the large area, the directional emissivities in SEVIRI channels 4 and 7 change between 0.5 and 1.0, and they are usually higher than 0.85 over the vegetated areas, such as the Europe, while they are very low over the bare areas, such as the Sahara desert. The directional emissivities in SEVIRI channels 9 and 10 are usually higher than 0.85, and the emissivities over the vegetated areas are higher than the ones over the bare areas. These results in this work qualitatively agree with the former results of Nerry et al. (1998) and Petitcolin et al. (2002a, 2002b).

5 Land surface temperature retrievals from MSG1-SEVIRI data and AATSR data

5.1 Introduction

Land Surface Temperature (LST) is one of the key parameters in the physics of land surface processes on regional as well as a global scale. It combines the results of all surface-atmosphere interactions and energy fluxes between the atmosphere and the ground (Mannstein, 1987; Sellers et al., 1988). In contrast with LSE, LST is not an intrinsic parameter of land surface, and it varies with the irradiance history and meteorological conditions. LST is widely used in many applications, such as the energy budget models, evaportranspiration models (Serafini, 1987; Bussieres et al., 1990), estimating soil moisture (Price, 1990), frost detection and forecasting, monitoring the state of the crops (Casellas and Sobrino, 1989), studying land and sea breezes and nocturnal cooling. Satellite-measured LST may be used to improve models and methods for evaluating land surface energy balance (Diak and Whipple, 1993). An accurate LST retrieval would not only help estimating surface energy and water balances, thermal inertia and soil moisture (Sobrino et al., 1998; Tarpley, 1994; Seguin et al., 1994), it would also enable an analysis of the global surface temperature and its variability within a long period of time. Some of the major research challenges are related to the removal from remotely sensed data of effects caused by atmospheric attenuation, surface emissivity, and the topography (Price, 1984). Satellite remote sensing is the only viable means to extract long-term and large-scale LSTs (Goïta and Royer, 1997). LST retrieval algorithms are based on the radiative transfer theory (Section 2.1), and the single channel method and the split-window method are two commonly used algorithms.

The single channel method takes advantage of the radiance measured by satellite instrument in one atmospheric window channel, and corrects it from the effects of the atmosphere and the LSE by the simple inversion of the radiative transfer equation (Ottlé and Vidal-Madjar, 1992). This method requires LSE, an accurate radiative transfer model and atmospheric profiles which must be given by either satellite soundings or conventional radiosonde data (Price, 1983; Susskind et al., 1984; Chedin et al., 1985; Ottlé and Vidal-Madjar, 1992).

The split-window method was firstly proposed by McMillin (1975) to estimate sea surface temperature from satellite measurements based on the differential absorption in two adjacent infrared channels, usually centered at ~11.0 μm and ~12.0 μm. Since then, a variety of split-window methods have been developed to retrieve sea surface temperature (Prabhakara et al., 1974; McMillin, 1975; Deschamps and Phulpin, 1980; Llewellyn-Jones et al., 1984; McClain et al., 1985).

Price (1984) applied the split-window method for measuring ocean temperature to land surface, by the use of the two split-window channels of NOAA-7 AVHRR. He found that the variation of the LSE could cause significant errors in the estimated LSTs. Becker (1987) showed the impact of spectral emissivity on the LST retrieval from satellite data, by correcting for atmospheric effects with the split-window method. He developed a series of linear approximations and concluded that accurate knowledge of LSE is required to determine LST from space. Wan and Dozier (1989) pointed out that the simple extension to the land surface of the methods developed for sea surface temperature measurements would lead to unacceptable errors, and the reasons lie in the spectral and spatial variations of LSE, temperature variation, heterogeneous land surfaces, and atmospheric profile variation. Until now, the split-window method have been successfully applied to the LST retrievals from the data acquired by the AVHRR, MODIS and SEVIRI instruments (Price, 1984; Becker, 1987; Becker and Li, 1990b; Vidal, 1991; Kerr et al., 1992; Ottlé and Stoll, 1993; Prata, 1994; Wan and Dozier, 1989 & 1996; Sobrino et al., 1991, 1994 & 1996; Sobrino and Romaguera, 2004).

In this work, we focused on the LST retrievals from the data in the thermal infrared channels of MSG1-SEVIRI and AATSR. In the following, this chapter is divided into five sections. In the section 5.2, the theoretical methods of land surface temperature retrieval will be presented, including the single channel method, the generalized split-window algorithm, the development of the generalized split-window algorithm for MSG1-SEVIRI and AATSR, the emissivities in the split-window channels, and the retrieval of atmospheric water vapor content. In the section 5.3, the application of the DTC model to the time normalization of LSTs is depicted. In the section 5.4, the study area, data and data processing will be described. The section 5.5 contains the derived results, the comparisons between the results derived by the two methods, and the analysis. The last section is devoted to the summary and conclusions.

5.2 Methods and algorithm development

According to the radiative transfer equations (2.7) and (2.8), the radiance L_i measured under clear sky conditions in an infrared channel *i* at TOA is given by

$$L_i(T_i,\theta_v) = \tau_i(\theta_v)\left[\varepsilon_i(\theta_v)L_i(T_s) + (1-\varepsilon_i(\theta_v))L_{atm\downarrow i}\right] + L_{atm\uparrow i}(\theta_v) \tag{5.1}$$

Inverting Equation (5.1), one can obtain

$$T_s = L^{-1}\left[\frac{L_i(T_i,\theta_v) - L_{atm\uparrow i}(\theta_v) - \tau_i(\theta_v)(1-\varepsilon_i(\theta_v))L_{atm\downarrow i}}{\tau_i(\theta_v)\varepsilon_i(\theta_v)}\right] \tag{5.2}$$

in which L^{-1} is the inversion of the Planck function.

In order to retrieve the LST from Equation (5.2), the atmospheric parameters ($\tau_i(\theta_v)$, $L_{atm\downarrow i}$ and $L_{atm\uparrow i}(\theta_v)$) and the directional emissivity $\varepsilon_i(\theta_v)$ should be known in advance. This method is named the single channel method. Because the channel centered at ~11 μm is less sensitive to the water vapor content in the atmosphere, when compared to the channel centered at ~12 μm, the measurements in the channel centered at ~11 μm are usually used in the single channel method.

In practice, because the meteorological data are temporally sparse, e.g., the ECMWF data are only available at four main UTC times 0:00, 6:00, 12:00 and 18:00, it is difficult to meet practical

requirements. To tackle this problem, another method, namely the split-window method, was widely used. It is based on the fact that the atmospheric attenuation to the radiances emitted from surface is proportional to the difference between the radiances measured simultaneously at TOA in two adjacent infrared channels (McMilin, 1975). Wan and Dozier (1996) proposed a view-angle dependent split-window method, so called the generalized split-window algorithm, dividing the average emissivity, LST, atmospheric water vapor content and atmospheric lower boundary temperature into several tractable subranges. Wan and Dozier (1996) showed that the generalized split-window algorithm can not only accurately estimate LST, but it is also less sensitive to uncertainties in the emissivities and atmospheric properties. Here, we adopted it in the LST retrieval from the SEVIRI data and the AATSR data.

$$T_s = C + (A_1 + A_2 \frac{1-\varepsilon}{\varepsilon} + A_3 \frac{\Delta\varepsilon}{\varepsilon^2}) \frac{T_i + T_j}{2} + (B_1 + B_2 \frac{1-\varepsilon}{\varepsilon} + B_3 \frac{\Delta\varepsilon}{\varepsilon^2}) \frac{T_i - T_j}{2} \qquad (5.3)$$

with $\varepsilon=(\varepsilon_i+\varepsilon_j)/2$ and $\Delta\varepsilon=\varepsilon_i-\varepsilon_j$. in which T_s is the land surface temperature, T_i and T_j are the brightness temperatures at TOA in channels *i* (~11.0 μm) and j (~12.0 μm), respectively, ε is the averaged emissivity, ε_i and ε_j are the emissivities in channels i and j, respectively, Δε is the emissivity difference, and C, A_1, A_2, A_3, B_1, B_2 and B_3 are unknown coefficients.

Although AATSR has dual-angle view capability, which was originally designed to measure the sea surface temperature to an accuracy of 0.3 K or better for climate change detection, because of the heterogeneity of land surface, the dual angle algorithm developed for the AATSR (Prata, 2002) may be not suitable for land surface (Sòria et al., 2002). Here, Equation (5.3) was also used to derive LST from the AATSR data.

5.2.1 Development of the generalized split-window algorithm

At present, there is no available database of in situ LSTs and radiosonding measurements in coincidence with the SEVIRI measurements. Numerical experiment is the only way to establish the database used in the statistical regression to obtain the coefficients in Equation (5.3). In this work, the six standard model atmospheres prescribed in the radiative transfer code MODTRAN 4.0, namely Tropical, MLS, MLW, SAS, SAW and U.S. 1976 standard, were used.

In order to make the six standard model atmospheres more representative, the profiles were again adjusted like what we did in the cross-calibration chapter. The temperature profiles were adjusted for all the levels below the tropopause. The adjusted amount is ±15 K for the first boundary level, and decreases with the increase of height until to the tropopause. For the levels higher than tropopause, the temperature profiles were kept as the original ones. After the air temperature adjustments, the first boundary temperature T_0 was extended into a range from 242.2 to 314.7 K. The water vapor profiles of the six standard model atmospheres were scaled from 0.1 to 1.5 with a step of 0.1. Those profiles with water vapor content greater than 6.5 g/cm^2 were discarded, because this seldom happens under clear-sky conditions.

In the simulations with MODTRAN 4.0, total eleven view zenith angles (0°, 10°, 20°, 30°, 35°, 40°, 45°, 50°, 55°, 60° and 65°) and six view zenith angles (Nadir and Forward: 0°, 10°, 20°, 25°, 50° and 55°) at a height of 100 km were considered for the SEVIRI and AATSR, respectively. It should be paid attention to the special view geometry of MSG1-SEVIRI. As shown in Figure 2.5, the view

zenith angles of the SEVIRI are a series of concentric circles centered at 0° longitude and 0° latitude. For the tropical region, the view zenith angle goes from 0° (center) to 90° (east or west along the equator). While all the view zenith angles are greater than 17° in the MLS and MLW regions, and are greater than 68° in the SAS and SAW regions. That is to say, for the SEVIRI instrument, at the view zenith angles 0° and 10°, only the Tropical model atmosphere is available, and the model atmospheres SAS and SAW are not included in the region with the view zenith angle less than 68°. Because AATSR is onboard a polar-orbit satellite-ENVISAT, all the six model atmospheres are possible for any view zenith angle.

For each view zenith angle, in order to improve the accuracy of the multiple regression, the atmospheric water vapor content, LST and LSE were divided into several tractable sub-ranges. The water vapor content (W) was divided into six groups with an overlap of 0.5 g/cm^2: 0-1.5, 1.0-2.5, 2.0-3.5, 3.0-4.5, 4.0-5.5 and 5.0-6.5 g/cm^2. The LSEs were also separated into two subgroups: one goes from 0.90 to 0.96 and the other varies from 0.94 to 1.0 with a step of 0.02, and the emissivity difference ($\Delta\varepsilon$) changes from -0.025 to 0.016 with an interval of 0.005. The LST, T_s, ranges from T_0-5 to T_0+20 K with an interval of 5 K, and is divided into 5 groups with an overlap of 5 K: ≤282.5, 277.5-297.5, 292.5-312.5, 307.5-327.5 and ≥322.5 K. Because SEVIRI and AATSR have no atmospheric sounding channels, the first boundary temperature of the atmosphere is not simultaneously available. Thus the first boundary temperature is not involved in the development of the generalized split-window algorithm for both SEVIRI and AATSR.

For a given LST, combined with the atmospheric parameters (τ_i, $L_{atm\downarrow i}$, $L_{atm\uparrow i}$) and LSE, the brightness temperatures in the two split-window channels at TOA can be determined in terms of the radiative transfer theory. Thus, LST is directly connected to the brightness temperatures at TOA through certain conditions. Multiple regressions were carried out on the simulations to obtain the seven unknown coefficients in Equation (5.3) for each view zenith angle and sub-range. In practice, LST is estimated in two steps. Firstly, approximate LSTs are estimated with the coefficients for the whole LST range from 237 K to 335 K, and then more accurate LST is determined in terms of the coefficients for the LST sub-range which the approximate LST is fallen in.

Figure 5.1 shows the coefficients of the generalized split-window algorithm for the SEVIRI and AATSR instruments with LST varying between 292.5 K and 312.5 K, and the W changing between 2.0 and 3.5 g/cm^2. The coefficients A_1, A_2 and A_3 are quiet constant when compared to the coefficients B_1, B_2 and B_3, which means that the LST is much more sensitive to the temperature difference than to the temperature average. As we described previously, only the Tropical model atmosphere was used at the SEVIRI view zenith angles 0° and 10°, the coefficients break between the angles 10° and 20°. In order to make the coefficients continuous as a function of the view zenith angles, the coefficients at the view zenith angles 0° and 10° were adjusted in the multiple regression, keeping the fitting accuracy. After the regressions, the coefficients at other view zenith angles between 0° and 65° can be obtained by a linear interpolation.

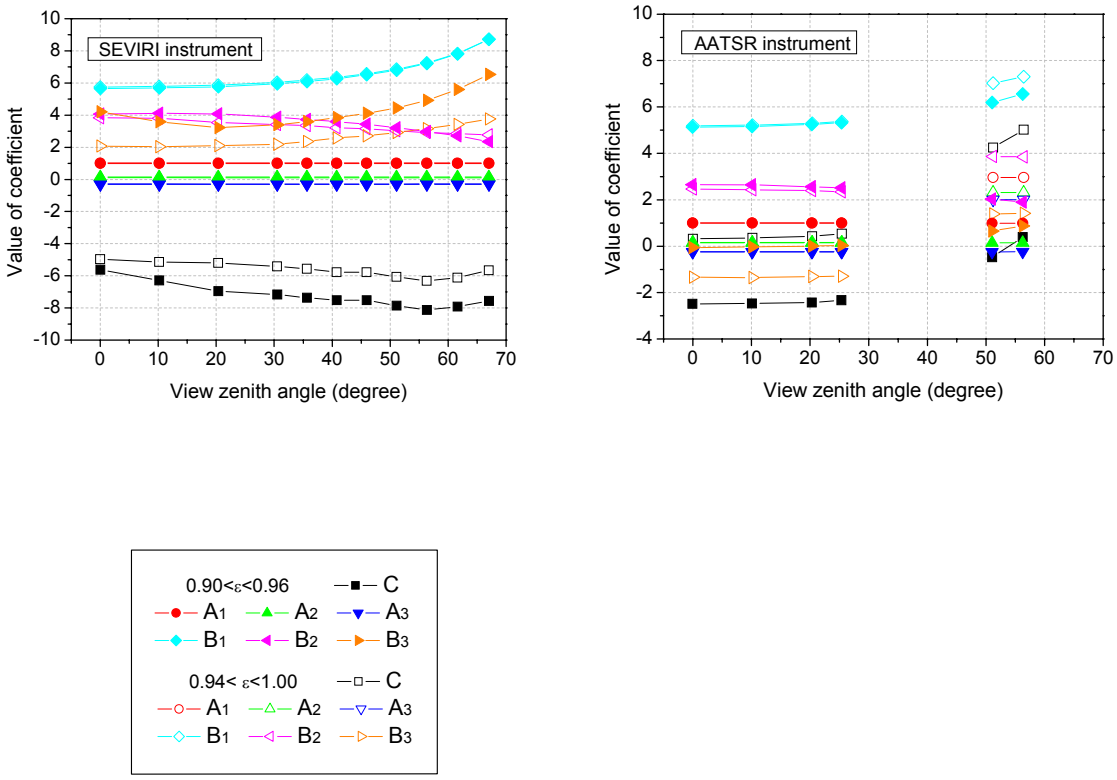

Figure 5.1. Coefficients of the generalized split-window algorithm for the SEVIRI and AATSR instruments
(LST varying between 292.5 K and 312.5 K, and the W changing between 2.0 and 3.5 g/cm^2 for both SEVIRI and AATSR; Here, the view zenith angles refer to the ones at ground level)

Figure 5.2 and Figure 5.3 display, respectively, the RMSEs of the generalized split-window algorithm for the SEVIRI and AATSR instruments with LST ranging between 237 K and 335 K and W varying from 0 to 6.5 g/cm^2. Note that, for the LSTs less than 282.5 K, the maximum W is 2.5 g/cm^2. While for the LSTs between 277.5 K and 297.5 K, the maximum W is 5.5 g/cm^2. The RMSEs increase with the augment of the view zenith angle, atmospheric water vapor content and LST. For the AATSR instrument, when LST is less than 335 K and W varies between 0 and 6.5 g/cm^2, the RMSEs are less than 1.0 K for the Nadir view zenith angles, and are less than 1.6 K for the Forward view zenith angles. The RMSEs for AATSR are also less than 1.0 K for both the nadir and forward views and all LST groups when W is less than 4.5 g/cm^2. While, for the SEVIRI instrument, when W varies between 0 and 6.5 g/cm^2, the RMSEs are less than 1.0 K for the view zenith angles less than 55° and LST less than 312.5 K, or for the view zenith angles less than 45° and all LST groups. The RMSEs for SEVIRI are also less than 1.0 K for all LST groups with the view zenith angles less than 60° and W less than 3.5 g/cm^2. For the high LST groups, the RMSEs increase dramatically when the view zenith angle is greater than 60°, and the maximum reaches 2.3 K.

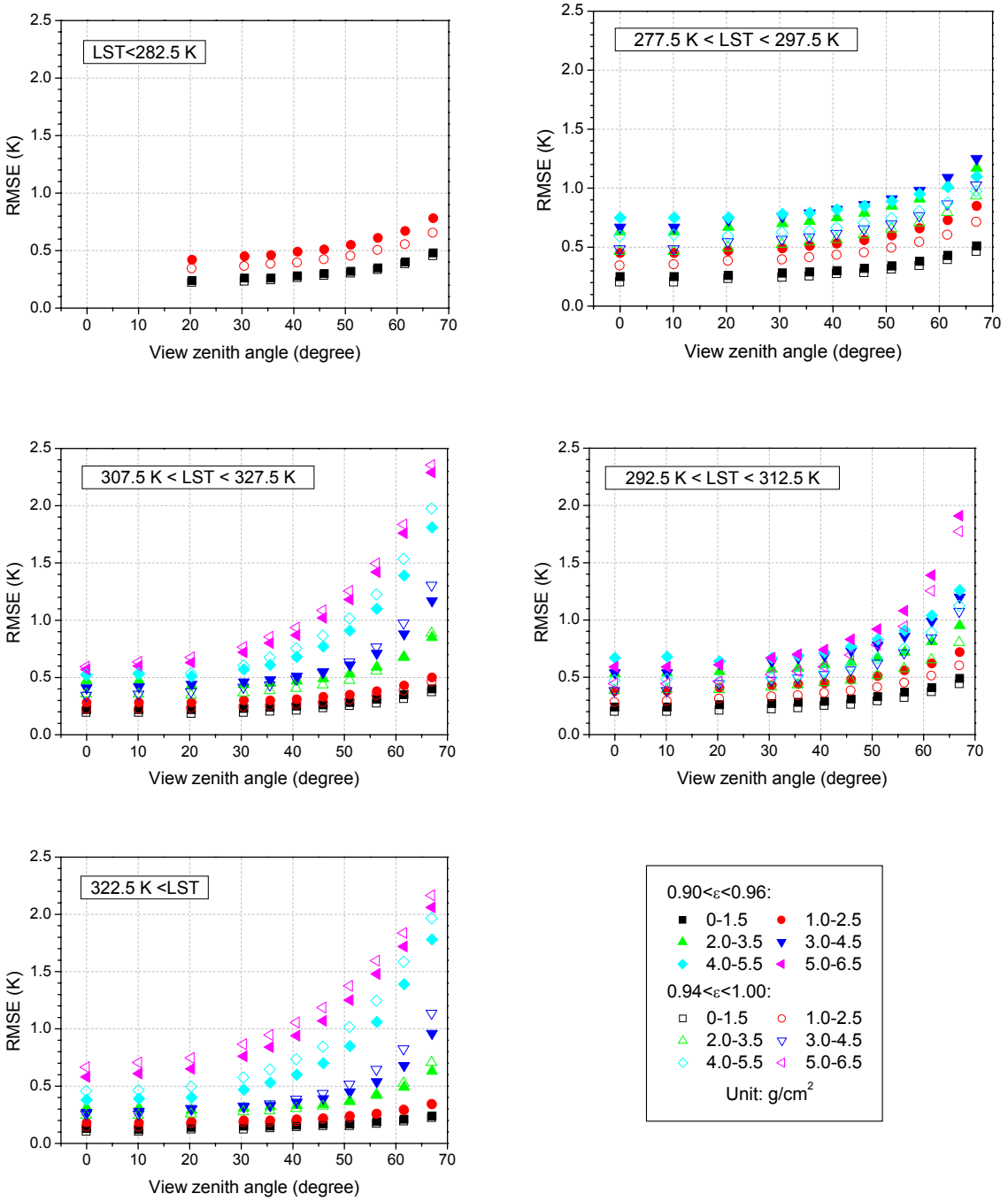

Figure 5.2. RMSEs of the generalized split-window algorithm for the SEVIRI instrument (LST ranging between 237 K and 335 K, and the atmospheric water vapor content varying between 0 and 6.5 g/cm^2; the view zenith angles refer to the ones at ground level; RMSE is the acronym of Root Mean Square Error)

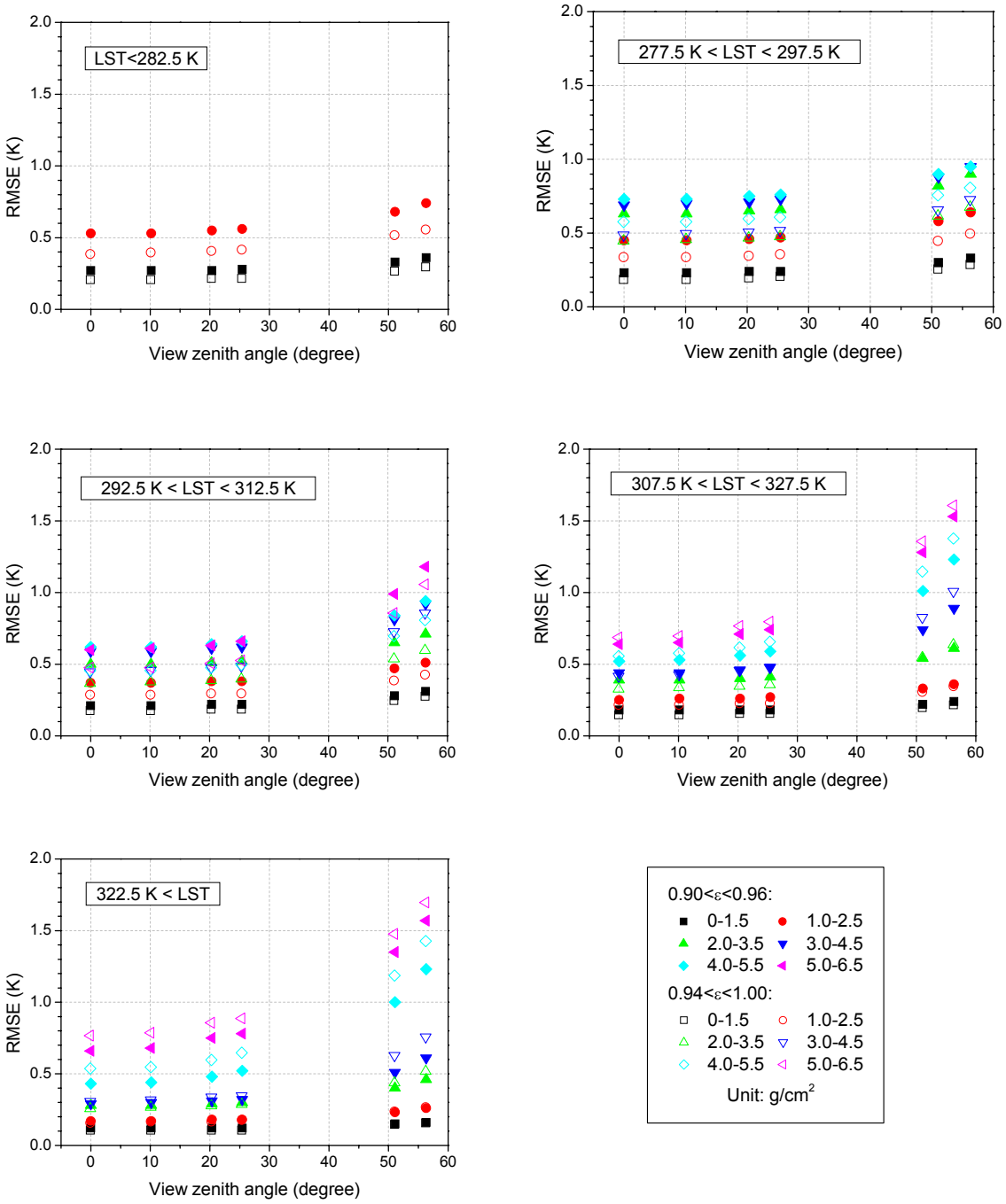

Figure 5.3. Same as the ones in Figure 5.2, but for the AATSR instrument

As Wan and Dozier (1996) indicated, the errors of LST retrieval by the generalized split-window algorithm come from the uncertainties of LSEs, atmospheric properties and the instrument noises. According to Equation (5.3), the factors on the emissivity terms $(1-\varepsilon)/\varepsilon$ and $\Delta\varepsilon/\varepsilon^2$ are, respectively, given in the following Equations (5.4) and (5.5)

$$\alpha = A_2 \frac{T_i + T_j}{2} + B_2 \frac{T_i - T_j}{2} \tag{5.4}$$

$$\beta = A_3 \frac{T_i + T_j}{2} + B_3 \frac{T_i - T_j}{2} \tag{5.5}$$

Assuming that T_i=308.9 K, T_j=306.1 K, ε=0.965, Δε=0.005, 1.0≤W≤2.5, and θ_v=45°, we obtained that α=57.834 and β=-102.137 according to the regression results for the SEVIRI instrument. If we expect that the uncertainties of (1-ε)/ε and $\Delta\varepsilon/\varepsilon^2$ are around 0.006 for well known land surfaces, the LST errors due to the uncertainties of (1-ε)/ε and $\Delta\varepsilon/\varepsilon^2$ are 0.35 K and -0.61 K, respectively, and the total error is -0.26 K. If we change the W (2.0≤W≤3.5) and keep other conditions, the LST error is -0.39 K due to the wrong sub-range selection of the water vapor content. The short term radiometric errors are 0.11 K and 0.15 K at 300 K for SEVIRI channels 9 and 10, respectively, and the LST error introduced by the radiometric performance of MSG1-SEVIRI is 0.84 K at worst.

5.2.2 Emissivities in the two split-window channels

The retrieval of LST by the generalized split-window algorithm requires LSEs as input. The directional emissvities in SEVIRI channels 9 and 10 were estimated by the method presented by Jiang et al. (2006). However, this method is difficult to apply to the retrievals of the emissivities in AATSR channels IR11 and IR12, because the channel IR3.7 is saturated around 311 K (That is to say, there is no data in AATSR IR3.7 channel over large areas in daytime). Here, the emissivities in the AATSR channels IR11 and IR12 were inferred from the emissivities in SEVIRI channels 4, 9 and 10 in terms of the RossThick-LiSparse-R model, the TISI concept and a spectral library. Firstly, the directional emissivities in SEVIRI channel 4 were modeled to the AATSR view zenith angles in terms of the RossThick-LiSparse-R model (Equation (4.23)). Secondly, based on the angle-independent properties of the TISI (Petitcolin and Vermote, 2002), the emissivities in SEVIRI channels 9 and 10 at the AATSR view zenith angles were calculated. Ultimately, the emissivities in AATSR channels IR11 and IR12 at AATSR view zenith angles were obtained by eliminating the spectral differences between the channels of SEVIRI and AATSR.

In this work, the emissivities extracted from the ASTER Spectral Library were used to build the statistical relationship between SEVIRI and AATSR channels. The emissivities in the two split-window channels of SEVIRI (ε_9 and ε_{10}) and AATSR (ε_{IR11} and ε_{IR12}) were obtained through the integrals of the spectral emissivity with the channel responses over the spectral channels. A linear regression analysis was performed to build a relationship between them. Figure 5.4 shows the emissivities and the linear regression results. The emissivities in AATSR channels IR11 and IR12 are, respectively, related to the emissivities in SEVIRI channels 9 and 10 by

$$\varepsilon_{IR11} = -0.011 + 1.0216\varepsilon_9 \tag{5.6}$$

$$\varepsilon_{IR12} = -0.008 + 1.0092\varepsilon_{10} \tag{5.7}$$

According to Equations (5.6) and (5.7), when the emissivities in SEVIRI channels 9 and 10 go from 0.85 to 1.00, the emissivity difference (ε_{IR11}-ε_9 or ε_{IR12}-ε_{10}) varies from 0.007 to 0.011 for AATSR channel IR11, and changes from 0.000 to 0.001 for AATSR channel IR12. The results reveal that the spectral differences between SEVIRI channel 10 and AATSR channel IR12 can be ignored.

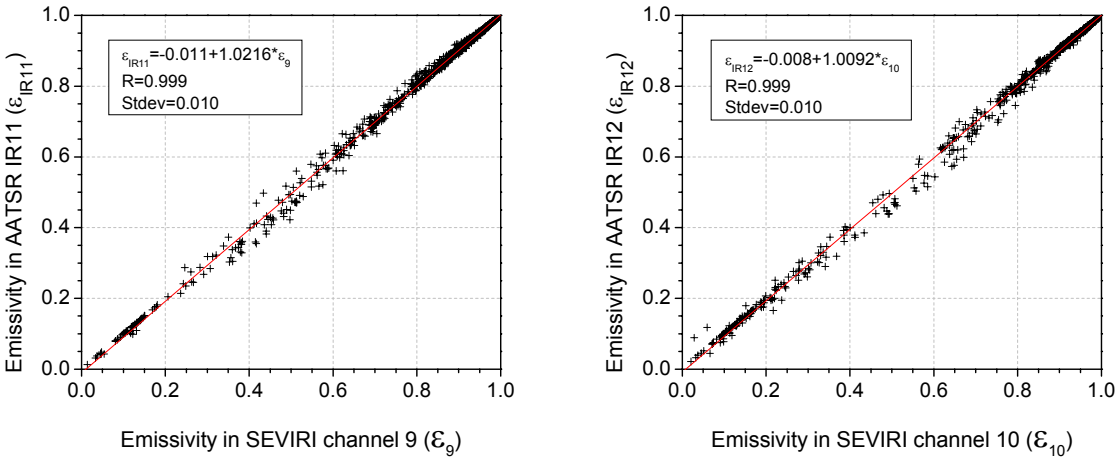

Figure 5.4. Emissivities in the split-window channels of SEVIRI and AATSR and the statistical relationships between them in terms of the ASTER Spectral Library

5.2.3 Retrieval of atmospheric water vapor content

According to the results of Li et al. (2003), the atmospheric water vapor content W is linearly related to the transmittance ratio of the two split-window channels.

$$W = A + B * \tau_j / \tau_i \tag{5.8}$$

where A and B are unknown coefficients. τ_i and τ_j are the atmospheric transmittances in the two split-window channels centered at ~11.0 μm and ~12.0 μm, respectively.

The transmittance ratio in Equation (5.8) can be expressed as a function of the brightness temperatures and the emissivities in the two split-window channels. Hereafter, we recalled the mathematical steps.

Under the condition that the atmosphere is unchanged over the neighboring pixels, but where the surface temperature and surface emissivity change, the variation of radiance measured from space, due to the change of surface temperature ($\Delta T_s=T_{s1}-T_{s0}$) and of surface emissivity ($\Delta\varepsilon_i=\varepsilon_{i1}-\varepsilon_{i0}$), can be expressed from Equations (2.7) and (2.8) as

$$\Delta L_i = L_i(T_{i1}) - L_i(T_{i0}) = \varepsilon_{i0}\left[L_i(T_{s1}) - L_i(T_{s0})\right]\tau_i + \Delta\varepsilon_i\left[L_i(T_{s1}) - L_{atm\downarrow i}\right]\tau_i \tag{5.9}$$

where T_{i1} and T_{i0} are the brightness temperatures for the two conditions.

If we expand the radiance $L_i(T)$ to a first order of approximation about its mean temperature T_{mean}, in the form

$$L_i(T) = L_i(T_{mean}) + (T - T_{mean})\frac{dL_i(T_{mean})}{dT} \tag{5.10}$$

then Equation (5.9) becomes

$$T_{i1} - T_{i0} - \Delta\varepsilon_i F_i \tau_i = \varepsilon_{i0}(T_{s1} - T_{s0})\tau_i \tag{5.11}$$

with $F_i = \dfrac{L_i(T_{s1}) - L_{atm\downarrow i}}{dL_i(T_{mean})/dT}$.

Similarly, for the measurements in channel j, we have

$$T_{j1} - T_{j0} - \Delta\varepsilon_j F_j \tau_j = \varepsilon_{j0}(T_{s1} - T_{s0})\tau_j \tag{5.12}$$

Dividing (5.12) by (5.11) gives

$$(T_{i1} - T_{i0})I_{ji} = (T_{j1} - T_{j0}) + \tau_j(\frac{\varepsilon_{j0}}{\varepsilon_{i0}}\Delta\varepsilon_i F_i - \Delta\varepsilon_j F_j) \tag{5.13}$$

where $I_{ji}=\tau_j\varepsilon_{j0}/\ \tau_i\varepsilon_{i0}$.

Equation (5.13) is similar to (A.8) of Klesspies and McMillin if the $\Delta\varepsilon$ term is neglected. Although it is clear that this term is zero when the neighboring pixels are homogeneous in emissivity, i.e., $\Delta\varepsilon_i=0$ and $\Delta\varepsilon_j=0$, it is not the case for adjacent pixels which represent different surface (crop, sand, sea, etc.). For most surfaces, it is reasonable to consider that the second term of the right-hand side of (5.13) is negligible in comparison with the first one, and the emissivity ratio is close to unity (Sobrino et al., 1999; Li et al, 2003). If the assumptions made above hold, for instance over N neighboring pixels by least square analysis of (5.13), the transmittance ratio, τ_j/τ_i, can be approximately expressed as

$$\frac{\tau_j}{\tau_i} \cong I_{ji} = \frac{\sum_{k=1}^{N}(T_{ik} - T_{i0})(T_{jk} - T_{j0})}{\sum_{k=1}^{N}(T_{ik} - T_{i0})^2} \tag{5.14}$$

If R denotes the linear correlation coefficient of the two measurements T_i and T_j, the square of this linear correlation coefficient, R^2, is given by

$$R^2 = \frac{\left[\sum_{k=1}^{N}(T_{i,k} - T_{i0})(T_{j,k} - T_{j0})\right]^2}{\sum_{k=1}^{N}(T_{i,k} - T_{i0})^2 \sum_{k=1}^{N}(T_{j,k} - T_{j0})^2} = I_{ji}I_{ij} \tag{5.15}$$

According to Equation (5.13), R^2 is theoretically equal to 1.0.

For each view angle, a pair of coefficients A and B can be obtained by the linear least square regression based on the results obtained by the radiative transfer modeling method described in the section 5.2.1. Figure 5.5 displays the relationship between the atmospheric water vapor content and the transmittance ratio for SEVIRI and AATSR. The water vapor content decreases with the increment of the transmittance ratio, and the linear fits move anticlockwise when view zenith angle becomes larger. It is interesting to note that the coefficients A and B are proportional or inversely proportional to $\cos(\theta_v)$ with high correlation (Figure 5.6). We obtained the following two formulae

For the SEVIRI instrument:

$$W = (4.15 + 10.495 * \cos(\theta_v)) - (3.78 + 10.468 * \cos(\theta_v)) * I_{ji} \quad (5.16)$$

For the AATSR instrument:

$$W = (4.47 + 9.093 * \cos(\theta_v)) - (4.41 + 9.052 * \cos(\theta_v)) * I_{ji} \quad (5.17)$$

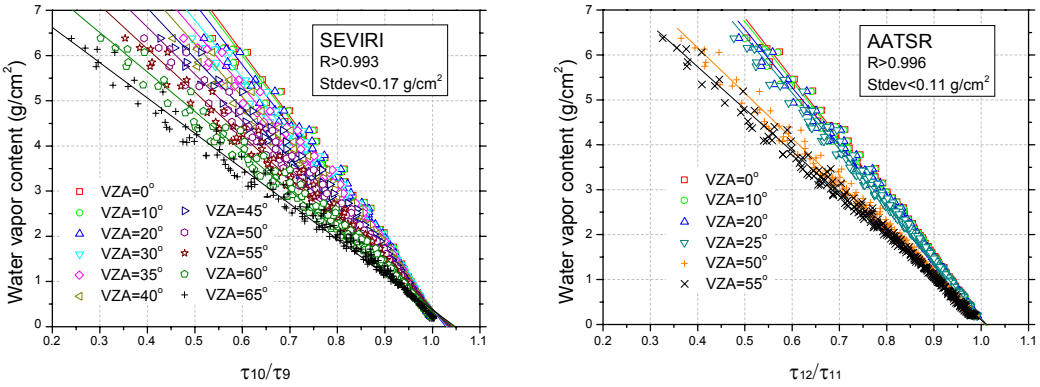

Figure 5.5. Water vapor content versus transmittance ratio at different view zenith angles for SEVIRI and AATSR
(Color lines are the linear fit results; R represents correlation coefficient; Stdev represents standard deviation)

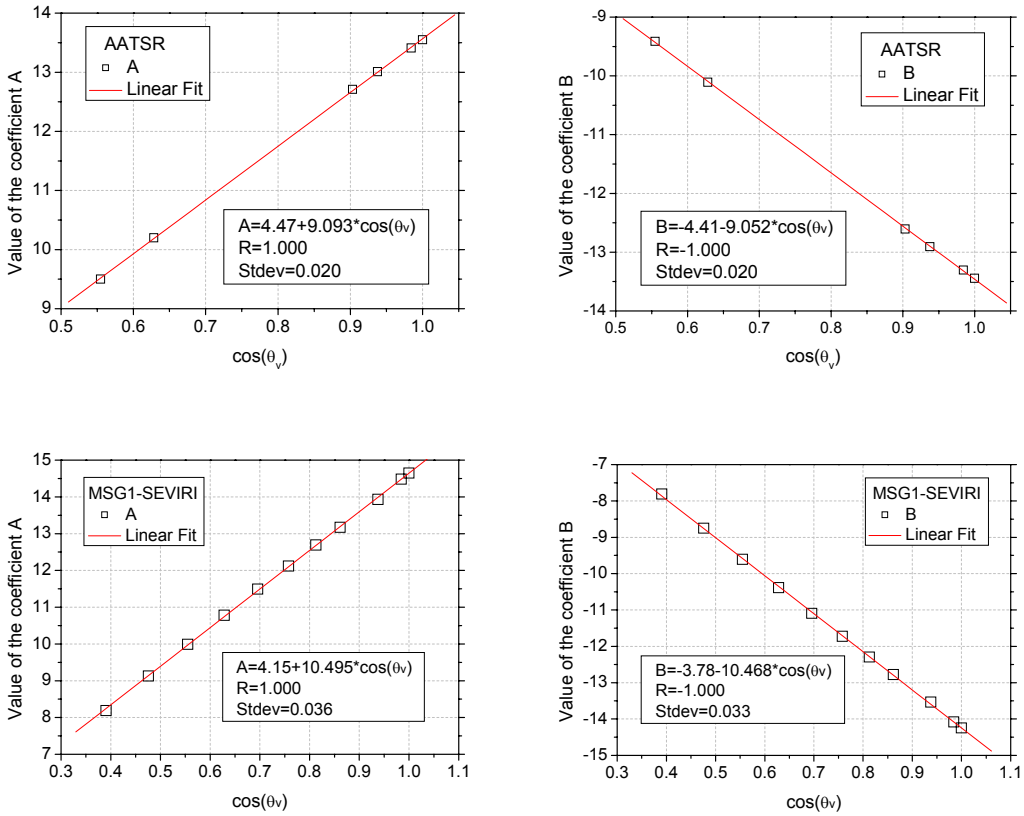

Figure 5.6. Angular dependence of the fitting coefficients A and B in Equation (5.8) for the AATSR (top) and SEVIRI (bottom) instruments

5.3 DTC model and time normalization of LSTs

Strictly speaking, the DTC model describes the temperature variation of land surface, NOT the brightness temperatures at TOA. One of the DTC model's abilities is to interpolate LST at any given time. As we know, in a satellite image, the acquired UTC times of all the pixels are almost the same, but the local solar times are much different from each other. For an instance, in a full-disc image acquired by MSG1-SEVIRI, the maximum local solar time difference between the east and the west along the equator is ~8 hours. For the sensors onboard the polar-orbit satellites, such as MODIS, AVHRR and AATSR, in addition to the local solar time differences within a scene, they are also suffering from the orbital drift (Privette et al., 1995; Arthur et al., 2002). The local solar time problem prevents the satellite data being used in climate change research (McGregor and Gorman, 1994; Jin and Dickinson, 2002; Jin and Treadon, 2003). The DTC model has the potential to handle this problem. When the LST variations of all pixels are modeled by the DTC model, the LST maps with all pixels in one local solar time can be easily generated. Here, we called it the time normalization of LSTs.

5.4 Study area and data processing

The study area covers the land surfaces with longitude going from 20W to 60E and latitude ranging from 0 to 60N. Because of the shortage of the AATSR data on hand, the LST retrieval from the AATSR data (Nadir and Forward) was limited over the Iberian Peninsula area.

In order to demonstrate the DTCs and the time normalization of LSTs by the DTC model, the four locations in Table 4.8 over the large study area were again used as examples.

In the LST retrievals, the input data include the brightness temperatures at TOA (MSG Level 1.5 data and AATSR L1B data), the MSG cloud masks, the directional emissivities in the two split-window channels, view zenith angles, atmospheric water vapor content, and land surface boundary data. For the single channel method, the atmospheric parameters were also required.

The extraction and processing of the MSG Level 1.5 product and the MSG cloud masks have been detailed in the above chapters. The directional emissivities used in the LST retrievals are the median composite maps from July 14 to July 19, 2004 (Figure 4.27) and from July 10 to July 14, 2005 (Figure 4.28). The atmospheric water vapor contents were retrieved from the data in SEVIRI channels 9 and 10, and from the data in AATSR channels IR11 and IR12 by the method developed in the section 5.2.3, and only the water vapor contents with R^2 greater than 0.95 were kept. Because of the algorithm's limitation, the water vapor content may not be successfully derived for a pixel (R^2<0.95 or cloud contaminated). To deal with this problem, the time-nearest and space-neighboring water vapor content extracted from the ECMWF data was used.

The processing of the AATSR data is relatively complicated. The longitude, latitude and view zenith angle of each pixel were linearly interpolated from the tie points in sizes of 17×23, and then corrections were added to the interpolated coordinates to obtain the final longitude and latitude of the Nadir and Forward images. After the interpolation, the images, coordinates and view zenith angles were all in sizes of 512×512. The emissivities in AATSR channels IR11 and IR12 were inferred from the emissivities in SEVIRI channels 4, 9 and 10 in terms of the TISI concept, the RossThick-LiSparse-R model (Equation (4.14)) and the emissivity relationships (Equations (5.6) and (5.7)). All the AATSR data were pixel aggregated into the SEVIRI coordinate system.

LSTs were estimated by both the single channel method and the generalized split-window algorithm for the land surface pixels indicated clear sky. It should be noted that, in the single channel method, LSTs were retrieved from the data in SEVIRI channel 9 only at the four UTC times when the ECMWF data are available. While the time-nearest and space-neighboring ECMWF data were used in the LST retrieval from the data in AATSR channel IR11.

LST maps over the study area from July 14, 2004 to July 19, 2004, and from July 10, 2005 to July 14, 2005 were generated from the SEVIRI data, and only four LST maps (Nadir and Forward & daytime and nighttime) on July 14, 2004 were produced from the AATSR data. The DTC model was then applied to the descriptions of the SEVIRI LSTs, and LST maps at local solar times 6:00, 12:00, 18:00 and 24:00 were generated from the modeling results.

5.5 Results and analysis

The water vapor contents over the study area were estimated from the SEVIRI data and the AATSR data (Nadir and Forward) by the methods developed in the section 5.2.3. We used the radiosounding data, which were measured by a balloon launched at 10:45 on July 14, 2004 at the Barrax site, Spain (2.07W, 39.03N), to validate the retrievals of the water vapor contents. Table 5.1 gives the water vapor contents estimated from the radiosounding data, the SEVIRI data, and the AATSR Nadir and Forward data at 10:45UTC on July 14, 2004 at the Barrax site, Spain. The results show that the water vapor contents estimated from the SEVIRI data, the AATSR Nadir and Forward data are, respectively, 0.15, 0.48 and 0.59 g/cm^2 higher than the radiosounding one. For atmospheric water vapor content retrieval, the results are quiet consistent.

Table 5.1. Estimated water vapor contents at 10:45UTC on July 14, 2004 at the Barrax site, Spain

	Radiosounding	SEVIRI	AATSR Nadir	AATSR Forward
W* (g/cm^2)	1.60	1.75	2.08	2.19

* W stands for Water vapor content

In order to demonstrate the LSTs estimated from the SEVIRI data and the AATSR data by the single channel method and the generalized split-window algorithm, we took the results on July 14, 2004 as examples. Figure 5.7 shows the LSTs estimated from the SEVIRI data by the generalized split-window algorithm at four UTC times 5:57, 11:57, 17:57 and 23:57 on July 14, 2004. The dynamic range of the LSTs is very large and is from 280 K to 340 K depending on the locations and the observation time. Generally speaking, the daytime LSTs are higher than the nighttime LSTs because of the contribution of solar irradiance, and the LSTs over bare area (e.g., desert area) are higher than the LSTs over the vegetated area in daytime. Not that, at the UTC time 5:57, the LST at the eastern region is higher than the LST at the western region, while the opposite is observed at the UTC time 18:57. This phenomenon happens because the intensity and duration of solar irradiance are different between the east and the west at the same UTC time.

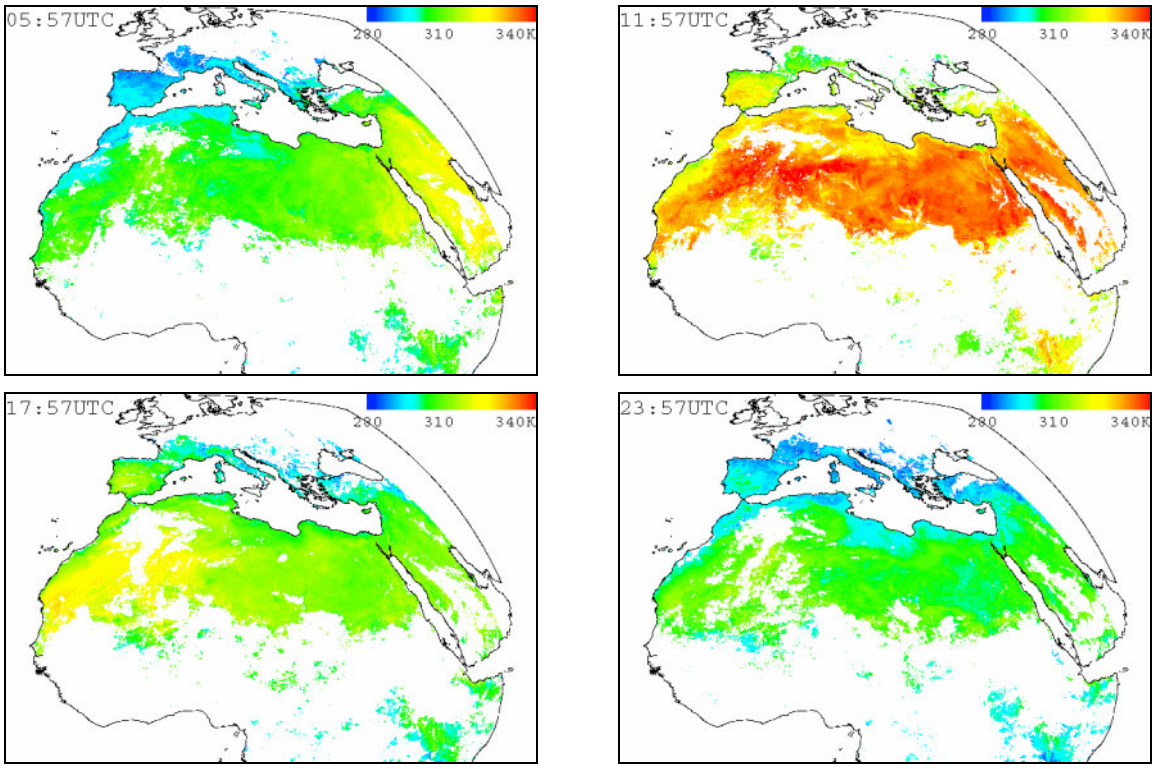

Figure 5.7. Maps of LSTs estimated from the SEVIRI data using the generalized split-window algorithm at four UTC times: 5:57, 11:57, 17:57 and 23:57 on July 14, 2004

LSTs at the four UTC times were also estimated by the single channel method from the data in SEVIRI channel 9. In order to carry out the comparisons, two parameters, the difference average (mean) and the Root Mean Square Error (RMSE) were introduced

$$Mean = \frac{1}{N}\sum_{i=1}^{N}(T_{i,1} - T_{i,2}) \tag{5.18}$$

$$RMSE = \sqrt{\frac{1}{N}\sum_{i=1}^{N}(T_{i,1} - T_{i,2})^2} \tag{5.19}$$

where $T_{i,1}$ and $T_{i,2}$ are the LSTs at pixel i estimated by different methods or from different data, and N is the total number of pixels. In this chapter, $T_{i,1}$ is the LST estimated by the generalized split-window algorithm, whereas $T_{i,2}$ is the LST estimated by the single channel method.

Table 5.2. Averages and RMSEs of the differences between the SEVIRI LSTs estimated by the two methods over the study area at UTC times 5:57, 11:57, 17:57 and 23:57 on July 14, 2004

(Unit: Kelvin)	05:57		11:57		17:57		23:57	
	Mean	RMSE	Mean	RMSE	Mean	RMSE	Mean	RMSE
July 14, 2004	0.76	2.11	-0.49	2.33	0.46	1.93	1.14	2.18

Table 5.2 gives the averages and RMSEs of the differences between the SEVIRI LSTs estimated by the generalized split-window algorithm and the single channel method over the study area at the UTC times 5:57, 11:57, 17:57 and 23:57 on July 14, 2004. The difference averages (mean) are ~1.0 K, and the RMSEs are ~2.0 K. We found from the LST maps that most of the pixels with large temperature differences are located at the transitional region from the clear sky area to the cloud contaminated area, and at the same area (e.g., Iberian Peninsula), the temperature differences vary with times.

Figure 5.8 shows the histogram of the temperature differences between the SEVIRI LSTs estimated by the generalized split-window algorithm and by the single channel method on July 14, 2004. The temperature differences obey the Gauss distribution function. The average temperature difference is ~1.0 K. Within a radius of 2 K around the histogram peak, there are 81.9% of pixels included.

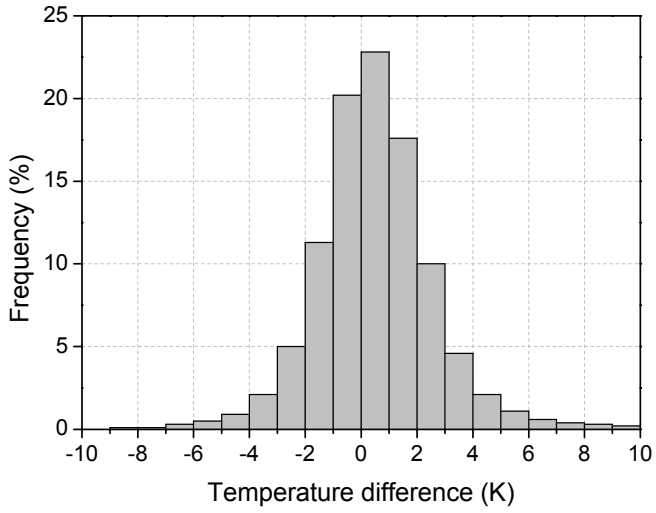

Figure 5.8. Histograms of the temperature differences between the LSTs estimated from the SEVIRI data by the generalized split-window algorithm and by the single channel method on July 14 of 2004

Figure 5.9 displays the LSTs estimated from the AATSR Nadir and Forward images by the generalized split-window algorithm and the differences between the AATSR Nadir LSTs and AATSR Forward LSTs over the Iberian Peninsula area at UTC times 10:31 and 21:46 on July 14, 2004. The AATSR LSTs range between 295 K and 325 K in the daytime (10:31UTC), and go from 285 K to 305 K at night (21:46UTC). It should be noted that, the AATSR Nadir LSTs are averagely 3.56 K warmer than the AATSR Forward LSTs in the daytime, while they are nearly equal at night. This phenomenon can be explained by the view zenith angle and the spatial structures of land surfaces. Because of the spatial structures of the vegetated Iberian Peninsula area, the AATSR Nadir images contain more information of bare area than the AATSR Forward images do, and in daytime under clear sky conditions, the temperatures of bare area are usually higher than the temperatures of vegetation. At night, temperatures of both bare area and vegetation trend to be homogenous, and the impacts of view zenith angle and the spatial structures of land surface are minimized. From the results, we may make a

conclusion that the dual-angle algorithm developed for the AATSR instrument (Prata, 2002) can not be used for daytime LST retrieval, but it may be suitable for nighttime LST retrieval with accuracy higher than 1.0 K.

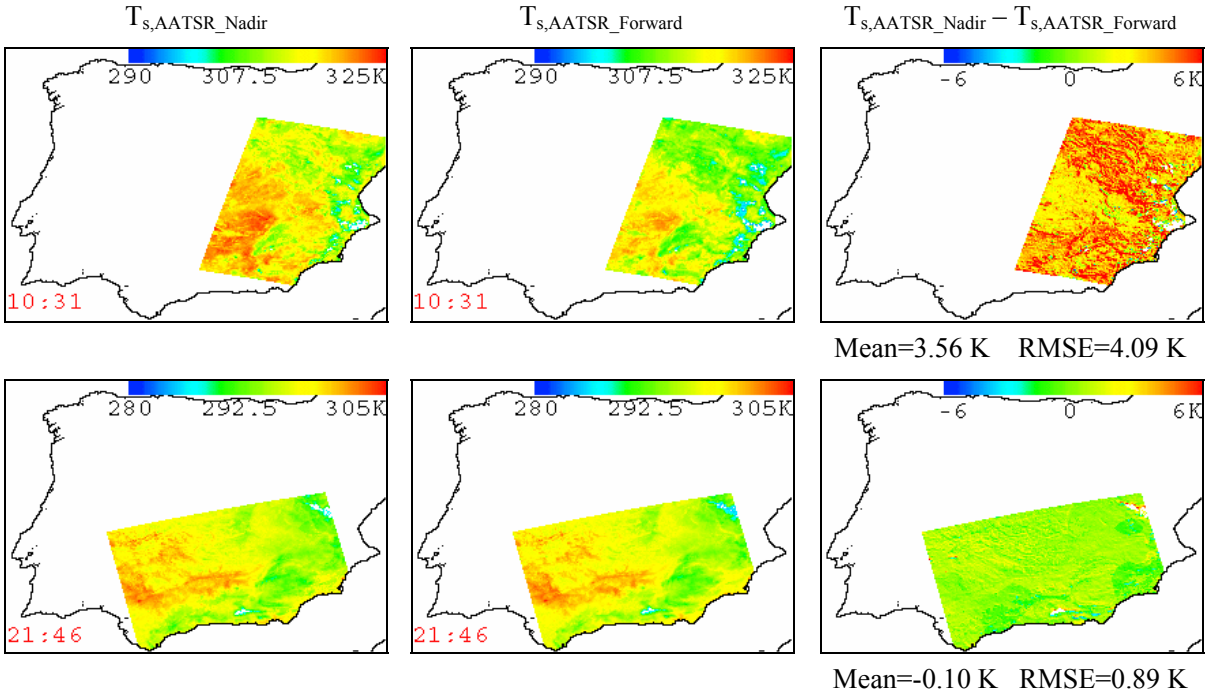

Figure 5.9 LSTs estimated from the AATSR Nadir and Forward images by the generalized split-window algorithm and the temperature differences over the Iberian Peninsula area at UTC times 10:31 and 21:46 on July 14, 2004

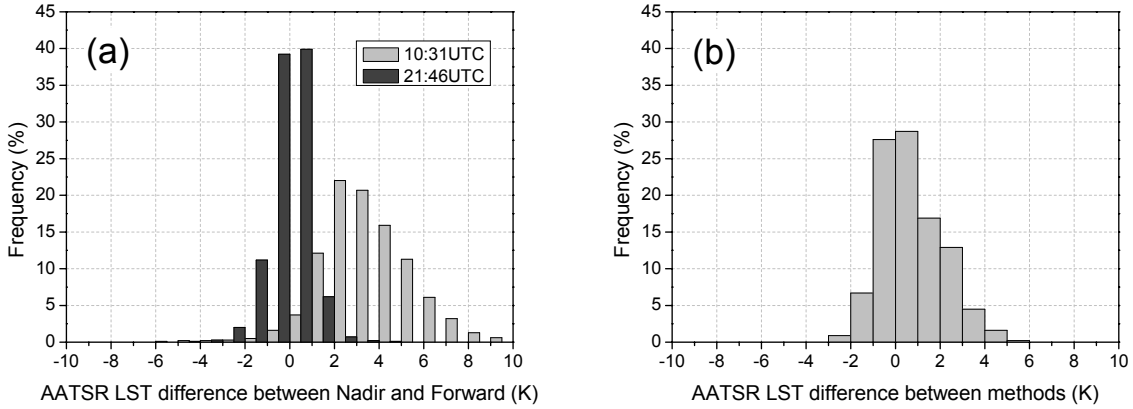

Figure 5.10. Histogram of the differences between the AATSR Nadir LSTs and the AATSR Forward LSTs estimated by the generalized split-window algorithm at UTC times 10:31 and 21:46 (a), and histogram of the differences between the AATSR LSTs estimated by the single channel method and the generalized split-window method (b) on July 14, 2004

Figure 5.10 shows the histogram of the differences between the AATSR Nadir LSTs and the AATSR Forward LSTs estimated by the generalized split-window algorithm at UTC times 10:31 and 21:46, and the histogram of the differences between the AATSR LSTs estimated by the single channel method and the generalized split-window method on July 14, 2004. Figure 5.10a is consistent with what shown in Figure 5.9, and within a radius of 2 K around the histogram peak, there are, respectively, 82.0% and 96.5% of pixels in the daytime and at night. In Figure 5.10b, within a radius of 2 K around the histogram peak, there are 92.8% of pixels included, which reveals that the AATSR LSTs estimated by the two methods are also consistent.

The reasons leading to the temperature differences are quiet complicated, such as the emissivities, the emissivity difference between the two split-window channels, the cloud contamination and the ECMWF data, however the LSTs estimated by the generalized split-window algorithm and the single channel method are basically consistent. The LST retrievals are mainly limited by clouds and the absence of the directional emissivities.

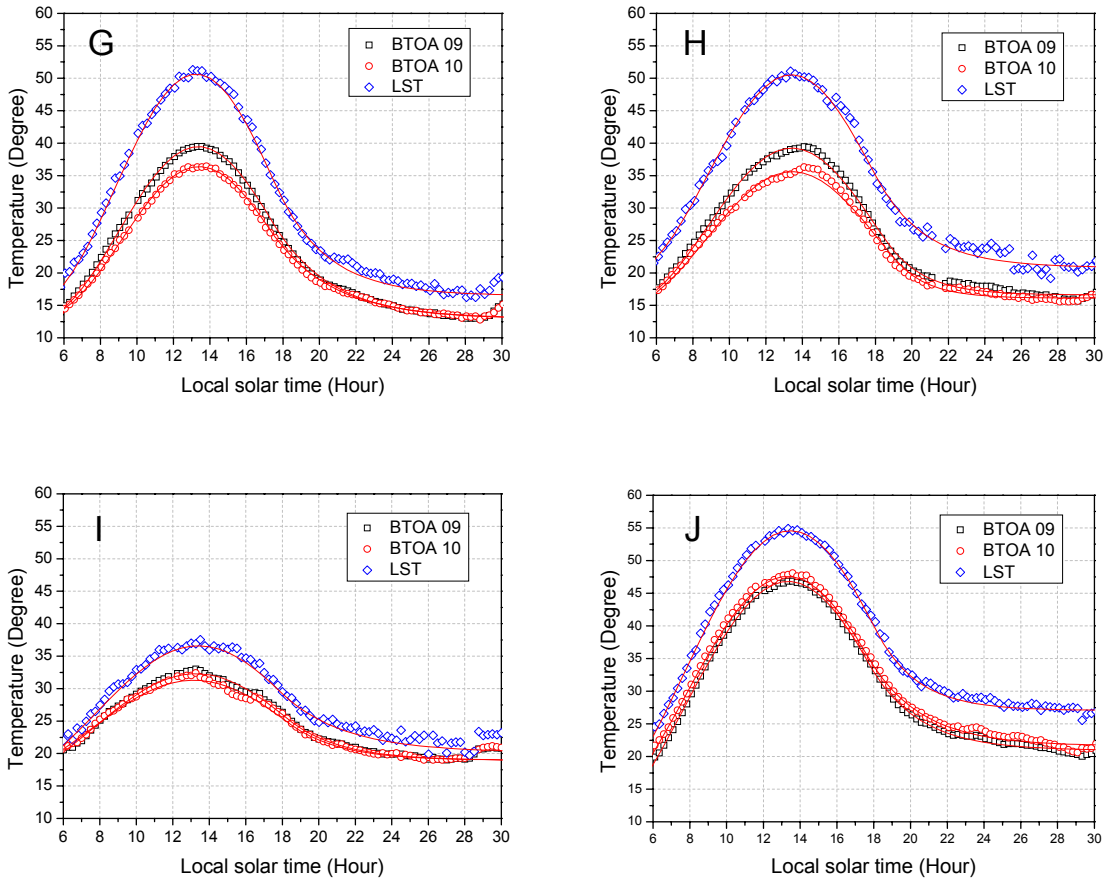

Figure 5.11. DTCs of the Brightness Temperatures at TOA (BTOA) in SEVIRI channels 9 and 10, and DTCs of the corresponding SEVIRI LSTs at the four specific locations on July 14, 2004 (Red curves are the modeled results)

The SEVIRI LSTs were estimated by the generalized split-window algorithm every 15 min over the study area, and the DTC model was applied to the descriptions of the DTCs of all pixels. Figure 5.11 shows the DTCs of the brightness temperatures at TOA in SEVIRI channels 9 and 10, and the DTCs of the corresponding SEVIRI LSTs at the four specific locations on July 14, 2004. The SEVIRI

LSTs are higher than the brightness temperatures, and the difference between them becomes larger with the rise of the temperatures and reaches the maximum around 13:30 (local solar time). The results show that the DTC model also works well in the LST modeling. It is interesting that, at the location J, the brightness temperatures in SEVIRI channel 10 are slightly higher than the ones in SEVIRI channel 9. This may due to the inverse atmosphere, in which the upper air temperature is warmer than the lower air temperature.

Table 5.3 gives the fitting parameters of the DTC model at the four specific locations for both LSTs and the brightness temperatures at TOA in SEVIRI channels 9 and 10. In contrast with the parameters β, td, α and t_s, the parameters a and b change in a larger range. In the atmospheric correction of the data in SEVIRI channels 9 and 10 by the DTC model, it was assumed that the parameters β and t_s do not change between the DTCs at TOA and at ground level. As shown in Equation (2.8), LST is connected to the brightness temperature at ground level by LSE in a TIR channel, and the fitting results of LSTs can therefore be approximately considered as the fitting results of the brightness temperature at ground level. From the results listed in Table 5.3, it can be concluded that the assumptions are quiet reasonable. It seems better to assume that the parameters td and t_s do not change between the DTCs at TOA and at ground level, but abnormal results will be produced for the desert area where LST is very high in daytime, because of the observation time of the ECMWF data.

Table 5.3. Parameters of the DTC model at the four specific locations in Table 4.8 on July 14, 2004

No.		a	b	β	td	α	t_s
G	T_s	33.07	17.57	0.354	13.23	-0.371	17.63
	T_9	25.64	13.31	0.356	13.31	-0.320	17.40
	T_{10}	24.40	11.49	0.366	13.36	-0.304	17.24
H	T_s	34.92	15.47	0.343	13.42	-0.381	18.05
	T_9	27.27	12.02	0.340	13.40	-0.501	18.64
	T_{10}	25.23	10.39	0.333	13.42	-0.566	19.09
I	T_s	26.16	10.56	0.276	13.41	-0.292	17.85
	T_9	23.96	8.39	0.279	13.23	-0.355	18.21
	T_{10}	23.76	7.59	0.277	13.13	-0.369	18.37
J	T_s	30.27	24.22	0.254	13.44	-0.451	18.05
	T_9	27.81	19.01	0.280	13.35	-0.377	17.71
	T_{10}	29.24	18.35	0.282	13.30	-0.352	17.62

T_s stands for LST, and T_i represents the brightness temperature at TOA in SEVIRI channel i (i=9 or 10).

Figure 5.12 displays the SEVIRI LSTs normalized to local solar times 6:00, 12:00, 18:00 and 24:00 by the DTC model. Compared to Figure 5.7, the differences of the time normalized LSTs between the east and the west are not so obvious, especially at the local solar times 6:00 and 18:00, and LSTs decrease from the south to the north as a whole.

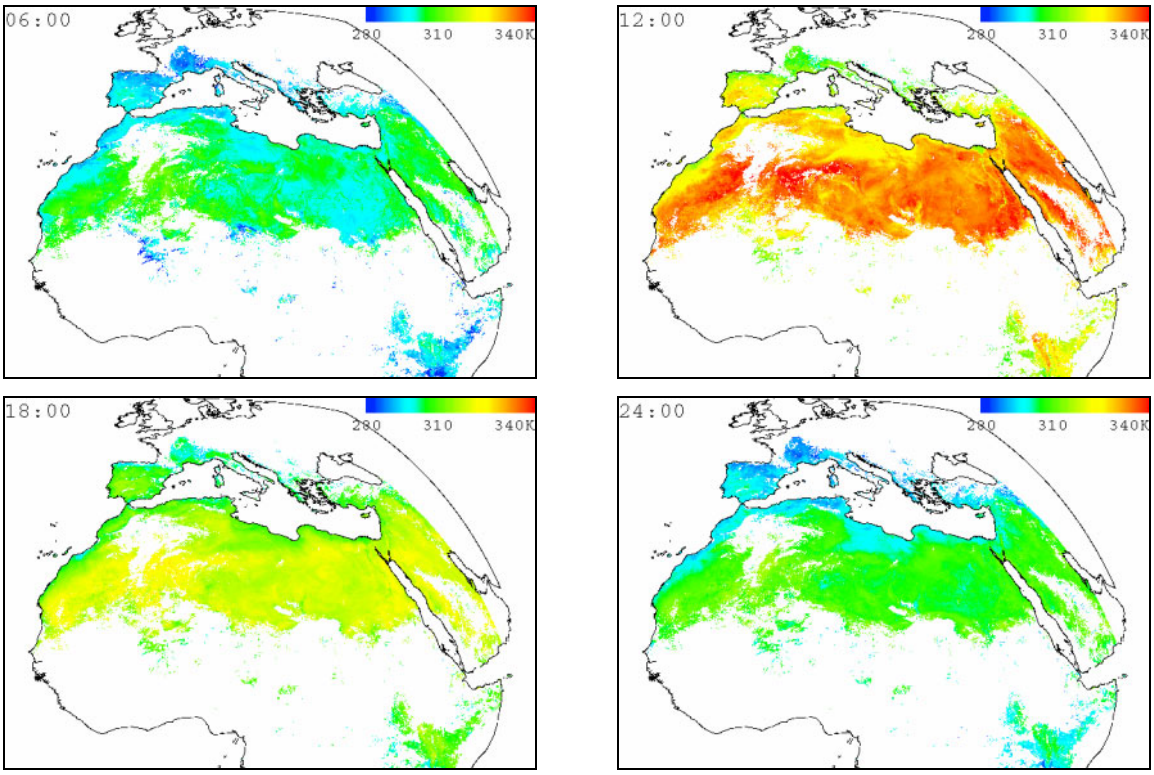

Figure 5.12. Maps of the SEVIRI LSTs normalized to local solar times 6:00, 12:00, 18:00 and 24:00 by the DTC model

5.6 Summary and Conclusions

This chapter addresses the LST retrievals from the SEVIRI data and AATSR data (Nadir and Forward) by the single channel method and the generalized split-window algorithm.

The single channel method is a simple inversion of the radiative transfer Equations (2.7) and (2.8).

The generalized split-window algorithm, which was proposed by Wan and Dozier (1996), was developed for both SEVIRI and AATSR instruments using the six standard model atmospheres prescribed in MODTRAN 4.0: Tropical, Mid-latitude Summer (MLS), Mid-latitude Winter (MLW), Sub-arctic Summer (SAS), Sub-arctic Winter (SAW) and U. S. 1976 Standard. Considering the special view geometry of MSG1-SEVIRI, only the Tropical model atmosphere is available for the SEVIRI view zenith angle less than 17°, and the SAS and SAW are excluded in the algorithm development because the view zenith angles within the SAS and SAW regions are greater than 68°. In order to make the radiative transfer simulations much more representative for natural cases, the temperature profiles and the water vapor profiles of the six standard model atmospheres were adjusted. The temperature adjustment quantity is ±15.0 K for the first boundary level and linearly decreases with the increment of the altitude until to tropopause. For the levels higher than tropopause, no adjustment was carried out. The water vapor content (W) was scaled from 0.1 to 1.5 with a step of 0.1. Eleven view zenith angles: 0°, 10°, 20°, 30°, 35°, 40°, 45°, 50°, 55°, 60° and 65°, and six view zenith angles: 0°, 10°, 20°, 25°, 50° and 55° a a height of 100 km were, respectively, taken into account for the SEVIRI and AATSR (Nadir and Forward). The LST ranges from T_0-5 to T_0+20 with an interval of 5 K. The average emissivity changes from 0.90 to 1.00 with a step of 0.02, and the emissivity difference ($\Delta\varepsilon$) varies from -0.025 to 0.016 with an interval of 0.005.

In order to further improve the accuracy of the generalized split-window algorithm, the LST, the average emissivity and W were divided into several tractable sub-ranges. The LST was divided into 5 groups with an overlap of 5.0 K: ≤282.5, [277.5, 297.5], [292.5, 312.5], [307.5, 327.5] and ≥322.5 K. The LSE was separated into two sub-ranges: one goes from 0.90 to 0.96 and the other varies from 0.94 to 1.0 with an overlap of 0.02. The W was divided into six groups and they are [0.0, 1.5], [1.0, 2.5], [2.0, 3.5], [3.0, 4.5], [4.0, 5.5] and [5.0, 6.5] in g/cm^2. Because both the SEVIRI and AATSR have no atmospheric sounding channels, the first boundary temperature of atmosphere is not known, and was not involved in the algorithm development like Wan and Dozier did (1997). For the AATSR instrument, when LST is less than 335 K and W varies between 0 and 6.5 g/cm^2, the RMSEs are less than 1.0 K for the Nadir view zenith angles, and are less than 1.6 K for the Forward view zenith angles. The RMSEs for AATSR are also less than 1.0 K for both the nadir and forward views and all LST groups when W is less than 4.5 g/cm^2. While, for the SEVIRI instrument, when W varies between 0 and 6.5 g/cm^2, the RMSEs are less than 1.0 K for the view zenith angles less than 55° and LST less than 312.5 K, or for the view zenith angles less than 45° and all LST groups. The RMSEs for SEVIRI are also less than 1.0 K for all LST groups with the view zenith angles less than 60° and W less than 3.5 g/cm^2. For the high LST groups, the RMSEs increase dramatically when the view zenith angle is greater than 60°, and the maximum reaches 2.3 K.

The LSEs in SEVIRI channels 9 and 10 were estimated by the method developed by Jiang et al. (2006), while the LSEs in AATSR channels IR11 and IR12 were inferred from the ones in SEVIRI channels in terms of the RossThick-LiSparse-R model, the Kirchhoff's law, the angular-independent properties of TISI and the ASTER Spectral Library. The atmospheric water vapor contents were estimated by means of the method given by Li et al. (2003). An area-weighted pixel aggregation was carried out to put the AATSR images into the SEVIRI image coordinates.

LSTs were retrieved over the study area (longitude: 20W—60E, latitude: 0—60N) from July 14, 2004 to July 19, 2004 and from July 10, 2005 to July 14, 2005 by the split-window method and the single channel method from the SEVIRI data and the AATSR Nadir and Forward data. The LST retrievals are mainly limited by the absence of emissivities and clouds. The results show that the LSTs in daytime are higher than the ones at night, and the LSTs over the bare area are higher than the ones over vegetated area in daytime. The LSTs estimated by the two methods are basically consistent. The AATSR Nadir LSTs are averagely 3.56 K warmer than the corresponding AATSR Forward LSTs in daytime, while they are almost equal at night. The results of the AATSR LSTs reveal that the dual-angle algorithm developed for the AATSR instrument (Prata, 2002) cannot be used in the daytime LST retrieval, but may be suitable for nighttime LST retrieval with accuracy higher than 1.0 K.

The results at the four specific locations show that the DTC model works well in the description of LSTs. Four maps of the time-normalized SEVIRI LST were generated by the DTC model over the whole study area, and the LSTs after the time normalization are very different from the orginal ones.

6 SEVIRI LST cross-validations with the MODIS/Terra LST products and AATSR LST

6.1 Introduction

LST validation with in situ measurements is very difficult because of the high spatial variations in LSTs. Snyder et al. (1997) pointed out that simple flat surfaces which are the most easily instrumented and characterized, such as inland water, sand, snow, ice, and playa, can serve as the validation sites.

In the LST validation, two approaches are often used, one is temperature-based and the other is radiance-based. The temperature-based approach directly compares the LSTs estimated from satellite data with in situ measured LSTs and then gives the LST accuracy (Wan et al., 2002 & 2004; Coll et al., 2005). For the radiance-based approach, radiative transfer simulations are made with the MODTRAN 4.0 code (Berk et al. 1999) to calculate the radiances at TOA in a channel usually centered at 11.0 μm using surface emissivity spectra measured in the field or estimated from land-cover types, atmospheric profiles measured by radiosonde balloons, and the retrieved LSTs. The input LSTs are adjusted in the simulations to match the calculated radiances to the satellite-measured radiances, and LSTs called radiance-inverted LSTs can be obtained. The validation is carried out through comparisons between the radiance-inverted LSTs and the retrieved LSTs (Wan and Li, 2007).

Wan et al. (2002) validated that the MODIS/Terra LST accuracy is better than 1 K in the range from 263 to 300 K over Lake Titicaca in Bolivia, Mono Lake, Bridgeport grassland, a rice field in Chico, CA, and Walker Lake, Nevada (NV), with the atmospheric column water vapor ranging from 0.4 to 3.0 cm. For the six cases over a silt playa in Railroad Valley, NV, the 1-km MODIS LSTs derived by the generalized split-window algorithm are a few Kelvin degrees lower than in situ measured LSTs because of the higher emissivities estimated in the 1 km MODIS/Terra LST product (MOD11_L2) over semi-arid and arid areas. After a correction with the difference between the 5-km LST estimated by the day/night LST method and the LST aggregated from the 1-km LSTs, the MODIS/Terra LSTs agree well with in situ measured LSTs within ±1 K in the range 263-322 K for the six cases in Railroad Valley and one case of snowcover in Bridgeport.

Coll et al. (2005) validated the AATSR LSTs and the 1km MODIS/Terra LST product with ground measurements over a large, flat and homogenous area of rice crops (1 km^2). They concluded that the AATSR LSTs yielded an average error of -0.9 °C with a standard deviation of 0.9 °C, and the MOD11_L2 agreed well with the ground LSTs with a bias of 0.1 °C and a standard deviation of 0.6°C.

Because of the much lower spatial resolution of the SEVIRI data in the TIR channels (3 km at the sub-satellite point), it is difficult to find such a large, flat and homogeneous land site. Even though such land site exists, it is still impossible to carry it out because of the financial limitation of our project. As mentioned above, the MODIS/Terra LST products have been well validated with in situ LSTs. Therefore, in this work, the SEVIRI LSTs will be cross-validated with the MODIS LST products (MOD11B1 and MOD11_L2) and the AATSR Forward LSTs estimated by the generalized split-window algorithm developed in Chapter 5.

In the following, this chapter will be divided into four sections. Section 6.2 describes the method, and Section 6.3 describes the study areas, the data description and the data processing. In the section 6.4, the results and analysis will be presented. In the last section, the summary and conclusions will be given.

6.2 Method

The LST cross-validations are the comparisons between the SEVIRI LSTs estimated by the split-window algorithm and the LSTs extracted from the MODIS/Terra LST products (MOD11B1 and MOD11_L2) and between the SEVIRI LSTs and the AATSR Forward LSTs estimated by the generalized split-window algorithm developed in Chapter 5 over coordinate-matched areas at same time. The averages and RMSEs of the temperature differences are two indicators to assess the relative SEVIRI LST accuracy.

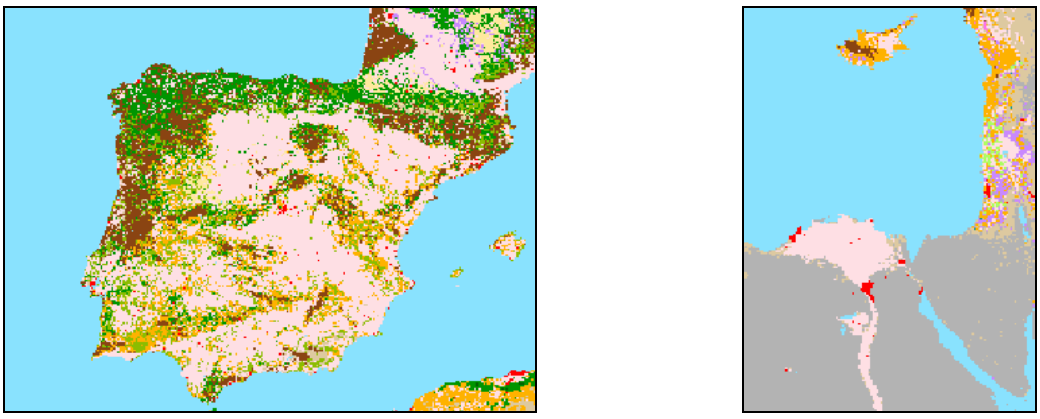

Figure 6.1. Study areas: the Iberian Peninsula area (left) and the Egypt & Middle East area (right) (MODIS sinusoidal grid projection for MOD11B1; Maps were generated from the Global Land Cover 2000 and the legends are the same as the ones in Figure 4.5)

6.3 Study areas, data description and data processing

Two regions are selected as study areas in the LST cross-validations: the Iberian Peninsula area occupied by Spain and Portugal (Longitude: 12.87W – 4.15E; Latitude: 35.86N – 44.98N) and an area covering Egypt, Israel, Lebanon, Syria, Jordan and Cyprus (Longitude: 27.65E – 37.59E; Latitude: 27.53N – 35.82N) (Figure 6.1). Hereafter, we call the second area the Egypt & Middle East area for convenience. The Iberian Peninsula area is a vegetated region, and the main land cover types are cultivated and managed areas, tree cover and herbaceous cover (Global Land Cover 2000). While for the Egypt & Middle East area, the bare area is dominated. Most of Egypt is covered by the low-lying

sand dunes and depressions of the Western and Libyan Deserts. East of the Nile River, the semi-arid Arabian Desert extends to the edges of the Red Sea. In this area, other land cover types, such as the cultivated and managed areas, herbaceous and shrub areas, are mainly distributed around the Mediterranean Sea and the Nile River. These two study areas, in which typical land types are covered, are suitable for the LST cross-validations.

The SEVIRI's view zenith angles at ground level over the Iberian Peninsula area and the Egypt & Middle East area are ~45° and ~53°, respectively, while MODIS's view zenith angles at ground level vary between 0° and 60°, and the view zenith angles at ground level of AATSR Forward view are ~53°. Because the SEVIRI view zenith angles are close to the AATSR Forward view zenith angles over the Iberian Peninsula area, the SEVIRI LSTs were cross-validated with the AATSR Forward LSTs.

Corresponding to the composite LSE maps generated in Chapter 4, two time spans were used in the LST cross-validations: the first time span goes from July 14, 2004 to July 19, 2004, and the second time span varies from July 10, 2005 to July, 14, 2005.

In this work, in addition to the LSTs estimated from the SEVIRI data and AATSR Forward data by the generalized split-window algorithm (see Chapter 5), the MODIS/Terra LST products, MOD11B1 and MOD11_L2, are used as references.

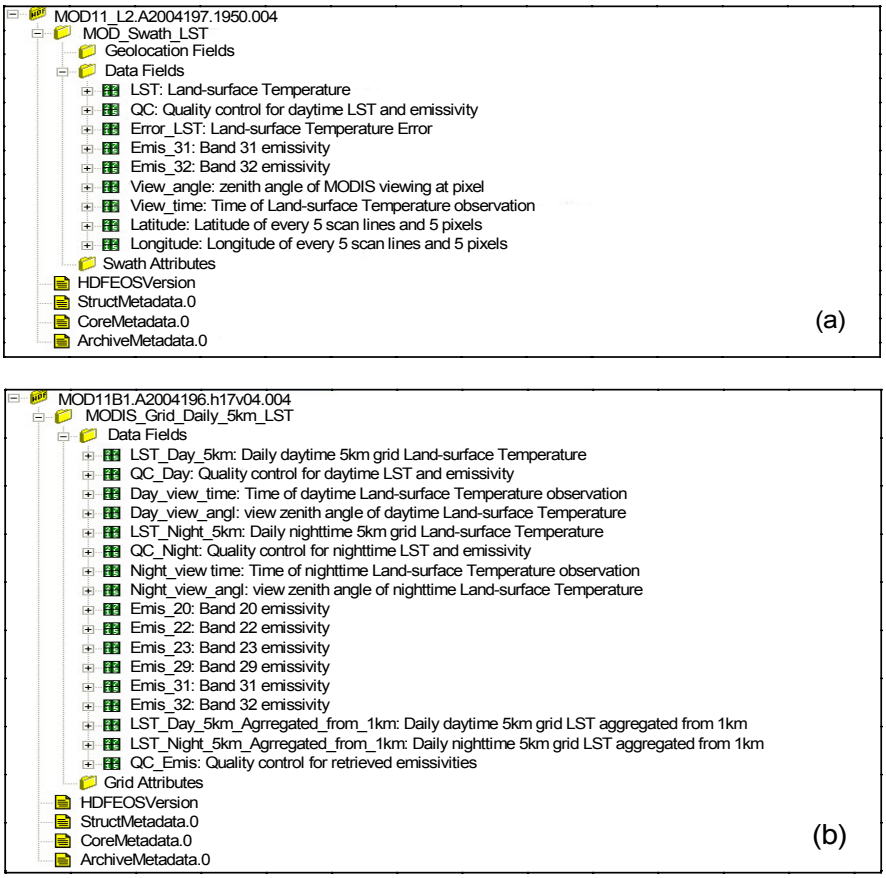

Figure 6.2. Data stored in the MODIS/Terra LST products MOD11_L2 (a) and MOD11B1 (b)

Table 6.1. Bit flags defined in the QC in the MOD11_L2 product (Version 004)

bits	Long Name	Key
1 & 0	Mandatory QA flags	00=Pixel produced, good quality, not necessary to examine more detailed QA 01=Pixel produced, unreliable or unquantifiable quality, recommend examination of more detailed QA 10=Pixel not produced due to cloud effects 11=Pixel not produced primarily due to reasons other than cloud (such as ocean pixel, poor input data)
3 & 2	Data quality flag	00=good 01=missing pixel 10=fairly calibrated 11=poorly calibrated, LST processing skipped
5 & 4	Cloud flag	00=cloud free pixel 01=pixel only with thin cirrus 10=fraction of sub-pixel clouds<= 2/16 11= LST affected by nearby clouds
7 & 6	LST model number	00=generalized split-window method 01=day/night method 10=high LST w/o atmospheric & emis corrections 11=cirrus effects corrected
9 & 8	LST quality flag	00=no multi-method comparison 01=multi-method comparison done 10=fair consistency 11=good consistency
11 & 10	Emissivity flag	00=inferred from land cover type 01=MODIS retrieved 10=TBD 11=default value used
13 & 12	Emis quality flag	00=emis quality not checked 01=emis quality checked with land cover type 10=emis quality checked with NDVI 11=emis view-angle dependence checked
15 & 14	Emis error flag	00=error in emis_31 emis_32 <= 0.01 01=error in emis_31 emis_32 <= 0.02 10=error in emis_31 emis_32 <= 0.04 11=error in emis_31 emis_32 > 0.04

The MODIS/Terra Land Surface Temperature/Emissivity 5-Min L2 Swath 1km product (MOD11_L2, version 004) is derived by the generalized split-window LST algorithm (Wan and Dozier, 1996) from the MODIS sensor radiance product (MOD021KM), the MODIS/Terra Geolocation product (MOD03), the MODIS/Terra cloud mask product (MOD32_L2), the quarterly land cover (MOD12Q1), and the snow product (MOD10_L2). In addition to temperature, Quality Assurance (QA), the error in LST, the emissivities in MODIS channels 31 and 32, the view angle and view time information, and the geolocation data (longitude and latitude) at 5 km resolution are also stored in this product (Figure 6.2a). It should be noted that the emissivities in the MOD11_L2 product were estimated by the classification-based emissivity method (Snyder and Wan, 1998) in terms of land cover types given by MOD12Q1 and MOD10_L2. A large uncertainty may exist in such estimated emissivities in semi-arid and arid regions. Table 6.1 gives the bit flags defined in the QC in the MOD11_L2 product (Version 004). According to Table 6.1, a value of 0 in the Quality Control (QC)

bit flags means good data quality, cloud free, small error in the emissivities in MODIS channel 31 and 32, and etc, if a pixel has a valid LST value (QC=0 for null areas).

Because the resolution of the geolocation data in MOD11_L2 is too low (5 km), the MODIS/Terra Geolocation product (MOD03, version 005), which has the same sizes and resolution as MOD11_L2, is used in the navigation.

The MODIS/Terra Land Surface Temperature/Emissivity (LST/E) Daily L3 product (MOD11B1, version 004) in sinusoidal projection provides per-pixel temperature and emissivity values with a resolution of ~4.63 km. The LST/E algorithms use the MODIS data as input, including geolocation, radiance, cloud mask, atmospheric temperature, water vapor, snow and land cover. Averaged LST in Kelvin and emissivities in MODIS channels 20, 22, 23, 29, 31 and 32 are estimated with the day/night LST method applied to a pair of MODIS daytime and nighttime measurements (Wan and Li, 1997; MODIS LST ATBD version 3.3). Besides the averaged LSTs and emissivities, view angle, view time information and QC for each pixel are also stored in the LST/E product (Figure 6.2b). The QCs, eight-bit flags, define the QA of each pixel (Table 6.2). From Table 6.2, a value of 0 in the QC bit flags means the estimated LST and data are good, the average emissivity error is less than 0.01 and the average LST error is less than 1.0 K.

Table 6.2. Bit flags defined in the QC in the MOD11B1 product

bits	Long Name	Key
1 & 0	Mandatory QA flags	00=LST produced, good quality, not necessary to examine more detailed QA 01=LST produced, other quality, recommend examination of more detailed QA 10=LST not produced due to cloud effects 11=LST not produced primarily due to reasons other than cloud
3 & 2	Data quality flag	00=good data quality 01=other quality data 10=LST affected by nearby clouds and/or sub-grid clouds and/or ocean 11=TBD
5 & 4	Emis Error flag	00=average emissivity error <= 0.01 01=average emissivity error <= 0.02 10=average emissivity error <= 0.04 11=average emissivity error > 0.04
7 & 6	LST LST Error flag	00=average LST error <= 1 K

As shown in Figure 6.3, the Iberian Peninsula area astride covers the MODIS sinusoidal grid tiles h17v04, h17v05, h18v04 and h18v05, while the Egypt & Middle East area is in the MODIS sinusoidal grid tiles h20v05, h20v06, h21v05 and h21v06. The LSTs, view angles, view times, quality control and emissivities in MODIS channel 31 and 32 over the two study areas and in the two time spans were extracted from MOD11B1, while the LSTs, quality control and the emissivities in MODIS channels 31 and 32 were extracted from MOD11_L2. The coordinates (longitude and latitude) of the MOD11B1 pixels were calculated by a modified program from the short program developed by Wan (http://www.icess.ucsb.edu/modis/lat_lon_to_row_col.c). The coordinates (longitude and latitude) and view angles of the MOD11_L2 pixels were directly extracted from the MODIS/Terra Geolocation product MOD03.

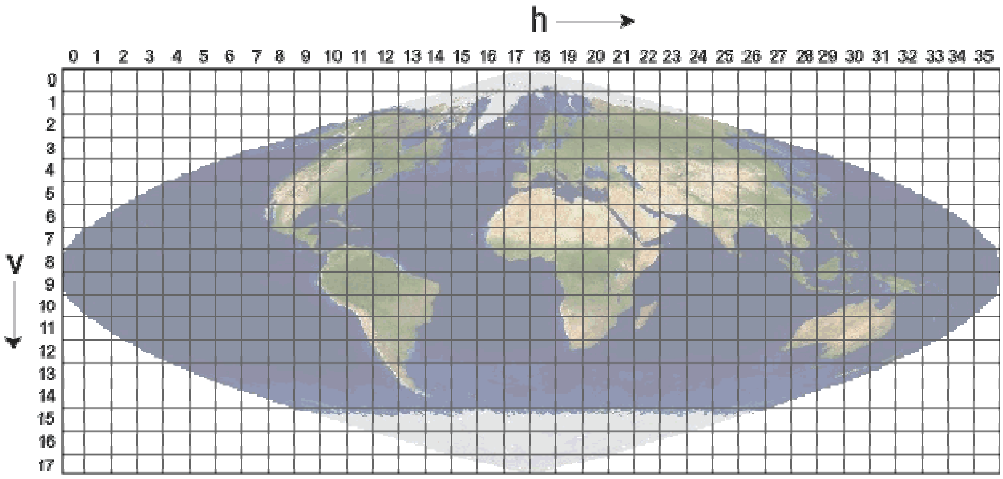

Figure 6.3. MODIS Sinusoidal Grid
(Cited from http://nsidc.org/data/modis/landgrid.html)

It should be noted that, the data in MOD11B1 are composite results, and the data over the study areas may come from several neighboring orbits with a difference in the acquired UTC time of ~90 min according to the Terra's orbit tracks (Figure 3.5). The view times (local time) stored in MOD11B1 are divided into small strips with a width of 12 min. One can determine the approximate UTC time of a pixel in terms of the longitude of that pixel (UTC time=Local time–Longitude/15), but this will introduce an error up to 12 min. It is strange that, we found in MOD11B1 that a pixel within the overlap areas of two neighboring orbits is different from the eight neighboring pixels with a time difference of 12 min or different from part of the neighboring pixels with a time difference greater than 12 min but less than 60 min (e.g., MOD11B1.A2005194.h17v04.004 shown in Figure 6.4). According to the Terra's orbit tracks and the MODIS view geometry, this may be the average time of two neighboring orbits.

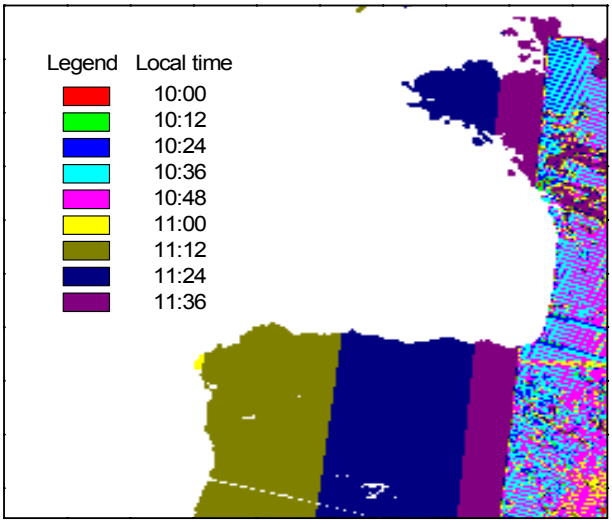

Figure 6.4. Time of the LST observation in MOD11B1
(MOD11B1.A2005194.h17v04.004; the right-hand part is the overlap area between two neighboring orbits)

If the view time is not accurately determined, it is difficult to carry out the cross-validations in good accuracy. In this work, instead of using the time extracted from MOD11B1, the UTC time of the MOD11B1 pixels was precisely determined from the corresponding MOD11_L2 product, in which the acquired UTC time is part of its file name, e.g., MOD11_L2.A2004197.1950.004 was acquired at UTC time 19:50 on Julian date 197 of 2004. Moreover, in the area-based validations, to avoid the time ambiguity within the overlapping areas of two neighboring orbits in MOD11B1, only those MODIS/Terra LST products covering the entire study area with a single orbit were considered. For the Iberian Peninsula area, the MODIS/Terra LST products on July 14, 2004, July 16, 2004, July 10, 2005 and July 12, 2005 are qualified. While for the Egypt & Middle East area, the MODIS/Terra LST products on July 15, 2004, July 17, 2004, July 11, 2005 and July 13, 2005 are qualified. As pointed out in Chapter 3, the SEVIRI sensor scans the Earth disc from the south towards the north with a time cycle of ~15 min, and the UTC time recorded in the file name of the SEVIRI data is the scan starting time, e.g., the data in MSG1-SEVI-MSG15-0100-NA-200407140557 were observed at UTC time 5:57 on July 14 of 2004. According to the locations of the two study areas, the time of the SEVIRI images are ~10 min less than the time of the corresponding MODIS/Terra images. In this work, the time matching accuracy is better than 10 min.

Besides the time matching, the coordinate matching is another requirement for the LST cross-validation. The LSTs and emissivities in the two split-window channels estimated from the SEVIRI and AATSR data and extracted from the MOD11_L2 product were aggregated into the two study areas (MODIS sinusoidal grid projection for MOD11B1) by Equation (3.5), and the aggregated SEVIRI data were then accurately matched with the MOD11B1 data in terms of the minimum RMSE principle (See Chapter 3). According to the QC criterion, the cross-validations were carried out between the SEVIRI LSTs and the LSTs extracted from MOD11B1 and MOD11_L2, and between the SEVIRI LSTs and the AATSR Forward LSTs under clear sky conditions.

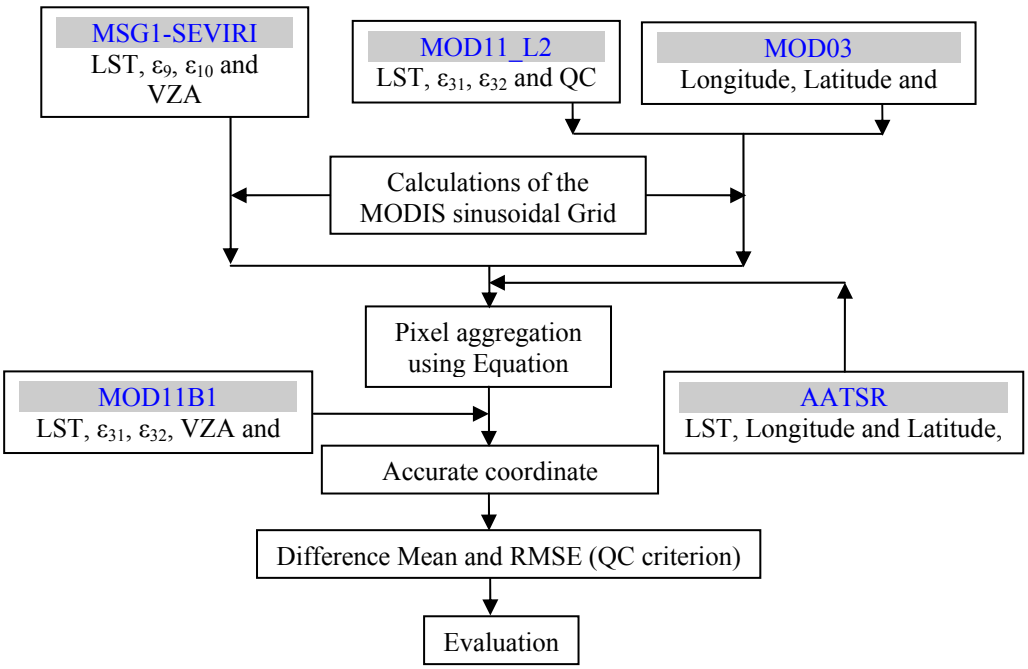

Figure 6.5. Data processing flow of the LST cross-validations

Figure 6.5 demonstrates the data processing flow of the LST cross-validations. It is mainly composed of three steps: (1) Data extraction and navigation. As described above, qualified LSTs, emissivities, coordinates, view zenith angles and QCs were extracted from MOD11B1 and MOD11_L2, or derived from the MSG1-SEVIRI data and the AATSR data (2) Pixel aggregation and accurate coordinate matching. The data extracted from MOD11_L2 or derived from the MSG1-SEVIRI data and the AATSR data were aggregated into the MODIS sinusoidal grid projection for MOD11B1 using Equation (3.5), and then accurate coordinate matching was carried out according to the minimum RMSE principal. (3) Calculations of the mean and RMSE of the temperature differences and result evaluation. After the time and coordinate matching, the averages and RMSEs of the temperature differences were easily implemented.

6.4 Results and analysis

In order to evaluate the LST differences, Equations (5.18) and (5.19) were also used here, but $T_{i,1}$ denotes LST derived from the SEVIRI data by the generalized split-window algorithm, and $T_{i,2}$ represents the LST extracted from the MODIS LST products (MOD11B1 and MOD11_L2) or estimated from the AATSR Forward data by the generalized split-window algorithm.

Figure 6.6, Figure 6.7, Figure 6.8 and Figure 6.9 show the LSTs derived from the SEVIRI data by the generalized split-window algorithm or extracted from the MODIS/Terra LST products and the LST differences between them over the Iberian Peninsula area on July 14, 2004, July 16, 2004, July 10, 2005 and July 12, 2005, respectively. When LSTs estimated from the SEVIRI data by the generalized split-window algorithm ($T_{s,SEVIRI}$) are compared to the LSTs extracted from the MOD11B1 ($T_{s,MOD11B1}$), in the daytime, the average of the temperature differences (mean) is less than 0.8 K, and the RMSE are less than 2.6 K, while at night, the mean and RMSE become smaller and they are less than 0.4 K and 2.1 K, respectively. This can be explained in this way: the LSTs are relatively low and trend to be homogenous at night, and low LSTs have small RMSEs by the use of the split-window method as shown in Figure 5.2 and Figure 5.3. When $T_{s,SEVIRI}$ is compared to the LST extracted from the MOD11_L2 ($T_{s,MOD11\_L2}$), the mean changes between 0.9 K and 2.3 K and RMSE varies between 1.9 K and 3.2 K. Note that, the differences between the RMSE and the mean of ($T_{s,SEVIRI}$-$T_{s,MOD11\_L2}$), which are approximately equal to the standard deviations of the temperature differences, are less than 1.6 K. Because the emissivities in the MOD11_L2 derived from classification types are overestimated, the relatively large differences between $T_{s,SEVIRI}$ and $T_{s,MOD11\_L2}$ are qualitatively consistent with the results of Wan et al. (2002). The results indicate that, in general speaking, the temperature differences in daytime are larger than the temperature differences at night, and the temperature differences between $T_{s,SEVIRI}$ and $T_{s,MOD11B1}$ are smaller than the temperature differences between $T_{s,SEVIRI}$ and $T_{s,MOD11\_L2}$.

Figure 6.10 displays the LSTs estimated from the SEVIRI data and the AATSR Forward data and the LST differences between them over the Iberian Peninsula area on July 14, 2004. When $T_{s,SEVIRI}$ is compared to the LST estimated by the generalized split-window algorithm from the AATSR Forward data ($T_{s,AATSR\_Forward}$), $T_{s,SEVIRI}$ is averagely 1.26 K warmer than $T_{s,AATSR\_Forward}$ with a RMSE of 2.4 K in the daytime, and the mean and RMSE of the temperature differences are, respectively, reduced to 0.3 K and 1.6 K at night (21:46UTC) shortly after the sunset. The LST differences between $T_{s,SEVIRI}$ and $T_{s,AATSR\_Forward}$ may be explained in this way. Because of the spatial structures of the vegetated Iberian Peninsula area, the SEVIRI images contain more bare area information than the AATSR Forward images due to differences in the view zenith angles, and in daytime with clear sky conditions, the temperatures of bare area are usually higher than the temperatures of vegetation. Shortly after sunset,

although the temperatures of the bare area are still higher than the temperatures of vegetation, the differences between them become smaller, and the impact of the view zenith angles is correspondingly minimized. Totally, the LSTs estimated from the SEVIRI data and the AATSR Forward data by the generalized split-window algorithm are consistent.

Figure 6.11, Figure 6.12, Figure 6.13 and Figure 6.14 present the maps of $T_{s,SEVIRI}$, $T_{s,MOD11B1}$ and $T_{s,MOD11\_L2}$ and the LST differences between them over the Egypt & Middle East area on July 15, 2004, July 17, 2004, July 11, 2005 and July 13, 2005, respectively. In the daytime, $T_{s,SEVIRI}$ is averagely 1.5 K lower than $T_{s,MOD11B1}$ and the average RMSE is 2.5 K. While, at night, $T_{s,SEVIRI}$ is averagely 0.2 K higher than $T_{s,MOD11B1}$ and the average RMSE is 1.9 K. The maps also show that, $T_{s,SEVIRI}$ is always lower than $T_{s,MOD11B1}$ in the Nile River region, while in the desert, $T_{s,SEVIRI}$ is generally lower than $T_{s,MOD11B1}$ in the daytime, and the opposite is observed at night. Similar to the results over the Iberian Peninsula area, $T_{s,MOD11\_L2}$ is still lower than $T_{s,SEVIRI}$, but the LST differences are much larger: the mean is up to 2.5 K and the RMSE is up to 3.5 K. The large temperature differences between $T_{s,SEVIRI}$ and $T_{s,MOD11\_L2}$ apear in the desert regions, where the emissivities in the MOD11_L2 are overestmated.

Table 6.3. Mean and RMSEs of the temperature differences between the SEVIRI LST and the MODIS/Terra LST over the two study area

Area	Date and time		$T_{s,SEVIRI} - T_{s,MOD11B1}$ (K)				$T_{s,SEVIRI} - T_{s,MOD11\_L2}$ (K)			
			$Mean_1$	$RMSE_1$	$Mean_2$	$RMSE_2$	$Mean_1$	$RMSE_1$	$Mean_2$	$RMSE_2$
Iberian Peninsula	July 14 2004	Day	0.72	2.34	0.83	2.14	2.28	3.22	2.15	2.84
		Night	-0.16	1.42	0.18	1.79	1.36	1.87	1.47	2.04
	July 16 2004	Day	0.08	2.54	1.02	2.03	1.48	2.90	1.55	2.22
		Night	-0.16	2.07	1.19	2.11	1.43	2.47	1.56	2.19
	July 10 2005	Day	-0.22	2.33	0.46	2.13	0.94	2.53	1.18	2.20
		Night	0.31	1.73	0.74	1.92	1.57	2.17	1.54	2.15
	July 12 2005	Day	0.50	1.94	0.79	1.88	1.63	2.45	1.58	2.18
		Night	0.39	1.81	0.88	1.85	1.49	2.24	1.63	2.13
	Total	Day	0.28	2.28	0.76	2.04	1.59	2.79	1.57	2.34
		Night	0.13	1.74	0.78	1.92	1.46	2.17	1.56	2.13
Egypt & Middle East	July 15 2004	Day	-0.68	1.90	-0.67	1.76	1.31	2.43	1.22	2.29
		Night	0.52	1.81	0.70	1.87	1.98	2.72	1.82	2.57
	July 17 2004	Day	-1.35	2.36	-0.47	2.23	0.23	2.19	0.69	2.18
		Night	0.47	1.66	0.60	1.79	2.13	2.79	1.88	2.66
	July 11 2005	Day	-1.31	2.27	-0.95	2.05	1.22	2.51	1.31	2.43
		Night	-0.11	1.56	1.31	2.42	2.03	2.76	1.88	2.68
	July 13 2005	Day	-2.67	3.65	-1.38	2.76	0.11	2.81	0.53	2.54
		Night	-0.02	2.66	0.06	2.54	2.44	3.45	1.73	2.71
	Total	Day	-1.50	2.62	-0.88	2.26	0.72	2.50	0.92	2.37
		Night	0.21	1.97	0.60	2.17	2.15	2.95	1.83	2.66

$Mean_1$ and $RMSE_1$ were calculated from all LST differences, while $Mean_2$ and $RMSE_2$ were calculated from the LST differences with QCs equal to zero.

Table 6.3 gives the averages and RMSEs of the temperature differences between the SEVIRI LST and the MODIS/Terra LST according to the QCs in the MODIS/Terra LST products over the two study area. Compared to the indicators for all LSTs, the averages and RMSEs for the LSTs with QC

equal to zero have no obvious improvement. Over the Iberian Peninsula area, the mean is less than 1 K for ($T_{s,SEVIRI}$–$T_{s,MOD11B1}$), and is ~1.5 K for ($T_{s,SEVIRI}$–$T_{s,MOD11\_L2}$). Over the Egypt & Middle East area, $T_{s,SEVIRI}$ is ~1.0 K lower than $T_{s,MOD11B1}$ in daytime, while $T_{s,SEVIRI}$ is slightly higher than $T_{s,MOD11B1}$ in nighttime; $T_{s,SEVIRI}$ is ~1.0 K higher than $T_{s,MOD11\_L2}$ in daytime, while the difference mean is ~2.0 K in nighttime. In Table 6.3, we found that, on some dates, the mean is close to zero, but the RMSE is very large, e. g., on July 16, 2004 over the Iberian Peninsula area. This can be explained in this way: the absolute temperature differences are very large, and the relative temperature differences are symmetric with respect to zero.

In order to further investigate the temperature differences, we divided them into twenty groups from -10.0 K to 10.0 K with an interval of 1.0 K and calculated the frequency of each group. Figure 6.15 displays the histograms of the temperature differences over the Iberian Peninsula area and the Egypt & Middle East area in both daytime and nighttime according to the QCs in MODIS/Terra LST products. No obvious differences are found between the results with different QC criterion. The histograms show that the temperature differences obey Gaussian distribution function (Equation (4.25)). $T_{s,MOD11\_L2}$ is ~2.0 K higher than $T_{s,SEVIRI}$ over the two areas, and $T_{s,MOD11B1}$ is ~1.0 K higher than $T_{s,SEVIRI}$ in the daytime over the Egypt & Middle East area. $T_{s,SEVIRI}$ is quiet consistent with $T_{s,MOD11B1}$ and $T_{s,AATSR\_Forward}$ in both daytime and nighttime over the Iberian Peninsula area. Compared to the histograms of the temperature differences over the Egypt & Middle East area, the histograms of the temperature differences over the Iberian Peninsula area are much more clustered around the peak. Over the Iberian Peninsula area, within a radius of 2.0 K around the hitogram peak, there are 76.4% of ($T_{s,SEVIRI}$-$T_{s,MOD11B1}$), 76.6% of ($T_{s,SEVIRI}$-$T_{s,MOD11\_L2}$), and 82.3% of ($T_{s,SEVIRI}$-$T_{s,AATSR\_Forward}$) in the daytime, and there are 87.0% of ($T_{s,SEVIRI}$-$T_{s,MOD11B1}$), 91.3% of ($T_{s,SEVIRI}$-$T_{s,MOD11\_L2}$) and 90.8% of ($T_{s,SEVIRI}$-$T_{s,AATSR\_Forward}$) avalaible at night. While over the Egypt & Iberian Peninsula area, within a radius of 2.0 K around the peak, there are 78.9% of ($T_{s,SEVIRI}$-$T_{s,MOD11B1}$) and 72.3.0% of ($T_{s,SEVIRI}$-$T_{s,MOD11\_L2}$) in the daytime, and there are only 80.3% of ($T_{s,SEVIRI}$-$T_{s,MOD11B1}$) and 77.3% of ($T_{s,SEVIRI}$-$T_{s,MOD11\_L2}$) at night. In general speaking, within the radius of 2.0 K around the histogram peaks, the temperature differences at night have higher frequencies than the ones in the daytime, and the temperature differences over the vegetated area also possess higher frequencies than the ones over the bare area, especially the temperature differences between $T_{s,SEVIRI}$ and $T_{s,MOD11\_L2}$.

According to the input parameters of the generalized split-window algorithm, the LST differences may come from the emissivities, the brightness temperatures at TOA, view zenith angles, atmospheric water vapor content and the algorithm itself. In chapter 3, SEVIRI channels 9 and 10 have been well cross-calibrated with MODIS/Terra channels 31 and 32, and therefore the differences that come from the brightness temperatures at TOA have been minimized. In Chapter 5, an example shows that the generalized split-window algorithm is not very sensitive to the change of atmospheric water vapor content. When the water vapor content is less than 3.5 g/cm^2 and LSTs vary between 277.5 K and 327.5 K, the RMSEs of the generalized split-window algorithm are less than 1.0 K for the view zenith angles of the SEVIRI and the AATSR less than 60° (Figure 5.2 and Figure 5.3).

Figure 6.16, Figure 6.17, Figure 6.18 and Figure 6.19 show the emissivities estimated from the SEVIRI data by the method developed in Chapter 4 (ε_9 and ε_{10}) and the emissivities extracted from the MOD11B1 ($\varepsilon_{31,MOD11B1}$ and $\varepsilon_{32,MOD11B1}$) and the differences between them over the Iberian Peninsula area and the Egypt & Middle East area on July 14, 2004, July 16, 2004, July 10, 2005 and July 12, 2005. The emissivities ε_9 and ε_{10} over the two study areas present clear textures and are rather homogenous in local regions. Over the vegetated area, ε_9 is slightly higher than ε_{10} and most of them

are greater than 0.95, whereas, over the bare area, ε_9 and ε_{10} are ~0.94 and ~0.96, respectively. However, the emissivities $\varepsilon_{31,MOD11B1}$ and $\varepsilon_{32,MOD11B1}$ over the two study areas are rather rough, and they look like noises over some regions. Over both the vegetated and bare areas, most of $\varepsilon_{31,MOD11B1}$ and $\varepsilon_{32,MOD11B1}$ are greater than 0.95, and $\varepsilon_{31,MOD11B1}$ are always less than $\varepsilon_{32,MOD11B1}$. It should be noted that, over the Egypt desert areas, $\varepsilon_{32,MOD11B1}$ is almost equal to 1.0, especially on July 15, 2004 and July 17, 2004. Totally, the ε_9 is ~0.01 lower than the $\varepsilon_{31,MOD11B1}$, and the ε_{10} is ~0.02 lower than the $\varepsilon_{32,MOD11B1}$. The maps also reveal that the emissivities $\varepsilon_{31,MOD11B1}$ and $\varepsilon_{32,MOD11B1}$ are quiet different in two close days in some regions.

Table 6.4 gives the averages and RMSEs of the emissivity differences over the two study areas according to the QCs defined in MOD11B1 and MOD11_L2. No obvious differences are observed between the emissivities for the entire areas and the emissivities with QCs equal to zero. Over the Iberian Peninsula area, the mean is close to zero for ($\varepsilon_9 - \varepsilon_{31,MOD11B1}$) and ε_9 is ~0.02 lower than $\varepsilon_{31,MOD11\_L2}$, while ε_{10} is averagely 0.015 lower than $\varepsilon_{32,MOD11B1}$ and ε_{10} is 0.026 lower than $\varepsilon_{32,MOD11\_L2}$. As mentioned in Chapter 4, ε_9 is slightly higher than ε_{10} over vegetated areas, however $\varepsilon_{32,MOD11B1}$ is always higher than $\varepsilon_{31,MOD11B1}$ in MOD11B1. That is why so large differences exist between ε_{10} and $\varepsilon_{32,MOD11B1}$. Over the Egypt & Middle East area, both $\varepsilon_{31,MOD11B1}$ and $\varepsilon_{32,MOD11B1}$ are, respectively, slightly higher than ε_9 and ε_{10}, while the emissivities estimated from the SEVIRI data are ~0.01 lower than the ones extracted from MOD11_L2.

Table 6.4. Averages and RMSEs of the differences between the emissivities estimated from the SEVIRI data and the ones extracted from MOD11B1 and MOD11_L2 over the two study areas

Area	Date	$\varepsilon_9 - \varepsilon_{31,MOD11B1}$				$\varepsilon_{10} - \varepsilon_{32,MOD11B1}$			
		$Mean_1$	$RMSE_1$	$Mean_2$	$RMSE_2$	$Mean_1$	$RMSE_1$	$Mean_2$	$RMSE_2$
Iberian Peninsula	July 14, 2004	-0.009	0.016	-0.008	0.015	-0.025	0.031	-0.023	0.028
	July 16, 2004	-0.007	0.016	-0.016	0.023	-0.023	0.031	-0.024	0.030
	July 10, 2005	0.001	0.014	-0.008	0.022	-0.004	0.020	-0.012	0.024
	July 12, 2005	0.002	0.013	-0.002	0.017	-0.004	0.019	-0.006	0.020
	Total	0.003	0.015	-0.008	0.020	-0.014	0.026	-0.015	0.025
Egypt & Middle East	July 15, 2004	-0.011	0.017	-0.010	0.017	-0.017	0.028	-0.023	0.027
	July 17, 2004	-0.010	0.017	-0.012	0.020	-0.005	0.012	-0.021	0.027
	July 11, 2005	0.007	0.021	0.004	0.022	0.001	0.019	-0.002	0.020
	July 13, 2005	0.008	0.022	0.006	0.022	0.001	0.019	-0.001	0.020
	Total	-0.001	0.019	-0.002	0.020	-0.005	0.019	-0.011	0.024
Area	Date	$\varepsilon_9 - \varepsilon_{31,MOD11\_L2}$				$\varepsilon_{10} - \varepsilon_{32,MOD11\_L2}$			
		$Mean_1$	$RMSE_1$	$Mean_2$	$RMSE_2$	$Mean_1$	$RMSE_1$	$Mean_2$	$RMSE_2$
Iberian Peninsula	July, 2004	-0.020	0.023	-0.021	0.025	-0.031	0.034	-0.029	0.032
	July, 2005	-0.017	0.019	-0.020	0.023	-0.022	0.025	-0.023	0.027
	Total	-0.018	0.021	-0.020	0.024	-0.026	0.030	-0.026	0.029
Egypt & Middle East	July, 2004	-0.012	0.016	-0.012	0.016	-0.011	0.018	-0.012	0.018
	July, 2005	-0.010	0.017	-0.010	0.017	-0.006	0.014	-0.007	0.014
	Total	-0.011	0.016	-0.011	0.017	-0.009	0.016	-0.009	0.016

$Mean_1$ and $RMSE_1$ were calculated from all emissivity differences, while $Mean_2$ and $RMSE_2$ were calculated from the emissivity differences with QCs equal to zero.

Figure 6.20 displays the maps of the emissivities extracted from the MOD11_L2 ($\varepsilon_{31,MOD11\_L2}$ and $\varepsilon_{32,MOD11\_L2}$) in 2004 and 2005 and of the emissivity differences between ε_9 and $\varepsilon_{31,MOD11\_L2}$ and between ε_{10} and $\varepsilon_{32,MOD11\_L2}$. The emissivities $\varepsilon_{31,MOD11\_L2}$ and $\varepsilon_{32,MOD11\_L2}$ are close to 1.0 over the vegetated area, and greater than 0.96 over the bare areas. Former results reveal that $\varepsilon_{31,MOD11\_L2}$ and $\varepsilon_{32,MOD11\_L2}$ are overestimated. The emissivities ε_9 and ε_{10} are ~0.02 lower than $\varepsilon_{31,MOD11\_L2}$ and $\varepsilon_{32,MOD11\_L2}$ over the Iberian Peninsula area, respectively, while the differences are ~0.01 over the Egypt & Middle East area.

Figure 6.22 shows the histograms of the emissivity differences over the Iberian Peninsula area and the Egypt & Middle East area from -0.1 to 0.1 with an interval of 0.01 accoding to the QCs. The emissivity histograms also obey Gaussian distribution function (Equation (4.25)). Compared to the histograms of the emissiviity differences over the Egypt & Middle East area (Figure 6.22b & d), the histograms of the emissivity differences over the Iberian Peninsula area (Figure 6.22a & c) are much more clustered around the histogram peaks. For different types of emissivity difference, the histogram (c) and (d) are much more clustered around the histogram peaks than the histogram (a) and (b), respectively. This reveals that the emissivities in SEVIRI channels 9 and 10 (ε_9 and ε_{10}) are highly correlated to the ones extracted from the MOD11_L2 except the large differences between them. The high correlation may due to the similar BRDF models used in the emissivity retrievals. Over the Iberian Peninsula area, with a radius of 0.02 around the histogram peaks, there are 91.4% of (ε_9-$\varepsilon_{31,MOD11B1}$), 76.3% of (ε_{10}-$\varepsilon_{32,MOD11B1}$), 95.3% of (ε_9-$\varepsilon_{31,MOD11\_L2}$) and 91.2% of ($\varepsilon_{10}$-$\varepsilon_{32,MOD11\_L2}$). While, over the Egypt & Middle East area, within a radius of 0.02 around the histogram peaks, there are only 81.6% of (ε_9-$\varepsilon_{31,MOD11B1}$), 72.5% of (ε_{10}-$\varepsilon_{32,MOD11B1}$), 94.7% of (ε_9-$\varepsilon_{31,MOD11\_L2}$) and 93.5% ($\varepsilon_{10}$-$\varepsilon_{32,MOD11\_L2}$). For the emissivities with QCs equal to zero, the absolute differences between the emissivities estimated from the SEVIRI data and the ones extracted from MOD11_L2 become larger, and no obvious differences are found between the emissivities derived from the SEVIRI data and the ones extracted from MOD11B1. The histograms confirm that the emissivity differences over the Egypt & Middle East area are larger than the emissivity differences over the vegetated Iberian Peninsula area.

According to the MODIS UCSB Emissivity Library, most emissivities in the two split-window channels of the vegetation, soil and sand are greater than 0.95, and only some manmade materials have low emissivities. The average emissivity differences in the two split-window channels due to the spectral differences between SEVIRI and MODIS are less than 0.006, if the vegetation, soils and sand were taken into account. Because the spectral emissivity data were measured at a point with close distance by a spectrometer, the volumetric and geometric effects in the bi-directional reflectivities and non-Lambertian properties of land surface at satellite scale are seldom presented. Furthermore, the emissivity spectra derived from field measurement and airborne sensor may be different from the spectra derived from laboratory data because of atmospheric effects (Rivard et al., 1993). Emissivity may also vary with view zenith angles (Labed and Stoll, 1991; Rees and James, 1992). Petitcolin et al. (2002a & b) and Jiang et al. (2006) found that, when view zenith angle change from 0° to 60°, the decreases of the directional emissivities in the two split-window channels are up to 0.02 over the bare areas. Considering SEVIRI's view zenith angles over the two study areas (~45° over the Iberian Peninsula area and ~53° over the Egypt & Middle East area), the emissivities in SEVIRI channels 9 and 10 are reasonable. As Figure 4.24 indicated, the large emissivity differences may come from the errors in the atmospheric data.

LSTs and LST related parameters at Locations G, I and J (Table 4.8) on July 14 of 2004, July 16 of 2004, July 10 of 2005 and July 12, 2005 are shown in Figure 6.23, Figure 6.24 and Figure 6.25,

respectively. At Locations G and I, although the water vapor contents extracted from the MODIS/Terra water vapor product MOD05_L2 are always higher than the ones estimated from SEVIRI data, LSTs are not regular, because of different brightness temperatures at TOA, emissivities and view zenith angles. At the bare area Location J, $T_{s,SEVIRI}$ is always higher than $T_{s,MOD11\_L2}$, and most of $T_{s,SEVIRI}$ are higher than $T_{s,MOD11B1}$, mainly due to the obviously lower emissivities in SEVIRI channels 9 and 10.

Table 6.5 lists the averages and RMSEs of the LST differences from July 14 to 19 of 2004 and from July 10 to 14 of 2005 at Locations G, I and J. The absolute averages of ($T_{s,SEVIRI}$-$T_{s,MOD11B1}$) are less than 1.2 K, and the RMSEs range between 0.4 K and 1.7 K. At Location G and I, the absolute averages of ($T_{s,SEVIRI}$-$T_{s,MOD11\_L2}$) are less than 1.6 K, and RMSEs range between 0.8 K 1.7 K, while at Location J, the averages and RMSEs of ($T_{s,SEVIRI}$-$T_{s,MOD11\_L2}$) are higher than 2.0 K due to the overestimated emissivities over bare areas in MOD11_L2. Totally, the results at Locations G, I and J are consistant with the area-based results.

Table 6.5. Averages and RMSEs of LST differences from July 14 to 19 of 2004 and from July 10 to 14 of 2005 at Locations G, I and J *

		$T_{s,SEVIRI} - T_{s,MOD11B1}$ (K)		$T_{s,SEVIRI} - T_{s,MOD11\_L2}$ (K)	
		Mean	RMSE	Mean	RMSE
G	Day	-0.77	1.57	0.87	1.31
	Night	-1.00	1.67	1.58	1.67
I	Day	-0.45	0.82	-0.10	0.82
	Night	-1.15	1.17	0.00	1.10
J	Day	-0.60	1.52	2.63	2.79
	Night	-0.10	0.41	2.73	2.83

* Locations G, I and J are listed in Table 4.8.

In the LST and LSE comparisons, we found two strange results in the V4 MOD11B1 product except the time prolems mentioned above: (1) Over the Egypt & Middle East area, both the emissivities and LSTs extracted from MOD11B1 are, respectively, higher than the emissivities and LSTs estimated from the SEVIRI data. (2) The abnormal emissivities in a local area do not lead to abnormal LSTs, e.g., the emissivities and LSTs on July 17, 2004 over the Egypt & Middle East area (Figure 6.12 and Figure 6.18). In the SEVIRI LST retrieval by the generalized split-window algorithm, we did an experiment to substitute $\varepsilon_{31,MOD11B1}$ and $\varepsilon_{32,MOD11B1}$ for ε_9 and ε_{10}, respectively, without considering the effects of view zenith angles and spectral differences, no obvious improvement had been observed in the temperature differences between $T_{s,SEVIRI}$ and $T_{s,MOD11B1}$, and the abnormal emissivities did cause obviously abnormal LSTs. In a personal communication, Dr. Wan at University of California, Santa Barbara said that, in the V4 MOD11B1 product, the emissivities in MODIS channels 31 and 32 may have large errors due to the influence of cloud contaminations, and the LST in MOD11B1 is retrieved by seven channels, rather than only two channels used by the split-window method. The experiment shows that the emissivity differences are not the single factor leading to the temperature differences between $T_{s,SEVIRI}$ and $T_{s,MOD11B1}$.

The view angles impact on the estimated LSTs in two folds: (1) Satellite images covering the same area with different view angles contain different land surface information because of the 3-demension structures of land surface. (2) The errors intrinsic to the LST retrieval methods are usually proportional

to the view zenith angles. We did a statistical analysis between the temperature differences ($T_{s,SEVIRI}$-$T_{s,MOD11B1}$) and the view zenith angle differences over the two study areas, and no obvious relationship has been found. Nowadays, the impact of the view azimuth angles on LST retrievals is little known.

The different pixel aggregation methods and cloud masks used in this work and in the day/night algorithm may be also the reasons leading to the temperature differences.

Actually, the temperature differences are synthetical results of the brightness temperatures at TOA, the directional emissivities, view zenith angles, atmospheric data and the algorithms etc. Because we have no adequate observations to separate these factors, it is hard to give quantitative analytical results how much error each factor contributes.

Totally, the SEVIRI LSTs estimated by the generalized split-window algorithm are consistent with the LSTs extracted from the MODIS/Terra LST products and the AATSR Forward LST derived by the generalized split-window algorithm with an averge accuracy of 1-2 K in daytime and nighttime over the vegetated area and bare area.

6.5 Summary and conclusions

In this chapter, the SEVIRI LSTs estimated by the generalized split-window algorithm ($T_{s,SEVIRI}$) were cross-validated with the LSTs extracted from the MODIS/Terra LST products ($T_{s,MOD11B1}$ and $T_{s,MOD11\_L2}$) and the AATSR Forward LSTs derived by the generalized split-window algorithm ($T_{s,AATSR\_Forward}$) over the Iberian Peninsula area and the Egypt & Middle East area in July of 2004 and July of 2005 . In order to carry out the comparisons, the average-weighted pixel aggregation method was used again to put the SEVIRI data and the AATSR data into the MODIS sinusoidal grid projection.

The LST cross-validations were carried out for the entire study areas and for the LSTs with QCs equal to zero, respectively. Over the vegetated Iberian Peninsula area, when $T_{s,SEVIRI}$ is compared to $T_{s,MOD11B1}$, in the daytime, the average of the temperature differences (mean) is less than 0.8 K, and the RMSE are ~2.6 K, while at night, the mean and RMSE are less than 0.4 K and 2.1 K, respectively. When $T_{s,SEVIRI}$ is compared to $T_{s,MOD11\_L2}$, the mean changes between 0.9 K and 2.3 K and RMSE varies between 1.9 K and 3.2 K, which is basically consistent with the results of Wan et al. (2002). The results indicate that, generally speaking, the temperature differences in daytime are larger than the temperature differences at night, and the temperature differences between $T_{s,SEVIRI}$ and $T_{s,MOD11B1}$ are smaller than the temperature differences between $T_{s,SEVIRI}$ and $T_{s,MOD11\_L2}$. When $T_{s,SEVIRI}$ is compared to the AATSR Forward LST estimated by the generalized split-window algorithm ($T_{s,AATSR\_Forward}$), $T_{s,SEVIRI}$ is averagely 1.26 K higher than $T_{s,AATSR\_Forward}$ with a RMSE of 2.4 K in the daytime, and the mean and RMSE of the temperature differences are, respectively, reduced to 0.3 K and 1.6 K at night (21:46UTC). The temperature differences between $T_{s,SEVIRI}$ and $T_{s,AATSR\_Forward}$ wer mainly caused by the view zenith angles. Totally, $T_{s,SEVIRI}$ and $T_{s,AATSR\_Forward}$ are consistent.

Over the Egypt & Middle East area, in the daytime, $T_{s,SEVIRI}$ is averagely 1.5 K lower than the $T_{s,MOD11B1}$ and the average RMSE is 2.5 K. The $T_{s,SEVIRI}$ is averagely 0.2 K higher than the $T_{s,MOD11B1}$ and the average RMSE is 1.9 K at night. Similar to the results over the Iberian Peninsula area, the $T_{s,MOD11\_L2}$ is still lower than $T_{s,SEVIRI}$, but the LST differences are much larger: the mean is up to 2.5 K and the RMSE is up to 3.5 K. The large temperature differences between $T_{s,SEVIRI}$ and $T_{s,MOD11\_L2}$ usually appear in the desert regions.

The histograms of the temperature differences over the two study area show that the temperature differences obey Gaussian distribution function. Compared to the histograms of the temperature differences over the Egypt & Middle East area, the histograms of the temperature differences over the Iberian Peninsula area are much more clustered around the peak. In general speaking, the histogram results are consistent with the maps of the temperature differences.

In order to further investigate the source of the temperature differences, we analyzed the factors which may lead to temperature differences: the brightness temperatures at TOA, the emissivities, view zenith angles, atmospheric water vapor content and the algorithms itself. The effects of the emissivity differences and the view zenith angle differences were emphasized.

Maps of the emissivities and emissivity differences in the two two split-window channels of the SEVIRI and MODIS show that the ε_9 is ~0.01 lower than $\varepsilon_{31,MOD11B1}$, and ε_{10} is ~0.02 lower than $\varepsilon_{32,MOD11B1}$. The emissivities ε_9 and ε_{10} are ~0.02 lower than $\varepsilon_{31,MOD11\_L2}$ and $\varepsilon_{32,MOD11\_L2}$ over the Iberian Peninsula area, respectively, while the emissivity differences are ~0.01 over the Egypt & Middle East area. The histograms of the emissivity differences also obey Gaussian distribution function, and reveal that the emissivities in SEVIRI channels 9 and 10 (ε_9 and ε_{10}) are highly correlated to the ones extracted from the MOD11_L2 except the large offsets between them. According to the MODIS UCSB Emissivity Library and the non-Lambertian properties of land surface, the emissivities in SEVIRI channels 9 and 10 are reasonable.

The comparisons of LSTs and LST related parameters at Location G, I and J (Table 4.8) were also carried out. Totally, the results at Locations G, I and J are consistant with the area-based results.

The cross-validations of LSTs and LSEs between the SEVRIR and MODIS reveal two problems in the V4 MOD11B1 product: (1) Over the Egypt & Middle East area, both the emissivities and LSTs extracted from the MOD11B1 are, respectively, higher than the emissivities and LSTs estimated from the SEVIRI data. (2) The abnormal emissivities in a local area do not lead to abnormal LSTs. Our experiment shows that the emissivity differences are not the single factor leading to the temperature differences between $T_{s,SEVIRI}$ and $T_{s,MOD11B1}$, and the abnormal emissivities did cause obviously abnormal LSTs.

The impact of the view zenith angle then was analyzed. We did a statistical analysis between the temperature differences ($T_{s,SEVIRI}$-$T_{s,MOD11B1}$) and the view zenith angle differences over the two study areas, and no obvious relationship has been found. Other reasons leading to the temperature differences may come from the pixel aggregation and cloud masks.

Actually, the temperature differences are synthetical results of the brightness temperatures at TOA, the directional emissivities, view zenith angles, atmospheric data and the algorithms etc. Because we have no adequate observations to separate these factors, it is hard to give quantitative analytical results how much error each factor contributes. Totally, the SEVIRI LSTs are consistent with the LSTs extracted from the MODIS/Terra LST products and the AATSR Forward LST derived by the generalized split-window algorithm with an averge accuracy of 1-2 K in both daytime and nighttime over the vegetated area and bare area.

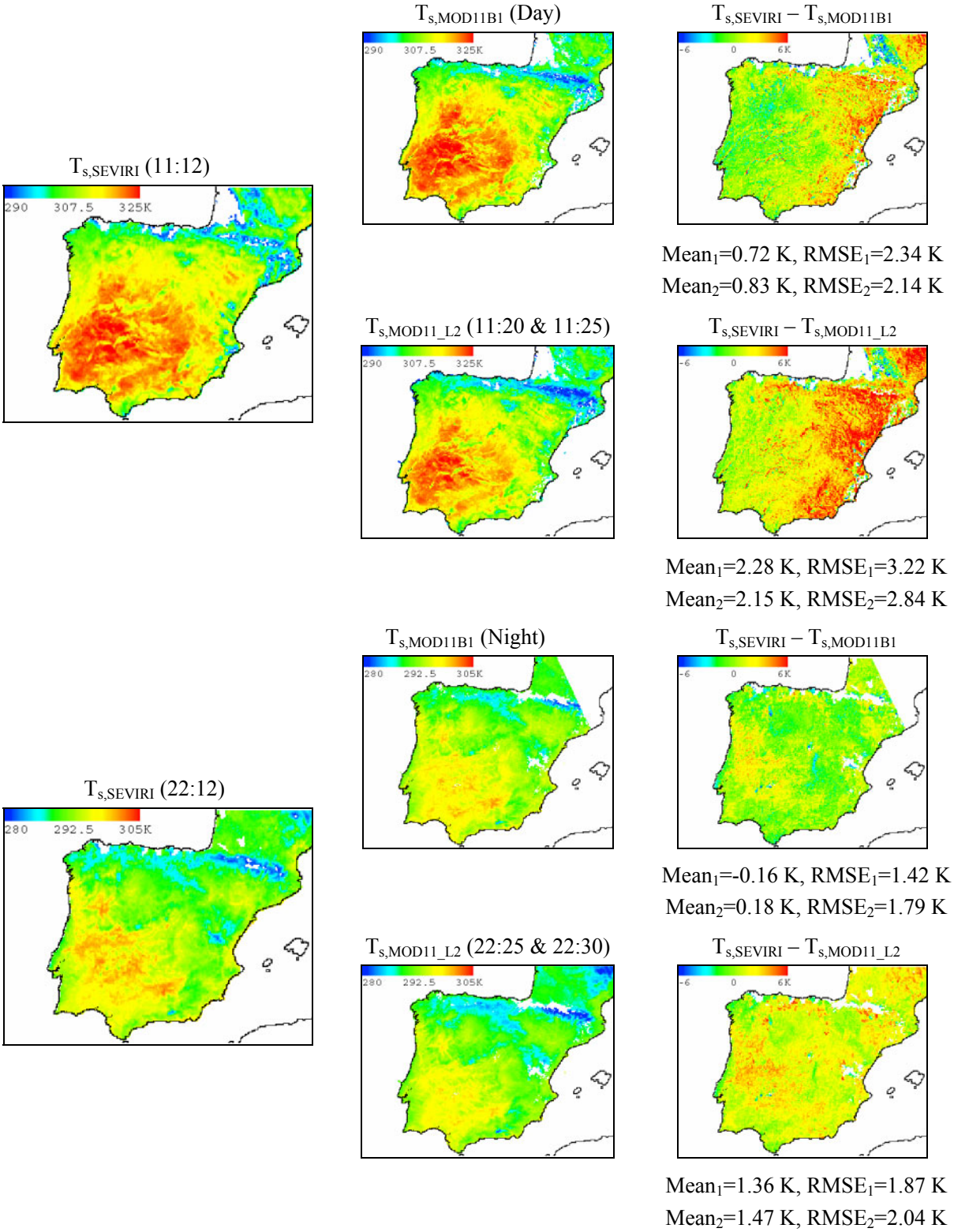

Figure 6.6. Maps of the SEVIRI LSTs and the MODIS/Terra LSTs and the temperature differences over the Iberian Peninsula area on July 14, 2004
($T_{s,SEVIRI}$ represents the SEVIRI LST estimated by the generalized split-window algorithm; $T_{s,MOD11B1}$ and $T_{s,MOD11\_L2}$ stand for the LSTs extracted from the MODIS/Terra LST products MOD11B1 and MOD11_L2, respectively; Time: the scan starting time of the disc for SEVIRI and the granule time for MODIS/Terra; $Mean_1$ and $RMSE_1$ were calculated from all LST differences, while $Mean_2$ and $RMSE_2$ were calculated from the LST differences with QCs equal to zero)

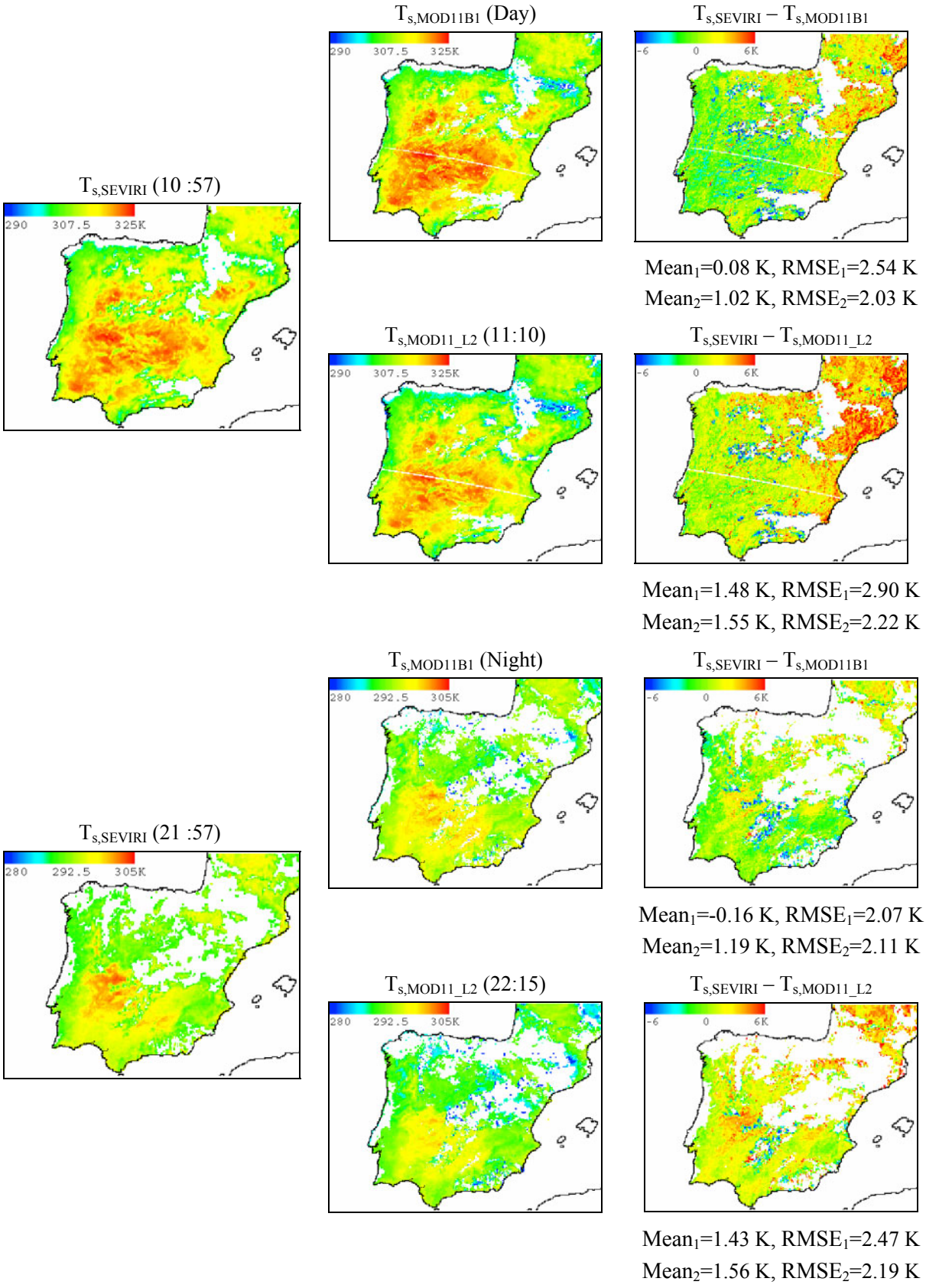

Figure 6.7. Same as the ones in Figure 6.6, but on July 16, 2004

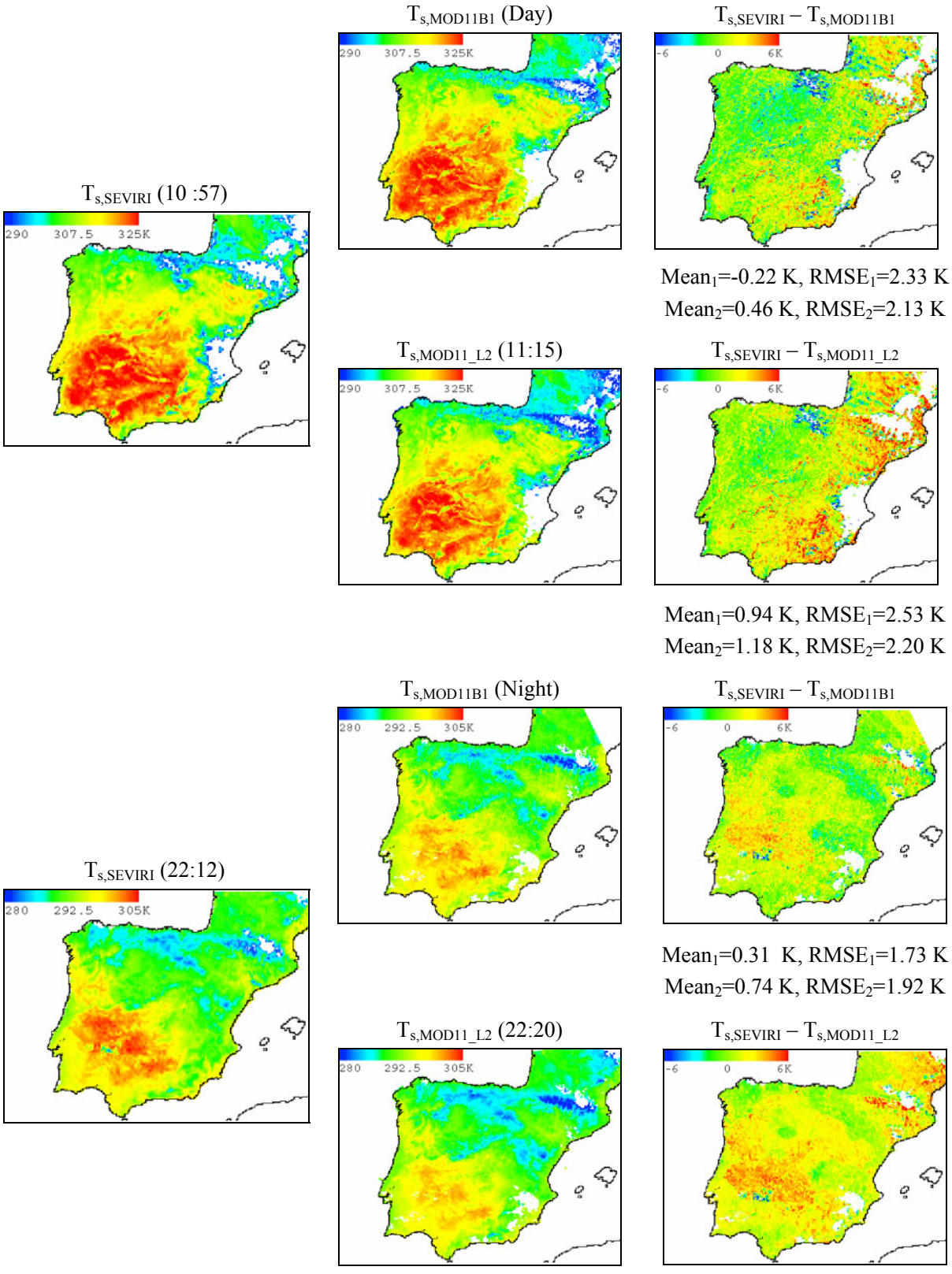

Figure 6.8. Same as the ones in Figure 6.6, but on July 10, 2005

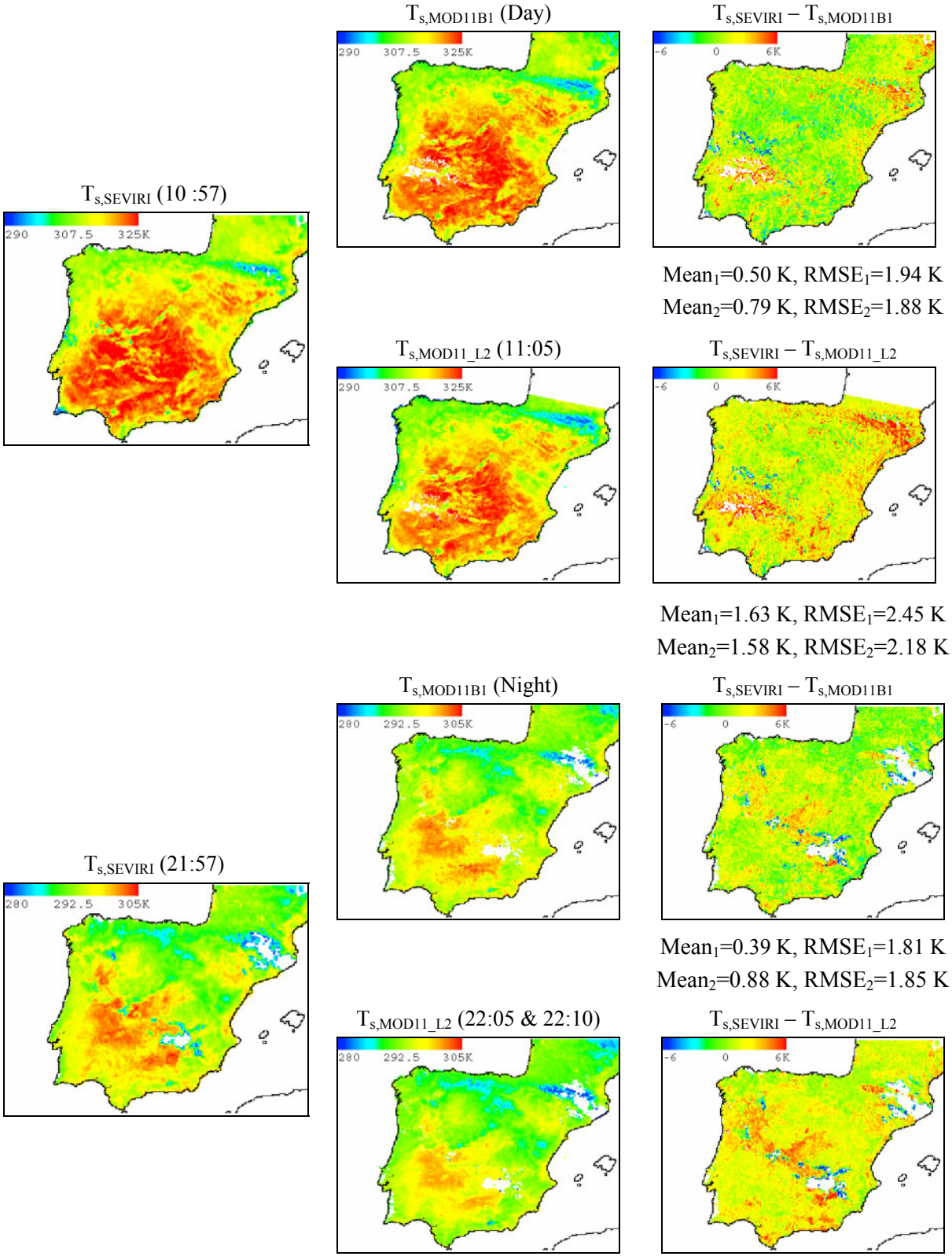

Figure 6.9. Same as the ones in Figure 6.6, but on July 12, 2005

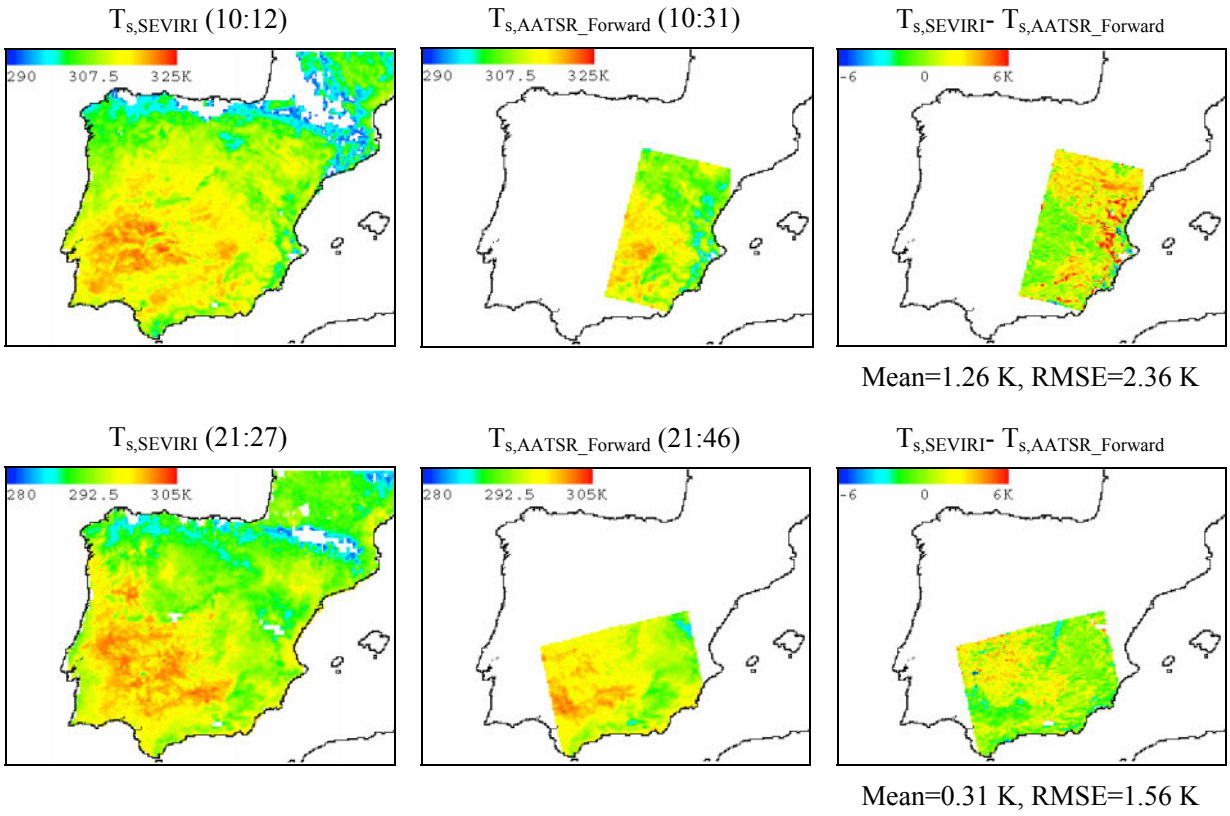

Figure 6.10. Maps of the SEVIRI LSTs and AATSR Forward LSTs and the differences between them over the Iberian Peninsula area on July 14, 2004
($T_{s,SEVIRI}$ is the same as the one in Figure 6.6 and $T_{s,\ AATSR\_Forward}$ represent the AATSR Forward LST estimated by the generalized split-window algorithm)

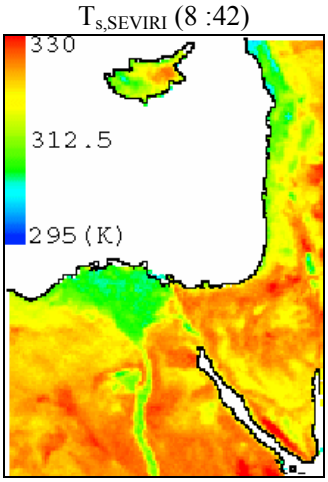

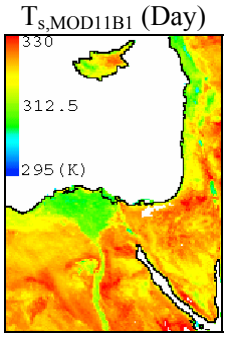

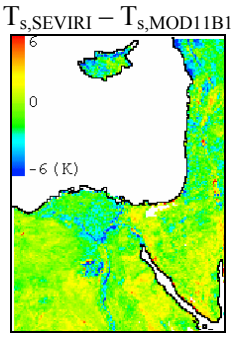

$Mean_1$=-0.68 K, $RMSE_1$=1.90 K
$Mean_2$=-0.67 K, $RMSE_2$=1.76 K

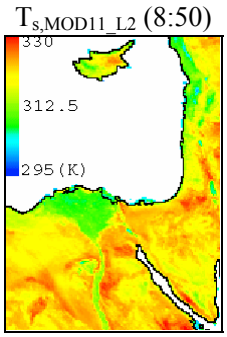

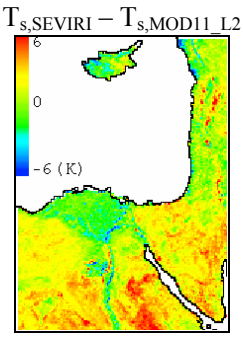

$Mean_1$=1.31 K, $RMSE_1$=2.43 K
$Mean_2$=1.22 K, $RMSE_2$=2.29 K

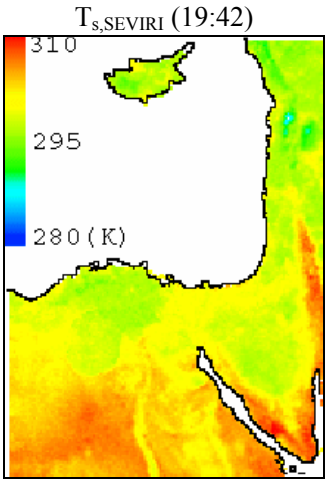

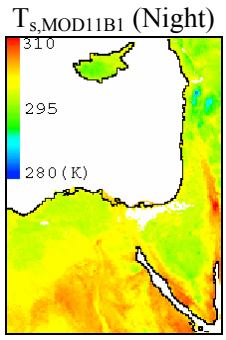

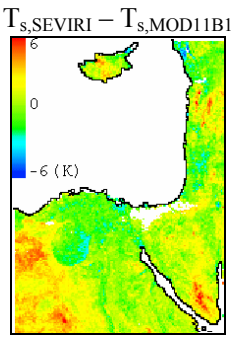

$Mean_1$=0.52 K, $RMSE_1$=1.81 K
$Mean_2$=0.70 K, $RMSE_2$=1.87 K

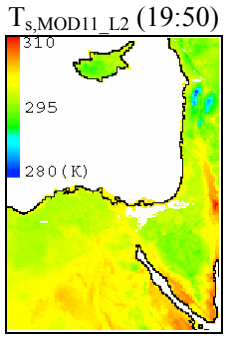

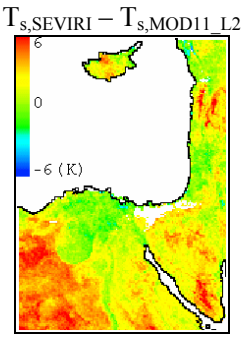

$Mean_1$=1.98 K, $RMSE_1$=2.72 K
$Mean_2$=1.82 K, $RMSE_2$=2.57 K

Figure 6.11. Maps of the SEVIRI LSTs and the MODIS LSTs and the differences between them over the Egypt & Middle East area on July 15, 2004
(Meanings of the symbols are the same as the ones in Figure 6.6)

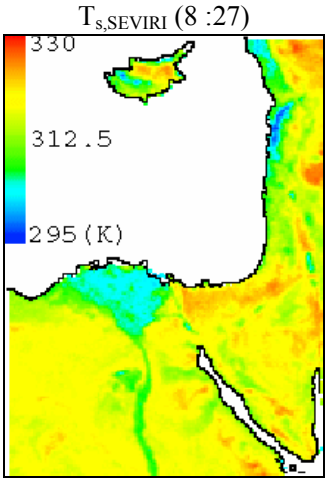

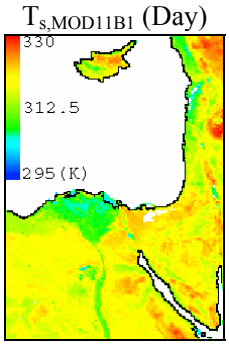

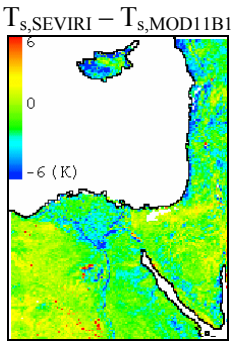

$Mean_1$=-1.35 K, $RMSE_1$=2.36 K
$Mean_2$=-0.47 K, $RMSE_2$=2.23 K

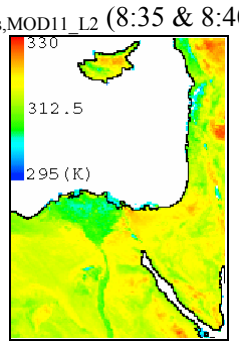

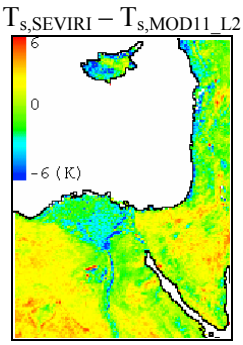

$Mean_1$=0.23 K, $RMSE_1$=2.19 K
$Mean_2$=0.69 K, $RMSE_2$=2.18 K

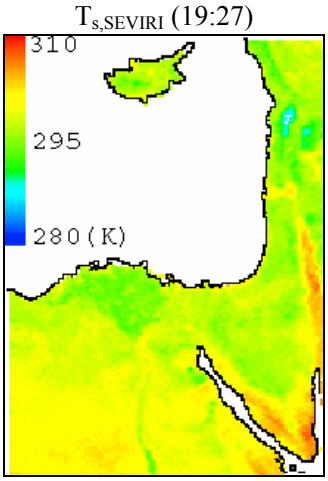

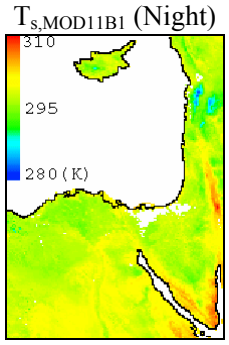

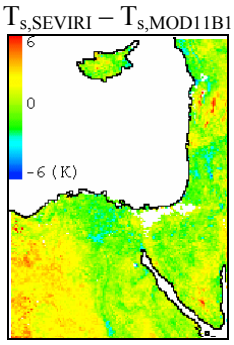

$Mean_1$=0.47 K, $RMSE_1$=1.66 K
$Mean_2$=0.60 K, $RMSE_2$=1.79 K

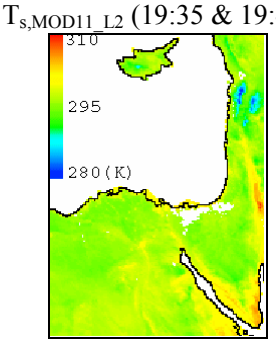

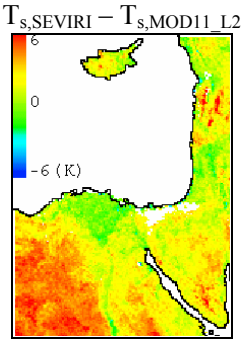

$Mean_1$=2.13 K, $RMSE_1$=2.79 K
$Mean_2$=1.88 K, $RMSE_2$=2.66 K

Figure 6.12. Same as the ones in Figure 6.11, but on July 17, 2004

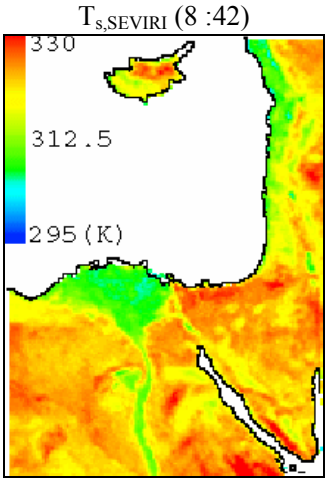

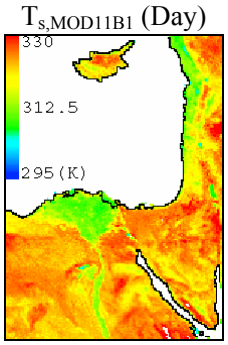

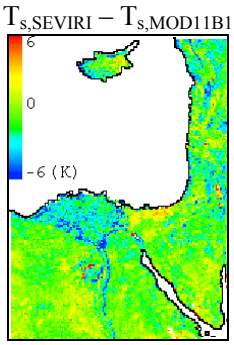

$Mean_1$=-1.31 K, $RMSE_1$=2.27 K
$Mean_2$=-0.95 K, $RMSE_2$=2.05 K

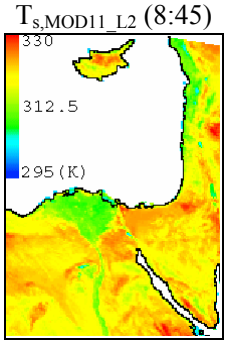

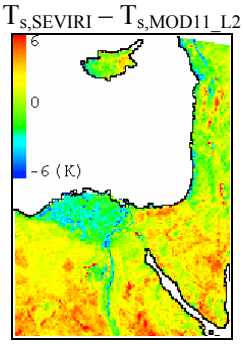

$Mean_1$=1.22 K, $RMSE_1$=2.51 K
$Mean_2$=1.31 K, $RMSE_2$=2.43 K

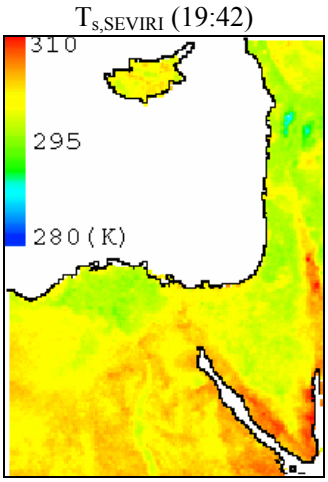

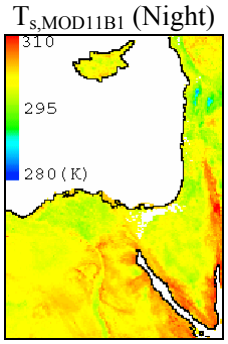

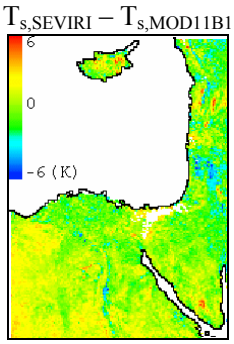

$Mean_1$=-0.11 K, $RMSE_1$=1.56 K
$Mean_2$=1.31 K, $RMSE_2$=2.42 K

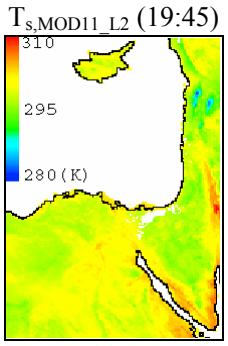

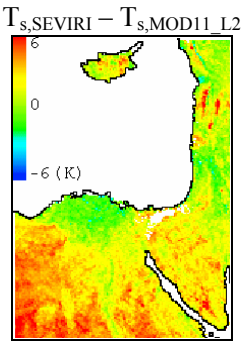

$Mean_1$=2.03 K, $RMSE_1$=2.76 K
$Mean_2$=1.88 K, $RMSE_2$=2.68 K

Figure 6.13. Same as the ones in Figure 6.11, but on July 11, 2005

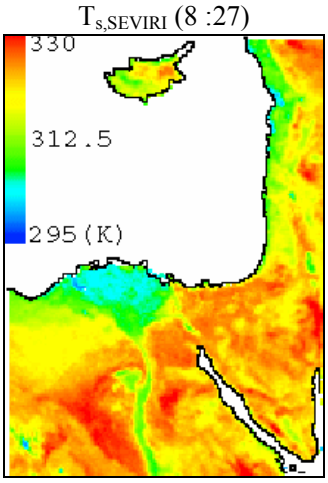

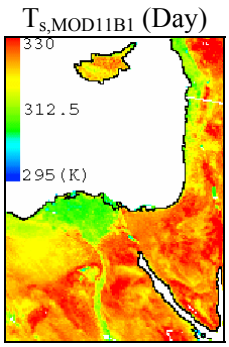

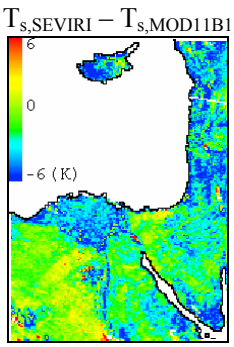

$Mean_1$=-2.67 K, $RMSE_1$=3.65 K
$Mean_2$=-1.38 K, $RMSE_2$=2.76 K

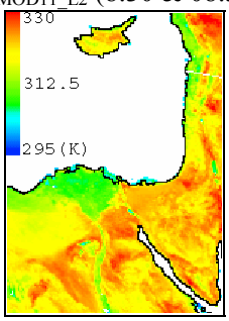

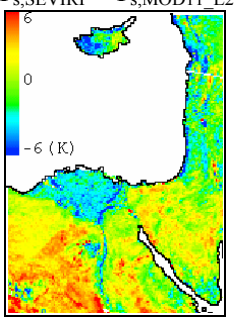

Mean1=0.11 K, RMSE1=2.81 K
Mean2=0.53 K, RMSE2=2.54 K

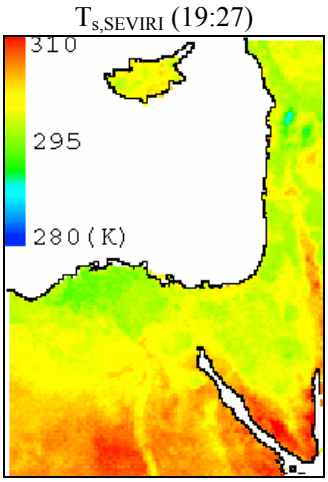

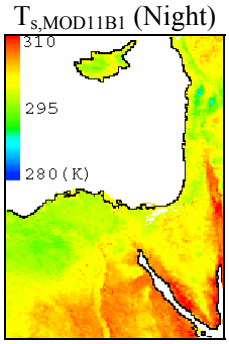

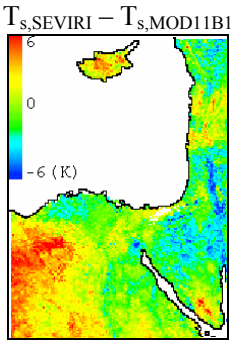

$Mean_1$=-0.02 K, $RMSE_1$=2.66 K
$Mean_2$=0.06 K, $RMSE_2$=2.54 K

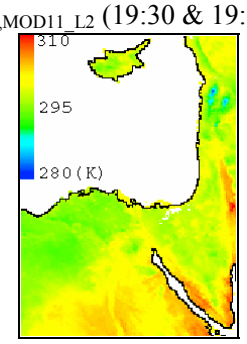

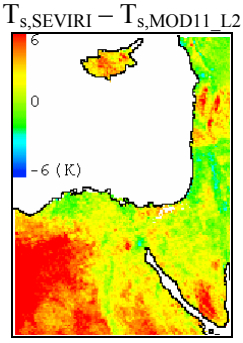

$Mean_1$=2.44 K, $RMSE_1$=3.45 K
$Mean_2$=1.73 K, $RMSE_2$=2.71 K

Figure 6.14. Same as the ones in Figure 6.11, but on July 13, 2005

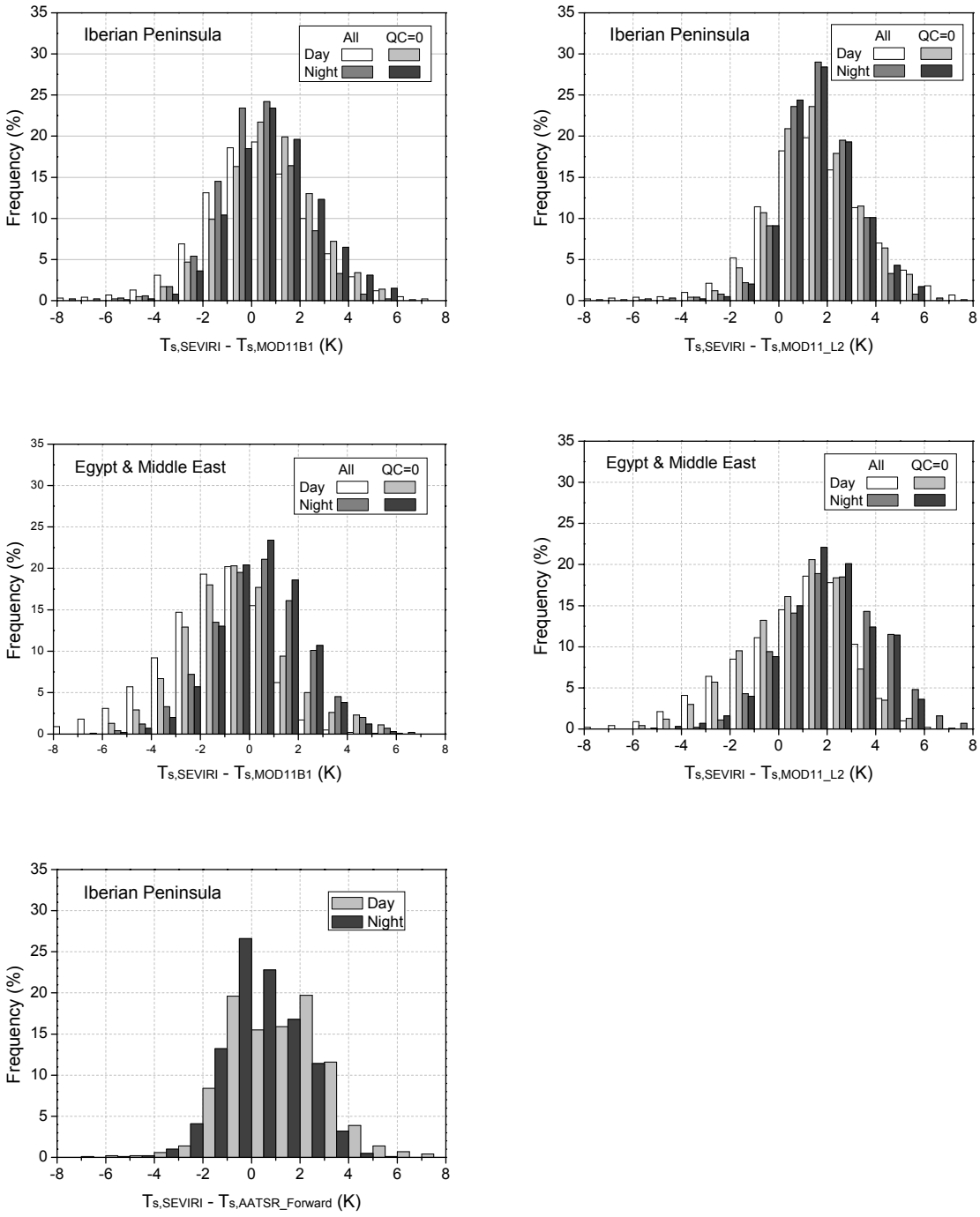

Figure 6.15. Histograms of the temperature differences over the Iberian Peninsula area and the Egypt & Middle East area
(QC is the acronym of Quality Control in MODIS/Terra LST products)

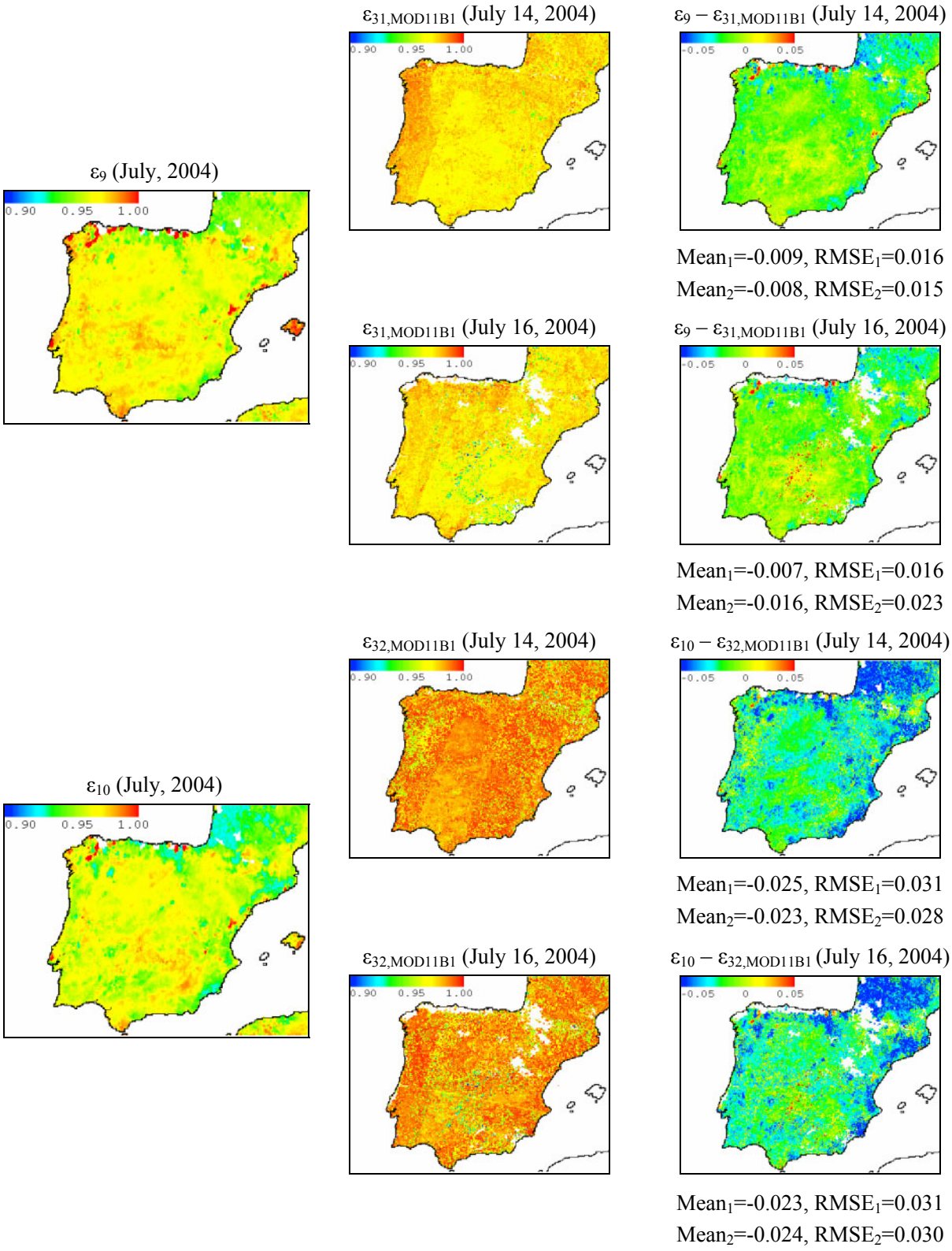

Figure 6.16. Maps of the emissivities estimated from the SEVIRI data or extracted from MOD11B1 and the differences between them over the Iberian Peninsula area on July 14, 2004 and July 16, 2004 ($Mean_1$ and $RMSE_1$ were calculated from all emissivity differences, while $Mean_2$ and $RMSE_2$ were calculated from the emissivity differences with QCs equal to zero)

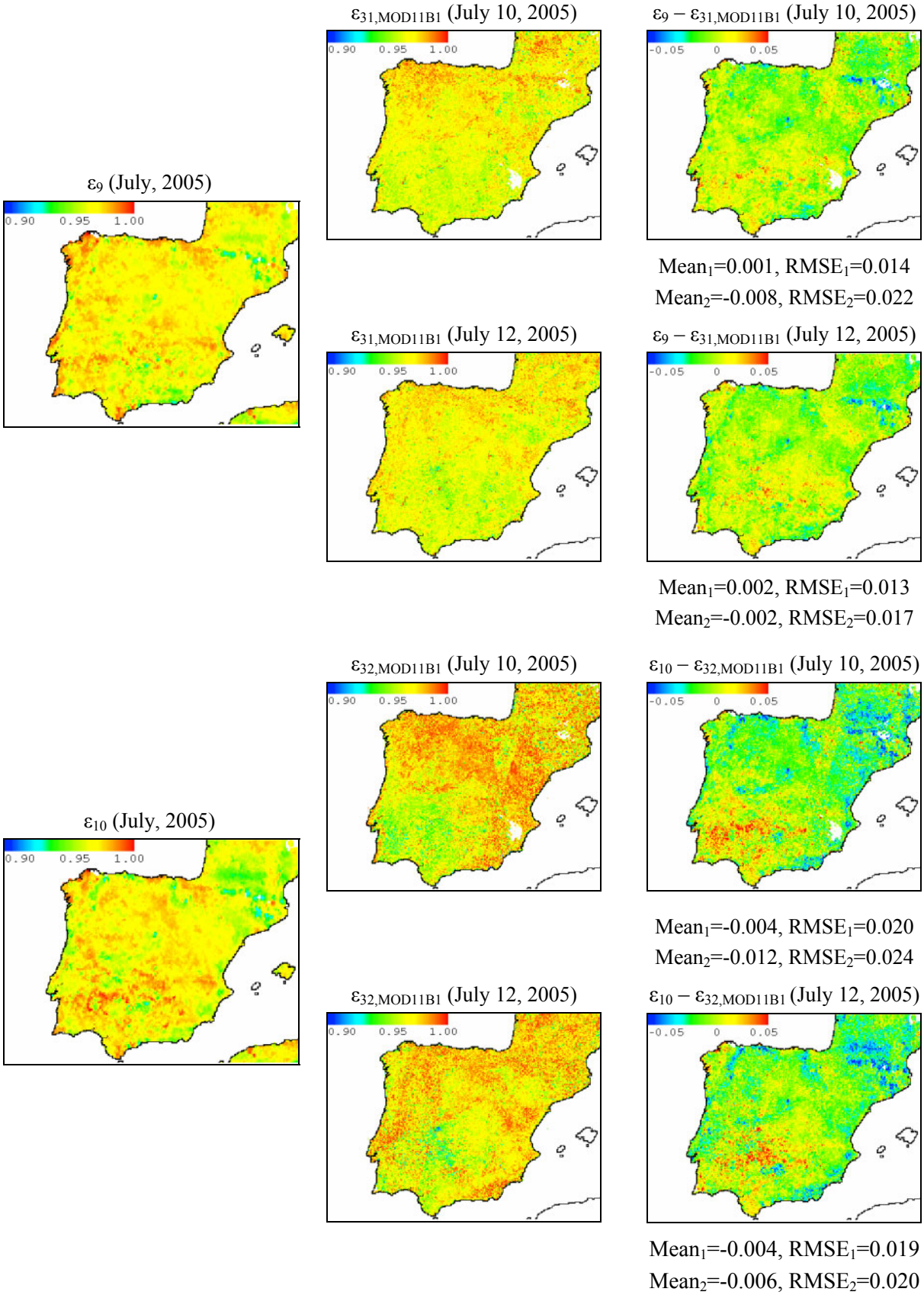

Figure 6.17. Same as the ones in Figure 6.16, but on July 10, 2005 and July 12, 2005

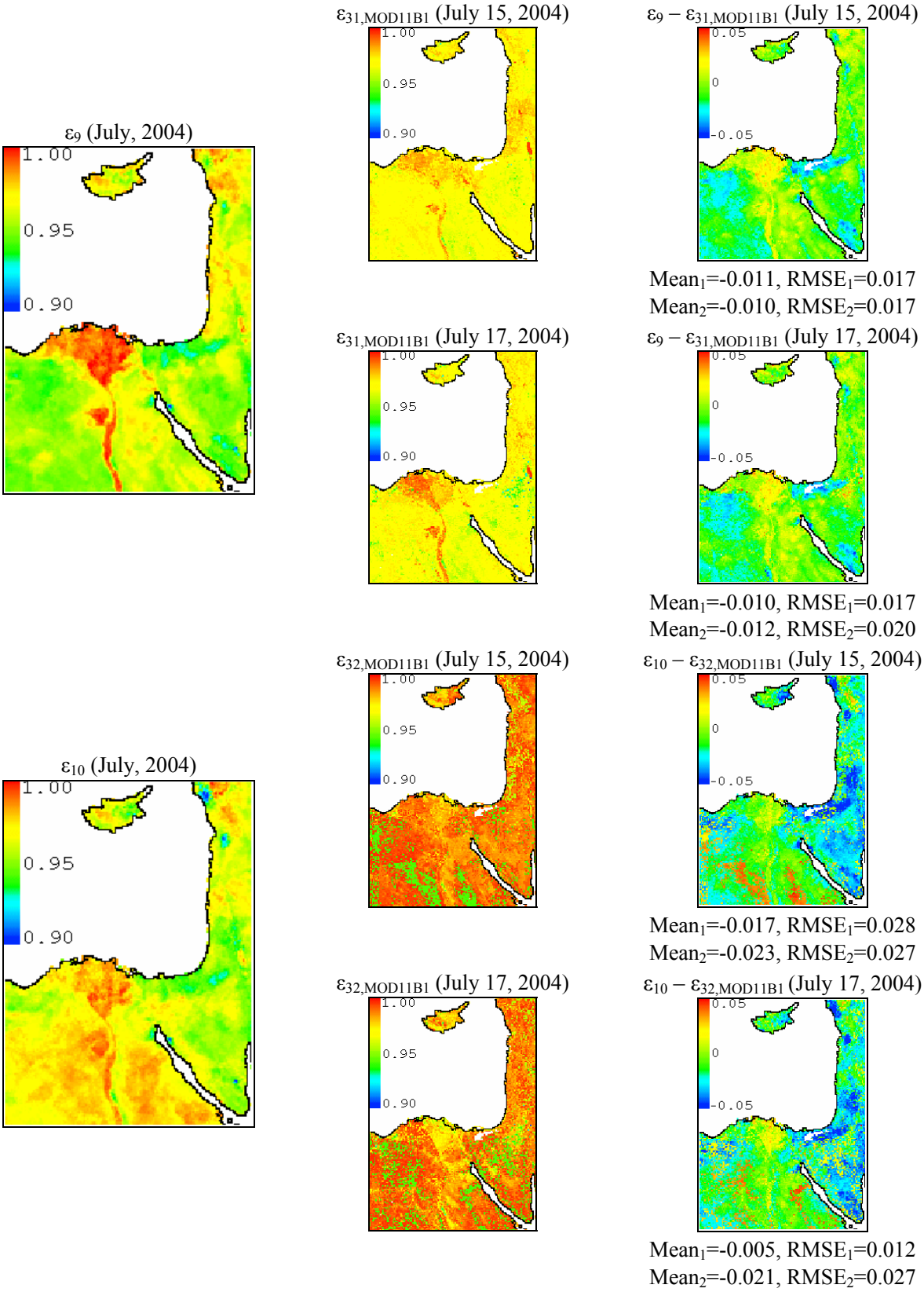

Figure 6.18. Maps of the emissivities estimated from the SEVIRI data or extracted from MOD11B1 and the emissivity differences over the Egypt & Middle East area on July 15, 2004 and July 17, 2004 ($Mean_1$ and $RMSE_1$ were calculated from all emissivity differences, while $Mean_2$ and $RMSE_2$ were calculated from the emissivity differences with QCs equal to zero)

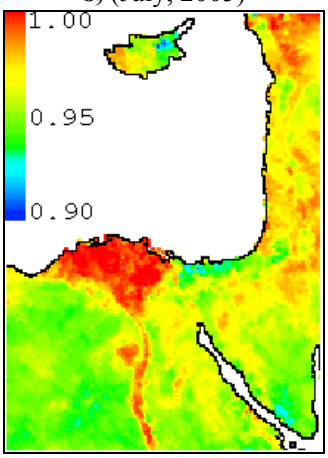

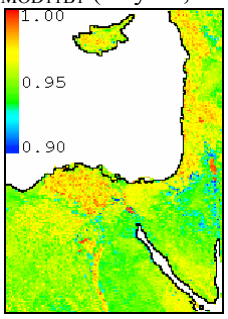

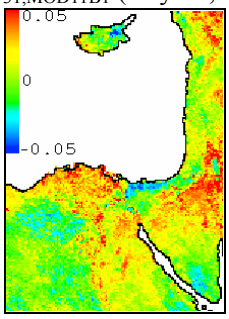

Mean$_1$=0.007, RMSE$_1$=0.021
Mean$_2$=0.004, RMSE$_2$=0.022

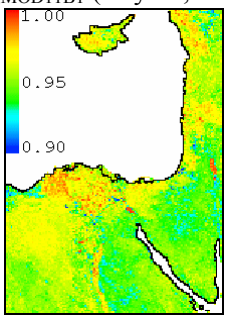

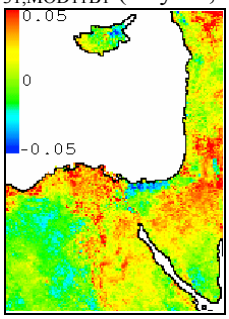

Mean$_1$=0.008, RMSE$_1$=0.022
Mean$_2$=0.006, RMSE$_2$=0.022

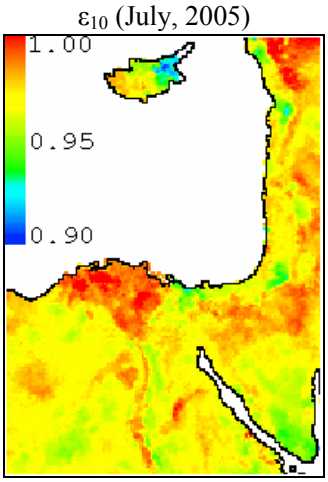

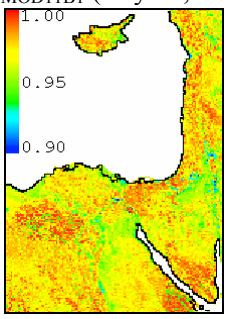

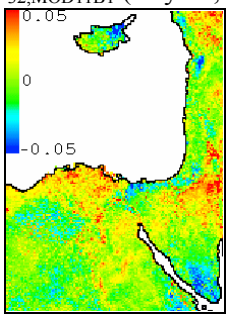

Mean$_1$=0.001, RMSE$_1$=0.019
Mean$_2$=-0.002, RMSE$_2$=0.020

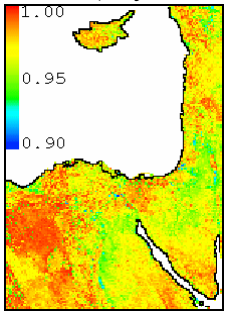

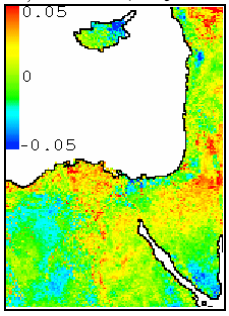

Mean$_1$=0.001, RMSE$_1$=0.019
Mean$_2$=-0.001, RMSE$_2$=0.020

Figure 6.19. Same as the ones in Figure 6.18, but on July 11, 2005 and July 13, 2005

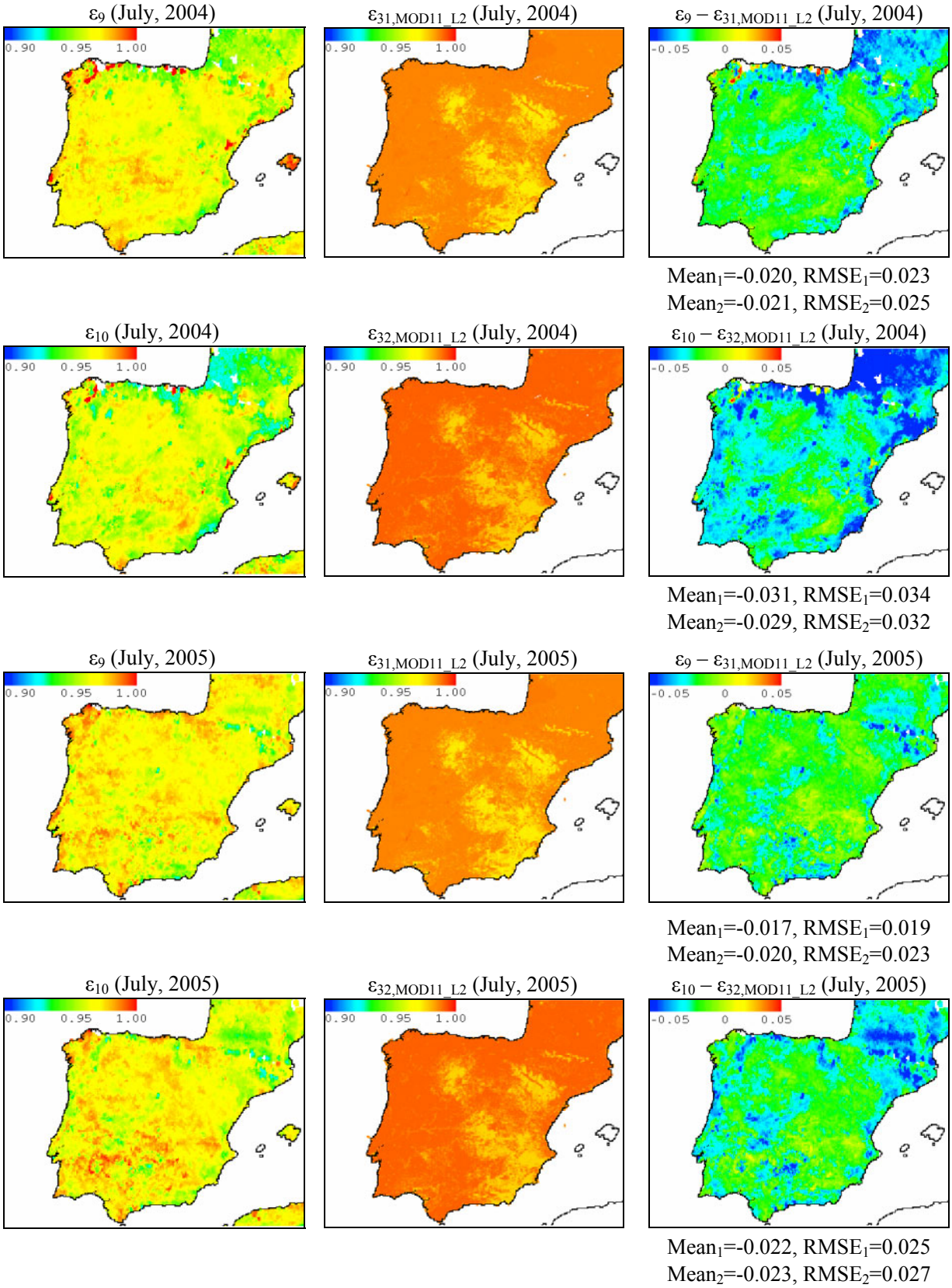

Figure 6.20. Maps of the emissivities derived from the SEVIRI data and extracted from MOD11_L2 and the emissivity differences over the Iberian Peninsula area in July of 2004 and July of 2005

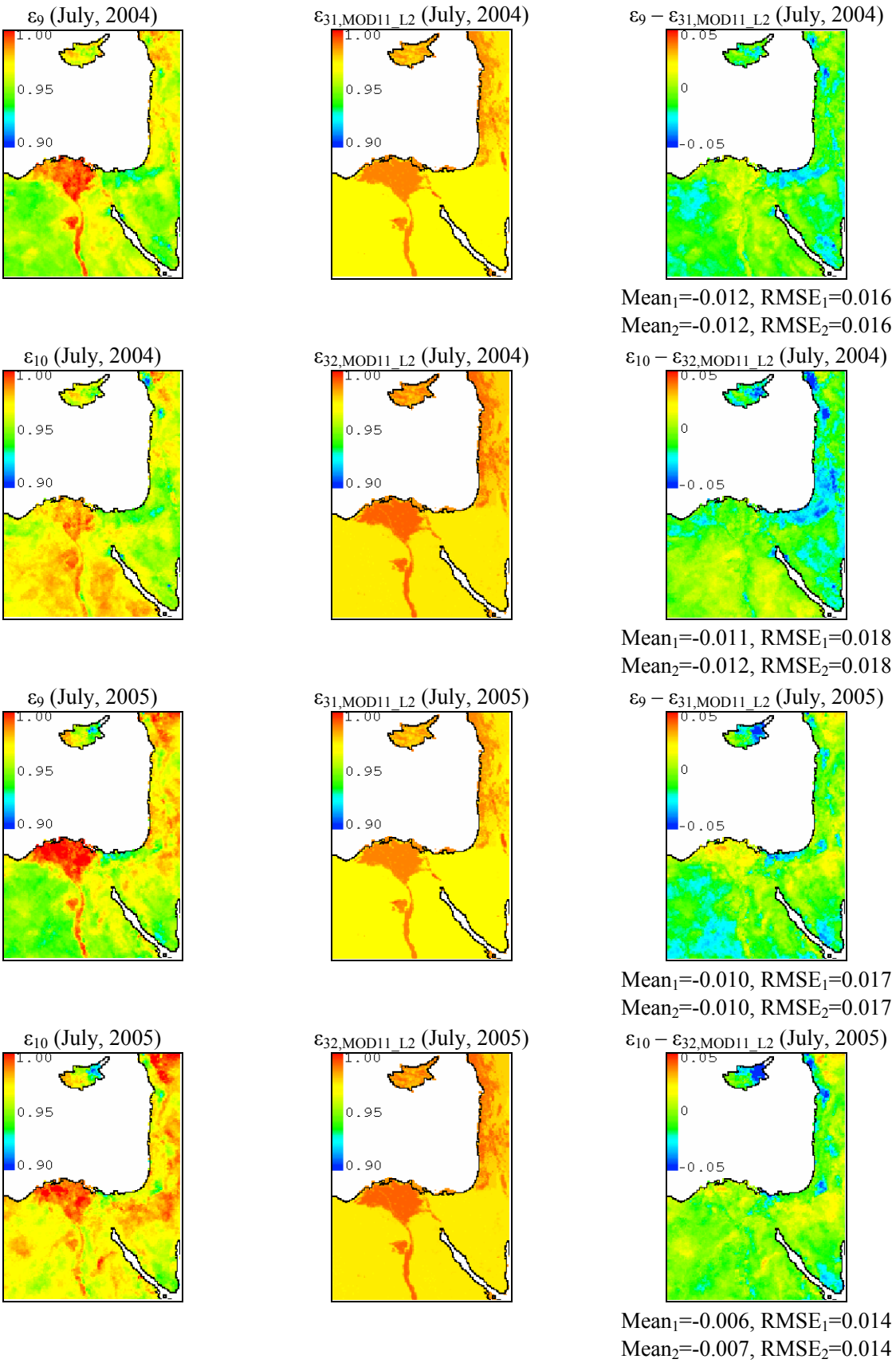

Figure 6.21. Maps of the emissivities derived from the SEVIRI data and extracted from MOD11_L2 and the emissivity differences over the Egypt & Middle East area in July of 2004 and July of 2005

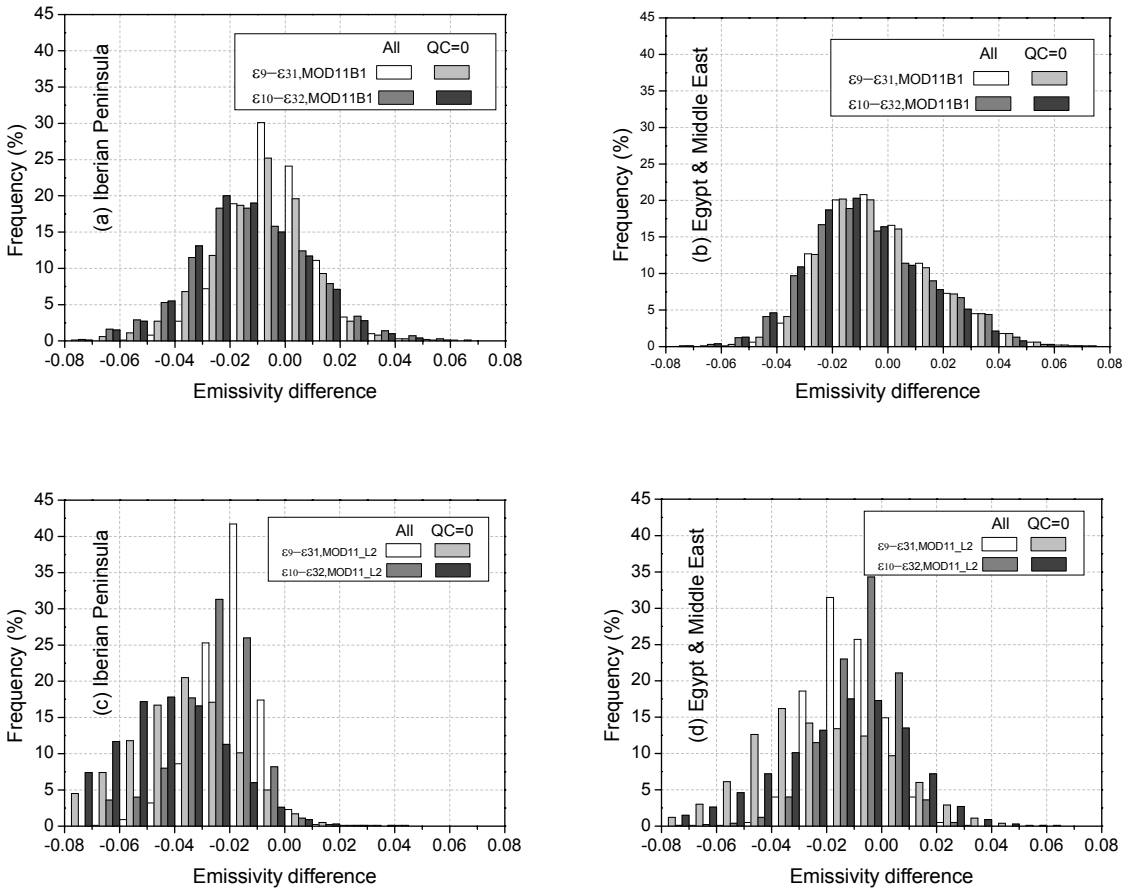

Figure 6.22. Histograms of the emissivity differences over the Iberian Peninsula area and the Egypt & Middle East area
(QC is the acronym of Quality Control in MODIS/Terra LST products)

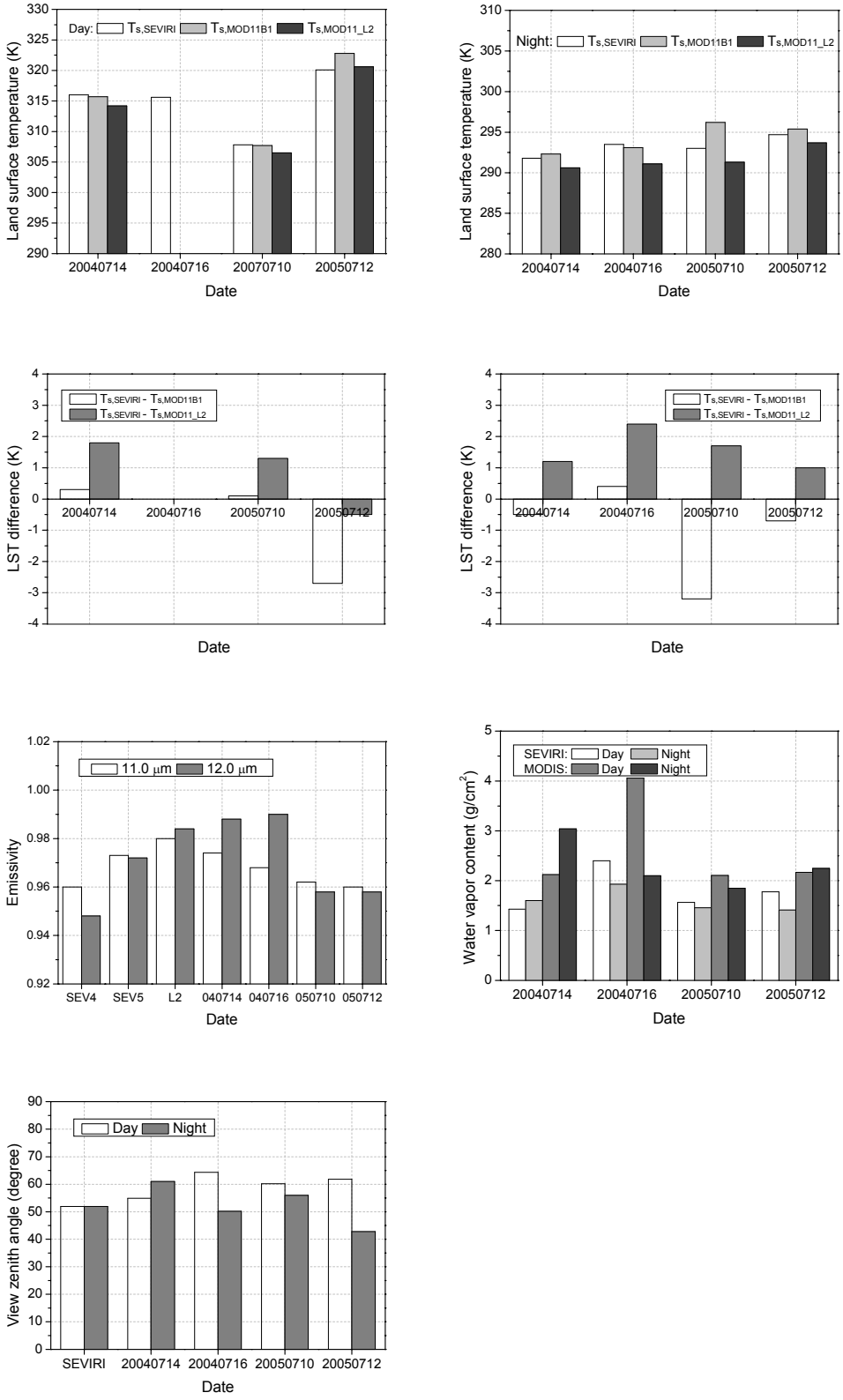

Figure 6.23. LSTs and LST related parameters at Location G (Barrax site: (2.07W, 39.03N)) from July 14 to 19, 2004 and from July 10 to 14, 2005
(SEV4 and SEV5 are the abbreviations of SEVIRI in 2004 and 2005, respectively; L2 stands for MOD11_L2)

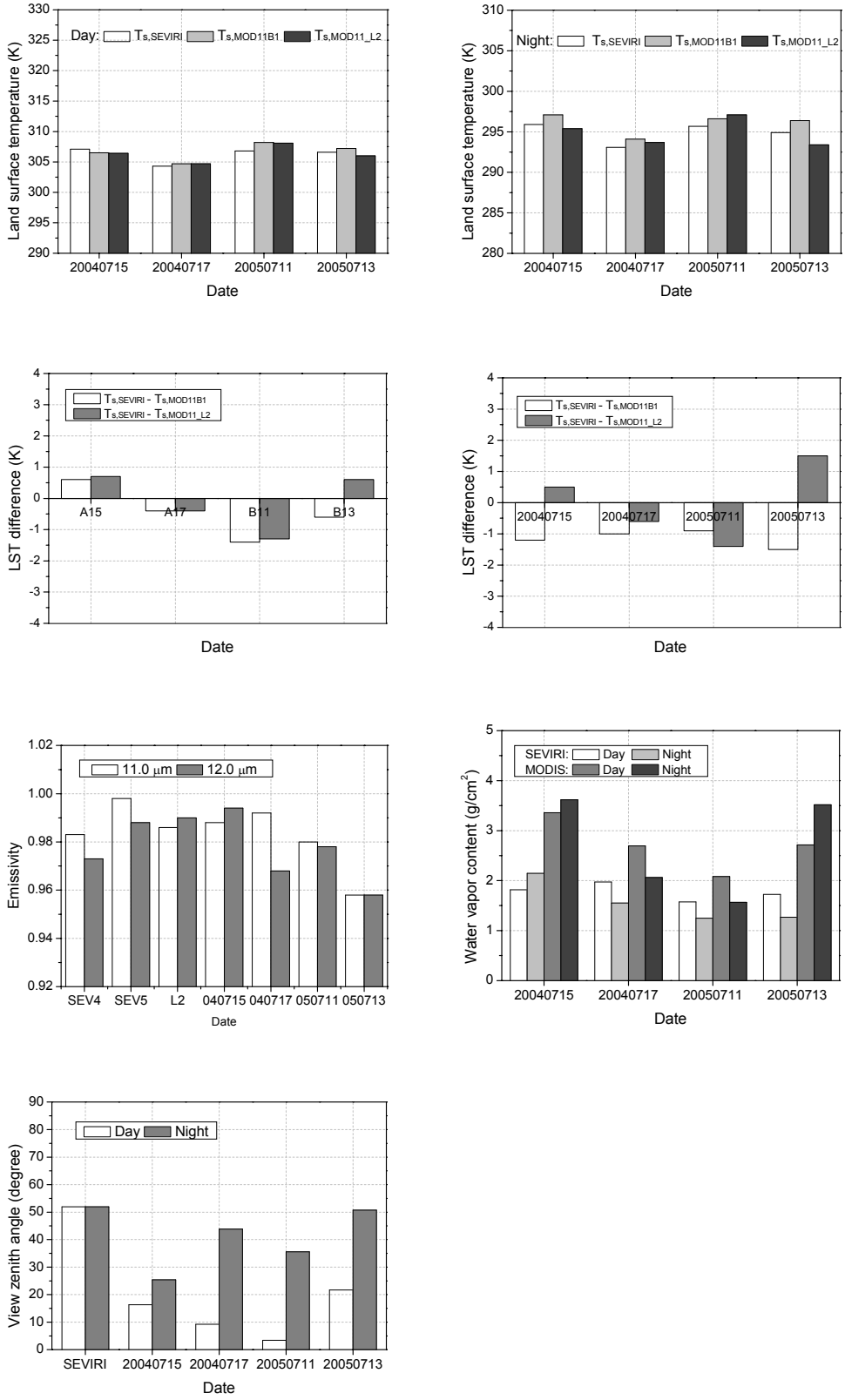

Figure 6.24. Same as the ones in Figure 6.23, but at Location I (30.96E, 30.90N)

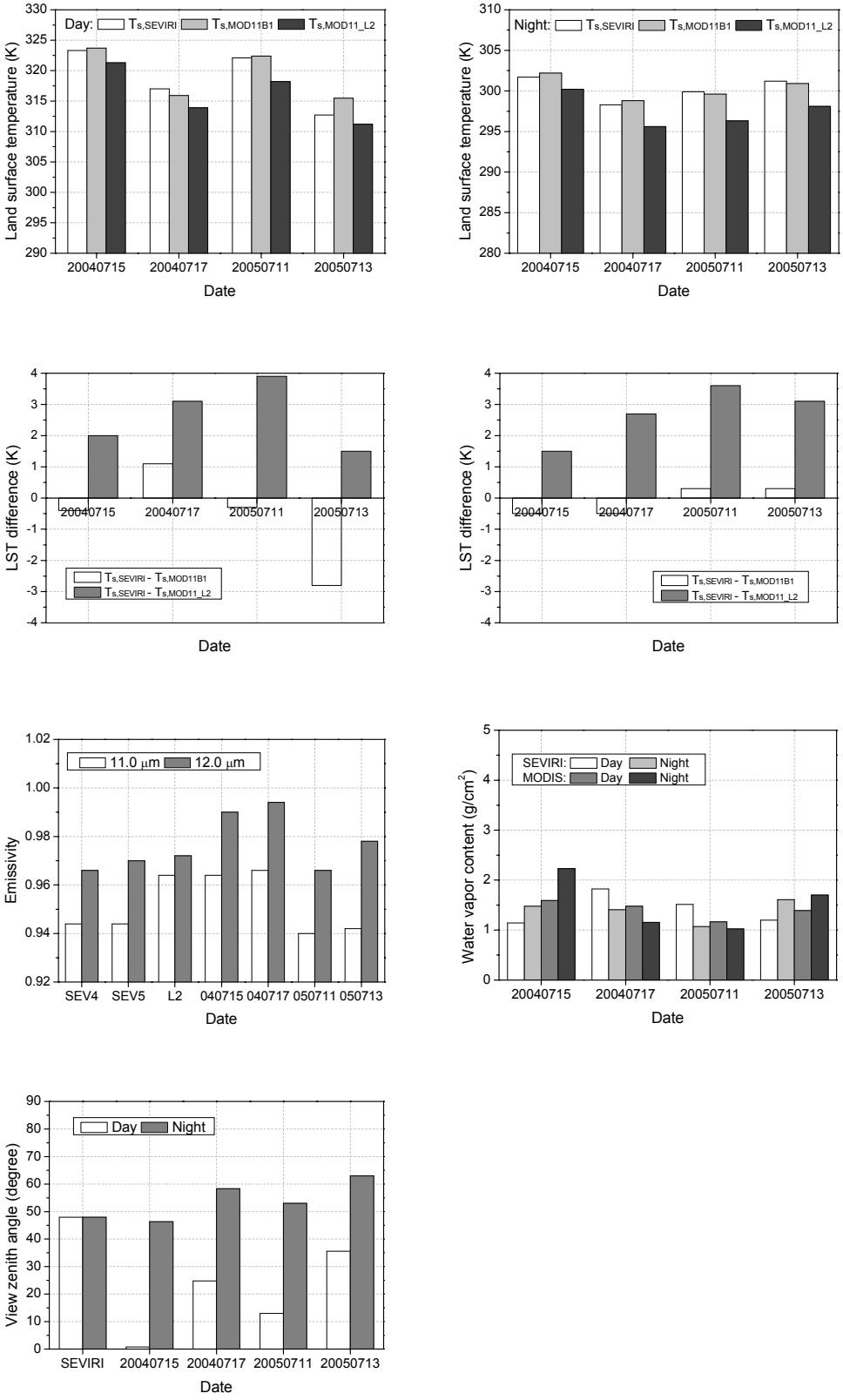

Figure 6.25. Same as the ones in Figure 6.23, but at Location J (28.29E, 27.98N)

7 Summary and conclusions

This thesis focuses on the retrievals of land surface emissivity and land surface temperature from MSG1-SEVIRI data. The primary work includes the cross-calibrations of MSG1-SEVIRI infrared channels with the channels of Terra-MODIS, the land surface emissivity retrievals from MSG1-SEVIRI data, the land surface temperature retrievals from MSG1-SEVIRI data and AATSR data, and the SEVIRI LST cross-validations with MODIS/Terra LST products and AATSR LSTs.

1. Cross-calibrations of MSG1-SEVIRI infrared channels with the channels of Terra-MODIS

The ray-matching method (Doelling et al, 2004a) and the radiative transfer modeling method (Asem et al., 1987) were recalled and applied to the cross-calibrations of MSG1-SEVIRI infrared channels 4, 9 and 10 with MODIS channels 20, 22, 23, 31 and 32.

The results obtained by the ray-matching method show that the calibrations of SEVIRI channels 4, 9 and 10 against MODIS channels are consistent in July 2005 and July 2006. The brightness temperatures measured in SEVIRI channel 4 are obviously lower than the ones measured in MODIS channel 20, while the brightness temperatures measured in SEVIRI channels 9 and 10 are, respectively, higher than the ones measured in MODIS channels 31 and 32. The results obtained by the ray-matching method show that, for brightness temperatures ranging from 280 K to 320 K, the temperature adjustments ΔBTs increases from 4.4 K to 5.9 K for SEVIRI channel 4, and they vary from -0.44 K to -0.75 K for SEVIRI channel 9 and from -0.03 K to -0.21 K for SEVIRI channel 10. The temperature adjustments found in this work are much smaller than these reported by Doelling et al. (2004a & 2004b). Because the ray-matching method can not account for the effects of the different spectral responses between SEVIRI and the MODIS, it is hard to decide whether the brightness temperatures in SEVIRI channels are overestimated or underestimated.

The radiative transfer modeling method was developed using MODTRAN fed with the adjusted Tropical model atmosphere, and the qualified measurement pairs were put together in the linear fits. The results obtained by the radiative transfer modeling method show that, for the range of the brightness temperatures in SEVIRI channels from 280 K to 320 K, the temperature adjustments (temperature difference between the SEVIRI brightness temperatures calculated from the measurements in the corresponding MODIS channel(s) by Equations (3.4a) and (3.4b) and the SEVIRI measured brightness temperatures) vary linearly from 0.81 K to -1.88 K for SEVIRI channel 4, from -0.51 K to -0.31 K for SEVIRI channel 9 and from -0.59 to 0.02 K for SEVIRI channel 10. Qualitative analysis shows that the results obtained by the radiative transfer modeling method are consistent with

the results obtained by the ray-matching method if the brightness temperature differences caused by the differences of spectral responses were taken into account in the ray-matching method. Because of the large differences of the spectral responses between SEVIRI and MODIS, the use of the results obtained by the radiative transfer modeling method to re-calibrate the SEVIRI data was recommended. The re-calibration will remove the overestimate of LST retrieved from SEVIRI data with the split-window method.

2. Land surface emissivity retrievals from MSG1-SEVIRI data

The land surface emissivities were estimated from the combined mid-infrared and thermal infrared data of the MSG1-SEVIRI. As known from the radiative transfer theory, the main difficulties in LST retrievals from satellite data are the need to correct for atmospheric perturbations and variable surface emissivities. To tackle the problems of the low temporal and spatial resolutions of the ECMWF data, a modified atmospheric correction scheme was developed. For the images acquired at UTC times 0:00, 6:00, 12:00 and 18:00, the atmospheric corrections were implemented using MODTRAN 4.0 fed with the ECMWF data. However, because SEVIRI channel 4 can not be regarded as a channel with narrow spectral range, the atmospheric corrections of the images in SEVIRI channel 4 was resolved by the introducing of the temperature dependent and channel-averaged transmittance. For the images acquired at times without atmospheric data available, the time-nearest and spatially interpolated atmospheric data were used for the images in SEVIRI channel 4, and the modeled results of the DTC model were used for the images in SEVIRI channels 9 and 10. The directional emissivities in SEVIRI channels 4, 7, 9 and 10 were estimated by the TISI concept, a BRDF model (the modified Minnaert's model or the RossThick-LiSparse-R model) and the Kirchhoff's law.

A small area (30.2N—37.7N, 7.0E—15.7E) and a large area (0—60N, 20W—60E) were selected as study areas (Figure 4.5). The MSG Level 1.5 product, the MSG cloud mask and the ECMWF profiles were the primary data used in the LSE retrievals. The time span of the SEVIRI data over the small study area is from July 15 to July 17, 2004, and six specific locations situated in the small area were selected to demonstrate the retrievals. While over the large study area, the LSEs were estimated from July 14 to July 19 of 2004 and from July 10 to July 14 of 2005, and on the 31 dates listed in Table 4.7.

Over the small study area, the modified Minnaert's model was applied. The results at the six specific locations, including vegetated areas and bare areas, show that: (1) The modified DTC model works well on both vegetated and bare areas, and the modified Minnaert's model can well describe the bi-directional reflectivities over bare area; (2) The differences between the values of each parameter ρ_0, ε_4, ε_9 and ε_{10} in two successive days and estimated using the two combinations are small; (3) The bi-directional reflectivities depend on the solar zenith angles, which verifies that the land surface is a non-Lambertian reflector and of course the derived emissivities are view zenith angle dependent. (4) The modeled bi-directional reflectivities and directional emissivities at the locations D and E are basically consistent with the results of Nerry et al. (1998) and Petitcolin et al. (2002a & 2002b).

The TISIs and directional emissivities in SEVIRI channels 4, 7, 9 and 10 were mapped over the small area on July 15, 2004. TISIs are found to be close to unity for vegetated areas and low in bare areas. The range of the directional emissivities in SEVIRI channel 4 is very large, going from 0.5 for the bare areas to 0.96 for the densely vegetated areas. The directional emissivities in SEVIRI channels 9 and 10 are usually from 0.9 to 1.0. Over the bare areas, they are usually less than 0.95, and the

emissivities in SEVIRI channel 10 are greater than the ones in SEVIRI channel 9. Over vegetated areas, they are usually greater than 0.95, and the directional emissivities in SEVIRI channel 9 are slightly higher than the ones in SEVIRI channel 10.

The modeling results at the six specific locations show that the RossThick-LiSparse-R model is much better than the modified Minnaert's model in the modeling of the bi-directional reflectivities, and the emissivity differences caused by the two models can not be ignored, especially over the bare areas. The use of the RossThick-LiSparse-R model in the estimation of the bi-directional emissivity in SEVIRI channel 4 is recommended.

Over the large study area and in the long terms, the bi-directional reflectivities were derived only by the combination of SEVIRI channels 4 and 9, and the RossThick-LiSparse-R model was used to describe the non-Lambertian property of land surface. In order to apply the LSE retrievals to the large area and long terms, some modifications were made in the data processing, such as the DTC modeling, the atmospheric corrections of the images in SEVIRI channel 4 and the TISI composite. The directional emissivities in SEVIRI channels 4, 7, 9 and 10 over the large area from July 14, 2004 to July 19, 2004 and from July 10, 2005 to July 14, 2005 and on the dates listed in Table 4.7 were estimated. The results of the emissivities in SEVIRI channels 4, 7, 9 and 10 at Locations G, H, I and J reveal that they do not significantly change in several days. Therefore, median composite maps of the emissivities in SEVIRI channels 4, 7, 9 and 10 were, respectively, generated for the two continuous time spans. The emissivity composite maps have clear textures. Over the large area, the directional emissivities in SEVIRI channels 4 and 7 change between 0.5 and 1.0, and they are usually higher than 0.85 over the vegetated areas, such as the Europe, while they are very low over the bare areas, such as the Sahara desert. The directional emissivities in SEVIRI channels 9 and 10 are usually higher than 0.85, and the emissivities over the vegetated areas are higher than the ones over the bare areas.

These results qualitatively agree with the former ones of Nerry et al. (1998) and Petitcolin et al. (2002a, 2002b).

3. Land surface temperature retrievals from MSG1-SEVIRI data and AATSR data

In this section, LSTs were estimated from the SEVIRI data and AATSR data (Nadir and Forward) by the generalized split-window algorithm and the single channel method.

The generalized split-window algorithms were, respectively, developed for the SEVIRI and AATSR instruments using the six standard model atmospheres prescribed in MODTRAN 4.0: Tropical, Mid-latitude Summer (MLS), Mid-latitude Winter (MLW), Sub-arctic Summer (SAS), Sub-arctic Winter (SAW) and U. S. 1976 Standard. Considering the special view geometry of SEVIRI, only the Tropical model atmosphere is available for the view zenith angle less than 17°, and the SAS and the SAW are excluded in the algorithm development because the view zenith angles within the SAS and SAW regions are greater than 65°. In order to make the radiative transfer simulations much more representative for natural cases, the temperature profiles and the water vapor profiles of the six standard model atmospheres were adjusted. The air temperature adjustment is ±15.0 K for the first boundary level and linearly decreases with the increment of the altitude until to tropopause. For the levels higher than tropopause, the adjusted amount is set to 0.0 K. The water vapor content (W) was scaled from 0.1 to 1.5 with a step of 0.1. Eleven view zenith angles at a height of 100 km: 0°, 10°, 20°, 30°, 35°, 40°, 45°, 50°, 55°, 60° and 65°, and six view zenith angles: 0°, 10°, 20°, 25°, 50° and 55° were used for SEVIRI and AATSR (Nadir and Forward), respectively. The LST ranges from T_0-5 to

T_0+20 with an interval of 5 K. The average emissivity changes from 0.90 to 1.00 with a step of 0.02, and the emissivity difference ($\Delta\varepsilon$) varies from -0.025 to 0.016 with an increment of 0.005. In order to further improve the accuracy of the generalized split-window algorithm, the LST, the average emissivity and the W were divided into several tractable sub-ranges. The LST was divided into 5 groups with an overlap of 5 K: ≤282.5, [277.5, 297.5], [292.5, 312.5], [307.5, 327.5] and ≥322.5 K. The LSE was separated into two sub-ranges: one goes from 0.90 to 0.96 and the other varies from 0.94 to 1.0 with an overlap of 0.02. The W was divided into six groups and they are [0.0, 1.5], [1.0, 2.5], [2.0, 3.5], [3.0, 4.5], [4.0, 5.5] and [5.0, 6.5] in g/cm^2. Because both SEVIRI and AATSR have no atmospheric sounding channels, the first boundary temperature of atmosphere is not known, and was not involved in the generalized split-window algorithm like Wan and Dozier did (1997). For AATSR, when LST is less than 335 K and W varies between 0 and 6.5 g/cm^2, the RMSEs are less than 1.0 K for the Nadir view, and are less than 1.6 K for the Forward view. The RMSEs for AATSR are also less than 1.0 K for both the nadir and forward views and all LST groups when W is less than 4.5 g/cm^2. While for SEVIRI, when W varies between 0 and 6.5 g/cm^2, the RMSEs are less than 1.0 K for the view zenith angles less than 55° and LST less than 312.5 K, or for the view zenith angles less than 45° and all LST groups. The RMSEs for SEVIRI are also less than 1.0 K for all LST groups with the view zenith angles less than 60° and W less than 3.5 g/cm^2.

The LSEs in SEVIRI channels 9 and 10 were estimated by the method developed by Jiang et al. (2006), while the LSEs in AATSR channels IR11 and IR12 were inferred from the ones in SEVIRI channels in terms of the RossThick-LiSparse-R model, the Kirchhoff's law, the angular-independent properties of TISI and the MODIS UCSB Emissivity Library. The W was estimated by means of the method given by Li et al. (2003). An area-weighted pixel aggregation was carried out to put the AATSR images into the SEVIRI image coordinates.

LSTs were retrieved over the study area (longitude: 20W—60E, latitude: 0—60N) from July 14, 2004 to July 19, 2004 and from July 10, 2005 to July 14, 2005 by the split-window method and the single channel method from the SEVIRI data and the AATSR (Nadir and forward) data. The results show that the LSTs in daytime are higher than the ones at night, and the LSTs over the bare area are higher than the ones over vegetated area in daytime. The LSTs estimated by the two methods are basically consistent. The AATSR Nadir LSTs are averagely 3.56 K higher than the corresponding AATSR Forward LSTs in daytime, while they are almost equal at night. The results of the AATSR LSTs indicate that the dual-angle algorithm developed for the AATSR instrument (Prata, 2002) cannot be used in the daytime LST retrieval, but may be qualified for nighttime LST retrieval. The LST retrievals are mainly limited by the absence of emissivities and clouds.

The DTC model was successfully applied to the modeling and the time normalization of the SEVIRI LSTs.

4. SEVIRI LST cross-validations with MODIS LST products and AATSR LST

The SEVIRI LSTs ($T_{s,SEVIRI}$) estimated by the generalized split-window algorithm were cross-validated with the LSTs ectracted from the MODIS/Terra LST products ($T_{s,MOD11B1}$ and $T_{s,MOD11\_L2}$) and the AATSR Forward LSTs derived by the generalized split-window algorithm ($T_{s,AATSR\_Forward}$) over the Iberian Peninsula area and the Egypt & Middle East area (Figure 6.1) in July of 2004 and July of 2005 according to the QCs defined in the MODIS/Terra LST products.

Over the vegetated Iberian Peninsula area, when $T_{s,SEVIRI}$ is compared to $T_{s,MOD11B1}$, in the daytime, the average of the temperature differences (mean) is less than 0.8 K, and the RMSE are ~2.6 K, while at night, the mean and RMSE become smaller. When $T_{s,SEVIRI}$ is compared to $T_{s,MOD11\_L2}$, the mean changes between 0.9 K and 2.3 K and RMSE varies between 1.9 K and 3.2 K, which is basically consistent with the results of Wan et al. (2002). The results indicate that, in general speaking, the temperature differences in daytime are larger than the temperature differences at night, and the temperature differences between $T_{s,SEVIRI}$ and $T_{s,MOD11B1}$ are smaller than the temperature differences between $T_{s,SEVIRI}$ and $T_{s,MOD11\_L2}$. When $T_{s,SEVIRI}$ is compared to the AATSR Forward LST estimated by the generalized split-window algorithm ($T_{s,AATSR\_Forward}$), $T_{s,SEVIRI}$ is averagely 1.26 K higher than $T_{s,AATSR\_Forward}$ with a RMSE of 2.4 K in the daytime, and the mean and RMSE of the temperature differences are, respectively, reduced to 0.3 K and 1.6 K at night (21:46UTC). The temperature differences between $T_{s,SEVIRI}$ and $T_{s,AATSR\_Forward}$ wer mainly caused by the view zenith angles. Totally, $T_{s,SEVIRI}$ and $T_{s,AATSR\_Forward}$ are also consistent.

Over the Egypt & Middle East area, in the daytime, $T_{s,SEVIRI}$ is averagely 1.5 K lower than the $T_{s,MOD11B1}$ and the average RMSE is 2.5 K. The $T_{s,SEVIRI}$ is averagely 0.2 K higher than $T_{s,MOD11B1}$ and the average RMSE is 1.9 K at night. Similar to the results over the Iberian Peninsula area, $T_{s,MOD11\_L2}$ is still lower than $T_{s,SEVIRI}$, but the LST differences are much larger: the mean is up to 2.5 K and the RMSE is up to 3.5 K. The large temperature differences between $T_{s,SEVIRI}$ and $T_{s,MOD11\_L2}$ usually happen in the desert regions.

The histograms of the temperature differences over the two study area show that the temperature differences obey Gaussian distribution function. The histogram results are consistent with the maps of the temperature differences.

In order to further investigate the source of the temperature differences, we analyzed the factors which may lead to temperature differences: the brightness temperatures at TOA, LSEs, view zenith angles, atmospheric water vapor content and the algorithms itself. The effects of the emissivity differences and the view zenith angle differences were emphasized. Actually, the temperature differences are synthetical results of these factors. Because we have no adequate observations to separate these factors, it is hard to give quantitative analytical results how much error is caused by each factor. Totally, the SEVIRI LSTs are consistent with the LSTs extracted from the MODIS/Terra LST products and the AATSR Forward LST derived by the generalized split-window algorithm with an average accuracy of 1-2 K over both vegetated area and bare area.

The comparisons of LSTs and LST related parameters at Location G, I and J (Table 4.8) were also carried out. Totally, the results at Locations G, I and J are consistant with the area-based results.

The cross-validations of LSTs and LSEs between SEVRIR and MODIS reveal two problems in V4 MOD11B1: (1) Over the Egypt & Middle East area, both the LSEs and LSTs extracted from the MOD11B1 are, respectively, higher than the LSEs and LSTs estimated from the SEVIRI data. (2) The abnormal LSEs in local areas do not lead to abnormal LSTs.

Perspectives

The research results in this thesis open some interesting perspectives. In the LSE retrieval, the accuracy of the estimated LSEs is mainly determined by the accuracy of atmospheric correction and

the performance of the BRDF model. Therefore, the new atmospheric correction scheme and the BRDF models need further evaluations.

The methods of the LSE and LST retrievals may need improvements to make the retrievals operational, and they are very promising to be applied to the data acquired by the China's FY series meteorological satellites.

Although LST retrieval from the passive thermal infrared data acquired by satellites is well developed, it is vulnerable to the impacts of clouds and atmospheric water vapor content. As we know, passive microwave can work under almost all-weather conditions, but the theory to retrieve LSTs from the passive microwave remote sensing data has not been well established. If we combine the two kinds of data, better algorithms may be found and much more accurate LSTs may be obtained.

Appendix A: Acronyms

AATSR	Advanced Along Track Scanning Radiometer
ASTER	Advanced Spaceborne Thermal Emission and Reflection Radiometer
ATSR	Along Track Scanning Radiometer
AVHRR	Advanced Very High Resolution Radiometer
BRDF	Bidirectional Reflectance Distribution Function
BSQ	Band SeQuential
BT	Brightness Temperature
DEM	Digital Elevation Model
DTC	Diurnal Temperature Cycle
EAGLE	Exploitation of AnGular effects in Land surfacE observations from satellites
ECMWF	European Center for Medium-range Weather Forecasts
EOS	Earth Observation System
ESA	European Space Agency
EUMETSAT	EUropean organization for the exploitation of METeorological SATellite
ETM+	Enhanced Thematic Mapper Plus
GMS	Geostationary Meteorological Satellite
GOES	Geostationary Operational Environmental Satellite
GP	Geo-Potential
HDF	Hierarchical Data Format
HRV	High Resolution Visible
IDL	Interactive Data Language
IR	Infra-Red
LSE	Land Surface Emissivity
LST	Land Surface Temperature
MIR	Middle Infra-Red
MLS	Middle-Latitude Summer
MLW	Middle-Latitude Winter

MODIS	MODerate resolution Imaging Spectroradiometer
MODTRAN	MODerate spectral resolution atmospheric TRANsmittance algorithm and computer model
MPEF	Meteorological Products Extraction Facility
MSG	Meteosat Second Generation
NASA	National Aeronautics and Space Administration
NDVI	Normalized Difference Vegetation Index
NEΔT	Noise Equivalent Temperature Difference
NOAA	National Oceanic & Atmospheric Administration
RAA	Relative Azimuth Angle
RH	Relative Humidity
RMSE	Root Mean Square Error
SAA	Solar Azimuth Angle
SAS	Sub-Arctic Summer
SAW	Sub-Arctic Winter
SEVIRI	Spinning Enhanced Visible and InfraRed Imager
SPT	SEVIRI Pre-processing Toolbox
SST	Sea Surface Temperature
SZA	Solar Zenith Angle
TIR	Thermal Infra-Red
TISI	Temperature Independent Spectral Indices
TISIE	Temperature Independent Spectral Indices of Emissivities
TM	Thematic Mapper
TOA	Top Of Atmosphere
UTC	Coordinated Universal Time
VAA	View Azimuth Angle
VZA	View Zenith Angle
WGS	World Geodetic System

Appendix B: MODIS Technical Specifications

Orbit:	705 km, 10:30 a.m. descending node (Terra) or 1:30 p.m. ascending node (Aqua), sun-synchronous, near-polar, circular
Scan Rate:	20.3 rpm, cross track
Swath Dimensions:	2330 km (cross track) by 10 km (along track at nadir)
Telescope:	17.78 cm diam. Off-axis, afocal (collimated), with intermediate field stop
Size:	1.0 x 1.6 x 1.0 m
Weight:	228.7 kg
Power:	162.5 W (single orbit average)
Data Rate:	10.6 Mbps (peak daytime); 6.1 Mbps (orbital average)
Quantization:	12 bits
Spatial Resolution:	250m (bands 1-2); 500 m (bands 3-7); 1000 m (bands 8-36)
Design Life:	6 years

Table A.1. Spectral characteristics of MODIS channels

Primary Use	Band	Bandwidth[1]	Spectral Radiance[2]	Required SNR[3]
Land/Cloud/Aerosols Boundaries	1	620 – 670	21.8	128
	2	841 – 876	24.7	201
Land/Cloud/Aerosols Properties	3	459 – 479	35.3	243
	4	545 – 565	29.0	228
	5	1230 – 1250	5.4	74
	6	1628 – 1652	7.3	275
	7	2105 – 2155	1.0	110
Ocean Color/ Phytoplankton/ Biogeochemistry	8	405 – 420	44.9	880
	9	438 – 448	41.9	838
	10	483 – 493	32.1	802
	11	526 – 536	27.9	754
	12	546 – 556	21.0	750
	13	662 – 672	9.5	910
	14	673 – 683	8.7	1087
	15	743 – 753	10.2	586
	16	862 – 877	6.2	516
Atmospheric Water Vapor	17	890 – 920	10.0	167
	18	931 – 941	3.6	57
	19	915 – 965	15.0	250

Primary Use	Band	Bandwidth[1]	Spectral Radiance[2]	Required NEΔT(K)[4]
Surface/Cloud Temperature	20	3.660 - 3.840	0.45 (300K)	0.05
	21	3.929 - 3.989	2.38 (335K)	2.00
	22	3.929 - 3.989	0.67(300K)	0.07
	23	4.020 - 4.080	0.79 (300K)	0.07
Atmospheric Temperature	24	4.433 - 4.498	0.17 (250K)	0.25
	25	4.482 - 4.549	0.59(275K)	0.25
Cirrus Clouds Water Vapor	26	1.360 - 1.390	6.00	150 (SNR)
	27	6.535 - 6.895	1.16 (240K)	0.25
	28	7.175 - 7.475	2.18 (250K)	0.25
Cloud Properties	29	8.400 - 8.700	9.58 (300K)	0.05
Ozone	30	9.580 - 9.880	3.69 (250K)	0.25
Surface/Cloud Temperature	31	10.780 - 11.280	9.55 (300K)	0.05
	32	11.770 - 12.270	8.94 (300K)	0.05
Cloud Top Altitude	33	13.185 - 13.485	4.52 (260K)	0.25
	34	13.485 - 13.785	3.76 (250K)	0.25
	35	13.785 - 14.085	3.11 (240K)	0.25
	36	14.085 - 14.385	2.08 (220K)	0.35

[1] Bands 1 to 19 are in nm; Bands 20 to 36 are in µm
[2] Spectral Radiance values are (W/m^2 -µm-sr)
[3] SNR = Signal-to-noise ratio
[4] NE(delta)T = Noise-equivalent temperature difference
Note: Performance goal is 30-40% better than required

References

Arthur, C. R. G., Stephen, D. P., Scott, J. G. and Jennifer, S. (2002). Effects of orbital drift on land surface temperature measured by AVHRR thermal sensors. *Remote Sensing of Environment*, 79, 147-165.

Asem, A., Deschamps, P. Y. and Ho, D. (1987). Calibration of METEOSAT infrared radiometer using split-window channels of NOAA AVHRR. Journal of Atmospheric and Oceanic Technology, Vol. 4, No. 4, 553-562.

Barnes, W. L., Xiong, X. and Salomonson, V. (2003). Status of Terra MODIS and Aqua MODIS. *Advances in Space Research*, 32, 2099–2106.

Becker, F. (1987). The impact of spectral emissivity on the measurement of land surface temperature from a satellite. *International Journal of Remote Sensing*, Vol. 8, No. 10, 1509-1522.

Becker, F. and Li, Z. L. (1990a). Temperature independent spectral indices in thermal infrared bands. *Remote Sensing of Environment*, 32, 17-33.

Becker, F. and Li, Z. L. (1990b). Toward a local split window method over land surface. *International Journal of Remote Sensing*, 3, 369-393.

Becker, F. and Li, Z.-L. (1995). Surface temperature and emissivity at various scales: Definition, measurement and related problems. *Remote Sensing Reviews*, 12, 225–253.

Berk, A., Bernstein, L. S., Anderson, G. P., Acharya, P. K., Robertson, D. C., Chetwynd, J. H. and Adler-Golden, S. M. (1998). MODTRAN cloud and multiple scattering upgrades with application to AVIRIS. *Remote Sensing of Environment*, 65: 367-375.

Byrne, G. F. (1979). Remotely sensed land cover temperature and soil water status—a brief review. *Remote Sensing of Environment*, 8, 291-305.

Bussieres, No., Louie, P.Y.T, and Hogg, W., (1990). Progress report on the implementation of an algorithm to estimate regional evaportanspiration using satellite data. *Proceeding of the workshop on applications of remote sensing in hydrology*, Saskaton Saskatchewan, 13-14 February 1990.

Casellas, V. and Sobrino, A. J., (1989). Determination of frosts in orange groves from NOAA-9 AVHRR data. *Remote Sensing of Environment*. 29: 135-146.

Chedin, A., Scott, M. A., Wahiche, C and Moulinier, P. (1985). The improved initialization inversion method: a high resolution physical method for temperature retrievals from the Trios-N series. *Journal of Climate and Applied Meteorology*, vol.24, 124-143.

Coll, C., Caselles, V., Galve, J. M., Valor, E., Niclòs, R., Sànchez, J. M. and Rivas, R. (2005). Ground measurements for the validation of land surface temperatures derived from AATSR and MODIS data. *Remote Sensing of Environment*, 97, 288-300.

Coste, P., Pasternak, F., Faure, F., Jacquet, B., Bianchi, S., Aminou, D. M. A., Luhmann, H. J., Hanson, C., Pili, P. and Fowler, G. (2004). Proceedings of the 5th International Conference on Space Optics (ICSO 2004), 30 March – 2 April 2004, Toulouse, France. Ed.: B. Warmbein. ESA SP-554, Noordwijk, Netherlands: ESA Publications Division, ISBN 92-9092-865-4, 2004, p. 165 – 172.

Dash, P., Göttsche, F. M. , Olesen, F. S. and Fischer, H. (2005). Separation surface emissivity and temperature using two-channel spectral indices and emissivity composites and comparison with a vegetation fraction method. *Remote Sensing of Environment*, 96, 1-17.

Deschamps, P. Y. and Phulpin, T. (1980), Atmospheric correction of infrared measurements of sea surface temperature using channels at 3.7, 11 and 12 μm. *Bound. Layer Met*. 18:131-143.

Diak, G. R. and Whipple, M. S. (1993). Improvements to models and methods for evaluating the land-surface energy balance and effective roughness using radiosonde reports and satellite-measured skin temperature data. *Agricultural and Forest Meteorology*, vol. 63, No. 3-4, 189-218.

Doelling, D. R., Nguyen, L. and Minnis, P. (2004a). Calibration comparisons between SEVIRI, MODIS, and GOES data. *Proc. 2004 EUMETSAT Meteorological Satellite Conference*, Prague, Czech Republic, May 17-20, 2004.

Doelling, D. R., Minnis, P. and Nguyen, L. (2004b). Calibration comparisons between SEVIRI, MODIS, and GOES data. *MSG RAO workshop*, Salzburg, Austria, 10-11 September, 2004.

Dozier, J. and Warren, S. G. (1982). Effect of viewing angles on the infrared brightness temperature of snow. *Water Resources Research*, vol. 18, no. 5, 1424-1434.

Franca, G. B. and Cracknell, A. P. (1994). Retrieval of land and sea surface temperature using NOAA-11 AVHRR data in north-eastern Brazil. *International Journal of Remote Sensing*, 15, 1695-1712.

Gillespie, A. R. (1985). Lithologic mapping of silicate rocks using TIMS. In the TIMS Data Users' Workshop, JPL Publication 86-38, Jet Propulsion Laboratory, Pasadena, CA, 29-44.

Gillespie, A. R., Rokugawa, S., Matsunaga, T., Cothern, J.S., Hook, S. and Kahle, A.B. (1998), A temperature and emissivity separation algorithm for Advanced Spaceborne Thermal Emission and Reflection Radiometer (ASTER) images. *IEEE Transactions on Geoscience and Remote Sensing*, 36(4), 1113-1126.

Goïta, K. and Royer, A. (1997). Surface temperature and emissivity separability over land surface from conbined TIR and SWIR AVHRR data. *IEEE Tansactions on Geoscience and Remote Sensing*, 35, 718-733.

Göttsche, F. M. and Olesen, F. S. (2001). Modeling of diurnal cycles of brightness temperature extracted from METEOSAT data. *Remote Sensing of Environment*, 76, 337-348.

Guenther, B., Xiong, X., Salomonson, V. V., Barnes, W. L. and Young, J. (2002). On-orbit performance of the Earth Observing System Moderate Resolution Imaging Spectroradiometer; first year of data. *Remote Sensing of Environment*, 83, 16-30.

Heidinger, A. K., Cao, C. and Sullivan, J. T. (2002). Using Moderate Resolution Imaging Spectrometer (MODIS) to calibrate advanced very high resolution radiometer reflectance channels. *Journal of Geophysical Research*, 107 (D23), 4702.

Hu, B., Lucht, W., Li, X. And Strahler, A. H. (1997). Validation of kernel-driven models for the BRDF of land surfaces. Remote Sensing of Environment, 62: 201-214.

Huang, C., Townshend, J. R. G., Liang, S., Kalluri, S. N. V. and DeFries, R. S. (2002). Impact of sensor's point spread function on land cover characterization: assessment and deconvolution. *Remote Sensing of Environment*, 80, 203 – 212.

Jiang, G.-M., Liu, R.-G., Niu, Z. and Zhuang, D.-F. (2004). An optimal geometric correction method for MODIS 1B data collection and its software development. *Journal of Remote Sensing* (China), Vol. 8, No. 2, 158-164.

Jiang, G. M. and Li, Z. L. (2005). Land surface temperature and emissivity retrieval from combined mid-infrared and thermal infrared data of MSG-SEVIRI. *The 9th International Symposium on Physical Measurements and Signature in Remote Sensing*, Beijing (P. R. China), 17-19th October, 2005. XXXVI: 7/W20, 307-309.

Jiang, G.-M., Li, Z.-L. and Nerry, F. (2006). Land surface emissivity retrieval from combined mid-infrared and thermal infrared data of MSG-SEVIRI. *Remote Sensing of Environment*, 105, 326-340.

Jin, M. and Dickinson, R. E., (2002). New observational evidence for global warming from satellite. *Geophysical Research Letters*, 29(10): 1-4.

Jin, M. and Treadon, R. E., (2003). Correction the orbit drift effect on AVHRR land surface skin temperature measurements. *International Journal of Remote Sensing*, 24(22): 4543-4558.

Kahle, A. B., Madura, D. P. and Soha, J. M. (1980). Middle infrared multispectral aircraft scanner data: analysis for geologic applications. *Applied Optics*, 19: 2279-2290.

Kahle, A. B. (1987). Surface emittance, temperature, and thermal inertia derived from Thermal Infrared Multispectral Scanner (TIMS) data for Death Valley, California. *Geophysics*, 52(7): 858-874.

Kahle, A. B. and Alley, R. E. (1992), Separation of temperature and emittance in remotely sensed radiance measurements. *Remote Sensing of Environment*, 42, 107-111.

Kealy, P. S. and Gabell, A. R. (1990). Estimation of emissivity and temperature using alpha coefficients. In *Proceedings of the Second TIMS Workshop*, JPL Publication 90-55, Jet Propulsion Laboratory, Pasadena, CA, pp. 11-15.

Kerr, Y. H., Lagouarde, J. P. and Imbernon. (1992). Accurate land surface temperature retrieval from AVHRR data with use of an improved split-window algorithm. *Remote Sensing of Environment*, Vol. 41, 197-209.

Labed, J. and Stoll, M. P. (1991). Angular variation of land surface spectral emissivity in the thermal infrared: laboratory investigations on bare soils. *International Journal of Remote Sensing*, vol. 12, No. 11, 2299-2310.

Li, X. and Strahler, A. H. (1992). Geometric-optical bidirectional reflectance modeling of the discrete crown vegetation canopy: Effect of crown shape and mutual shadowing. *IEEE Transactions on Geoscience and Remote Sensing*, Vol. 30, 276-292.

Li, Z.-L. and Becker, F. (1993). Feasibility of land surface temperature and emissivity determination from AVHRR data. *Remote Sensing of Environment*, 43, 67-85.

Li, Z.-L., Becker, F., Stoll, M. P. and Wan, Z. (1999). Evaluation of six methods for extracting relative emissivity spectra from thermal infrared images. *Remote Sensing of Environment*, 69: 197-214.

Li, Z.-L., Petitcolin, F. and Zhang, R. H. (2000). A physically based algorithm for land surface emissivity retrieval from combined mid-infrared and thermal infrared data. *Science in China* (Series E), 43 Supply, 22-33.

Li, Z.-L., Jia, L., Su, Z., Wan, Z. and Zhang, R. (2003). A new approach for retrieveing precipitable water from ATSR2 split-window channel data over land area. *International Journal of Remote Sensing*, 24(24), 5095-5117.

Liu, J.-J. and Li, Z. (2004). A new method for cross-calibration of two satellite sensors. *International Journal of Remote Sensing*, Vol. 25, No. 23, 5267-5281.

Liu, Y., Hiyama, T. and Yamaguchi, Y. (2006). Scaling of land surface temperature using satellite data: A case examination on ASTER and MODIS products over a heterogeneous terrain area. *Remote Sensing of Environment*, 105, 115-128.

Llewellyn-Jones, D. T., Minnett, P. J., Saunders, R. W. and Zavody, A. M. (1984), Satellite Multichannel Infrared Measurement of Sea Surface Temperature of the N. E. Atlantic Ocean Using AVHRR/2. *Quarterly Journal of the Royal Meteorological Society*, 110, 613-631.

Lucht, W. (1998). Expected retrieval accuracies of bidirectional reflectance and albedo from EOS-MODIS and MISR angular sampling. *Journal of Geophysical Research*, 103: 8763-8778.

Lucht, W. and Louis, P. (2000). Theoretical noise sensitivity of BRDF and albedo retrieval from EOS-MODIS and MISR sensors with respect to angular sampling. *International Journal of Remote Sensing*, 21(1): 81-98.

Mannstein, H. (1987). Surface energy budget, surface temperature and thermal initia. *Remote Sensing Applications in Meteorology and Climatology*, ed. Vaughan R. A. and Reidel D., NATO ASI Ser. C: Math. Phys. Sci., Vol. 201, 391-410, Dordrecht, Netherlands: A Reidel Publishing Co.

McClain, E. P., Pichel, W. G. and Walton, C. C. (1985). Comparative performance of AVHRR-based multichannel sea surface temperature. *Journal of Geophysical Research*, 90(C6): 11587-11601.

McGregor, J. and Gorman, A. J. (1994). Some considerations for using AVHRR data in climatological studies: 1. Orbital characteristics of NOAA satellites. *International Journal of Remote Sensing*, 15 (3), 537-548.

McMillin, L. M. (1975). Estimation of sea surface temperature from two infrared window measurements with different absorption. *Journal of Geographical Research*, 80, 5113-5117.

Merchant, C. J., Simpson, J. J. and Harris, A. R. (2003). A cross-calibration of GMS-5 thermal channels against ATSR-2. *Remote Sensing of Environmrnt*, 84, 268-282.

Minnaert, M. (1941). The reciprocity principle of linear photometry. *Astrophysical Journal*, 93, 403-410.

Minnis, P., Nguyen, L., Doelling, D. R., Young, D. F., Miller, W. F. and Kratz, D. P. (2002). Rapid calibration of operational and research meteorological satellite imagers, Part I: Use of the TRMM VIRS or ERS-2 ATSR-2 as a reference. *Journal of Atmospheric and Oceanic Technology,* 19, 1233-1249.

Nerry, F., Petitcolin, F. and Stoll M. P. (1998). Bidirectional Reflectivity in AVHRR Channel 3: Application to a Region in North Africa. *Remote Sensing of Environment*, 66, 298-316.

Nerry, F., Stoll, M. P. and Malaplate, A. (2004). Multi temporal regression method for mid infrared [3-5μm] emissivity outdoor measurements. *Optical Express*, 12, 6574-6588.

Nicodemus, F. E. (1965). Directional reflectance and emissivity of an opaque surface. *Applied Optics*, 4, 767-773.

Nilson, T. and Kuusk, A. (1989). A reflectance model for the homogeneous plant canopy and its inversion. *Remote Sensing of Environment*, Vol. 27, 157-167.

Norman, J. M. and Becker, F. (1995). Terminology in thermal infrared remote sensing of natural surfaces. *Agricultural and Forest Meteorology*, 77: 153-166.

Ottlé, C. and Vidal-Madjar, D. (1992). Estimation of land surface temperature with NOAA9 data. *Remote Sensing of Environment*, 40(1), 27-41.

Ottlé, C. and Stoll, M. P. (1993). Effect of atmospheric absorption and surface emissivity on the determination of land surface temperature from infrared satellite data. *International Journal of Remote Sensing*, vol. 14, No. 10, 2025-2037.

Peres, L. F. and DaCamara, C. C. (2004). Land surface temperature and emissivity estimation based on the two-temperature method: sensitivity analysis using simulated MSG/SEVIRI data. *Remote Sensing of Environment*, 91, 377-389.

Pokrovsky, I., Pokrovsky, O. and Roujean, J. L. (2003). Development of an operational procedure to estimate surface albedo from the SEVIRI/MSG observing system by using POLDER BRDF measurements II: Comparison of several inversion techniques and ncertainty in albedo estimates. *Remote Sensing of Environment*, 87, 215-242.

Petitcolin, F., Nerry, F. and Stoll, M. P. (2002a). Mapping directional emissivity at 3.7 μm using a simple model of bi-directional reflectivity. *International Journal of Remote Sensing*, 23, 3443-3472.

Petitcolin, F., Nerry, F. and Stoll, M. P. (2002b). Mapping temperature independent spectral indice of emissivity and directional emissivity in AVHRR channels 4 and 5. *International Journal of Remote Sensing*, 23, 3473-3491.

Petitcolin, F. and Vermote E. (2002). Land surface reflectance, emissivity and temperature from MODIS middle and thermal infrared data. *Remote Sensing of Environment*, 83, 112-134.

Prabhakara, C., dalu, G. and Kunde, V.G. (1974), Estimation of sea surface temperature from remote sensing in the 11 and 13 micrometer window region. *Journal of Geophysical Research,* 79: 5039-5044.

Prata, A. J. (1993), Land surface temperature derived from the AVHRR and the ATSR. *Journal of Geophysical Research*, 98(D9): 1689-1702.

Prata, A. J. (1994). Land surface temperature derived from the advanced very high resolution radiometer and along-track scanning radiometer 2. Experimental results and validation of AVHRR algorithms. *Journal of Geophysical Research*, Vol. 99, No. D6, 13025-13058.

Prata, A. J., Caselles, V., Coll, C., Sobrino, J. A. and Ottlé, C. (1995). Thermal remote sensing of land surface temperature from satellite: current status and future prospects. *Remote Sensing Reviews*, 12, 175-224.

Prata, F. (2002). Land surface temperature measurement from space: AATSR algorithm theoretical basis document, CSIRO Atmospheric Research, Aspendale, Australia.

Price, J. C. (1983). Estimating surface temperature from satellite thermal infrared data – a simple formulation for the atmospheric effect. *Remote Sensing of Environment*, Vol. 13, 353-361.

Price, J. C. (1984). Land surface temperature measurements from the split window channels of the NOAA 7 AVHRR. *Journal of Geophysical research*, No. D5, 7231-7237.

Price, J. C. (1990). The potential of Remotely Sensed Thermal Infrared data to Infer Surface Soil Moisture and Evaporation. *Water Resources*, 16, pp. 787-795.

Privette, J. L., Fowler, C., Wick, G. A., Baldwin, D. and Emery, W. J. (1995). Effects of orbital drift on Advanced Very High Resolution Radiometer products: normalized difference vegetation index and sea surface temperature. *Remote Sensing of Environment*, 53, 164-171.

Privette, J. L., Eck, T. F. And Deering, D. W. (1997). Estimating spectral albedo and nadir reflectance through inversion of simple BRDF models with AVHRR/MODIS-like data. *Journal of Geophysical Research*, 102(D24): 29,529-29,542.

Realmuto, V. J. (1990). Separating the effects of temperature and emissivity: emissivity spectrum normalization. In Proceedings of the Second TIMS Workshop, JPL Publication 90-55, Jet Propulsion Laboratory, Pasadena, CA, 23–27.

Rees, W. G. and James, S. P. (1992). Angular variation of the infrared emissivity of ice and water surfaces. *International Journal of Remote Sensing*, vol. 13, 2873-2886.

Rivard, B., Petroy, S. B. and Miller, J. R. (1993). Measured effects of desert varnish on mid-infrared spectra of weathered rocks as an aid to TIMS imagery interpolation. *IEEE Transactions on Geoscience and Remote Sensing*, vol. 31, No. 1, 284-291.

Ross, J. K. (1981). The radiation regime and architecture of plant stands. W. Junk, The Hague, Netherland.

Roujean, J. L., Leroy, M., and Deschamps, P. Y. (1992). A bidirectional reflectance model of the Earth's surface for the correction of remote sensing data. *Journal of Geophysical Research*, 97, 20,455-20,468.

Salisbury, J. W. and D'Aria, D, M. (1992). Emissivity of terrestrial materials in the 8-14 μm atmospheric window. *Remote Sensing of Environment*, 42, 83-106.

Sandmeier, S. R. and Itten, K. I. (1999). A Field Goniometer System (FIGOS) for Acquisition of Hyperspectral BRDF data. *IEEE Transactions on Geoscience and Remote Sensing*, 37 (2):978-986.

Schädlich, S., Göttsche, F. M. and Olesen, F. S. (2001). Influence of land sueface parameters and atmosphere on METEOSAT brightness Temperatures and generation of land surface temperature

maps by temporally and spatially interpolating atmospheric correction. *Remote Sensing of Environment*, 75, 39-46.

Schmetz, J., Pili, P., Tjemkes, S., Just, D., Kerkmann, J., Rota, S. and Ratier, A. (July, 2002a). An introduction to Meteosat Sencond Generation (MSG). *Bulletin of the American Meteorological Society*, Volume 83, Issue 7, 977-992.

Schmetz, J., Pili, P., Tjemkes, S., Just, D., Kerkmann, J., Rota, S. and Ratier, A. (July, 2002b). SEVIRI calibration. *Bulletin of the American Meteorological Society*, Volume 83, Issue 7, 992-992.

Schroedter, M., Olesen, F. and Fischer, H. (2003). Determination of land surface temperature distributions from single channel IR measurements: an effective spatial interpolation method for the use of TOVS, ECMWF and radiosonde profiles in the atmospheric correction scheme. *International Journal of Remote Sensing*, Vol. 24, No. 6, 1189-1196.

Schumaker, L. L. (1976). Fitting surfaces to scattered data. *In Approximation Theory II*, edited by Lorentz, G. G., Chui, C. K. and Schumaker, L. L. (London: Academic Press).

Seguin, B., Courault, D. and Guerif, M. (1994). Surface temperature and evapotranspiration: Application of local scale methods to regional scales using satellite data. *Remote Sensing of Environment*, 49: 287-295.

Sellers, P. J., Hall, F. G., Asrar, G., Strebel, D. E. and Murphy, R. E. (1988). The first ISLSCP field experiment (FIFE). *Bulletin of the American Meteorology Society*, Vol. 69, No. 1, 22-27.

Serafini, V.V., (1987). Estimation of the evapotranspiration using surface and satellite data. International journal of remote sensing, 8,pp. 1547-1562.

Shepard, D. (1968). A two-dimensional interpolation function for irregularly-spaced data. Proc. ACM National Conference, Princeton, USA (New York: ACM), 517-524.

Simpson, J. J. and Gobat, J. I. (1995a). Improved cloud detection in GOES Scenes over land. *Remote Sensing Of Environment*, 52: 36-54.

Simpson, J. J. and Gobat, J. I. (1995b). Improved cloud detection in GOES Scenes over the oceans. *Remote Sensing Of Environment*, 52: 79-94.

Sinha, A. (1995). Relative influence of lapse rate and water vapor on the greenhouse effect. *Journal of Geophysical Research*, vol. 100, No. D3, 5095-5103.

Snyder, W., Wan, Z., Zhang, Y. and Feng, Y. Z. (1997). Requirements for satellite land surface temperature validation using a silt playa. *Remote Sensing of Environment*, 61, 279-289.

Snyder, W. C., Wan, Z., Zhang, Y. and Feng, Y.-Z. (1998). Classification-based emissivity for land surface temperature measurement from space. *International Journal of Remote Sensing*, 19(14), 2753-2774.

Sobrino, J. A., Coll, C. and Caselles, V. (1991). Atmospheric corrections for land surface temperature using AVHRR channels 4 and 5. *Remote Sensing of Environment*, Vol. 38, No. 1, 19-34.

Sobrino, J. A., Li, Z-L., Stoll, M. P. and Becker, F. (1994), Improvements in the split window technique for land surface temperature determination. *IEEE Transactions on Geoscience and Remote Sensing*, 32(2): 243-253.

Sobrino, J. A., Li, Z-L., Stoll, M. P. and Becker, F. (1996), Multi-channel and multi-angle algorithms for estimating sea and land surface temperature with ATSR. *Intional Journal of Remote Sensing*, 17(11): 2089-2114.

Sobrino, J. A., El Kharraz, M. H., Cuenca, J. and Raissouni, N, (1998). Thermal inertia mapping from NOAA-AVHRR data. *Advances in Space Research*, 22(5): 665-667.

Sobrino, J. A., Raissouni, N., Simarro, J., Nerry, F. and Petitcolin, F. (1999). Atmospheric water vapor content over land surface derived from the AVHRR data: Application to the Iberian Peninsula. *IEEE Transactions on Geoscience and Remote Sensing*, Vol. 37, No. 3, 1425-1434.

Sobrino, J. A. and Raissouni, N. (2000). Toward remote sensing methods for land cover dynamic monitoring: Application to Morocco. *International Journal of Remote Sensing*, 21: 353-366.

Sobrino, J. A., Raissouni, N. and Li, Z. L. (2001). A comparative study of land surface emissivity retrieval from NOAA data. *Remote Sensing of Environment*, 75, 256-266.

Sobrino, J. A. and Romaguera, M. (2004). Land surfacemperature retrieval from MSG1-SEVIRI data. *Remote Sensing of Environment*, 92, 247-254.

Sòria, G., Sobrino, J. A., Cuenca, J., Prata, A. J., Jiménez-Muñoz, J. C., El-Kharraz, J. and Gómez, M. (2002). Surface temperature retrieval from AATSR data: multichannel and multiangle algorithms, *1st International Symposium Recent Advances in Quantitative Remote Sensing*, Valencia (Spain), 16-20 September, 2002.

Susskind, J., Rosenfield, J., Reuter, D. and Chahine, M. T. (1984). Remote Sensing of weather and climate parameters from HIRS2/MSU on TIROS-N. *Journal of Physical Research*, Vol. 89, No. D3, 4677-4697.

Sutherland, R. A. (1979). Broadband and spectral emissivities of natural sands and vegetation (2-20 μm). *Journal of Atmospheric and Oceanic Technology*, 3, 199-202.

Tarpley, D., (1994). Monthly evapotranspiration from satellite and conventional meteorological observations. *Journal of Climate*, 7: 704-713.

Teillet, P. M., Barker, J. L., Markham, B. L., Irish, R. R., Fedosejevs, G. and Storey, J. C. (2001). Radiometric cross-calibration of the Landsat-7 ETM+ and Landsat-5 TM sensors based on tandem data sets. *Remote Sensing of Environment*, 78, 39-54.

Trokhimovski, Y. G., Westwater, E. R., Han, Y. and Leuski, V. Y. (1998). Air and sea surface temperature measurements using a 60-GHz microwave rotating radiometer. *IEEE Transactions on Geoscience and Remote Sensing*, Vol. 36, No. 1, 3-15.

Valor, E. and Caselles, V. (1996). Mapping land surface emissivity from NDVI: Application to European, Africa, and South American areas. *Remote Sensing of Environment*, 57: 167-184.

Van-De-Griend, A. A. and Owe, M. (1993). On the relationship between thermal emissivity and the normalized difference vegetation index for natural surface. *International Journal of Remote Sensing*, vol. 14, no. 6: 2449-2460.

Vincent, R. K., Rowan, L. C., Gillespie, R. E. and Knapp, C. (1975). Thermal-infrared spectra and chemical analyses of twenty-six igneous rock samples. *Remote Sensing of Environment*, 4: 199-209.

Vermote, E. F. and Saleous, N. Z. (2006). Calibration of NOAA16 AVHRR over a dersert site using MODIS data. *Remote Sensing of Environment*, 105, 214-220.

Vidal, A. (1991). Atmospheric and emissivity correction of land surface temperature measured from satellite using ground measurements or satellite data. *International Journal of Remote Sensing*, vol. 12, No. 12, 2449-2460.

Walthall, C. L., Norman, J. M., Welles, J. M., Gampbell, G., and Blad, B. L. (1985). Simple eqution to approximate the bidirectional reflectance from vegetation canopies and bare soil surfaces. *Applied Optics*, Vol. 24, 383-387.

Wan, Z., and Dozier, J. (1989). Land-surface temperature measurement from space: physical principles and inverse modeling. *IEEE Transections on Geoscience and Remote Sensing*, Vol. 27, No. 3, 268-278.

Wan, Z. and Dozier, J. (1996). A generalized split-window algorithm for retrieving land-surface temperature from space. *IEEE Transections on Geoscience and Remote Sensing*, Vol. 34, No. 4, 892-905.

Wan, Z., and Li, Z. L. (1997). A physics-based algorithm for retrieving land-surface emissivity and temperature from EOS/MODIS data. *IEEE Transections on Geoscience and Remote Sensing*, Vol. 35, No. 4, 980-996.

Wan, Z., Zhang, Y., Zhang, Q. and Li, Z. L. (2002). Validation of the land-surface temperature products retrieved from Terra Moderate Resolution Imaging Spectroradiometer data. *Remote Sensing of Environment*, 83, 163-180.

Wan, Z., Zhang, Y., Zhang, Q. and Li, Z.-L. (2004). Quality assessment and validation of the MODIS global land surface temperature. *International Journal of Remote Sensing*, **25,** 261-274.

Wanner, W., Li, X., and Strahler, A. H. (1995). On the derivation of kernels for kernel-driven models of bidirectional reflectance. *Journal of Geophisical Research*, Vol. 100, No. D10, 21,077-21,089.

Watson, K. (1992a). Spectral ratio method for measuring emissivity. *Remote Sensing of Environment*, 42, 113-116.

Watson, K. (1992b). Two-temperature method for measureing emissivity. *Remote Sensing of Environment*, 42, 117-121.

Xiong, X., Chiang, K., Guenther, B. and Barnes, W. (2002). MODIS Thermal Emissive Bands Calibration Algorithm and On-orbit Performance. *Proceedings SPIE, Optical Remote Sensing of the Atmosphere and Clouds III*, Vol. 4891.

Xiong, X., Chiang, K., Esposito, J., Guenther, B. and Barnes, W. (2003). MODIS On-orbit Calibration and Characterization, *Metrologia*, Vol. 40, S89-S92.

ABSTRACT:

This thesis focuses on the retrievals of land surface emissivity and land surface temperature from MSG1-SEVIRI data. The primary work includes:

(1) Cross-calibrations of MSG1-SEVIRI infrared channels 4, 9 and 10 with the channels of Terra-MODIS. Two methods, the ray-matching method and the radiative transfer modeling method, were applied. The results reveal that calibration discrepancies exist between SEVIRI and MODIS channels. The use of the results obtained by the radiative transfer modeling to re-calibrate the SEVIRI data is recommended.

(2) Land surface emissivity retrievals from MSG1-SEVIRI data. LSEs in SEVIRI channels 4, 7, 9 and 10 over large areas and in long term were estimated based on the TISI concept. A new atmospheric correction scheme was developed mainly based on the DTC model, and two BRDF models, the modified Minnaert's model and the RossThick-LiSparse-R model, were evaluated.

(3) Land surface temperature retrievals from MSG1-SEVIRI data and AATSR data. The single channel method and the split-window method were used. The generalized split-window algorithms were developed for the SEVIRI and AATSR instruments using MODTRAN fed with the adjusted profiles of the standard model atmospheres, and then applied to the LST retrievals from the SEVIRI and AATSR data.

(4) SEVIRI LST cross-validations with the MODIS/Terra LST products and AATSR LSTs. The SEVIRI LSTs were directly compared with the LSTs extracted from the MODIS/Terra LST products and the AATSR Forward LSTs estimated by the generalized split-window method over the Iberian Peninsula area and the Egypt and Middle East area. The results reveal that the SEVIRI LSTs agree with the LSTs extracted from the MODIS/Terra LST products and the AATSR LST with accuracy of 1-2 K.

Key words: MSG1-SEVIRI, Cross-calibration, Land surface emissivity (LSE), Land surface temperature (LST), Cross-validation.

RESUME

Les objectifs de cette thèse sont concentrés sur la détermination de l'émissivité (LSE) et de la température de surface (LST) des surfaces terrestres à partir des données de MSG1-SEVIRI.

Dans un premier temps l'inter-calibrage des canaux infrarouges 4, 9 et 10 de MSG1-SEVIRI avec les canaux de Terra-MODIS est réalisé. Deux méthodes, la méthode « ray-matching » et une méthode basée sur l'équation transfert radiatif ont été appliqués. Les résultats indiquent que les anomalies de calibrage existent entre les canaux de SEVIRI et de MODIS. L'utilisation des résultats obtenus par la méthode basée sur le transfert radiatif pour recalibrer les données de SEVIRI est recommandée. Ce recalibrage permet de supprimer la surestimation des LSTs obtenues à partir des données de SEVIRI avec une méthode Split-Window.

Les émissivités sont ensuite estimées dans les canaux 4, 7, 9 et 10 sur des grandes étendues spatiales et temporelles en utilisant une méthode basée sur le concept des TISI. Une nouvelle méthode de corrections atmosphériques a été développée, principalement basée sur le modèle de DTC (Diurnal Time Cycle), et deux modèles de BRDF, le modèle du Minnaert modifié et le modèle de RossThick-LiSparse-R, ont été évalués.

Les températures de surface sont déterminées à partir des données MSG1-SEVIRI et AATSR. La méthode mono canal simple et la méthode Split Window ont été utilisées. Les algorithmes généralisés de Split Window ont été développés pour les instruments SEVIRI et AATSR en utilisant le code MODTRAN et les profils atmosphériques standards et ont été appliqués avec succès aux déterminations des LST à partir des données de SEVIRI et d'AATSR.

Les températures de surface obtenues à partir de SEVERI ont été validées par comparaison directe avec les produits MODIS/Terra LST et les AATSR LST estimées par la Split Window généralisée au-dessus de la péninsule ibérienne et d'une région de l'Egypte et du l'Moyen-est. Les résultats indiquent que les LST SEVIRI sont conformes au LST extraites des produits MODIS/Terra LST et AATSR LST avec une exactitude comprise entre 1-2 K.

Mots-cles: MSG1-SEVIRI; Inter-étalonnage; L'émissivité de surface; La température de surface; Inter-validation